



CZECH TECHNICAL UNIVERSITY IN PRAGUE

**Faculty of Civil Engineering
Department of Mechanics**

Quasicontinuum-inspired modeling of inelastic materials

DOCTORAL THESIS

Ing. Karel Mikeš

Doctoral study programme: Physical and Materials Engineering
Branch of study: Civil Engineering

Doctoral thesis supervisor: Prof. Ing. Milan Jirásek, DrSc.

Prague, 2021



DECLARATION

Ph.D. student's name: Karel Mikeš

Title of the doctoral thesis: Quasicontinuum-inspired modeling of inelastic materials

I hereby declare that this doctoral thesis is my own work and effort written under the guidance of the supervisor Prof. Ing. Milan Jirásek, DrSc.

All sources and other materials used have been quoted in the list of references.

The doctoral thesis was written in connection with the following research projects:
Czech Science Foundation projects Nos. 14-00420S and 17-04150J. European
Regional Development Fund project No. CZ.02.1.01/0.0/0.0/16_19/0000778.

In Prague on 15. 4. 2021

.....
signature

Abstract

The QuasiContinuum (QC) method is a concurrent multiscale technique combining the accurate but expensive atomistic/particle description only in regions where it is required with a cheap continuum approximation elsewhere. The QC method was originally introduced in 1996 to simplify large atomistic systems with long-range conservative interaction potentials.

In the first part of the thesis, the QC method is extended to irregular lattices with elastic and elastic-brittle axial interactions. In the proposed extension, an effective stiffness tensor is assembled from geometry of the lattice to represent the homogenized irregular lattices in the region of low interest. Five different homogenization-based QC approaches with various levels of simplification are proposed.

The next part of the thesis is focused on adaptive algorithms for QC simulation. Firstly, an adaptive scheme for modeling of elastic-brittle disordered lattices is introduced with a refinement criterion based on identification of broken links according to their maximal strain. Then, three different adaptive refinement indicators for regular atomic lattices in the classical QC method are proposed. The proposed indicators are based on (i) the Zienkiewicz–Zhu criterion (used for the deformation gradient), (ii) local atoms' site energy, and (iii) local lattice disregistry.

In the next part, the QC approaches for elastic irregular lattices, introduced in the first part, are further extended to plastic interactions. For that purpose, certain ideas of the microplane theory are adopted and analogy between the disordered particle model and microplane model is used to derive a microplane-based summation rule for the QC method. Furthermore, an additional refinement criterion based on the strain of individual microplanes is proposed for adaptive simulations.

The final part of the thesis provides a thorough comparison of the QC method with another class of multiscale techniques. In this class of so-called homogenization-based methods, first the discrete system is homogenized into an equivalent continuum formulation, into which the main phenomena are added through specific enrichments. Comparison of the two different modeling philosophies in terms of their accuracy, performance, and theoretical framework is realized for two examples with microstructures at the nano- and meso-scale level.

Accuracy, efficiency, and specific properties of all methods proposed in this thesis are evaluated by comparison of results with the fully resolved particle model in various numerical examples that reveal their strengths and weaknesses.

Abstrakt

Metoda kvazikontinua je hojně využívaná technika víceúrovňového modelování, která spočívá v použití přesného, ale výpočetně náročného atomistického nebo částicového modelu pouze v místech, kde je to vyžadováno, v kombinaci s jednoduchým spojitým modelem ve zbytku oblasti. Tato metoda byla původně navržena v roce 1996 pro zjednodušení velkých soustav atomů interagujících pomocí konzervativních potenciálů dlouhého dosahu.

V první části této práce je metoda kvazikontinua rozšířena na nepravidelné mřížky s pružnými a pružnokřehkými osovými interakcemi. Navrhované rozšíření využívá efektivní tenzor tuhosti, který je sestaven na základě geometrie jednotlivých nepravidelných vazeb. V oblasti, kde je aplikováno zjednodušení, jsou následně tyto vazby reprezentovány pomocí homogenizovaného materiálu. Je navrženo celkem pět homogenizačních přístupů, které uvažují různý stupeň zjednodušení.

Další část práce je zaměřena na adaptivní algoritmus pro metodu kvazikontinua. Nejprve je představeno adaptivní schéma pro modelování nepravidelných mřížek s pružnokřehkými vazbami. Pro toto schéma je použito adaptivní kritérium založené na identifikaci porušených vazeb na základě jejich maximální dosažené deformace. Dále jsou navržena tři různá adaptivní kritéria pro pravidelné atomární mřížky. Tato kritéria využívají (i) indikátor typu Zienkiewicz–Zhu aplikovaný na deformační gradient, (ii) lokální energii vazeb v okolí atomu a (iii) lokální narušení pravidelnosti mřížky.

V další části je metoda kvazikontinua pro nepravidelné mřížky, která byla prezentována v první části, dále rozšířena pro pružnoplastické vazby. Zde je použité zjednodušení inspirováno myšlenkou pocházející z teorie mikroploškového materiálu a analogie mezi nepravidelným částicovým modelem a spojitým mikroploškovým modelem je využita k odvození mikroploškového sumačního pravidla pro metodu kvazikontinua. Dále je navržen adaptivní indikátor využívající hodnoty deformace na jednotlivých mikroploškách.

Poslední část práce představuje detailní porovnání metody kvazikontinua s další třídou víceúrovňových technik pro modelování materiálů. V této třídě tzv. homogenizačních metod je nejprve diskrétní materiál nahrazen odpovídajícím spojitým modelem, ve kterém jsou následně důležité materiálové jevy modelovány pomocí speciálních dodatečných obohacení. Porovnání přesnosti, výkonosti a teoretického hlediska těchto dvou odlišných metodologií je provedeno pro dva různé příklady s mikrostrukturou jak na mikro měřítku, tak i na středním měřítku.

Přesnost, efektivita a jednotlivá specifika všech metod navržených v této práci jsou vyhodnoceny na základě porovnání s přesným částicovým modelem. Pro tento účel byla použita celá řada příkladů, které odhalují jejich jednotlivé přednosti a slabiny.

Acknowledgement

First and foremost, I would like to express my deepest gratitude to my supervisor, Milan Jirásek, for his invaluable advice and friendly supervision. His immense knowledge and plentiful experience have encouraged me in all the time of my academic career. I would also like to thank to all my colleagues, friends, and especially office mates at Czech Technical University in Prague for making such a positive and friendly atmosphere. Special thanks go to Martin Horák for his willing help with solving OOFEM issues.

Hereby I would like to thank Ron H.J. Peerlings and Ondřej Rokoš from Eindhoven University of Technology (TU/e) for their hospitality and collaboration during my stay in Eindhoven. I would also like to thank Jan Zeman for his cooperation and project support which gave me an opportunity to study abroad.

Most importantly, my appreciation also goes out to my family for their support all through my studies.

The work was supported by the Czech Science Foundation, projects Nos. 14-00420S and 17-04150J. This research has been performed in the Center of Advanced Applied Sciences (CAAS), financially supported by the European Regional Development Fund (project No. CZ.02.1.01/0.0/0.0/16_19/0000778). Continued support by the Grant Agency of the Czech Technical University in Prague through student projects Nos. SGS15/031/OHK1/1T/11, SGS16/038/OHK1/1T/11, SGS17/043/OHK1/1T/11, SGS18/037/OHK1/1T/11, SGS19/032/OHK1/1T/11, and SGS20/038/OHK1/1T/11 is also gratefully acknowledged.

Contents

1	Introduction	1
2	Quasicontinuum method extended to irregular lattices	5
2.1	Introduction	6
2.2	Methods	8
2.2.1	Overview	8
2.2.2	Generation of input geometry	8
2.2.3	Application of simplifying rule	9
2.2.4	Numerical simulation	14
2.2.5	Error measures	14
2.3	Simple tests of elastic response	15
2.3.1	Two-dimensional periodic lattices	15
2.3.2	Two-dimensional lattices with randomized cells	18
2.3.3	Two-dimensional tests – conclusions	25
2.3.4	Three-dimensional patch tests	25
2.4	Failure simulations	28
2.4.1	Cylindrical fully resolved domain	29
2.4.2	Fully resolved domain for crack propagation	30
2.4.3	Large-scale computations	35
2.5	Conclusions and future work	39
3	Adaptive quasicontinuum simulation of disordered lattices	45
3.1	Introduction	46
3.2	QC method	46
3.2.1	Interpolation	46
3.2.2	Summation	46
3.2.3	Adaptivity	47
3.3	QC-based approaches	47
3.3.1	Fully resolved approach	47
3.3.2	QC approach with interpolation	47
3.3.3	QC approach with interpolation and homogenization	48
3.4	Adaptive algorithm	48
3.4.1	Area of high interest update	48
3.4.2	Interpolation mesh update	49
3.4.3	Stiffness tensors update	49
3.5	Results	50
3.6	Conclusions	53
4	Adaptive quasicontinuum simulation for molecular statics	55
4.1	Introduction	56
4.2	Full atomistic model	56
4.3	Quasicontinuum Method	57

4.3.1	Interpolation	59
4.3.2	Summation	59
4.3.3	Adaptivity	60
4.4	Results	61
4.5	Conclusions	64
5	Quasicontinuum method combined with microplane model	67
5.1	Introduction	68
5.2	The idea of quasicontinuum method	69
5.2.1	Interpolation	69
5.2.2	Summation	69
5.2.3	Adaptivity	70
5.3	Elastoplastic microplane model	71
5.3.1	Basic equations	71
5.3.2	Analysis of macroscopic response	73
5.3.3	Comparison of particle model and microplane model	82
5.3.4	Extension to additional material phenomena	85
5.4	Microplane-base quasicontinuum approaches with different level of simplification	85
5.4.1	Fully resolved particle model approach (A0)	85
5.4.2	Interpolated model with explicit summation (A1)	85
5.4.3	Microplane-based summation rule	86
5.4.4	Microplane-based global homogenization approach (A2)	87
5.4.5	Microplane-based local homogenization approach (A3)	87
5.4.6	Microplane-based adaptive refinement criterion	88
5.5	Results	88
5.5.1	2D patch tests	89
5.5.2	2D clustering analysis	93
5.5.3	3D patch tests	96
5.5.4	3D bar tension test with area of high interest	99
5.5.5	Adaptive bending test (2D)	101
5.5.6	L-shaped specimen with softening and crack localization	103
5.6	Conclusion	105
6	Comparison of multiscale techniques	107
6.1	Introduction	108
6.1.1	Quasicontinuum based approach	108
6.1.2	Homogenization based approach	110
6.1.3	Objectives	111
6.1.4	Outline and notation	111
6.2	Molecular statics: dislocation transmission across a phase boundary	112
6.2.1	Full atomic model	112
6.2.2	Quasicontinuum model	115
6.2.3	Peierls–Nabarro formulation	117
6.2.4	Calibration	118
6.2.5	Results and comparison	120
6.3	Lattice model: crack propagation in a concrete specimen	126
6.3.1	Full lattice model	126
6.3.2	Quasicontinuum model	129

6.3.3	Finite element cohesive zone model	130
6.3.4	Calibration	131
6.3.5	Results and comparison	132
6.4	Summary and conclusion	137
7	Conclusions and summary	141
7.1	Potential extensions	143
	References	145

Chapter 1

Introduction

Numerical modeling of material behavior plays an important role across all engineering fields. At sufficiently large scales, almost all existing materials can be considered as a continuum, whereas at smaller scales, some materials such as foams, textiles, concrete, or paper reveal discrete microstructures. Once we take a look even closer, at the smallest possible scale, i.e., nano-scale, all materials become discrete and their behavior is dictated by the underlying atomic lattice. For materials where localized mechanical phenomena such as the nucleation and propagation of dislocations, cracks, or other defects play an important role, the inherently non-local behavior of the underlying discrete microstructure becomes essential to obtain the exact macroscopic response. To capture those non-localities that dictate the final response of material, sufficiently accurate numerical models are required. The most accurate option is to use discrete models that fully resolve the microstructure (at a sufficient scale) and hence inherently incorporate the underlying non-locality at the level of the individual interactions.

However, simulations of large problems with fully refined microstructure are usually associated with enormous computational costs. Because of this limitation, such models are usually not applicable for practical engineering problems where large samples are modeled or multiple model evaluations are required (e.g., optimization, reliability, or stochastic modeling) even if computational clusters or powerful super computers are used. Therefore, multiple numerical techniques have been developed to simplify full-scale simulations of large problems by combining modeling approaches on different scales. This thesis is focused on extension and analysis of one particular representative of those multi-scale techniques, namely the QuasiContinuum (QC) method, which combines an accurate but expensive discrete description with a cheaper continuum approximation.

The main idea of the QC method is to reduce the number of degrees of freedom (DOFs) and the associated computational cost without losing the exact atomistic/particle description in regions where it is required. Therefore, the investigated domain is divided into two parts: (i) the fully-resolved region (so-called region of high interest), in which the full non-local discrete model is used, seamlessly coupled with (ii) a coarse-grained continuum region (so-called region of low interest), in which continuum assumptions are applied and the computational model is significantly simplified. The procedure that results from the QC method can be briefly presented in the following three steps:

1. *Interpolation* of DOFs is used in regions of low interest. To simplify the full particle model, only a small subset of particles is selected to represent the kinematic behavior of the entire system. These so-called renodes (representative nodes) serve as the

nodes of a background triangular finite element mesh that is used to interpolate the DOFs of other particles in regions of low interest.

2. *Summation* efficiently estimates the stored energy and internal forces of the system in which the interpolation step has been applied. The contribution of all particles in each interpolation element is estimated based on so-called sampling nodes and proper scaling of their contribution given by a corresponding summation scheme.
3. *Adaptivity* provides suitable changes of the regions of high interest during the simulation process according to a specific refinement criterion. An appropriate modification of the regions of high interest leads to a substantial increase of accuracy. Moreover, in specific cases such as simulation of crack propagation or damage evolution, adaptivity is necessary in order to represent the correct physical behavior.

The QC method was originally introduced in 1996 by Tadmor et al. [99, 100] to simplify large atomistic systems with long-range conservative interaction potentials. The original version of the QC method has been successfully used for simulation of localized phenomena, such as crack nucleation and propagation [45, 67], motion and interaction of dislocations [80], or nanoindentation [46, 96]. An overview of applications and current directions of the original QC methods has been provided by Miller and Tadmor in [69, 68, 95] and in part IV of their book [98]. Afterwards, the application of QC methods has been successfully extended to other lattices and interaction potentials. The extension to regular discrete lattice networks with short-range nearest-neighbor interactions was provided by Beex et al. for both conservative [11, 12] and non-conservative [13, 14] interaction potentials including dissipation and fiber sliding. A further extension was provided for planar beam lattices [16, 10] and general periodic beam lattices with nonlinear deformations [81]. The energy-based variational formulation of the dissipative QC method has been developed by Rokoš et al. for a regular lattice with plasticity [83] and localized damage [85, 84]. Additional research focused, for example, on the finite-temperature QC method [35, 97], goal-oriented adaptivity [3, 58], or a meshless QC method developed by Kochmann et al. [48]. The extension of QC method to irregular lattices was provided as a part of this thesis [65] and has been recently applied to irregular polymer networks [38].

To extend the existing concept of QC method and expand its applicability to additional materials and phenomena, the objectives of this thesis were the following:

- i) Provide further extensions of the original concept of the QC method especially for applications to materials with disordered microstructure and various inelastic material phenomena.
- ii) Design an algorithmic framework for adaptive QC modeling of materials with inelastic disordered microstructures including its implementation in OOFEM [75], an open-source object-oriented code.
- iii) Demonstrate the applicability, accuracy, and efficiency of the proposed QC framework.

The presented thesis is a collection of five individual manuscripts (three already published and two under review) presented in Chapters 2-6 that are related to extending the original concept of QC method and address the above-mentioned objectives. In these manuscripts, the author of this thesis performed most of the work, including implementation of the proposed algorithms and material models, post-processing and interpretation of

results, and writing the manuscripts. Other authors contributed mainly to formulation of methodologies, reviewing the manuscripts, and supervising the research directions. With only one exception, all the results presented within this thesis have been obtained by the author of this thesis. Only the results of Peierls–Nabarro model presented in section 6.2.3 for the purpose of comparison with the QC simulation were provided by Franz Bormann [19] from the Eindhoven University of Technology as a part of his Ph.D. thesis.

The second chapter of this thesis is focused on development of QC method for irregular lattices with axial elastic interactions. To simplify the energy of irregular lattices, the homogenization-based summation rule is derived and lattice network in the region of low interest is represented by effective stiffness tensor which can be assembled from geometry of the lattice. Five different homogenization approaches with various levels of simplification have been proposed. Their accuracy and efficiency have been evaluated in two- and three-dimensional patch test and then those approaches were used to model crack propagation in elastic-brittle disordered lattice.

Next two chapters are dedicated to adaptive algorithms for QC simulation. Namely in Chapter 3, an adaptive scheme is developed for modeling of elastic-brittle disordered lattices considered in Chapter 2. In this case, a refinement criterion is based on identification of broken links according to their maximum strain. Chapter 4 then proposes three different adaptive refinement indicators for regular atomic lattices in classical QC method. The proposed indicators are based on (i) the Zienkiewicz–Zhu criterion (used for the deformation gradient), (ii) local atoms' site energy, and (iii) local lattice disregistry.

In Chapter 5, the QC approaches for elastic irregular lattices, proposed in Chapter 2, are further extended to plastic interactions. For that purpose, the concept of microplane material [8] is used to homogenized disordered interactions. The microplane-based summation rule for QC method is derived from relation between particle model and microplane model. And for adaptive simulations, a new refinement criterion based on strain of individual microplanes is proposed.

Finally, Chapter 6 provides a thorough comparison of two different classes of multiscale techniques. The first class, represented by the QC method, considers the fully-resolved discrete system, which is subsequently reduced through suitable mathematical tools such as projection and reduced integration. The second class of methods first homogenizes the discrete system into an equivalent continuum formulation, to which the main phenomena are added through specific enrichments. Comparison of the two different modeling philosophies in terms of their corresponding theoretical framework and resulting performance is realized for two examples with microstructures at the nano- and meso-scale level.

The last chapter then summarizes the thesis and discusses additional potential extensions and outlooks for future work. Since each of Chapters 2-6 is represented by a standalone publication, certain overlaps may occur mainly in the introductory parts of each chapter where the main idea of QC method is repeatedly explained.

Chapter 2

Quasicontinuum method extended to irregular lattices

Abstract:

The quasicontinuum (QC) method, originally proposed by Tadmor, Ortiz and Phillips in 1996, is a computational technique that can efficiently handle regular atomistic lattices by combining continuum and atomistic approaches. In the present work, the QC method is extended to irregular systems of particles that represent a heterogeneous material. The paper introduces five QC-inspired approaches that approximate a discrete model consisting of particles connected by elastic links with axial interactions. Accuracy is first checked on simple examples in two and three spatial dimensions. Computational efficiency is then assessed by performing three-dimensional simulations of an L-shaped specimen with elastic-brittle links. It is shown that the QC-inspired approaches substantially reduce the computational cost and lead to macroscopic crack trajectories and global load-displacement curves that are very similar to those obtained by a fully resolved particle model.

Introduction

Discrete particle models use a network of particles interacting via discrete links or connections that represent a discrete microstructure of the modeled material. An advantage of this approach is that discrete models can naturally capture small-scale phenomena. Therefore, a variety of sophisticated discrete material models have been developed and applied in simulations of materials such as paper [52], textile [17, 15], fibrous materials [106, 82, 49], woven composite fabrics [79] or fiber composites [9]. Extensive effort has been invested into the formulation of a discrete model of concrete [42, 29, 51, 53].

Discrete mechanical models can accurately capture complex material response, especially localized phenomena such as damage or plastic softening. However, they suffer from two main disadvantages. Firstly, a large number of particles is needed to realistically describe the response of large-scale physically relevant models. This results in huge systems of equations, which are expensive to solve. Secondly, the process of assembling of this system is also computationally expensive because all discrete connections must be individually taken into account.

Both of the aforementioned disadvantages of discrete particle models can be removed by using simplified continuous models based on one of the conventional homogenization procedures. However, standard continuous models cannot capture localized phenomena in an objective way and require enrichments, e.g., by nonlocal and gradient terms, which are again computationally expensive. According to Bažant [7], the most powerful approach to softening damage in the multi-scale context is a discrete (lattice-particle) simulation of the mesostructure of the entire structural region in which softening damage can occur.

Another way to reduce the computational cost of discrete particle models is a combination of a simplified continuous model with an exact discrete description in the parts where it is needed. Such a combination of two different approaches entails that some hand shaking procedure is needed at the interface between the continuous and discrete domains [28]. The quasicontinuum (QC) method is a suitable technique combining the advantages of continuous models with the exact description of discrete particle models without additional coupling procedures.

The quasicontinuum method was originally proposed by Tadmor, Ortiz and Phillips [99, 100] in 1996. The original purpose of this computational technique was a simplification of large atomistic lattice models described by long-range conservative interaction potentials. Since that time, QC methods have been widely used to investigate local phenomena of atomistic models with long-range interactions [28, 95]. Recently, the application of QC methods has been successfully extended to other lattices and interaction potentials. For example, an application of the QC method to structural lattice models of fibrous materials with short-range nearest-neighbour interactions has been developed by Beex et al. for conservative [12] and non-conservative [13, 14] interaction potentials including dissipation and fiber sliding as well as for planar beam lattices [16], still applied to regular lattices only. An overview of applications and current directions of QC methods has been provided by Miller and Tadmor in [69, 68, 95] and in part IV of their book [98]. In last few years, a variational formulation of dissipative QC method has been done by Rokoš et al. [83], a goal-oriented adaptive version of QC algorithm has been introduced in [58] or a meshless QC method has been developed by the Kochmann research group [48]. But the application of all mentioned QC methods is still restricted only to systems with a regular geometry of particles.

In the present work, we extend the QC approach to irregular systems of particles with

short-range interactions by axial forces. The main idea has been tentatively presented in a conference paper [62]. Here we proceed to a more systematic evaluation of the performance of various QC formulations applied to systems with elastic-brittle links. The proposed models are implemented in OOFEM [76, 77, 75], an open-source object-oriented simulation platform initially developed for finite element methods but extensible to other discretization methods.

The procedure that results from the QC method combines the following three ingredients:

1. Interpolation of particle displacements is used in the regions of low interest. Only a small subset of particles is selected to characterize the behavior of the entire system. These so-called *repnodes* (representative nodes) are used as nodes of an underlying triangular finite element mesh, and the displacements of other particles in the region of low interest are interpolated. In the regions of high interest, all particles are selected as repnodes, in order to provide the exact resolution of the particle model. This interpolation leads to a significant reduction of the number of degrees of freedom (DOFs) without inducing a large error in the regions of high interest.
2. A summation rule can be applied in order to eliminate the requirement of visiting all particles during assembly of the global equilibrium equations. If such a rule is not imposed, all particles need to be visited to construct the system of equations, which makes the process computationally expensive. If the summation rule is adopted, the contribution of all particles in each interpolation triangle is estimated based on sampling of the links that surround one single particle and proper scaling of their contribution. This makes the computational process faster, but some problems occur on the interface between regions of high and low interest. The piecewise linear interpolation of displacements combined with the summation rule means that the deformation is considered as constant within each interpolation element in the regions of low interest, while the deformations of individual links in the regions of high interest are evaluated exactly. Consequently, forces of nonphysical character, called the ghost forces, appear on the interface [69, 90].

In our work, the summation procedure is based on homogenization of link networks contributing to the interpolation elements. Some of the links (truss elements) are selected to be processed exactly, in order to properly treat the interface between the exactly solved and interpolated domains and thus to eliminate the ghost forces.

3. Adaptivity provides suitable changes of the regions of high interest during the simulation process. A new triangulation of the interpolation mesh could be done, but this is actually not necessary because the type of region can be changed by adding repnodes before each step. A suitable change of the regions of high interest may lead to a substantial increase of accuracy and, in several specific cases, it is necessary in order to represent the correct physical behavior, e.g., in a crack propagation process. In numerical examples presented in this paper, sufficiently large fixed areas of high interest are used and additional changes during simulations do not need to be considered. For periodic lattices, efficient adaptive QC techniques have been developed in [58, 90].

Methods

Overview

The original QC approach was developed for regularly arranged crystal lattices, in which atoms interact at a longer distance (not just with immediate neighbors) and the interaction forces can be derived from suitable potentials. In regions of low interest, displacements were interpolated in a piecewise linear fashion, using a selected set of representative atoms (repatoms). In this context, imposition of an affine displacement field on the periodic crystal lattice can be interpreted as an application of the Cauchy-Born rule.

In the present paper, we focus on discrete particle systems with short-range elastic or elastic-brittle interactions. Such systems are typically used in simulations of heterogeneous materials. Particles in these systems are distributed randomly and, in contrast to atomistic systems, do not form regular lattices, but the idea of QC can still be used.

Three approaches based on the QC idea are introduced here and are compared with the fully resolved particle model, which is considered as the reference case. Accuracy is assessed in terms of displacement and strain errors. The number and position of repnodes are adapted to achieve the optimal result.

The computational procedure consists of the following steps:

- generation of particles and of connecting links,
- selection of repnodes and generation of interpolation elements,
- application of a simplification rule,
- assembly of global equations with renode displacements as basic unknowns,
- solution of global equations (for nonlinear models using an incremental-iterative scheme),
- post-processing of results and error evaluation.

The details of individual steps are described in the following subsections.

Generation of input geometry

In the first step, the input geometry of the particle system is generated; it is specified by the position of all particles in the system and by the information which pairs of particles are connected by links. This process depends on the type of represented material.

The second step consists of renode selection and generation of interpolation elements. There are two possible reasons why a certain particle is selected as a renode:

1. All particles located in a region of high interest are selected as repnodes to represent the “exact” behaviour in this region.
2. In regions of low interest, a sufficient number of repnodes are needed to construct the approximation of the displacements of other particles. Such repnodes represent vertices of the interpolation elements. The basic triangulation is constructed by the T3D mesh generator [86]. Subsequently, all newly created vertices of the mesh elements are either added as new repnodes, or shifted to the position of the nearest particles, which become repnodes. The second option results in a smaller number

of links that need to be solved explicitly on the interface between regions of high and low interest. Therefore, shifting the position of all mesh nodes to the nearest particles is used in all examples presented here.

Application of simplifying rule

Once the input geometry is given, it is possible to apply a suitable simplifying rule based on the idea of QC. In this paper, five approaches using various levels of simplification are considered.

Pure particle approach (A0)

This approach does not use any simplification and corresponds to the reference model. Only the particles and links defining the particle model are used as input. Reprnodes and interpolation elements are not needed. Every single particle represents a node with independent DOFs (displacements) and the links are described by 1D truss elements (i.e., only axial interaction between particles is considered). Consequently, all links are taken into account explicitly and contribute directly to the internal forces and to the stiffness matrix.

This approach fully resolves the “exact” particle model, and the corresponding results are used as a reference solution for evaluation of accuracy and efficiency of the simplified approaches, to be presented next. Note that the simple discrete model considered here is limited in application to materials with microstructural interactions dominated by pure stretching.

Hanging node approach (A1)

The first technique which exploits the QC idea for simplification of the full particle model is based on approximation of DOFs of those particles that have not been selected as reprnodes. Such particles are called the hanging nodes because their DOFs are not independent unknowns but are “hanging” on auxiliary elements with displacements interpolated from the neighboring reprnodes. Linear triangular (2D) or tetrahedral (3D) interpolation elements with vertices at the reprnodes are used here. For each hanging node, the corresponding interpolation element is found. It is either the element in which the hanging node is located, or the nearest element if the hanging node is not located in any interpolation element, which sometimes occurs at a curved part of the physical boundary of the particle system; see Figure 2.1.

The displacement of each hanging node (grey) is a linear combination of the displacements of the vertices of the corresponding interpolation element (black). This means that DOFs of all hanging nodes are interpolated (or extrapolated) using the DOFs of reprnodes as the primary unknowns. Linear interpolation is used.

All links (truss elements connecting particles) contribute to the structural stiffness matrix, but only the reprnodes possess independent DOFs. The reprnodes represent the nodes of interpolation mesh elements. These elements are used only for approximation of displacements of the nodes not selected as reprnodes and do not provide a direct contribution to the internal force vector and the structural stiffness matrix.

In OOFEM implementation, the particles carrying DOFs (reprnodes) are modeled as regular nodes. The particles with interpolated DOFs (hanging nodes) are represented by a special type of node for which the subset of interpolation elements can be specified.

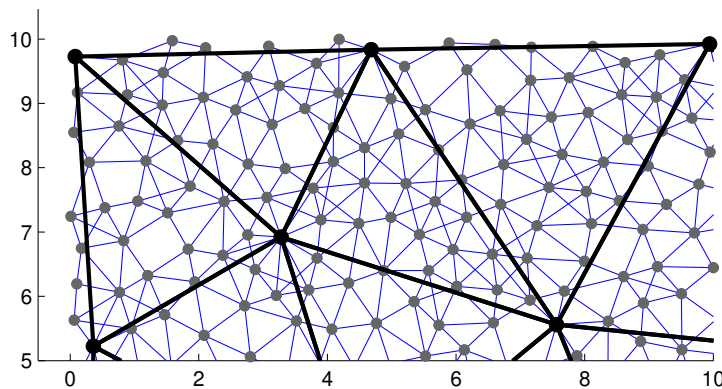


Figure 2.1: Example of an area of low interest, with renodes (black circles), hanging nodes (grey circles), link connections (blue lines) and interpolation elements (triangles plotted by thick black lines)

The nearest interpolation element is taken from this subset and not from all interpolation elements. This technique allows to distinguish overlapping elements on the opposite sides of a crack.

The set of links that contribute to the global equilibrium equations is the same as in the A0 approach. In regions of high interest, all nodes are renodes and the contribution of these regions is the same as in the pure particle approach (A0).

Global homogenization approach (A2)

In regions of low interest, this approach replaces the stiffness that corresponds to the links by the stiffness of 2D or 3D elements “filled” by a fictitious continuum material with properties obtained by homogenization of the discrete network. Thereby, a substantial number of truss elements can be removed from the assembly procedure, and the number of operations is significantly reduced.

In the A2 approach, only one (global) effective elastic stiffness tensor, common to all elements, is assembled from the contribution of all links. Such a tensor can be derived from the Hill-Mandel condition [40, 56], which requires that the virtual macroscopic work density at a point be equal to the average microscopic virtual work in a corresponding volume V_0 of the microstructure. This condition can be written as

$$\delta W_{mac} = \delta W_{mic} \quad (2.1)$$

where

$$\delta W_{mac} = \boldsymbol{\sigma} : \delta \boldsymbol{\varepsilon} \quad (2.2)$$

is the virtual macroscopic work density (i.e., work per unit volume) and

$$\delta W_{mic} = \frac{1}{V_0} \int_{V_0} \boldsymbol{\sigma}_{mic} : \delta \boldsymbol{\varepsilon}_{mic} \, V_0 \quad (2.3)$$

is the average virtual microscopic work density in the discrete microstructure. Here, $\boldsymbol{\sigma}$ and $\boldsymbol{\varepsilon}$ are the macroscopic stress and strain tensors, and $\boldsymbol{\sigma}_{mic}$ and $\boldsymbol{\varepsilon}_{mic}$ are the microscopic stress and strain tensors.

For a microstructure consisting of particles connected by links that transmit axial

forces only, the integral in (2.3) can be replaced by a sum over all links, which leads to

$$\delta W_{mic} = \frac{1}{V_0} \sum_{p=1}^{N_t} L_p A_p \sigma_{Np} \delta \varepsilon_{Np} = \frac{1}{V_0} \sum_{p=1}^{N_t} F_{Np} \delta \Delta L_p \quad (2.4)$$

where N_t is the number of links in volume V_0 , L_p and A_p is the length and cross-sectional area of link number p , σ_{Np} and ε_{Np} is the axial stress and strain in that link, $F_{Np} = A_p \sigma_{Np}$ is the axial force and $\Delta L_p = L_p \varepsilon_{Np}$ is the elongation (change of length).

In analogy to the Cauchy-Born rule used in the original quasicontinuum theory for atomic lattices [91], we will use the simplifying assumption that the microscopic strains (actual strains as well as virtual ones) can be evaluated by projecting the macroscopic strain tensor. This assumption, in microplane theory referred to as the kinematic constraint [71], is written as

$$\varepsilon_{Np} = \mathbf{n}_p \cdot \boldsymbol{\varepsilon} \cdot \mathbf{n}_p = \mathbf{N}_p : \boldsymbol{\varepsilon}, \quad \delta \varepsilon_{Np} = \mathbf{n}_p \cdot \delta \boldsymbol{\varepsilon} \cdot \mathbf{n}_p = \mathbf{N}_p : \delta \boldsymbol{\varepsilon} \quad (2.5)$$

where \mathbf{n}_p is a unit vector specifying the direction of the link and $\mathbf{N}_p = \mathbf{n}_p \otimes \mathbf{n}_p$ is a second-order tensor, introduced for convenience. Based on (2.2)–(2.5), the virtual work equality (2.1) can be rewritten as

$$\boldsymbol{\sigma} : \delta \boldsymbol{\varepsilon} = \frac{1}{V_0} \sum_{p=1}^{N_t} L_p A_p \sigma_{Np} \mathbf{N}_p : \delta \boldsymbol{\varepsilon} \quad (2.6)$$

Since (2.6) should hold for all symmetric second-order tensors $\delta \boldsymbol{\varepsilon}$, and since \mathbf{N}_p is symmetric, the macroscopic stress must be given by

$$\boldsymbol{\sigma} = \frac{1}{V_0} \sum_{p=1}^{N_t} L_p A_p \mathbf{N}_p \sigma_{Np} \quad (2.7)$$

Formula (2.7) provides a rule for the evaluation of the macroscopic stress tensor $\boldsymbol{\sigma}$ from the microscopic stresses, in our case from the axial stresses in individual links, σ_{Np} . The formula is generally applicable, even to inelastic materials. In the particular case of a linear elastic material response, the constitutive behavior of links is described by Hooke's law

$$\sigma_{Np} = E_p \varepsilon_{Np} \quad (2.8)$$

where E_p is the microscopic elastic modulus of link number p (often considered as the same for all links). Substituting (2.8) into (2.7) and exploiting the first part of (2.5), we obtain

$$\boldsymbol{\sigma} = \frac{1}{V_0} \sum_{p=1}^{N_t} L_p A_p E_p \mathbf{N}_p \otimes \mathbf{N}_p : \boldsymbol{\varepsilon} = \mathbf{D}_e : \boldsymbol{\varepsilon} \quad (2.9)$$

where

$$\mathbf{D}_e = \frac{1}{V_0} \sum_{p=1}^{N_t} L_p A_p E_p \mathbf{N}_p \otimes \mathbf{N}_p \quad (2.10)$$

is the fourth-order macroscopic elastic stiffness tensor.

In the A2 approach, the sum in (2.10) is taken over all links of the discrete model, and V_0 corresponds to the volume of the entire domain of analysis. Major and minor symmetries of the computed stiffness tensor \mathbf{D}_e are guaranteed because all these symmetries

are exhibited by the fourth-order tensor $\mathbf{N}_p \otimes \mathbf{N}_p$, for each p . Once the global stiffness tensor is evaluated, the corresponding material parameters are assigned to all 2D and 3D elements. The nature of these parameters depends on the assumed type of material (e.g., isotropic, orthotropic, or general anisotropic).

Continuous elements, which were in the A1 approach considered as interpolation elements for hanging nodes, are now used directly for evaluation of the structural stiffness matrix, based on the material stiffness tensor obtained in the homogenization process. Thus, all hanging nodes with interpolated DOFs and all truss elements connecting them can be removed from the computational model. This leads to a significant reduction of the computational cost, but the elimination of links must be done carefully.

Links connecting two hanging nodes (located both in the same element or in two different elements) can be removed because their stiffness is represented by the effective stiffness of the homogenized material assigned to the elements. Links connecting one renode and one hanging node located in the same element can be removed, too, because their stiffness is also reflected by the effective material stiffness.

A special case occurs if a link passes through more than one element and connects one hanging node with one renode. This can happen if the interpolation elements are too small, or on the interface between regions of low and high interest (see Fig. 2.2, in which the pink rectangle is a region of high interest and the light blue rectangle is a region of low interest). Such links should not be removed because their stiffness is not reflected by the homogenized material. Therefore, the involved hanging nodes are kept and the contribution of the links is taken into account explicitly, in addition to the contribution of the 2D or 3D elements.

For a general arrangement of particles and links, the global effective elastic stiffness tensor \mathbf{D}_e is considered as anisotropic. If the internal structure of the material exhibits no preferential directions and is expected to be macroscopically isotropic, the numerically evaluated effective elastic stiffness is replaced by its best isotropic approximation characterized by two elastic constants. The details are explained in Appendix A. To distinguish between the general anisotropic case and the special isotropic case, the corresponding versions of the A2 approach are referred to as A2a and A2i.

In failure simulations based on a model with elastic-brittle links, the effective stiffness needs to be updated only if a link breaks outside the area of high interest. In the area of high interest, all links are solved explicitly and do not affect the homogenized stiffness. If one of the homogenized links breaks, the stiffness contribution of this link is subtracted from the global stiffness tensor.

Local homogenization approaches (A3i, A3a)

These approaches are refinements of A2 and aim at improving the following deficiencies:

1. In the A2 approach, the effective material stiffness takes into account all links. However, certain links that partially cross homogenized elements are treated explicitly, and thus a part of their stiffness is actually accounted for twice, which artificially increases the resulting structural stiffness.
2. The A2 approach assumes that, from the macroscopic point of view, material properties are the same at all points of the investigated domain, while in reality the local arrangement of links is variable across the domain.

The A3 approaches remove these deficiencies by identifying effective properties of the homogenized material for each element separately. The A3i approach treats the material

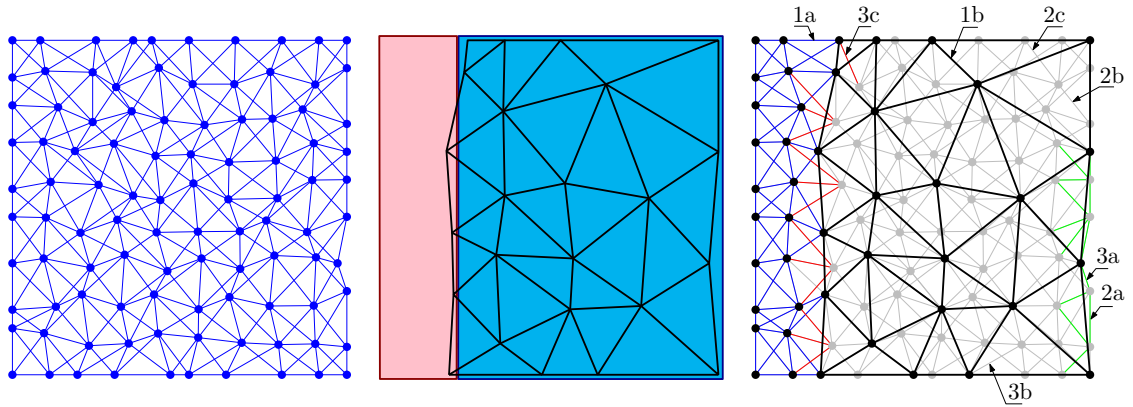


Figure 2.2: (a) Network of links, (b) regions of high (pink) and low (light blue) interest and interpolation mesh, (c) repnodes (black circles), interpolation elements (black triangles), links replaced by homogenized material (grey lines), and links modeled explicitly (blue, red and green lines)

as isotropic while the A3a approach accounts for local anisotropy. For computation of local material parameters, it makes sense to consider general anisotropy even if the overall material behavior is isotropic. The reason is that, for small elements, the particular local arrangement of a few links can result in a significant deviation from isotropy.

Evaluation of local stiffness for all homogenized elements

The material stiffness for each element is evaluated only from the contributions of those parts of the links that are really located inside the element. Certain links are still explicitly treated as 1D truss elements and do not contribute to the stiffness of any homogenized element. In a loop over all links, the contribution of each link is computed according to the following set of rules, depending on the types of particles connected by the link. For better understanding of the rules, examples of links that correspond to individual cases (described below under labels 1ab, 2abc, 3ab) are provided in Fig. 2.2c.

1. Reprnode – reprnode

- (a) If a link is located in the region of high interest:
The link is taken into account explicitly as a 1D truss element. It does not contribute to the stiffness of any homogenized element.
- (b) If a link is located in the region of low interest:
A link connecting two repnodes in the region of low interest is always located on an edge of an interpolation element. The stiffness contribution of this link is taken into account according to Equation (2.10). The stiffness contribution is equally distributed to all elements sharing this edge.

2. Hanging node – hanging node

- (a) If one or both ends of the link are located outside of all homogenized elements:
The link is taken into account as a truss element. It does not contribute to the stiffness of any homogenized element.

- (b) If both ends of the link are located in the same homogenized element:
The stiffness contribution of this link is taken into account according to Equation (2.10). The entire contribution is assigned to the corresponding element.
- (c) If the ends of the link are located in two different homogenized elements:
The stiffness contribution of this link is taken into account according to Equation (2.10). All elements intersected by the link are detected. The stiffness contribution is distributed to all the detected elements in proportion to the length of the part of the link inside each element.

3. Reprnode – hanging node

- (a) If the hanging node is located outside of all homogenized elements:
The link is taken into account as a truss element. It does not contribute to the stiffness of any homogenized element.
- (b) If both ends of the link are located in the same element:
The stiffness contribution of this link is taken into account according to Equation (2.10). The entire contribution is assigned to the present element.
- (c) If the ends of the link are located in two different elements:
The link is taken into account as a truss element. It does not contribute to the stiffness of any homogenized element.

If a crack is modeled by overlapping elements, the same rules can be used. It is only necessary to take a decision on which side of the crack the link is located. Based on this decision, the stiffness contribution is assigned to one of the overlapping elements.

In failure simulations, after breakage of one of the homogenized links, the effective stiffness is updated by subtracting the local contributions of this link from all corresponding local stiffness tensors.

Numerical simulation

Approaches A0–A3 described above have been implemented into the OOFEM open-source code [76, 77, 75]. OOFEM computes displacements of reprnodes and hanging nodes and strains and stresses in truss elements and homogenized planar or spatial elements. Afterwards, some post-processing procedures are required to evaluate the error of each approach and to plot the computed results.

The OOFEM input for the A3i/A3a approaches is almost the same as for A2i/A2a, with only one exception. An A3i/A3a input file contains a large number of materials with different parameters, which are then assigned to individual elements. Numerical tests show that computations with A3 are slightly slower than with A2 because approaches A3 deal with more materials. However, this difference is almost negligible. The process of identifying material parameters is visibly slower for A3 and the difference depends on the type of homogenization. Even if the time of the initial set-up process is taken into account, simulations based on A2–A3 turn out to be several times faster than those based on A0 and A1.

Error measures

Accuracy of the simplifying approaches A1–A3 is evaluated by comparing the results to the exact approach, A0. The following error measures are used for that purpose:

1. The relative stiffness error (RSE) is measured via the relative reaction error, defined as

$$RSE_{Ai} = \frac{\sum_k R_k^{(Ai)} - \sum_k R_k^{(A0)}}{\sum_k R_k^{(Ai)}} \quad (2.11)$$

where $\sum_k R_k^{(Ai)}$ is the sum of reactions in the loading direction at all reprododes k with a prescribed nonzero displacement (the simulations are performed under direct displacement control).

2. The energy error indicator (EEI) is defined as

$$EEI_{Ai} = \sqrt{\frac{1}{2} \sum_j^{NoL} E_j A_j L_j (\varepsilon_j^{(Ai)} - \varepsilon_j^{(A0)})^2} \quad (2.12)$$

where $\varepsilon_j^{(Ai)}$ is the axial strain at link j , and the sum is taken over all links (NoL denotes the number of links).

3. The total displacement error indicator (DEI) is defined as

$$DEI_{Ai} = \sqrt{\sum_j^{NoN} \|\mathbf{u}_j^{(Ai)} - \mathbf{u}_j^{(A0)}\|^2} \quad (2.13)$$

where $\mathbf{u}_j^{(Ai)}$ is the displacement vector at node j and NoN is the number of nodes.

Simple tests of elastic response

Two-dimensional periodic lattices

For verification of the implemented methods, the first tests are run for regular lattices composed of periodically repeated cells. The properties of the cells are adjusted such that the resulting macroscopic behavior be isotropic. Details are explained in Appendix B.

Direct tension test

The presented QC approaches are first subjected to simple tests in direct tension and shear on a regular lattice shown in Fig. 2.3a, with boundary conditions according to Fig. 2.4. The lattice is composed of 50×50 periodic isotropic cells. No region of high interest is defined in these elementary tests.

For direct tension (Fig. 2.4a), the displacements of individual particles computed using the A0 approach (fully resolved particle model) exactly correspond to a linear displacement field that would arise in a homogeneous continuum. All horizontal links are stretched in the same way and transmit the same axial forces, and similar statements apply to the vertical links and to the diagonal links. The purpose of this test is to check whether the simplified approaches A1–A3 lead to the exact results. Indeed, this is the case, even on irregular meshes shown in Fig. 2.5, provided that the link stiffnesses are tuned up such that the macroscopic behavior is isotropic. The test is analogous to patch tests of finite elements, because it demonstrates that a solution with a uniform strain field is captured exactly by the numerical method. Neither interpolation nor homogenization errors arise and all approaches pass the patch test.

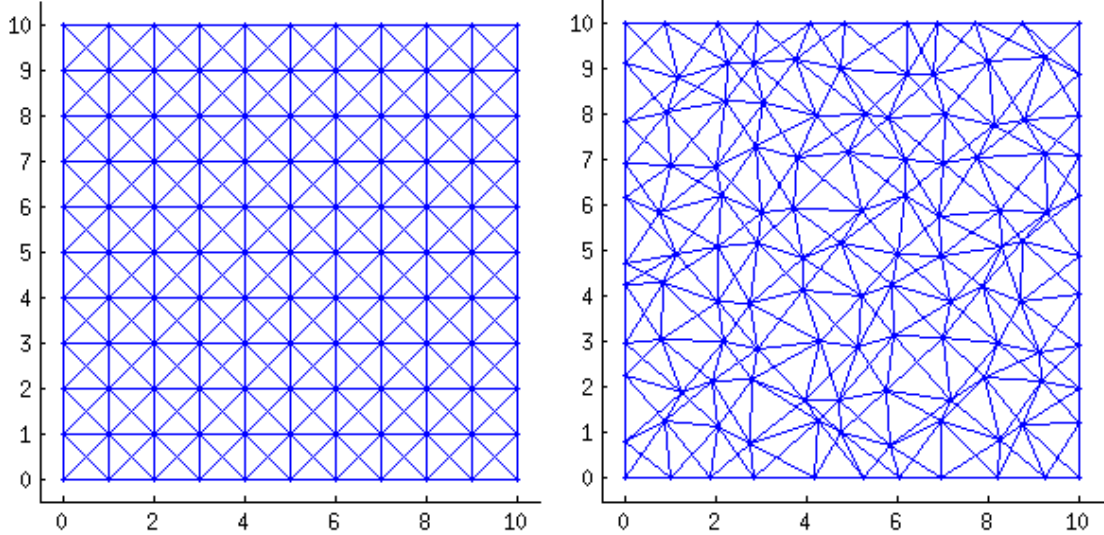


Figure 2.3: Examples of periodic (left) and randomized (right) microstructures with 10×10 cells

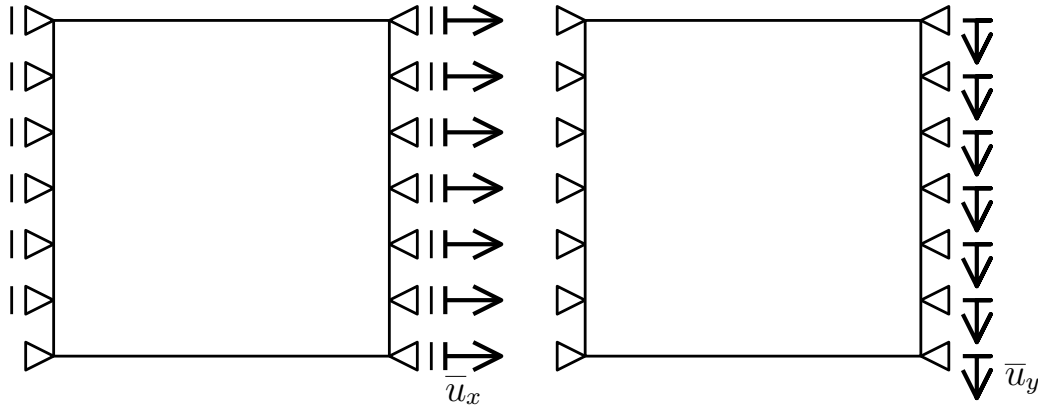


Figure 2.4: Boundary conditions of uniform tension test (left) and shear test (right)

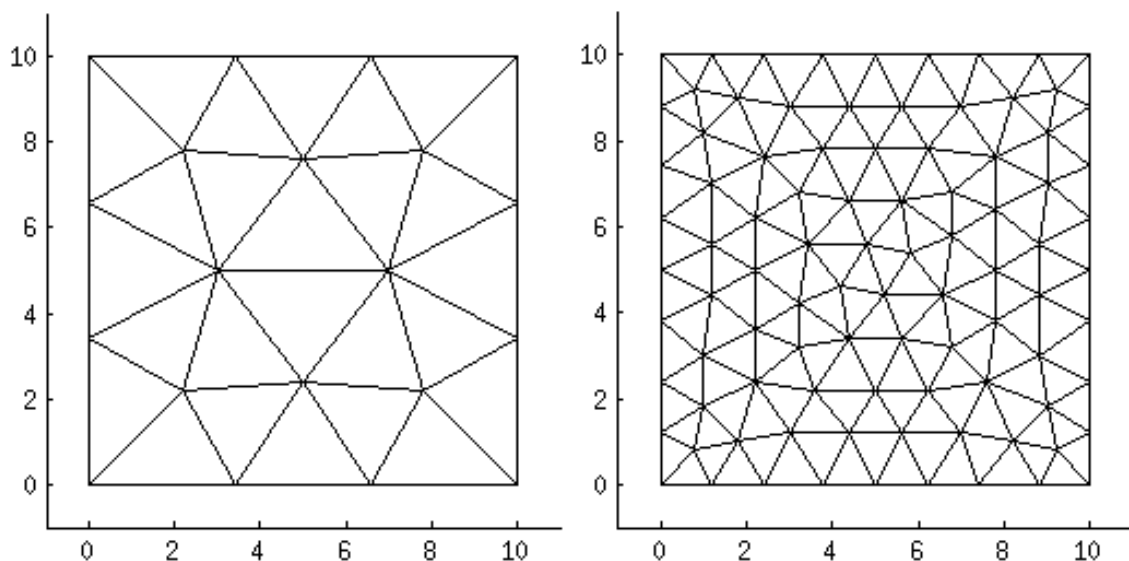


Figure 2.5: Examples of interpolation meshes with 3 (left) and 8 (right) elements per edge

If the macroscopic behavior of the lattice is not isotropic, approaches A1 and A3a still lead to the exact results, while approach A2 does so only if the globally homogenized material stiffness is considered as anisotropic. For A3i, the locally homogenized material stiffness is by definition isotropic, which induces a homogenization error.

The fact that the global homogenization procedure gives exactly the same stiffness matrix \mathbf{D}^{num} given by (2.35) as the homogenization of one cell is obvious, because the whole domain is composed of an integer number of identical cells. On the other hand, it is not immediately clear that the same stiffness matrix is obtained by local homogenization over an arbitrary triangular element, including cases when edges of the element are not aligned with lattice directions (horizontal, vertical and diagonal).

A graphical proof of this interesting property is sketched in Fig. 2.6, which shows a typical triangular element and the underlying regular lattice. The key point is that the sum of the lengths of intersections of the triangle with vertical links, $\sum_p L_{y,p}$, is exactly equal to the triangle area, A_e , divided by the horizontal spacing between the horizontal links, L_x . As shown in Fig. 2.6, this sum multiplied by L_x directly corresponds to evaluation of the triangle area by numerical integration using the trapezoidal rule. Since the function to be integrated is piecewise linear and one of the integration points is always located at the point where the slope changes (i.e., at the projection of one vertex), the numerical quadrature is exact, which means that

$$A_e = L_x \sum_p L_{y,p} \quad (2.14)$$

An analogous statement holds for horizontal links, for ascending diagonal links, and for descending diagonal links. Consequently, the relative proportions of horizontal, vertical, ascending diagonal and descending diagonal links in each single triangular element are the same as the overall relative proportions, and formula (2.10) always leads to the same material stiffness as formula (2.35), valid for one periodic cell. This would not be the case if the vertices of the triangle were placed at arbitrary locations and not at grid points. The same idea can be used for 3D lattices.

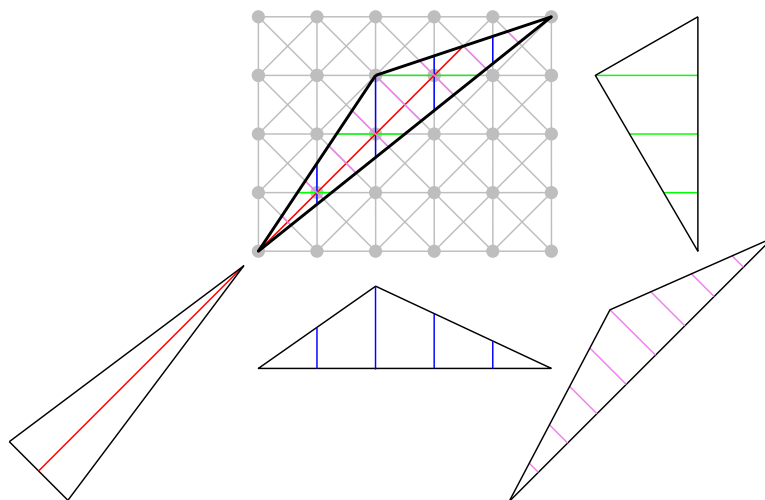


Figure 2.6: Graphical illustration of the reason why homogenization of a regular lattice over an arbitrary triangular element (with vertices at grid points) always leads to the same material stiffness

Shear test

For shear, the boundary conditions shown in Fig. 2.4b do not lead to a uniform strain field (note that the top and bottom parts of the boundary are considered as traction-free and their displacements are not prescribed). The relative stiffness errors evaluated according to formula (2.11) for meshes with different numbers of elements (NoE) are graphically presented in Fig. 2.8a. The error decreases fast with increasing number of elements, which indicates that the error is due to interpolation. The homogenization procedure, even when performed for each triangular element separately, does not introduce any error, for the same reasons as explained in the previous subsection on direct tension (see Fig. 2.6).

An exception is the finest interpolation mesh with 26 elements per edge, for which the elements are not much bigger than the lattice cells. As illustrated in Fig. 2.7, for such fine meshes there exist links (marked in red) that connect a renode with a particle located in an interpolation element not connected to that renode. Such links are accounted for explicitly and are excluded from homogenization, which leads to disturbances. The A3a approach with locally evaluated anisotropic material stiffness is then superior to the A2i and A3i approaches, which assume isotropy.

In terms of the stiffness error (RSE), the A1 approach (hanging nodes) gives in the present example somewhat higher accuracy than the other approaches, even though the difference is not dramatic. As shown in Fig. 2.8b, the energy error indicator (EEI) has the same value for all approaches (A1–A3) and decreases to very low levels as the interpolation mesh is refined.

Two-dimensional lattices with randomized cells

Lattice geometry and properties

In this series of tests, the microstructure is obtained by randomization of a periodic microstructure composed of 50×50 cells. The randomization is achieved by random shifts

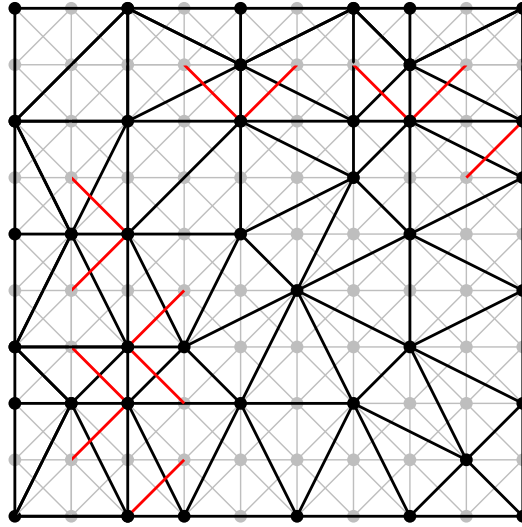


Figure 2.7: Example of a configuration in which some links (marked in red) are excluded from the local homogenization procedure

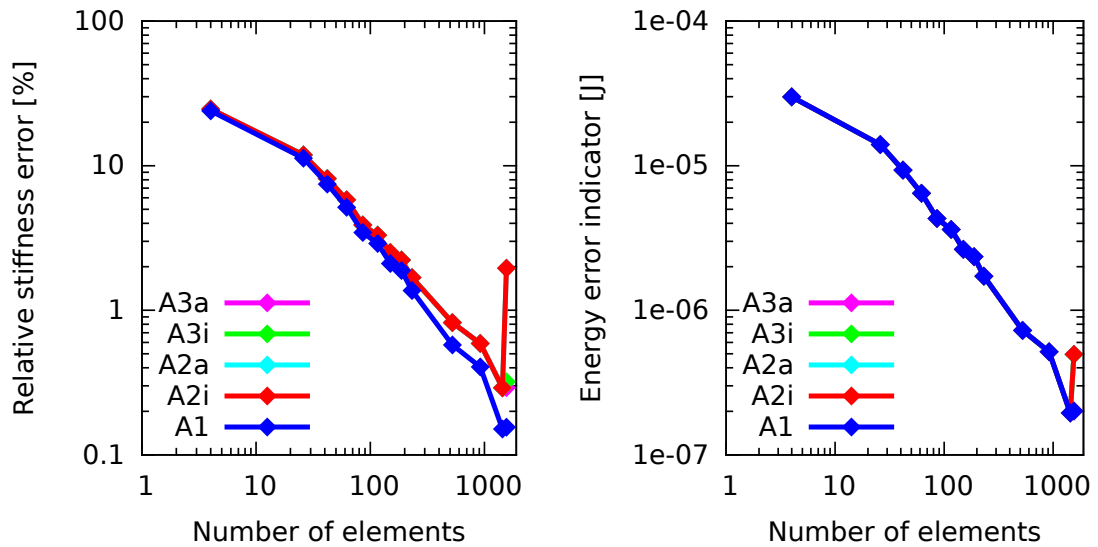


Figure 2.8: Relative stiffness error (a) in linear scale, (b) in logarithmic scale.

of particle positions. The maximal shift values in x and y directions are $0.3L_x$ and $0.3L_y$, respectively. The nodes located on edges are shifted along the edges only. The final result is evaluated as an average of computations with five different randomized microstructures. An example of a randomized microstructure is plotted in Fig. 2.3b.

Patch tests have been performed for a number of triangular meshes with various sizes of elements; see Fig. 2.5.

		Total Error					Homogenization Error			
NoE per edge	NoE	A1	A2i	A2a	A3i	A3a	A2i	A2a	A3i	A3a
2	4	6.48	7.34	6.48	7.33	6.48	0.86	0.00	0.86	0.00
3	26	6.47	7.34	6.48	7.33	6.47	0.86	0.01	0.86	0.00
4	42	6.46	7.34	6.48	7.33	6.46	0.87	0.02	0.87	0.00
5	62	6.46	7.34	6.48	7.32	6.46	0.88	0.02	0.86	0.00
6	86	6.44	7.34	6.48	7.31	6.44	0.89	0.04	0.87	0.00
7	116	6.43	7.34	6.48	7.31	6.43	0.91	0.05	0.88	0.00
8	150	6.40	7.34	6.48	7.30	6.41	0.94	0.08	0.90	0.01
9	188	6.38	7.34	6.48	7.28	6.39	0.96	0.10	0.90	0.01
10	232	6.33	7.34	6.48	7.27	6.35	1.00	0.15	0.94	0.02
15	524	6.09	7.34	6.48	7.11	6.16	1.24	0.39	1.02	0.07
20	920	5.63	7.67	6.70	6.73	5.80	2.04	1.07	1.10	0.18
25	1438	5.03	11.17	8.58	5.76	5.35	6.14	3.55	0.72	0.32

Table 2.1: Relative stiffness error (RSE) [in %] for a microstructure with randomized cells subjected to a uniform tension test.

Direct tension test

For the direct tension test, the relative stiffness errors (RSE) corresponding to different meshes and to approaches A1–A3 are listed in Table 2.1 and graphically presented in Fig. 2.9. The energy errors (EEI) are plotted in Fig. 2.13. Isotropic parameters for A2i and A3i have been determined according to (2.19). For comparison, the RSEs are plotted again in Fig. 2.10, this time with parameters A2i and A3i determined according to (2.22). The isotropic stiffness is overestimated for both matrix norms. Nevertheless, norm (2.22) provides a significantly higher error and seems to be unacceptable for application to uniform tension. The error induced by the A2 approach is independent of the refinement of the interpolation mesh, except for very fine meshes. The reason is that the A2 approach deals with the same homogenized stiffness matrix in all elements, and if the whole sample is replaced by a homogeneous continuum, the prescribed boundary conditions induce uniform strain across the sample. Such a state of uniform strain is then captured by all meshes because the underlying finite elements pass the standard patch test. Of course, the reference solution obtained using the fully resolved particle model is somewhat different, because the microstructure is not completely regular. The error of the A2 approach is thus nonzero; it does not depend on the mesh, with the exception of very fine meshes, for which some links are considered explicitly, as already discussed in Section 2.3.1.2 (see Fig. 2.7). For approaches A3i and A3a, the total error slowly decreases as the mesh is refined. As expected, A3i is seen to be more accurate than A2i, and A3a is still more accurate.

The last four columns in Table 2.1 present the homogenization errors for approaches A2–A3. The homogenization error is defined as the difference between the total error of the given approach and the total error of the A1 approach, which does not use any homogenization. The homogenization errors are seen to be below 1%, and for the A3a approach to be virtually nil, with the exception of very fine meshes. Even for coarser meshes, the homogenization error slightly increases with mesh refinement. For approaches A2i and A3i, this can be attributed to the anisotropic character of the local arrangements of links. The deviation from isotropy is more pronounced on fine interpolation meshes.

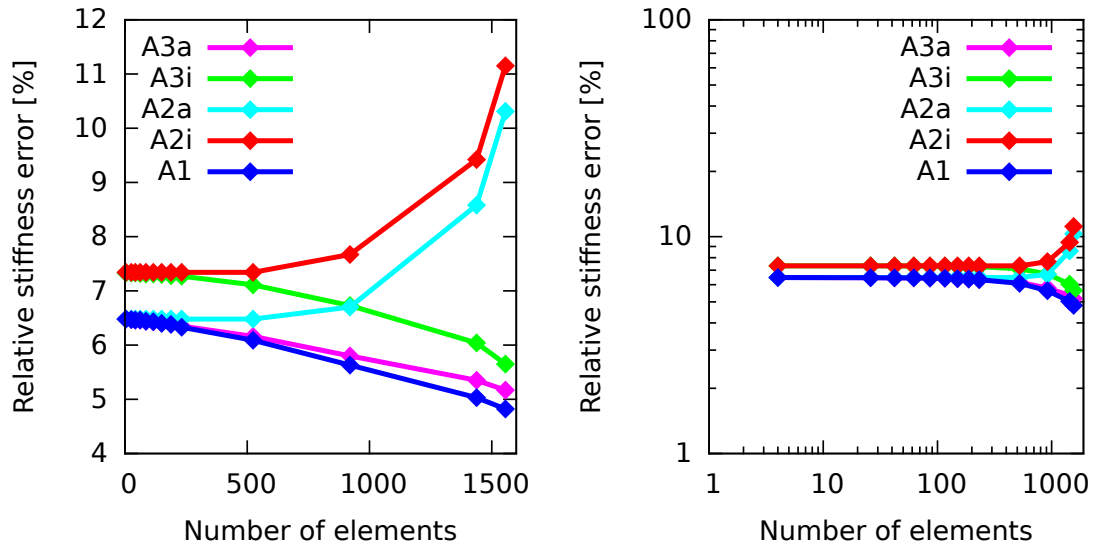


Figure 2.9: Relative stiffness error for a microstructure with randomized cells subjected to a uniform tension test (a) in linear scale, (b) in logarithmic scale. Isotropic parameters (for A2i and A3i) obtained according to (2.19).

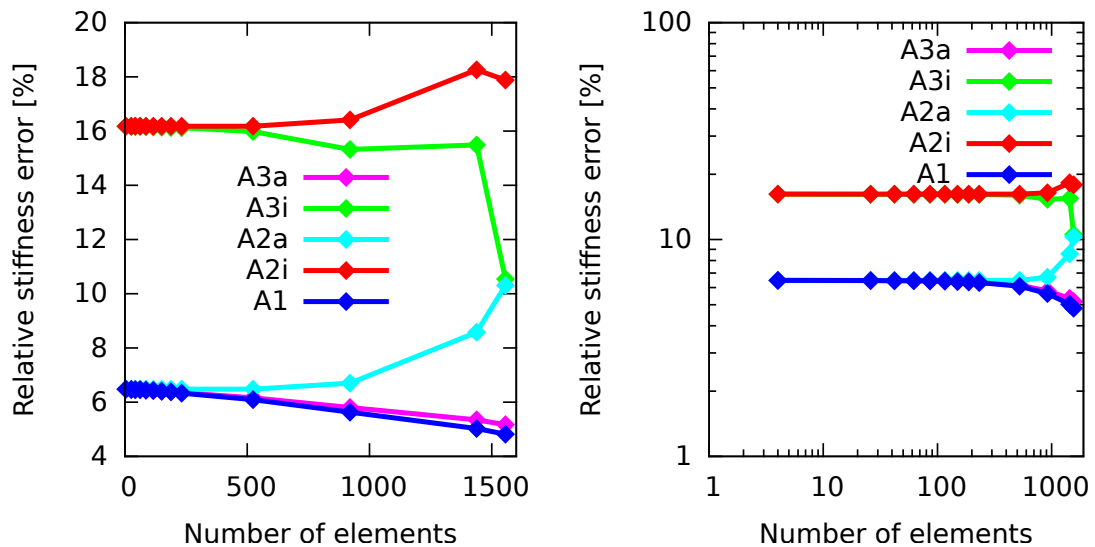


Figure 2.10: Relative stiffness error for a microstructure with randomized cells subjected to a uniform tension test (a) in linear scale, (b) in logarithmic scale. Isotropic parameters (for A2 and A3i) obtained according to (2.22).

Shear test

For the shear test of a randomized lattice, the relative stiffness error is listed in Table 2.2 and graphically presented in Fig. 2.11 with A2i and A3i according to the first matrix norm, and again in Fig. 2.12 with A2i and A3i according to the second matrix norm. For this shear test, the results of comparison of different matrix norms is totally opposite to the results for tension. The second matrix norm predicts correct results comparable with other approaches, whereas the stiffness predicted with the first norm is significantly underestimated and the total stiffness error can even become negative, which indicates that the response is too compliant. The energy error is listed in Table 2.3. It is seen that A3a gives almost the same total error as A1, and the error decreases with refinement of the interpolation mesh. On the other hand, approaches A2i and A3i give seemingly a smaller relative relative stiffness error, which can even become negative. Their energy error is larger than for A1 and A3a.

Most of the error is due to interpolation. The homogenization error is smaller, and for the A3a approach it is negligible.

		Total Error					Homogenization Error			
NoE per edge	NoE	A1	A2i	A2a	A3i	A3a	A2i	A2a	A3i	A3a
2	4	36.36	21.06	37.14	21.05	37.28	-15.30	0.78	-15.30	0.92
3	26	21.59	8.89	22.08	8.93	22.50	-12.70	0.49	-12.66	0.90
4	42	17.31	5.33	17.76	5.32	18.18	-11.98	0.45	-11.99	0.87
5	62	14.57	3.01	15.10	2.97	15.45	-11.56	0.53	-11.61	0.88
6	86	12.95	1.49	13.34	1.40	13.74	-11.46	0.39	-11.55	0.78
7	116	12.02	0.63	12.33	0.58	12.71	-11.39	0.31	-11.44	0.70
8	150	11.17	-0.11	11.48	-0.14	11.78	-11.28	0.31	-11.32	0.61
9	188	10.80	-0.43	11.12	-0.58	11.38	-11.23	0.32	-11.38	0.58
10	232	10.30	-0.88	10.60	-0.98	10.83	-11.18	0.30	-11.28	0.53
15	524	9.25	-1.71	9.63	-1.95	9.69	-10.96	0.38	-11.20	0.44
20	920	8.54	-0.99	9.95	-2.03	9.03	-9.53	1.41	-10.57	0.49
25	1438	7.51	4.38	10.57	-0.86	8.05	-3.13	2.97	-8.37	0.54

Table 2.2: Relative stiffness error (RSE) [in %] for a microstructure with randomized cells subjected to shear.

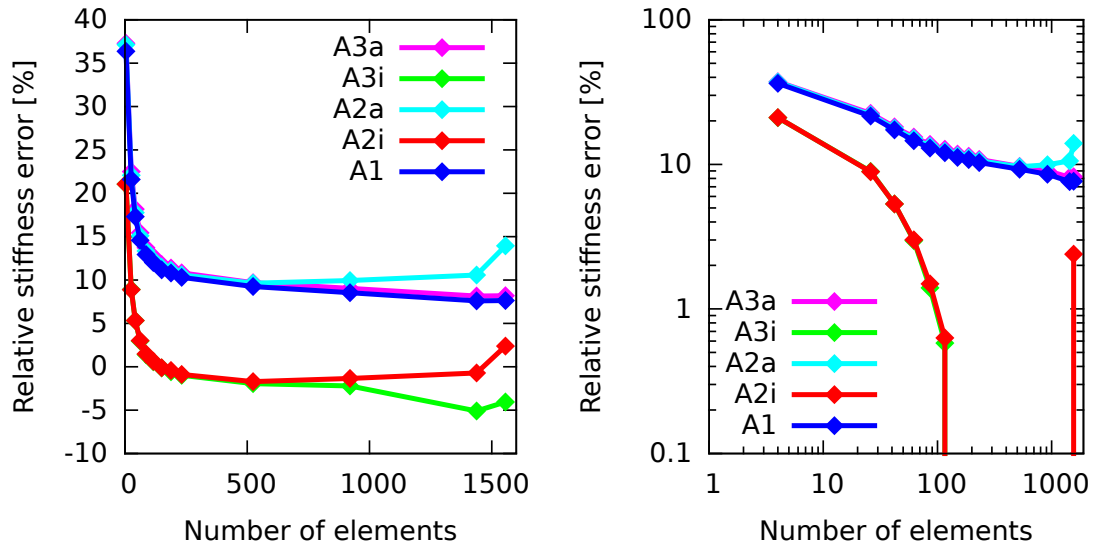


Figure 2.11: Relative stiffness error for a microstructure with randomized cells subjected to shear (a) in linear scale, (b) in logarithmic scale. Isotropic parameters (for A2i and A3i) obtained according to (2.19).

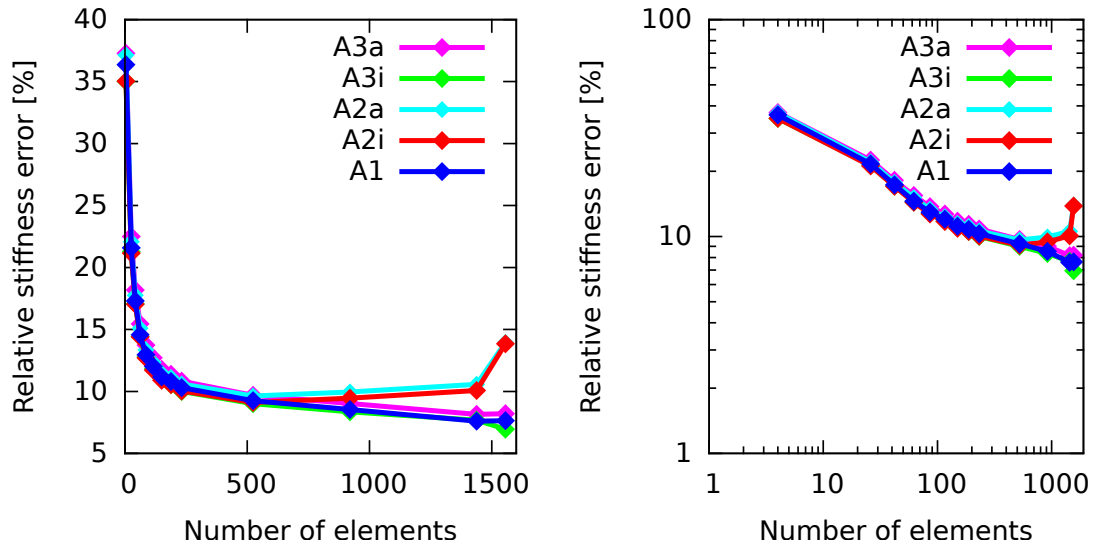


Figure 2.12: Relative stiffness error for a microstructure with randomized cells subjected to a shear (a) in linear scale, (b) in logarithmic scale. Isotropic parameters (for A2i and A3i) obtained according to (2.22).

NoE per edge	total NoE	A1	A2	A3i	A3a
2	4	4.46	4.52	4.52	4.46
3	26	2.65	2.71	2.72	2.65
4	42	2.13	2.19	2.19	2.13
5	62	1.79	1.85	1.86	1.79
6	86	1.59	1.65	1.66	1.59
7	116	1.48	1.54	1.55	1.48
8	150	1.37	1.44	1.45	1.37
9	188	1.33	1.40	1.41	1.33
10	232	1.27	1.34	1.35	1.27
15	524	1.14	1.24	1.28	1.14
20	920	1.06	1.22	1.29	1.06

Table 2.3: Energy error indicator (EEI) [in 10^{-5}] for a microstructure with randomized cells subjected to a shear test.

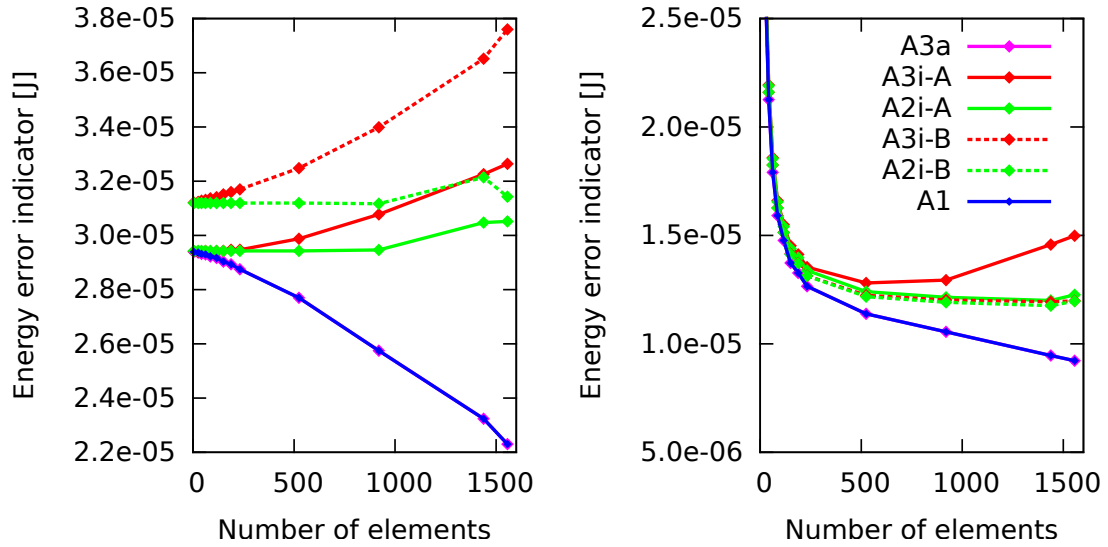


Figure 2.13: Energy error indicator (EEI) for a microstructure with randomized cells subjected to direct tension (left) and shear test (right)

Two-dimensional tests – conclusions

In partial summary, the tensile test of a regular lattice serves as a patch test that verifies that the implementation is correct because all the approaches reproduce the exact solution with no error. The shear test of a regular lattice shows that, upon refinement, the error tends to zero.

For the tensile test of a randomized lattice, the error in stiffness caused by interpolation remains above 5% even on very fine meshes. For the shear test, it remains above 7.5%. This is the intrinsic error that needs to be accepted. Isotropic homogenization in some cases leads to an increase of compliance, which counteracts the increase of stiffness due to interpolation. The resulting total error in stiffness is thus in certain cases near zero or even negative, but the energy error always remains positive.

Differences in the performance of homogenization based on error measures (2.19) and (2.22) in different patch tests indicate that isotropic homogenization of anisotropic materials can be dangerous. Therefore, it is better to avoid approaches A2i and A3i if the homogenized microstructure is strongly anisotropic.

Three-dimensional patch tests

To check the performance in three dimensions, basic patch tests are performed on cube samples composed of $24 \times 24 \times 24$ cells. All presented QC approaches are again applied to direct tension and shear. The initial periodic 3D microstructure is randomized in the same way as in 2D. The final result is evaluated as an average of computations with five different randomized microstructures. Parameters of isotropic stiffness (for the A2i and A3i approaches) are obtained by using matrix norm (2.22) only. Same as in the 2D case, no region of high interest is defined in these tests.

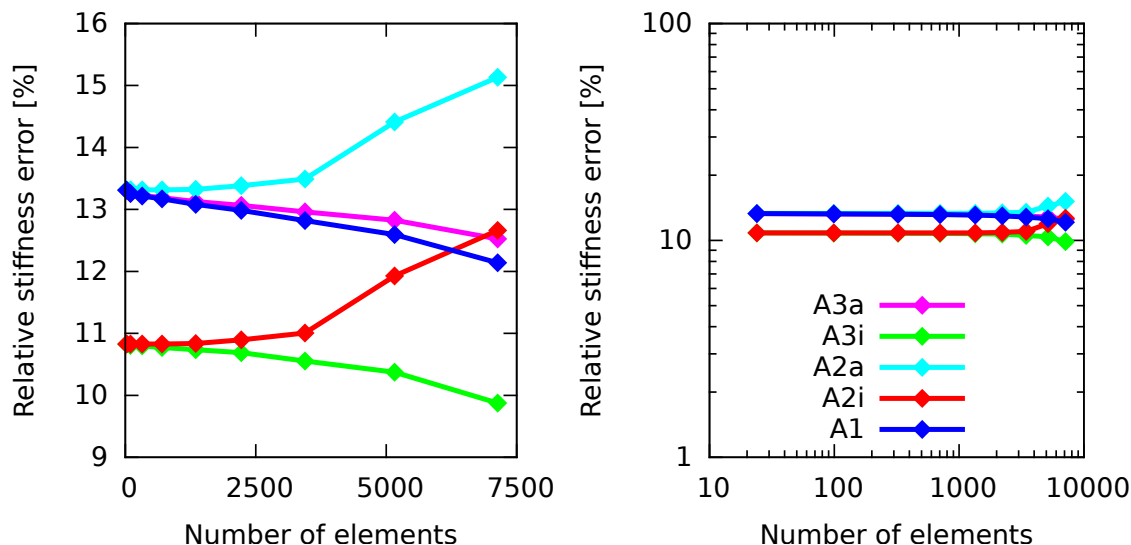


Figure 2.14: Relative stiffness error for a 3D randomized microstructure subjected to tension (a) in linear scale, (b) in logarithmic scale.

Direct tension test

For the three-dimensional direct tension test, the relative stiffness errors (RSE) corresponding to different meshes and to approaches A1–A3 are plotted in Fig. 2.14. The energy errors (EEI) are plotted in Fig. 2.15 and the total displacement error indicator (DEI) in Fig. 2.16.

In terms of the RSE, all approaches exhibit the same behavior as in two dimensions. The only difference is that the homogenized isotropic stiffness is underestimated instead of overestimated. The EEI of A2i and A2a remains constant for all mesh sizes (except the finest mesh). This confirms the fact that, for a uniform displacement field, homogenization used by these approaches is independent of the refinement of the interpolation mesh. On the other side, the EEI of A3i increases with mesh refinement because smaller elements are statistically more anisotropic. The order of DEI reflects the quality of homogenized procedures used in all QC approaches.

Shear test

For the three-dimensional shear test, the RSE and EEI are plotted in Fig. 2.17 and Fig. 2.18, respectively. The performance of all approaches is quite similar. The response of A2i and A3i is too compliant due to homogenization. Therefore these approaches appear to be more accurate than A1 and A3a in terms of RSE but not in terms of EEI.

Three-dimensional tests – conclusions

Three-dimensional patch tests have shown that local anisotropic homogenization (i.e., the A3a approach) provides results with an almost zero homogenization error, but an intrinsic stiffness error around 15% due to interpolation must be taken into account.

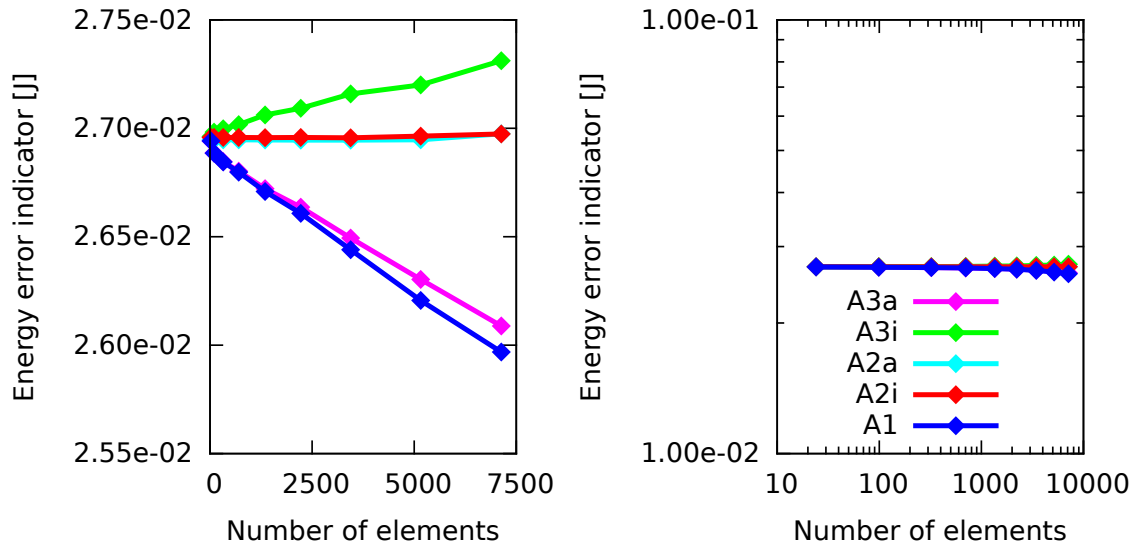


Figure 2.15: Energy error indicator for a 3D randomized microstructure subjected to tension (a) in linear scale, (b) in logarithmic scale.

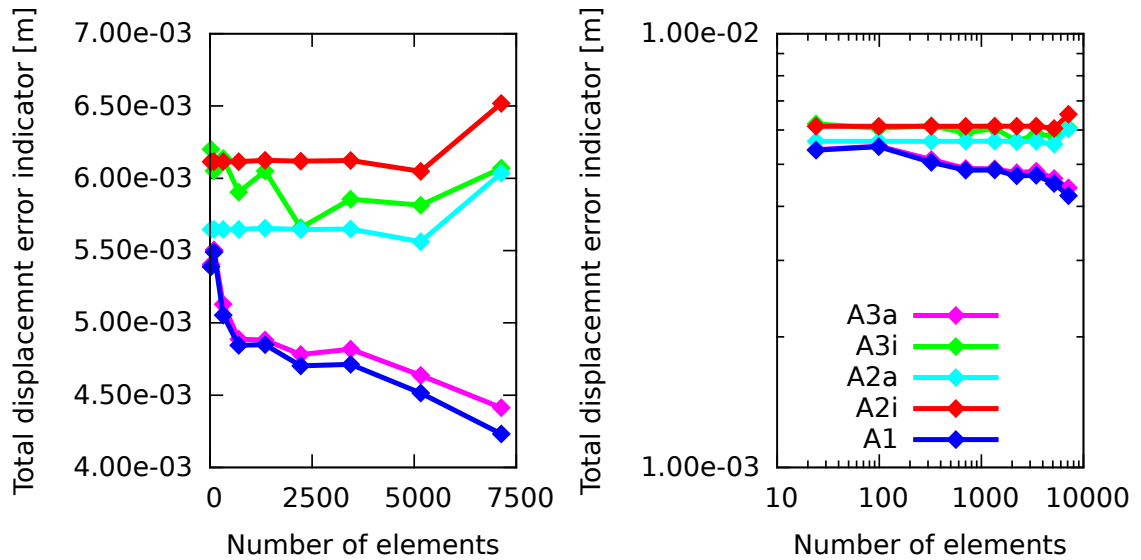


Figure 2.16: Total displacement error indicator for a 3D randomized microstructure subjected to tension (a) in linear scale, (b) in logarithmic scale.

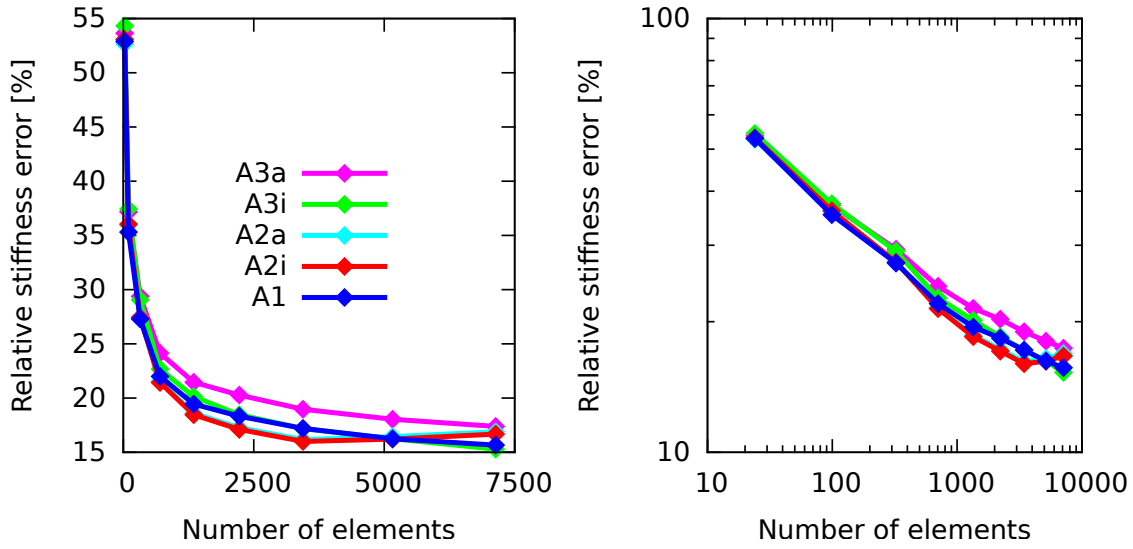


Figure 2.17: Relative stiffness error for a 3D randomized microstructure subjected to shear (a) in linear scale, (b) in logarithmic scale.

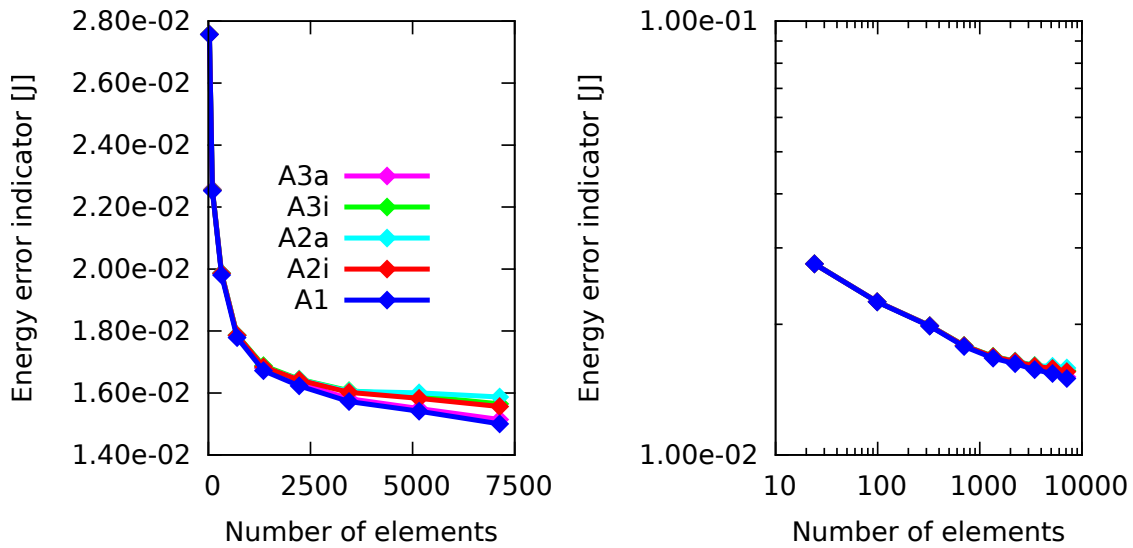


Figure 2.18: Energy error indicator for a 3D randomized microstructure subjected to shear (a) in linear scale, (b) in logarithmic scale.

Failure simulations

To assess the efficiency and accuracy of QC-based approaches in applications that involve inelastic material response, failure of an L-shaped specimen is simulated in three dimensions. The behavior of links that connect particles is assumed to be elastic-perfectly brittle, with link breakage occurring at a critical level of tensile strain.

The L-shaped specimen shown in Fig. 2.19 has dimensions $300 \times 300 \times 100$ mm. It is

fixed at the bottom section and loaded by prescribed vertical and horizontal displacements imposed at the left end section. As a result, the non-convex corner is opened, the upper part of the specimen is bent and the horizontal part is twisted.

The microstructure is generated with a density of 20 nodes along the short edge and randomized. This procedure results in 38,400 particles (with 113,200 unknown DOFs) connected by 324,672 links. Material parameters are considered to be the same for all links.

In the simulation, the prescribed displacement is increased to the level at which the critical value of tensile strain is attained in one link while strains in all other links remain in the elastic range. Since the behavior of all links is linear elastic, this can be done in one single computational step, without any iterations. Subsequently, the broken link is removed and the level of prescribed displacement at which the next link breakage occurs is determined, again in one computational step without any iterations. Repeating this process results in a series of link breakages that define the macroscopic crack trajectory.

Cylindrical fully resolved domain

For the purpose of this test, a cylindrical fully resolved domain (FSD) is specified around the non-convex corner; see Fig. 2.19. The FSD radius is set to 50 mm, i.e., to one half of the length of the shortest specimen edge. This FSD occupies 11.8 % of the volume of the entire domain. Basic characteristics of models used by simplified QC approaches are listed in Table 2.4.

The simulation proceeds until 1000 links are cracked. Relative errors evaluated by comparing the results of simplified approaches to the full particle model (approach A0) are depicted in Fig. 2.20 and 2.21. Crack opening error and the energy error indicator (EEI) defined in (2.12) are depicted in Fig. 2.22. The ranking of individual QC approaches according to EEI in the first step reflects the quality of homogenization methods used by these approaches. On the other side, in the last step, the ranking of approaches is different and depends on which links are cracked.

The capability of all simplified approaches A1–A3 to correctly predict the link that will break next (i.e., the link with maximum strain) depends on the current microstructure. The numbers of incorrectly cracked links during the failure process are compared in Table 2.5. The numbers in the line denoted as 500/1000 indicate how many of the first 500 cracked links for the given approach are not found in the list of the first 1000 cracked links in the exact solution (approach A0). For simplified approaches, the precise sequence of cracked links is not always the same but just a small number of cracked links are predicted incorrectly. Even though a few incorrectly cracked links appear, the simplified approaches are able to predict a correct overall crack trajectory, provided that the FSD is selected properly.

Another important quantity is the maximum value of loading force F_{\max} observed in the force-displacement diagram. The results are shown in Table 2.6. For all simplified approaches, the maximum force is predicted in the 35th step, while the full particle model (approach A0) gives the maximum force in the 36th step. However, relative errors in F_{\max} as well as relative errors in the corresponding displacement are just a few percent.

Computational times consumed by individual components of various QC-based approaches are summarized in Table 2.7. Two most demanding procedures are the assignment of interpolation elements to all particles and the assembly of individual stiffness tensors from all elements. Searching for the interpolation element is done independently for each particle. The distribution of link stiffnesses to individual tensors is also done

	A0	A1	A2–A3
NoP	38,400	38,400	6,752
NoL	324,672	324,672	39,695
NoE	0	4,457	4,457
NoRN	38,400	5,388	5,388
NoHN	0	33,012	1,364
DOFs	113,200	16,014	16,014

Table 2.4: Numbers of particles, links, elements, repnodes, hanging nodes and DOFs for various QC approaches.

	A1	A2i	A2a	A3i	A3a
Incorrectly outside FSD	4	6	13	10	7
Incorrectly cracked 1000/1000	48	60	55	86	52
Incorrectly cracked 500/1000	15	4	4	24	4

Table 2.5: Numbers of incorrectly cracked links.

independently for each link. Therefore, parallelization of the loop over particles or links can easily be envisaged with an almost ideal expected speed-up.

The computational times of one step and of the whole simulation are shown in Table 2.8. The QC approaches are able to reduce the computational time of one step more than ten times. Even if the computational time needed for the initial simplification is high, the total simulation time is significantly reduced if the total number of steps is huge.

Fully resolved domain for crack propagation

The cylindrical FSD used in the previous section is not convenient for simulations of a long crack trajectory. Even if cracking of individual links outside the FSD is implemented, propagation of the crack outside the FSD is not accurate. To be able to predict the correct crack trajectory, it is necessary to change the FSD adaptively or set up a priori an FSD in the region where crack propagation is expected. For that purpose a new wedge-shaped FSD is selected; see Fig. 2.23. For this FSD, cracking of 2000 links is computed and cracked links for approaches A0 and A3a are depicted in Fig. 2.24. The list of cracked links for the A3a approach is not the same as for the exact approach A0, but the macroscopic shape of the crack is quite similar to the exact solution.

	F_{\max} error	F_{\max} displacement error	F_{\max} step number
A0	-	-	36
A1	3.2%	-4.5%	35
A2i	1.1%	0.4%	35
A2a	2.9%	-2.1%	35
A3i	1.4%	-1.1%	35
A3a	4.3%	-5.7%	35

Table 2.6: Tensile strength errors.

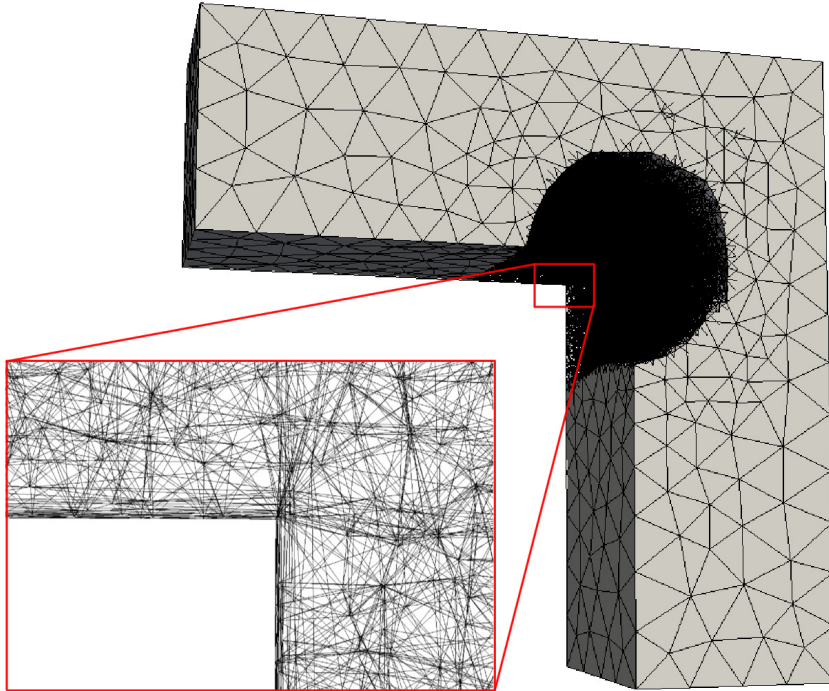


Figure 2.19: Geometry of interpolation mesh and the fully resolved domain with a detail of microstructure.

	A0	A1	A2i, A2a	A3i, A3a
Generate interpolation mesh	-	0.09s	0.09s	0.09s
Transform mesh to particles	-	0.19s	0.19s	0.19s
Find element for all particles	-	0.92s	0.92s	0.92s
Global stiffness tensor	-	-	0.15s	-
Connectivity table	-	-	-	0.17s
Individual stiffness tensors	-	-	-	19.27s
Total simplification time	0.0s	1.20s	1.35s	20.64s

Table 2.7: Time consumption of QC simplifications (i.e., of the preparatory stage before the actual simulation).

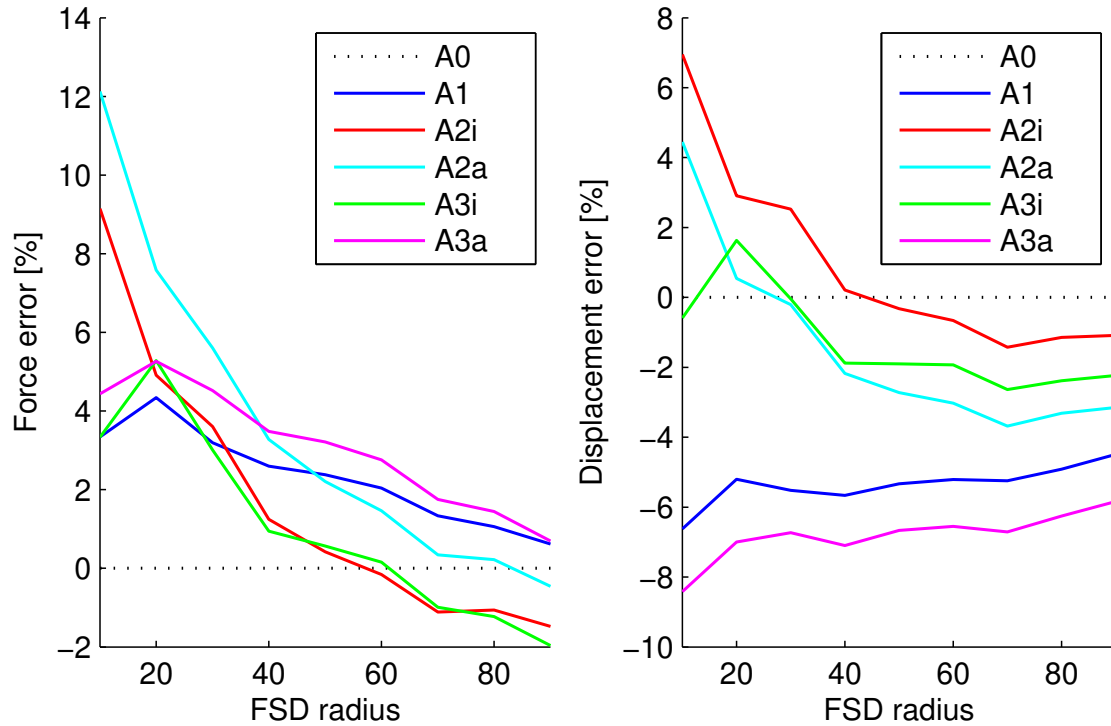


Figure 2.20: Relative force error (left) and relative prescribed displacement error (right) for different radii of the fully resolved domain.

	Time of QC simplification	Computational time of one step step time / solver time	Total comp. time of 1000 steps
A0	-	8.2s / 5.72s (1.00 / 1.00)	2h 16m 40s (1.00)
A1	1.2s	13.66s / 0.47s (1.67 / 0.08)	3h 47m 41s (1.67)
A2i	1.35s	0.85s / 0.38s (0.10 / 0.07)	14m 11s (0.10)
A2a	1.35s	0.85s / 0.39s (0.10 / 0.07)	14m 11s (0.10)
A3i	20.64s	0.85s / 0.39s (0.10 / 0.07)	14m 30s (0.11)
A3a	20.64s	0.85s / 0.38s (0.10 / 0.07)	14m 30 (0.11)

Table 2.8: Computational times consumed by various QC approaches for a conjugate gradient (CG) solver with incomplete Cholesky preconditioning and symmetric compressed column matrix storage scheme.

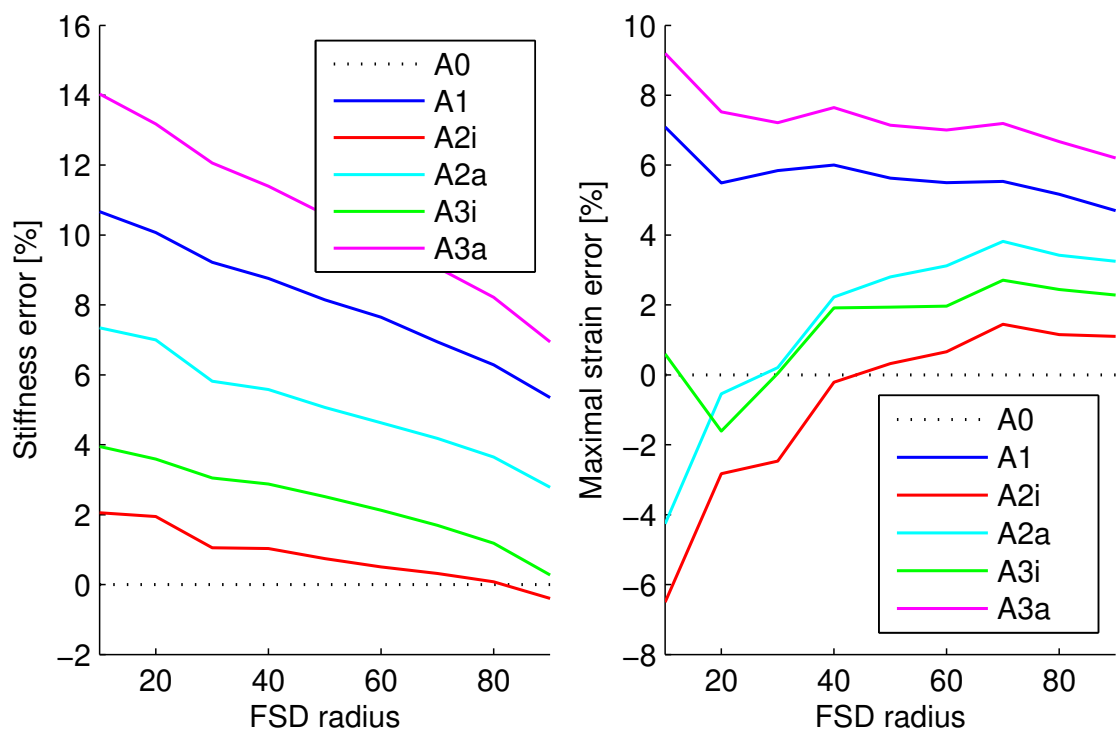


Figure 2.21: Relative stiffness error (left) and relative error of strain in the most loaded link (right) for different radii of the fully resolved domain.

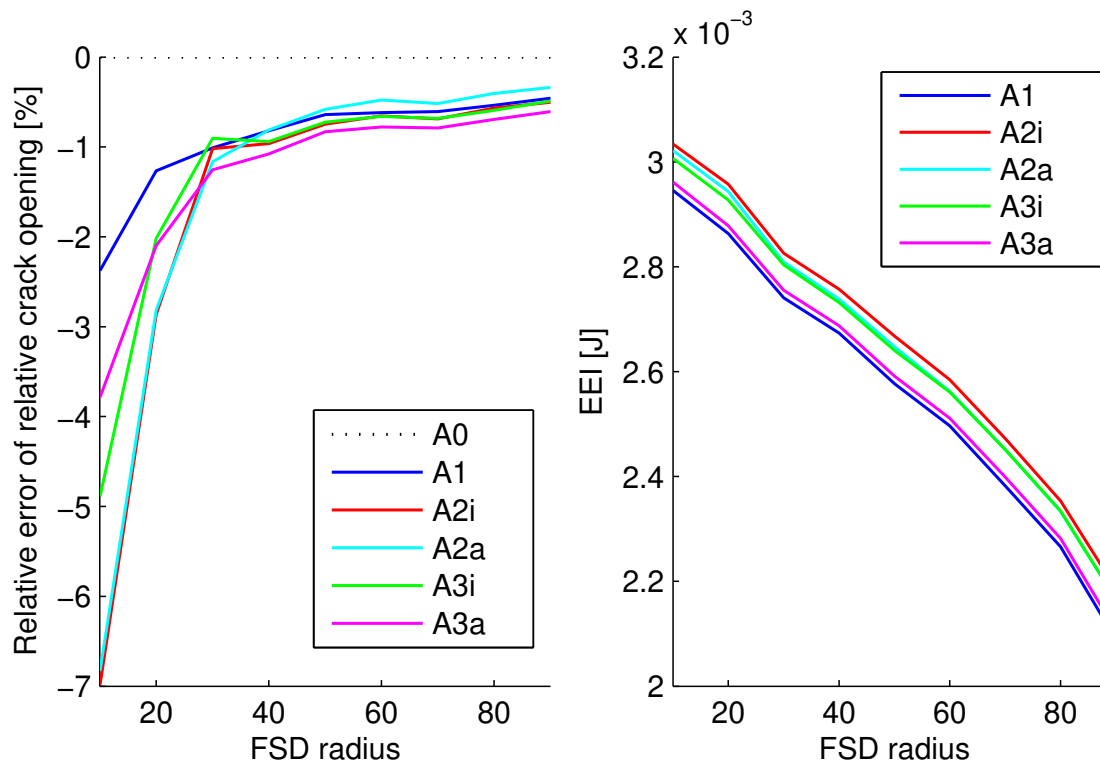


Figure 2.22: Crack opening error at the moment when critical strain is reached (left) and energy error indicator (right) for different radii of the fully resolved domain.

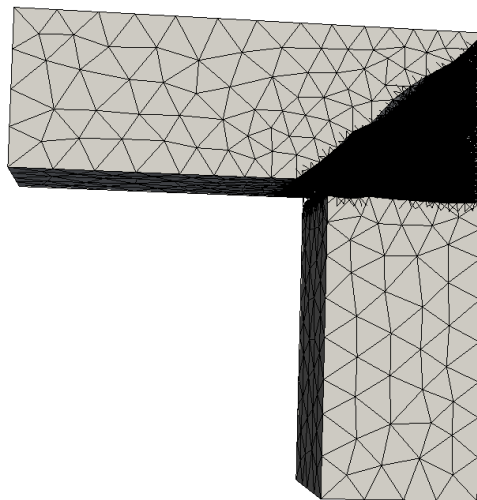


Figure 2.23: Geometry of interpolation mesh and the fully resolved domain.

	F_{\max} error [%]	F_{\max} displacement error [%]	F_{\max} step number [%]
A0	-	-	13 / 36
A1	0.12 / 2.28	-7.91 / -6.77	11 / 15
A2i	-1.30 / 2.15	-1.13 / -0.05	32 / 17
A2a	-0.38 / 4.01	-4.61 / -2.65	32 / 18
A3i	-0.77 / 0.80	-2.17 / -2.73	32 / 17
A3a	0.18 / 3.31	-9.68 / -7.94	18 / 18

Table 2.9: Tensile strength errors for two different random microstructures.

The force-displacement diagram corresponding to a crack growth simulation in a microscopically elastic-brittle material exhibits high oscillations; see the scattered gray lines in Figs. 2.25–2.26. Interpretation and comparison of such force-displacement diagrams is facilitated by smoothing the results. The smoothing procedure replaces the values of force and displacement in each characteristic point by their weighted averages around this point. Different numbers of neighboring points have been used, ranging from ± 5 to ± 100 . Three types of weight functions have been considered, namely constant, linear (closer points have a stronger influence) and bell-shaped polynomial (in the form often used by nonlocal material models) given by

$$w(s) = \left\langle 1 - \frac{s^2}{R^2} \right\rangle^2 \quad (2.15)$$

where s is one plus the number of points between the averaged point and the point for which the weight is evaluated. Parameter R equals to one plus the number of considered neighboring points, and $\langle \dots \rangle$ are Macauley brackets denoting the positive part. The results for different numbers of neighboring points are compared for constant and linear weight functions in Fig. 2.25 and 2.26, respectively. The results obtained with the bell-shaped weight function are very similar to the results with linear weights. Constant weights lead to sharper shapes of the final diagrams and, for the same number of used neighboring points, the oscillations are smaller in comparison with linear or polynomial weights. All three variants of smoothing reflect the character of the original diagram and reduce oscillations.

Diagrams for all approaches smoothed with constant weights for 10 neighboring points are compared in Fig. 2.27. The same diagrams smoothed with linear weights for 50 neighboring points are compared in Fig. 2.28.

In accordance with patch tests, the initial elastic response of the simplified approaches is stiffer than the exact solution. However, the shape of the softening branch is captured by all approaches very well.

Large-scale computations

The maximum size of the problem to be solved is limited by the size of available memory. Typically, today's office PCs are equipped with 4GB of RAM. For such a computer, the maximum size of the L-shaped specimen that can be solved by OOFEM depends on the fineness of the microstructure. For a direct solver with a symmetric skyline matrix storage format, the maximum fineness of microstructure that can be solved using the pure particle model (approach A0) is 27 particles along the shortest edge, which leads to 282,852 DOFs and 820,846 links. The more powerful conjugate gradient iterative

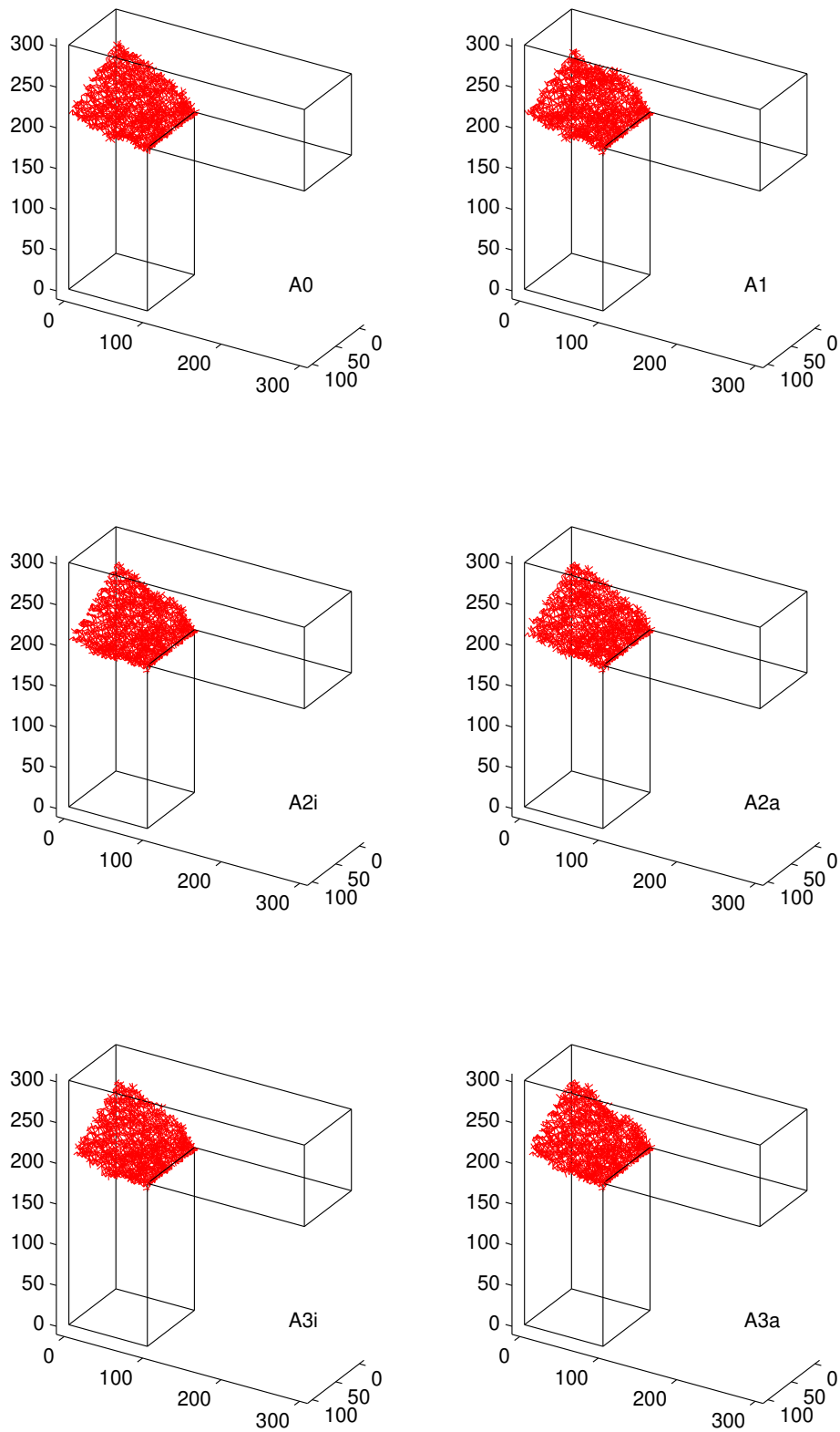


Figure 2.24: Cracked links computed with all approaches A0–A3.

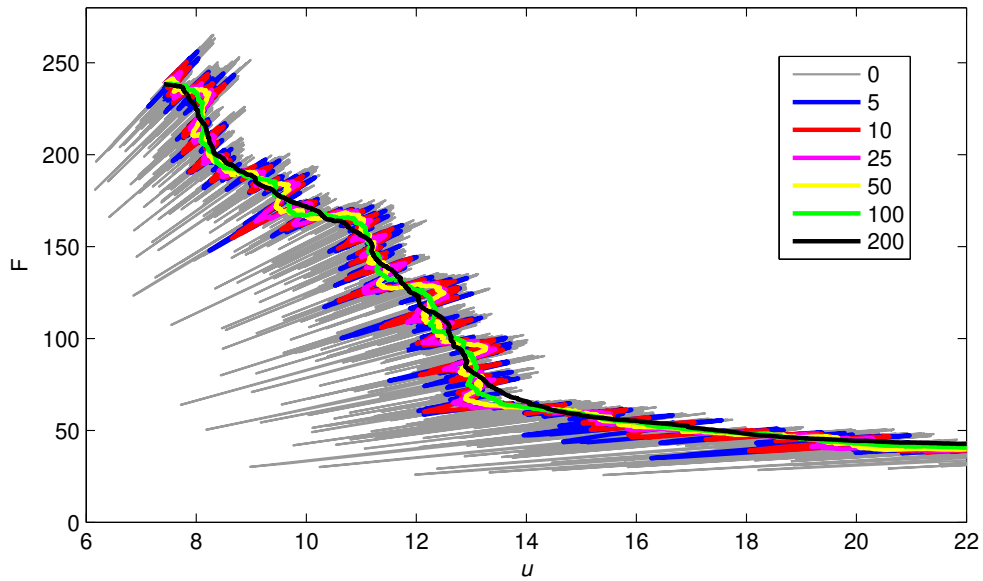


Figure 2.25: Descending branch of force-displacement diagram smoothed by averaging with different numbers of neighboring values, using a constant weight function.

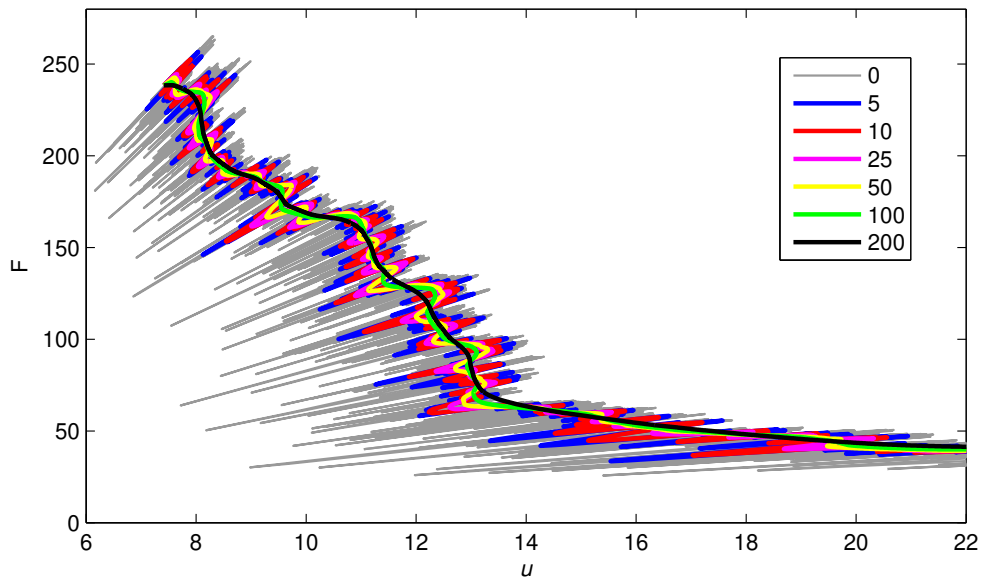


Figure 2.26: Descending branch of force-displacement diagram smoothed by averaging with different numbers of neighboring values, using a linear weight function.

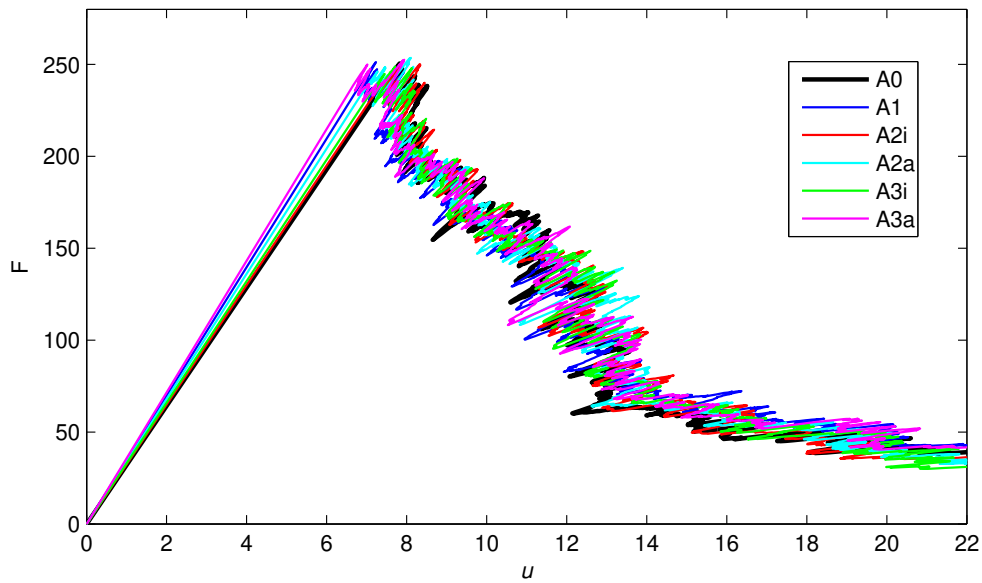


Figure 2.27: Force-displacement diagrams for microstructure with 3000 cracked links computed according to different approaches and smoothed by averaging ± 10 neighboring values with constant weight functions.

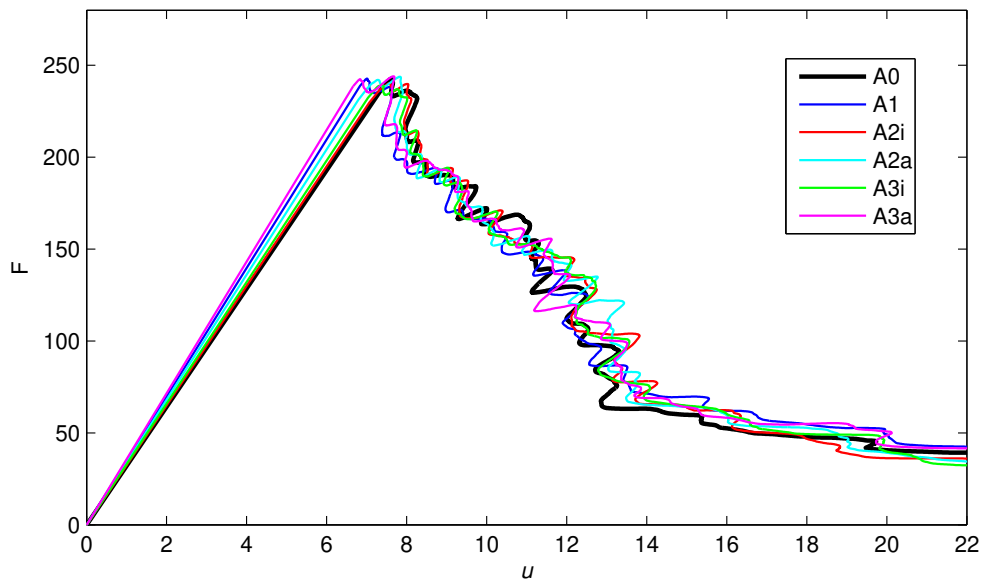


Figure 2.28: Force-displacement diagrams for microstructure with 3000 cracked links computed according to different approaches and smoothed by averaging ± 50 neighboring values, using a linear weight function.

solver with a dynamically growing compressed column matrix storage format is able to solve examples with 46 particles along the shortest edge and with 1,424,068 DOFs and 4,190,040 links. Larger examples cannot be run on a single standard PC due to lack of memory.

QC-based approaches can handle particle models with microstructure density up to 89 particles along the shortest edge using the same cheap PC with 4GB of RAM. The full particle model has 3,493,161 particles, 31,007,592 links and 10,439,878 DOFs. The QC approach uses a fully resolved domain with 433,265 renodes and 3,694,490 links that cover 11.8 % of the solved domain. In the remaining part of the domain, an interpolation mesh consisting of 4,457 elements and 1,098 mesh nodes is used, which results into a total of 3,698,947 elements and 1,302,939 DOFs. In this simplified solution, the link with the maximum strain is predicted correctly and the relative error in maximum strain is just a few percent.

Modern supercomputers would allow to solve problems with a finer microstructure but such computations can be quite expensive. Furthermore, even for supercomputers, a finite limit on the size of the problem always exists and QC-based approaches can make even larger systems solvable.

Conclusions and future work

The presented example has demonstrated that QC-based methods can lead to a substantial reduction of the computational cost. The error induced by this reduction can be kept within acceptable limits by suitably selecting the region of high interest (fully resolved domain, FSD).

Macroscopic properties associated with the global stiffness are naturally affected by a certain error induced by interpolation. Local phenomena such as cracking are well captured by sufficiently large FSDs.

Approaches A2i and A3i based on isotropic homogenization tend to underestimate the global stiffness if the material is significantly anisotropic. In such cases, these approaches seemingly appear to be more accurate in certain examples but accuracy and convergence of this approach are not guaranteed. On the other hand, the A3a approach based on local anisotropic homogenization seems to be very powerful. The homogenization error of A3a is negligible and this approach provides almost as accurate results as A1, while running substantially faster.

Both elastic and simple inelastic material models have been presented. So far, the inelastic behavior has been considered to have the form of brittle failure on the microscopic level. Future work will deal with optimization of efficiency and extensions to elastoplasticity and to softening material response, e.g., to damage-based models.

Appendix A. Homogenization of material stiffness

Two-dimensional models

Formula (2.10) is written in tensorial notation and provides the effective material stiffness tensor. In the actual numerical implementation, the tensor is represented by the corresponding matrix, based on the Voigt notation. For instance, in the two-dimensional

setting, the resulting material stiffness matrix is given by

$$\mathbf{D}^{num} = \begin{pmatrix} D_{1111} & D_{1122} & D_{1112} \\ D_{2211} & D_{2222} & D_{2212} \\ D_{1211} & D_{1222} & D_{1212} \end{pmatrix} \quad (2.16)$$

where D_{ijkl} are components of the material stiffness tensor \mathbf{D}_e . Note that, in two dimensions, only five of these components are independent. Matrix \mathbf{D}^{num} exhibits symmetry and, on top of that, $D_{1122} = D_{1212}$, because formula (2.10) leads to

$$D_{1122} = \frac{1}{V_0} \sum_{p=1}^{N_t} L_p A_p E_p n_{p1} n_{p1} n_{p2} n_{p2} = \frac{1}{V_0} \sum_{p=1}^{N_t} L_p A_p E_p n_{p1} n_{p2} n_{p1} n_{p2} = D_{1212} \quad (2.17)$$

If the material stiffness is considered as anisotropic, matrix \mathbf{D}^{num} is used directly. This is done by the A3a approach, with local evaluation of \mathbf{D}^{num} for each homogenized element separately, and also by the A2a approach, if it is decided to use an anisotropic, globally evaluated stiffness (e.g., if the structure of the particle model is indeed anisotropic).

, In approaches A2i and A3i with isotropic stiffness, \mathbf{D}^{num} is approximated by a matrix

$$\mathbf{D}^{iso} = \frac{E}{1-\nu^2} \begin{pmatrix} 1 & \nu & 0 \\ \nu & 1 & 0 \\ 0 & 0 & \frac{1-\nu}{2} \end{pmatrix} \quad (2.18)$$

which corresponds to the isotropic material stiffness under plane stress conditions, with E and ν denoting the Young modulus and Poisson ratio of the homogenized material. Alternatively, one could adopt the plane strain assumptions, which would lead to different auxiliary values of E and ν but to the same resulting matrix \mathbf{D}^{iso} .

Optimal values of parameters E and ν are identified by minimizing a certain measure of the difference between matrices \mathbf{D}^{num} and \mathbf{D}^{iso} . Several choices of such a measure are possible, but the results remain quite similar. The calculations presented here are based on the error measure defined as

$$e(\mathbf{D}^{num}, \mathbf{D}^{iso}) = \sum_{I=1}^3 \left(\mathbf{v}_I^T (\mathbf{D}^{num} - \mathbf{D}^{iso}) \mathbf{v}_I \right)^2 \quad (2.19)$$

where \mathbf{v}_I is the I -th eigenvector of matrix \mathbf{D}^{iso} . For this choice, the optimal parameters can be expressed explicitly as

$$E = \frac{4(D_{1111} + 2D_{1122} + D_{2222})(4D_{1111} - 7D_{1122} + 4D_{2222})}{33D_{1111} + 6D_{1122} + 33D_{2222}} \quad (2.20)$$

$$\nu = \frac{D_{1111} + 62D_{1122} + D_{2222}}{33D_{1111} + 6D_{1122} + 33D_{2222}} \quad (2.21)$$

Note that the above expressions for E and ν do not depend on stiffness coefficients D_{1112} and D_{2212} , which are always zero for isotropic materials. If the numerically computed coefficients D_{1112} and D_{2212} are not small (compared to the other coefficients), the assumption of isotropy is not appropriate and a fully anisotropic stiffness should be used. Also note that a perfect matching between \mathbf{D}^{num} and \mathbf{D}^{iso} is possible only if coefficients D_{1112} and D_{2212} vanish and the other coefficients satisfy conditions $D_{2222} = D_{1111}$ and $D_{1122} = D_{1111}/3$. In this case, formulae (2.20)–(2.21) give $E = (8/9)D_{1111}$ and $\nu = 1/3$.

An alternative error measure can be based on the standard Euclidean norm of fourth-order tensors. The tensorial expression $(D_{ijkl}^{num} - D_{ijkl}^{iso})(D_{ijkl}^{num} - D_{ijkl}^{iso})$, with sum over i, j, k and l implied by the summation convention, would be in the Voigt notation rewritten as

$$e(\mathbf{D}^{num}, \mathbf{D}^{iso}) = \sum_{I=1}^3 \sum_{J=1}^3 W_{IJ} (D_{IJ}^{num} - D_{IJ}^{iso})^2 = (\mathbf{D}^{num} - \mathbf{D}^{iso}) \mathbf{W} (\mathbf{D}^{num} - \mathbf{D}^{iso}) \quad (2.22)$$

where W_{IJ} are suitable weight coefficients that can be arranged into the matrix

$$\mathbf{W} = \begin{pmatrix} 1 & 1 & 2 \\ 1 & 1 & 2 \\ 2 & 2 & 4 \end{pmatrix} \quad (2.23)$$

For plane stress, the corresponding expression for the optimized elastic constants is

$$E = \frac{(D_{1111} + 2D_{1122} + D_{2222})(D_{1111} + 14D_{1122} + D_{2222})}{2(3D_{1111} + 12D_{1122} + 3D_{2222})} \quad (2.24)$$

$$\nu = \frac{2(D_{1111} - D_{1122} + D_{2222})}{3D_{1111} + 12D_{1122} + 3D_{2222}} \quad (2.25)$$

For $D_{2222} = D_{1111}$ and $D_{1122} = D_{1111}/3$, we obtain again $E = (8/9)D_{1111}$ and $\nu = 1/3$.

Alternatively, condition $\nu = 1/3$ could be imposed directly. Minimization of (2.19) with Young's modulus considered as the only fitting variable would lead to

$$E = \frac{8}{81}(4D_{1111} + 3D_{1122} + 4D_{2222}) \quad (2.26)$$

while minimization of (2.22) would give

$$E = \frac{2}{9}(D_{1111} + 6D_{1122} + D_{2222}) \quad (2.27)$$

Three-dimensional models

In the three-dimensional setting, the resulting material stiffness matrix is given by

$$\mathbf{D}^{num} = \begin{pmatrix} D_{1111} & D_{1122} & D_{1133} & D_{1123} & D_{1113} & D_{1112} \\ D_{2211} & D_{2222} & D_{2233} & D_{2223} & D_{2213} & D_{2212} \\ D_{3311} & D_{3322} & D_{3333} & D_{3323} & D_{3313} & D_{3312} \\ D_{2311} & D_{2322} & D_{2333} & D_{2323} & D_{2313} & D_{2312} \\ D_{1311} & D_{1322} & D_{1333} & D_{1323} & D_{1313} & D_{1312} \\ D_{1211} & D_{1222} & D_{1233} & D_{1223} & D_{1213} & D_{1212} \end{pmatrix} \quad (2.28)$$

Only fifteen components of the above matrix are independent because the coefficients D_{ijkl} are invariant with respect to any permutation of the subscripts.

In the A2i and A3i approaches, \mathbf{D}^{num} is approximated by an isotropic stiffness matrix

in the form

$$\mathbf{D}^{iso} = \frac{E}{(1+\nu)(1-2\nu)} \begin{pmatrix} 1-\nu & \nu & \nu & 0 & 0 & 0 \\ \nu & 1-\nu & \nu & 0 & 0 & 0 \\ \nu & \nu & 1-\nu & 0 & 0 & 0 \\ 0 & 0 & 0 & 1-2\nu & 0 & 0 \\ 0 & 0 & 0 & 0 & 1-2\nu & 0 \\ 0 & 0 & 0 & 0 & 0 & 1-2\nu \end{pmatrix} \quad (2.29)$$

The weight coefficients used in the error measure according to formula (2.22) are

$$\mathbf{W} = \begin{pmatrix} 1 & 1 & 1 & 2 & 2 & 2 \\ 1 & 1 & 1 & 2 & 2 & 2 \\ 1 & 1 & 1 & 2 & 2 & 2 \\ 2 & 2 & 2 & 4 & 4 & 4 \\ 2 & 2 & 2 & 4 & 4 & 4 \\ 2 & 2 & 2 & 4 & 4 & 4 \end{pmatrix} \quad (2.30)$$

By minimizing this error we obtain

$$E = \frac{(a+2b)(a+11b)}{15a+39b} \quad (2.31)$$

$$\nu = \frac{2a+b}{5a+13b} \quad (2.32)$$

where

$$a = D_{1111} + D_{2222} + D_{3333} \quad (2.33)$$

$$b = D_{2233} + D_{1133} + D_{1122} \quad (2.34)$$

In the special case of a perfectly isotropic matrix with $D_{3333} = D_{2222} = D_{1111}$ and $D_{2233} = D_{1133} = D_{1122} = D_{1111}/3$, the expressions can be simplified to $E = (5/6)D_{1111}$ and $\nu = 1/4$.

Appendix B. Macroscopically isotropic cells

The microstructure is generated by periodically repeating a square-shaped basic cell of size $L_x \times L_y$ with crossed diagonals; see Figure 2.29. The cross-sectional areas of individual links in horizontal, vertical and diagonal directions are denoted as A_x , A_y and A_d , respectively. The elastic modulus E_l of all links within a cell is considered to be the same. When multiple cells are combined into a rectangular pattern, the horizontal and vertical links on the inter-cell boundaries are merged and their resulting area is doubled.

Due to periodicity, evaluation of the homogenized stiffness can be based on formula (2.10) applied to one single cell and combined with formula (2.16). The resulting stiffness matrix of a homogenized two-dimensional continuum is

$$\mathbf{D}^{num} = 2 \frac{E_l}{L_x L_y t} \begin{pmatrix} A_x L_x + A_d L_d \cos^4 \alpha & A_d L_d \cos^2 \alpha \sin^2 \alpha & 0 \\ A_d L_d \cos^2 \alpha \sin^2 \alpha & A_y L_y + A_d L_d \sin^4 \alpha & 0 \\ 0 & 0 & A_d L_d \cos^2 \alpha \sin^2 \alpha \end{pmatrix} \quad (2.35)$$

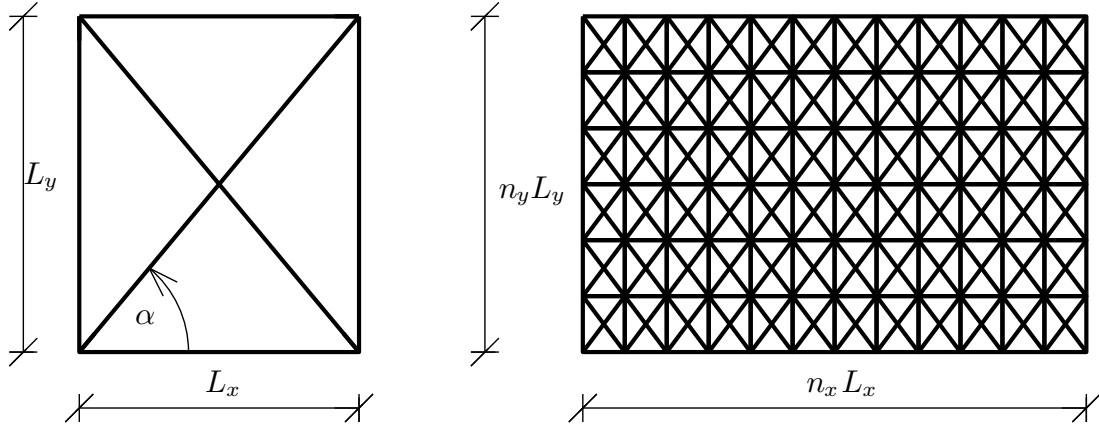


Figure 2.29: Geometry of characteristic cell (left) and periodic microstructure (right)

where t is the out-of-plane thickness, $L_d = \sqrt{L_x^2 + L_y^2}$ is the length of the diagonal link, and $\alpha = \arctan(L_y/L_x)$ is an angle characterizing the inclination of diagonals; see Fig. 2.29. In general, the stiffness matrix given by (2.35) corresponds to an orthotropic material.

By comparing (2.35) with formula (2.18) for the stiffness matrix of an isotropic material under plane stress conditions, we find that the periodic cell leads to macroscopic isotropy if the following conditions are satisfied:

$$A_x L_x + A_d L_d \cos^4 \alpha = A_y L_y + A_d L_d \sin^4 \alpha \quad (2.36)$$

$$A_d L_d \cos^2 \alpha \sin^2 \alpha = \nu (A_y L_y + A_d L_d \sin^4 \alpha) \quad (2.37)$$

$$\nu = \frac{1 - \nu}{2} \quad (2.38)$$

Condition (2.38) implies that, in the case of isotropy, the macroscopic Poisson ratio is restricted to $\nu = 1/3$. From conditions (2.36)–(2.37) combined with relations $L_x = L_d \cos \alpha$ and $L_y = L_d \sin \alpha$ we obtain

$$A_x = A_d \cos \alpha (3 - 4 \cos^2 \alpha) \quad (2.39)$$

$$A_y = A_d \sin \alpha (3 - 4 \sin^2 \alpha) \quad (2.40)$$

Finally, we can substitute $\nu = 1/3$ and (2.39)–(2.40) into condition

$$\frac{E}{1 - \nu^2} = 2 \frac{E_l}{L_x L_y t} (A_x L_x + A_d L_d \cos^4 \alpha) \quad (2.41)$$

and link the diagonal cross-sectional area

$$A_d = \frac{3EtL_d}{8E_l \sin 2\alpha} \quad (2.42)$$

to geometrical parameters of the cell and to the macroscopic and microscopic elastic moduli.

For a cell of a given geometry and for a prescribed macroscopic and microscopic elastic moduli, the characteristics of individual links in the cell can be obtained from (2.42) and

(2.39)–(2.40). To ensure that all areas are positive, angle α must be between $\pi/6$ and $\pi/3$, which means that the ratio $L_x : L_y$ must be between $1 : \sqrt{3}$ and $\sqrt{3} : 1$.

Chapter 3

Adaptive Quasicontinuum Simulation of Elastic-Brittle Disordered Lattices

Abstract:

The quasicontinuum (QC) method is a computational technique that can efficiently handle atomistic lattices by combining continuum and atomistic approaches. In this work, the QC method is combined with an adaptive algorithm, to obtain correct predictions of crack trajectories in failure simulations. Numerical simulations of crack propagation in elastic-brittle disordered lattices are performed for a two-dimensional example. The obtained results are compared with the fully resolved particle model. It is shown that the adaptive QC simulation provides a significant reduction of the computational demand. At the same time, the macroscopic crack trajectories and the shape of the force-displacement diagram are very well captured.

Reproduced from:

Mikeš K, Jirásek M., 2017. Adaptive quasicontinuum simulation of elastic-brittle disordered lattices. Acta Polytechnica CTU Proceedings 13. [63]

Introduction

Discrete particle models can effectively capture complex material responses, especially localized phenomena such as damage or plastic softening. The main disadvantage of particle-based approaches is that a huge number of particles is needed to describe the response of large-scale physically relevant models. This results in an extensive system of equations, which is expensive to solve. Furthermore, the process of assembling this system is also computationally expensive because all discrete connections must be individually taken into account.

A quasicontinuum (QC) based method can remove both of these disadvantages by combining continuum and atomistic approaches. In order to simulate crack propagation, the QC method needs to be combined with an adaptive algorithm that allows crack growth in arbitrary directions and initialization of new cracks.

In this work, the material is represented by particles interacting via elastic-brittle links forming a disordered two-dimensional lattice. Only axial interaction between particles is considered and the behavior of links is assumed to be perfectly elastic-brittle, with link breakage occurring at a critical level of tensile strain.

QC method

The QC method can efficiently handle high-resolution particle models by combining continuum and discrete approaches. This method was originally proposed in 1996 [99] for regular atomistic lattices with long-range interactions. Since that time, the QC method has been widely used and extended to applications for a variety of materials represented by regular lattices [47]. An extension of the QC method to irregular lattices has recently been developed by the authors [65].

The main idea of the QC method is to reduce the number of degrees of freedom (DOFs) and the associated computational cost without losing the exact atomistic description in regions of interest. Therefore, two types of regions in the investigated domain are considered. In regions of high interest, the pure particle approach is used and all particles carry their own independent DOFs. By contrast, in regions of low interest, continuum assumptions are applied and the computational model is significantly simplified.

The procedure that results from the QC method can be briefly presented in the following three steps: (i) interpolation, (ii) summation, and (iii) adaptivity.

Interpolation

Interpolation of DOFs is used in regions of low interest. To simplify the full particle model, only a small subset of particles is selected to represent the entire system. These so-called *repnodes* serve as the nodes of a background triangular mesh that is used to interpolate the DOFs of other particles in regions of low interest. On the other hand, in regions of high interest, all particles are selected as repnodes to provide the exact particle representation. This interpolation leads to a significant reduction of the number of DOFs without losing the exact particle description in regions where a high resolution is needed.

Summation

The interpolation provides a significant reduction of the number of DOFs but all particles still need to be visited to construct the system of governing equations, which makes

the process computationally expensive. The summation rule can be applied in order to eliminate the requirement of visiting all particles during the assembly of the system. If the summation rule is adopted, the contribution of all particles in each interpolation triangle is estimated based on sampling of the links that surround one single particle and properly scaling the contribution. This makes the computational process faster but some problems can occur on the interface between regions of high and low interest.

Because of the interpolation and the summation, the deformation is considered as constant within each interpolation element in the regions of low interest while the deformations of individual links in the regions of high interest are evaluated exactly. Consequently, forces of nonphysical character, called the *ghost forces*, appear on the interface between the regions of low and high interest [69].

In this work, the summation procedure is realized by a homogenization of links contributing to the interpolation elements. To eliminate the ghost forces, some specific links are selected to be processed exactly, in order to capture the interface between the fully resolved and interpolated domains.

Adaptivity

Adaptivity allows to adjust the regions of low and high interest during the simulation process. The type of region can be changed by adding repnodes before each step. An appropriate modification of the regions of high interest leads to a substantial increase of accuracy. Moreover, in specific cases such as simulation of crack propagation or damage evolution, adaptivity is necessary in order to represent the correct physical behavior. After the insertion of new repnodes, a new triangulation of the interpolation mesh can be constructed, in order to improve the accuracy of interpolation and summation in areas of low interest.

QC-based approaches

In this section, the exact approach and two approaches based on the idea of QC with different levels of simplification are introduced.

Fully resolved approach

This approach does not use any simplification. Every single particle represents a node with independent DOFs. All links are taken into account explicitly and contribute directly to the stiffness matrix. Consequently, this approach provides the “exact” result, which is used as a reference solution for evaluation of accuracy and efficiency of the following, simplified approaches.

QC approach with interpolation

In this approach, only the interpolation rule is used to simplify the full particle model. In the regions of high interest, all particles are selected as repnodes. By contrast, in the area of low interest, only the particles forming the vertices of interpolation elements are selected as repnodes. All remaining particles are kept in the model and their DOFs are linearly interpolated by using the underlying interpolation mesh. Such particles are called *hanging nodes* because their DOFs are not independent but are “hanging” on appropriate repnodes.

All link connections are considered explicitly in the whole domain.

QC approach with interpolation and homogenization

In this approach, 2D finite elements are used not only to interpolate DOFs but also to replace the stiffness that corresponds to the microstructure. Consequently, a substantial number of links and hanging nodes can be removed from the particle model.

Material properties of 2D elements are identified by homogenization of the effective elastic stiffness tensor \mathbf{D}_e representing the microstructure of the links. Applying the equivalence of the overall virtual work expressed for the continuous material and for the microstructure represented by discrete links, the following formula for the effective elastic stiffness tensor can be derived:

$$\mathbf{D}_e = \frac{1}{V} \sum_{i=1}^{N_t} L_i E A_i \mathbf{n}_i \otimes \mathbf{n}_i \otimes \mathbf{n}_i \otimes \mathbf{n}_i \quad (3.1)$$

Here, \mathbf{n}_i is the unit vector specifying the direction of the given link, E is the Young modulus, A is the cross-sectional area and L is the length of the link. The summation is taken over N_t links occupying volume V .

The effective stiffness tensor \mathbf{D}_e can be evaluated globally for all elements, or locally for each element separately. Afterwards, the material parameters of 2D elements can be identified as isotropic, orthotropic, or arbitrarily anisotropic. Different homogenization procedures for disordered lattices with normal interactions are described in [65].

In this work, only the most accurate homogenization rule with a local anisotropic stiffness tensor and an arbitrarily anisotropic material is used. Evaluation of the effective material stiffness tensor given by (3.1) is done for each element separately. The stiffness tensor of each element is obtained only from the contributions of the parts of the links that are located in that particular element.

Adaptive algorithm

Adaptivity is one of the key ingredients of the QC method. The area of high interest and the geometry of interpolation mesh can be arbitrarily changed during the simulation to optimize the accuracy and computational costs. Furthermore, for QC simulation of materials with softening or damage, an adaptive algorithm is required to be able to predict the exact failure mechanism.

In this paper, it is assumed that cracked links tend to form a macroscopic crack. The QC adaptive algorithm is designed to be able to simulate the growth of existing macroscopic crack as well as the initialization of new cracks. In each simulation step, this algorithm is able to change both the area of high interest and the interpolation elements in the area of low interest.

The overall algorithm of an adaptive CQ simulation is organized as follows:

Area of high interest update

The change of the area of high interest is realized around newly cracked links to allow crack growth. When a new link is broken, all particles within a given *updating radius* are labeled as renodes. This update is realized only if the breaking link is located not too far from existing macroscopic cracks. Therefore, a number of previously cracked links

Algorithm 3.1 Adaptive QC simulation

```

1: load input geometry
2: generate interpolation mesh
3: calculate local stiffness tensors and material parameters
4: assemble stiffness matrix
5: assemble load vector
6: repeat
7:   solve one elastic step
8:   break link with maximal strain
9:   update area of high interest
10:  update interpolation mesh
11:  update local stiffness tensors and material parameters
12:  update stiffness matrix and load vector
13: until <stopping criterion>
14: postprocessing

```

within a *checking radius* is evaluated and the update is realized only if a given critical number of previously cracked links is reached. Consequently, the area of high interest is updated frequently but not necessarily in all steps. This allows to account not only for crack branching but also for nucleation of new macroscopic cracks in different locations.

This procedure frequently requires searching for particles within a given radius, which can be time-consuming for large sets of particles. Therefore, it is convenient to store particles in an octree structure that enables fast spatial searching.

Interpolation mesh update

If the area of high interest has changed, it seems natural to change the geometry of the interpolation mesh as well to provide a better shape of interpolation elements at the interface between areas of low and high interest. However, this change is extremely expensive, as explained in section 3.4.3, and does not bring any significant improvement of accuracy. Therefore, it turns out to be more effective to use relatively small elements with fixed geometry instead of changing the size of elements during the simulation. Only the elements that are completely covered by the extended area of high interest become useless and can be removed from the model.

If the interpolation elements are not changed, the *updating radius* must be larger than the size of interpolation elements to ensure that the nodes of one interpolation element are not located on the opposite sides of the crack (otherwise, special finite element techniques such as XFEM must be used).

Stiffness tensors update

Generally, there are three reasons why stiffness tensors must be updated.

1. Breakage of a link
2. Change of a region of high interest
3. Change of the interpolation mesh

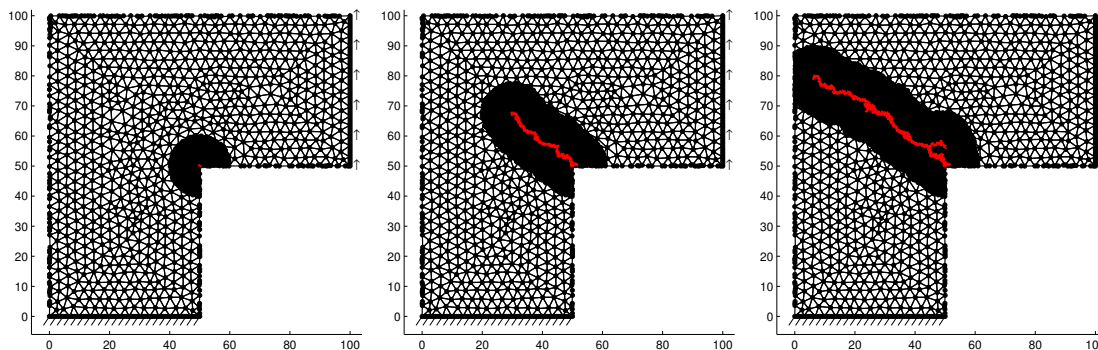


Figure 3.1: Interpolation elements and area of high interest (black) and broken links (red) in the first (left), 100-th (middle) and the last step of simulation (right).

The breakage of one link occurs in each simulation step. The resulting update of stiffness tensors can be simply realized by subtracting the stiffness contributions of broken links from all corresponding stiffness tensors.

The change of the area of high interest is realized by adding new repnodes. Consequently, the type of ending particles of some links is changed. All links changed to type renode–renode and some specific links changed to type renode–hangingnode need to be solved explicitly from this moment. All such links must be identified and their stiffness influence is subtracted in the same way as for broken links.

The change of the geometry of interpolation mesh requires a recalculation of local stiffness tensors. This recalculation is extremely demanding because all links must be visited. Even if the mesh is changed only locally near a newly created area of high interest and only some elements are affected, it is not easy to identify which links contribute to these elements and this step significantly slows down the simulation time. The recalculation of stiffness can be sped up by storing the information of element contributions during the assemblage of stiffness tensors at the beginning of the simulation. But this can be done only at the price of additional memory demands, which may become critical for large numbers of links.

Results

To assess the efficiency and accuracy, the presented adaptive QC algorithm has been used to simulate failure in two dimensions. The L-shaped specimen with dimensions 100×100 mm (which may correspond to a joint of a frame) is fixed at the bottom section and loaded by prescribed vertical displacements imposed at the right end section; see Figure 3.1. As a result of this loading, the non-convex corner is opened and cracking of links is expected to start in this region. Therefore, a small initial area of high interest is prescribed around this corner; see Figure 3.1 (left). The random microstructure is generated with a density that corresponds to 67 particles along the short edge, leading to a total of 19,000 particles connected by 64,064 links. Basic characteristics of models used by full particle and QC simplified simulations are listed in Table 3.1. Material parameters are considered to be the same for all links.

As expected, cracking starts in the non-convex corner. During crack growth, the area of high interest is increased around newly broken links. Interpolation elements completely covered by the area of high interest are removed from the model, but the geometry of the

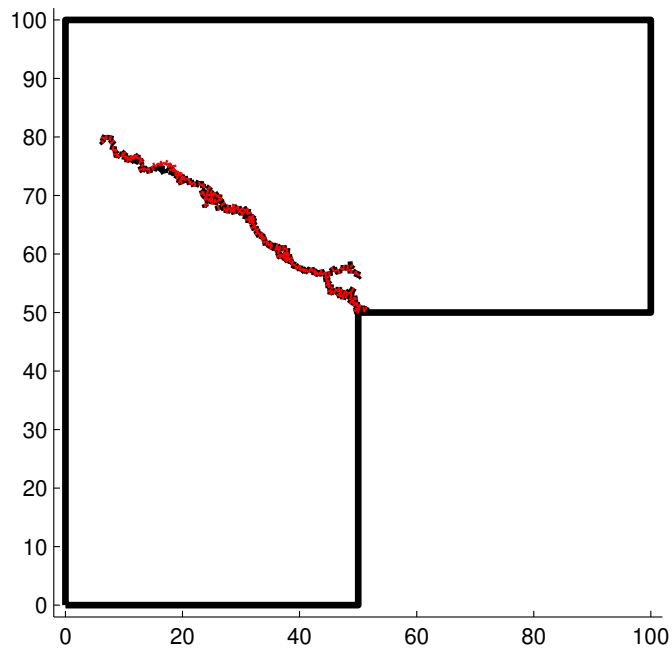


Figure 3.2: Broken links computed with exact particle approach A0 (black) and with QC approach with local anisotropic homogenization A3 (red).

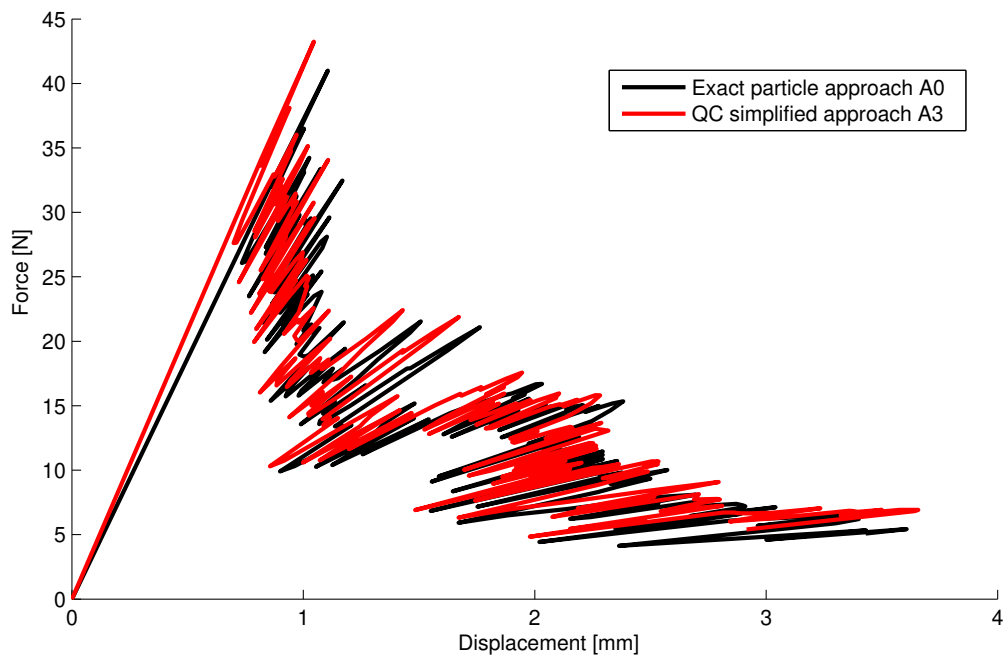


Figure 3.3: Force-displacement diagrams computed with exact particle approach A0 (black) and with QC approach with local anisotropic homogenization A3 (red).

	A0	A1	A3
Particles	19,000	19,000	2,199
Links	64,064	64,064	2,929
Elements	0	1,542	1,542
Repnodes	19,000	1,665	1,665
Hnaging nodes	0	17,335	534
DOFs	37,799	3,129	3,129

Table 3.1: Numbers of particles, links, elements, repnodes, hanging nodes and unknown DOFs for exact approach (A0), QC approaches with interpolation only (A1) and QC approach with local anisotropic homogenization (A3).

remaining interpolation elements is not changed. The areas of high interest in different loading steps are depicted in Figure 3.1. Overall 240 simulation steps are performed until the specimen is almost completely split; see Figure 3.1 (right).

Three different levels of simplification are used and compared.

- Full (exact) particle approach (A0).
- QC simplified approach with interpolation only (A1).
- QC simplified approach with interpolation and local anisotropic homogenization (A3).

The results obtained for both QC simplified approaches are almost equivalent. Both approaches predict the same broken links in the same order. Generally, approaches involving homogenization tend to a stiffer response in comparison with the interpolation approach. In this case, the influence of homogenization is negligible and the maximum difference in relative stiffness is just 0.24 %.

In comparison with the exact approach, the QC approaches give a slightly stiffer response. The relative stiffness error of the initial elastic branch is 11.8 %. The maximum relative stiffness error is below 18 % during almost the whole simulation. Only in the last six steps (when the specimen is almost completely split) the error increases up to 25 %. The prediction of cracked links is not perfectly exact, but more than 90 % of links are broken correctly and the difference in the final shape of the macroscopic crack is almost negligible; see Figure 3.2.

The simplified results are also very accurate in terms of the force-displacement diagram. Despite a stiffer elastic response, the trend of the unloading branch is very well captured and the shape of the QC simplified force-displacement diagram resembles the exact solution; see Figure 3.3.

Times consumed by individual parts of the simulation for various approaches are listed in Table 3.2. The initialization procedures are realized just once at the beginning of the simulation. On the other hand, the repeated procedures are realized in each simulation step. For QC approach A1, with interpolation only, the realization of QC simplification is relatively fast, but the initial assemblage of the stiffness matrix and load vector is extremely slow because of a huge number of hanging nodes with interpolated DOFs. By contrast, QC approach A3, involving local homogenization, needs a relatively long time to realize QC

	A0	A1	A3
Times of initial procedures [s]:			
QC simplification	-	0.83	8.08
Assemble stiffness matrix	1.09	5.81	0.15
Assemble load vector	1.92	6.36	0.21
Times of repeated procedures [s]:			
Solve one step	3.99	0.25	0.15
Update one step	1.08	2.31	0.12

Table 3.2: Time consumed by individual parts of simulation for various approaches.

simplification including local effective stiffness tensors calculation. However, the initial assemblage is very fast because the number of links and hanging nodes is significantly reduced. For both QC approaches, a long extra time is needed only at the beginning of the simulation. This initial time becomes negligible in simulations with a large number of repeated steps. The most important fact is that each simulation step of the simplified approach is twice as fast for A1 and almost 19 times faster for A3 in comparison with the full particle model.

Conclusions

This paper described a QC adaptive algorithm with automatic changes of area of high interest designed for simulation of crack propagation in disordered lattices. The presented algorithm allows not only propagation of an existing crack but also initialization of new cracks.

The presented example has shown that QC based approaches in combination with an adaptive algorithm are able to capture the exact macroscopic crack trajectory even if the area of crack propagation is not known at the beginning of simulation. The force-displacement diagram can be predicted with high accuracy in spite of the fact that the initial elastic response of simplified models is slightly stiffer. The adaptive extension of the area of high interest has turned out to be sufficient to obtain accurate results and a new triangulation of interpolation mesh is not necessary.

The application of QC approaches provides a significant reduction of the number of unknown DOFs and of links used in numerical models. This reduction leads to a significant speed-up of one simulation step, at the price of an increased cost of the initial preparation (model simplification) before the first step. If both interpolation and homogenization are applied, the speed-up factor of one step is 18.8 and the whole simulation of crack propagation (including 240 steps) gets more than 15 times faster.

Chapter 4

Molecular Statics Simulation of Nanoindentation using Adaptive Quasicontinuum Method

Abstract:

In this work, molecular statics is used to model a nanoindentation test on a two-dimensional hexagonal lattice. To this end, the QuasiContinuum (QC) method with adaptive propagation of the fully resolved domain is used to reduce the computational cost required by the full atomistic model. Three different adaptive mesh refinement criteria are introduced and tested, based on: (i) the Zienkiewicz–Zhu criterion (used for the deformation gradient), (ii) local atoms' site energy, and (iii) local lattice disregistry. Accuracy and efficiency of individual refinement schemes are compared against the full atomistic model and obtained results are discussed.

Reproduced from:

Mikeš, K., Rokoš, O. and Peerlings, R.H., 2018. Molecular static simulation of nanoindentation using adaptive quasicontinuum method. *Acta Polytechnica CTU Proceedings* 15. [66]

Introduction

Nanoindentation is a commonly used testing procedure applied to small volumes of materials for measuring their micromechanical properties. Typically, a hard tip (i.e. indenter) with known mechanical properties is pressed into an examined sample of unknown mechanical properties. Loading force and penetration depth of the indenter are recorded during the loading and unloading stages, providing a basis for the estimation of the unknown mechanical properties.

Numerical models are typically used as a tool for better understanding the underlying phenomena, and to obtain detailed information about local mechanisms occurring below the indenter tip (such as dislocation nucleation, propagation, and interaction), which directly influence measured reaction force. To this end, both the indenter and specimen are typically modelled at the atomistic level using molecular statics or molecular dynamics, entailing high computational costs when realistic configurations and dimensions are used. The QuasiContinuum (QC) method (cf. e.g. [98]) is employed to simplify the full atomistic model, to reduce the associated computational costs, and to allow for modelling of realistic situations.

This paper focuses on the predictive abilities of an adaptive QC methodology (recalled in Section 4.3) in combination with three types of error indicators/estimators for local mesh refinement compared against the full atomistic simulations. In particular, (i) the Zienkiewicz–Zhu error estimator (used for the deformation gradient), (ii) an indicator based on local atoms’ site energy, and (iii) an estimator based on local disregistry profiles are tested for a simple two-dimensional indentation test. The individual definitions are outlined in Section 4.3.3, whereas the accuracy and associated computational costs are discussed in Section 4.4.

The paper closes with conclusions and recommendations in Section 4.5.

Full atomistic model

Atomistic models based on molecular statics are characterized by an underlying lattice in combination with an interatomic potential. In this work, a two-dimensional hexagonal lattice with lattice spacing d_0 is used, as shown in Fig. 4.1. Individual atom interactions are described by the Lennard–Jones (LJ) potential, defined as

$$\phi^{\alpha\beta}(r^{\alpha\beta}) = \varepsilon \left[\left(\frac{r_m}{r^{\alpha\beta}} \right)^{12} - 2 \left(\frac{r_m}{r^{\alpha\beta}} \right)^6 \right], \quad (4.1)$$

where $r^{\alpha\beta} = \|\mathbf{r}^\beta - \mathbf{r}^\alpha\|_{\ell^2}$ denotes the distance between two atoms α and β , r_m denotes the distance at which the interaction energy reaches its minimum, and ε is the energy well depth.

The total potential energy associated with the entire atomic structure is computed as a sum over all interactions, i.e.

$$E(\mathbf{r}) = \frac{1}{2} \sum_{\alpha, \beta; \alpha \neq \beta}^{N^{\text{Atm}}} \phi^{\alpha\beta}(r^{\alpha\beta}), \quad (4.2)$$

where N^{Atm} represents the number of atoms, and \mathbf{r} is a column storing their positions.

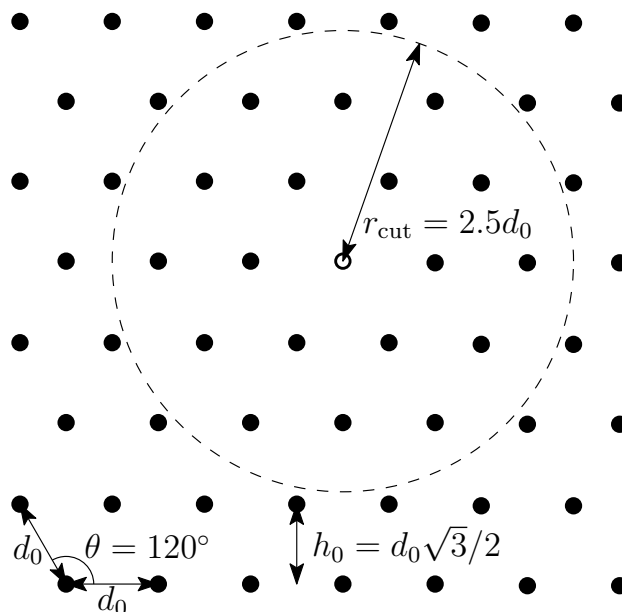


Figure 4.1: A geometry of hexagonal lattice and corresponding cut-off radius (dashed line).

Because evaluation of the interatomic potential for all pairwise combinations is computationally expensive, and because long-distance interactions have negligible contributions to the total potential energy, a *cut-off radius* r_{cut} is considered [98], beyond which interactions are neglected. Such a simplification introduces a discontinuity of $\phi^{\alpha\beta}$ at r_{cut} , which is removed by subtracting a linear function to assure zero value and zero slope of $\phi^{\alpha\beta}$ at r_{cut} . As sketched in Fig. 4.1, a cut-off radius $r_{\text{cut}} = 2.5d_0$ is employed to provide next-to-nearest interactions.

In order to find a stress-free configuration, an initial relaxation is carried out on an ideal periodic lattice with spacing $d_0 = r_m$, which results in a reduced lattice spacing $d_0 = 0.9917496 r_m$ used for constructing the initial system.

The geometry of employed indentation test is sketched in Fig. 4.2. The specimen domain is of the size $128d_0 \times 128h_0$, contains 16,862 atoms, and considers atoms near the bottom and both vertical edges as fixed, whereas the top edge is a free surface. The flat indenter is modelled at the atomistic level using the same hexagonal lattice as used for the specimen, but having infinite stiffness. Its geometry is specified through a width $11d_0$ at the tip and two surfaces inclined by 60° , as shown in Fig. 4.3 (left). The positions of all indenter atoms are prescribed in 80 uniform loading, and 80 uniform unloading steps, achieving the maximum indentation depth $8d_0$. The interaction strength between atoms of the indenter and the tested material is reduced by a factor of 0.55 (compared to the atoms of the tested material) to prevent tearing of the indented specimen during the unloading stage. The total potential energy of the atomistic system $E(\mathbf{r})$ is minimized at each time step using the trust-region algorithm; for further details see e.g. [27].

Quasicontinuum Method

The Quasicontinuum (QC) method is a concurrent multiscale technique introduced in [99]. The key idea consists in combining the accurate but expensive atomistic description only in regions of high interest with a cheap continuum approximation elsewhere. The

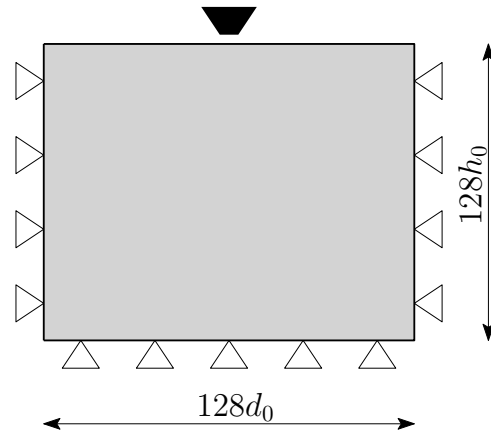


Figure 4.2: A sketch of the tested setup: specimen being indented (grey), and indenter (black).

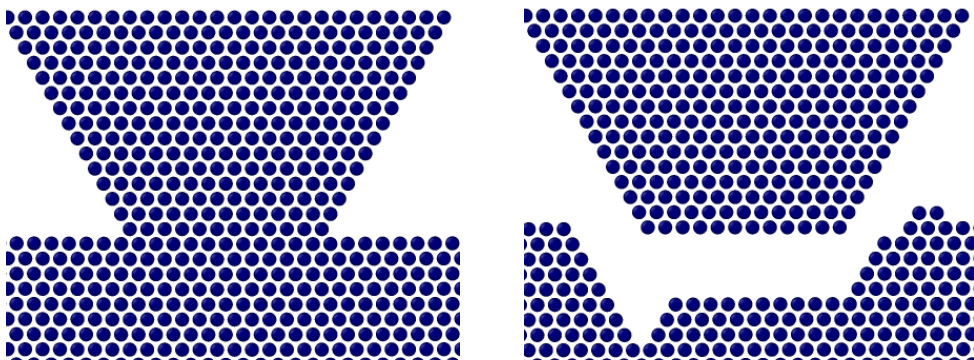


Figure 4.3: Detail of indenter area at the beginning of the loading process (left), and after unloading (right).

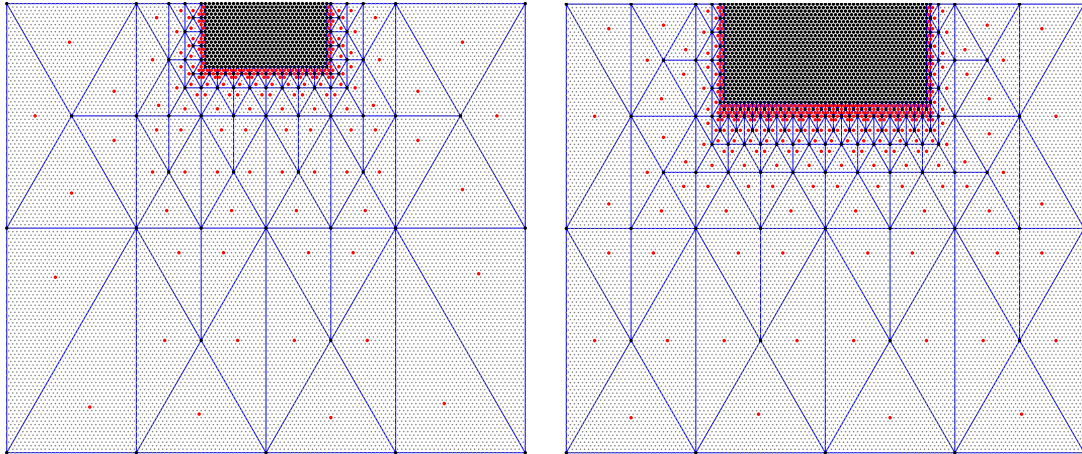


Figure 4.4: Initial triangulation with small (left) and large (right) fully-resolved region. Reatoms are shown as black dots, interpolation elements as blue triangles, sampling atoms as red dots, and remaining atoms as grey dots.

specimen domain therefore is divided into two parts: (i) the fully-resolved region, in which the full non-local atomistic model is used, seamlessly coupled with (ii) a coarse-grained continuum region, in which interpolation through triangular elements along with an efficient summation scheme is introduced.

Interpolation

The first step in the QC reduction is *interpolation*, which introduces the so-called *reatoms* through which the kinematic behaviour of the entire system is reconstructed according to

$$\mathbf{r} = \mathbf{\Phi} \mathbf{r}_{\text{rep}}, \quad (4.3)$$

where \mathbf{r}_{rep} is a column storing positions of all reatoms, interpolated through an interpolation matrix $\mathbf{\Phi}$ associated with the adopted triangulation. The number of reatoms is typically much smaller compared to the number of all atoms, reducing thus the computational effort required. Two example triangulations associated with different sizes of the fully-resolved regions are shown in Fig. 4.4.

Summation

In the second QC reduction step, a so-called *summation* rule is introduced to avoid the necessity of visiting all atoms when assembling the total potential energy in Eq. (4.2). To this end, the site energies of all atoms situated inside a triangular element are approximated by the energy of only a few, or even one *sampling atom* and its corresponding weight factor w_α , i.e.

$$E = \sum_{\alpha}^{N_{\text{SampAtm}}} w_{\alpha} \phi_{\alpha}. \quad (4.4)$$

In Eq. (4.4), ϕ_α is the site energy of a sampling atom α , defined as

$$\phi_\alpha = \frac{1}{2} \sum_{\substack{\beta; \alpha \neq \beta \\ r^{\alpha\beta} < r_{\text{cut}}}}^{N^{\text{Atm}}} \phi^{\alpha\beta}(r^{\alpha\beta}). \quad (4.5)$$

Although multiple possibilities are available in the literature to select sampling atoms and their corresponding weight factors, the central summation rule introduced in [12] is used hereafter (cf. Fig. 4.4).

Adaptivity

The area of high interest (i.e. the fully-resolved region and hence also the associated triangulation) can adaptively evolve at each time increment or iteration to accommodate dislocation movements, while retaining QC efficiency.

To this end, the fully-resolved region is sequentially updated as follows. At each time increment, the system is equilibrated for a fixed fully-resolved region. Using a selected refinement criterion (detailed below), the triangulation is checked and refined if required. Any additional atoms are added as repatoms, the interpolation mesh is updated, and equilibrium is restored. Such a procedure is repeated until the mesh refinement criterion is satisfied for all elements, proceeding subsequently to a new load increment.

In total three refinement criteria are tested:

- (i) *The Zienkiewicz–Zhu error estimator (ZZ)*, as introduced in [111], used for the deformation gradient. That is, projection of the deformation gradient is used to estimate the local error inside each element. A threshold value ZZ_{tr} is specified to determine elements to be refined, and atoms located in those elements to become repatoms.
- (ii) *The error indicator based on a local energy criterion* uses the local atoms' site energy to determine elements to be refined. First, the site energy of each sampling atom is tested for the following condition

$$\phi_\alpha \geq E_{\text{tr}}, \quad (4.6)$$

where E_{tr} is a selected critical energy threshold. Sampling atoms satisfying the condition of Eq. (4.6), as well as their neighbours within radius r_{ref} , are labelled as critical atoms. Interpolation elements that contain at least one critical atom are refined, i.e. all atoms in such elements are added as repatoms.

- (iii) *The error indicator based on disregistry profile* works in a similar way as the local energy criterion. The only difference consists in the condition for the selection of critical atoms, now specified as

$$\sum_{\substack{\beta; \alpha \neq \beta \\ r^{\alpha\beta} < r_{\text{cut}}}}^{N^{\text{Atm}}} \|\mathbf{r}^\beta - \mathbf{r}_t^\alpha\|_{\ell^2} \geq D_{\text{tr}}, \quad (4.7)$$

where D_{tr} is a selected disregistry threshold, and $\|\mathbf{r}^\beta - \mathbf{r}_t^\alpha\|_{\ell^2}$ denotes the distance of atom β from the closest position of its theoretical neighbouring atom α considered in the reference configuration. The positions of either all eighteen nearest- and next-to-nearest-neighbour atoms or just the six nearest-neighbour atoms can be used to

	Initial/final repatoms	Iterations	Mesh iterations	Time
Full solution	16862/16862	4980	-	1.00 (1:26:31)
QC fix small	952/952	3549	-	0.061
QF fix large	1900/1900	3560	-	0.099
QC zz	952/6224	8957	242	0.772
QC dis	952/8143	7536	149	0.751

Table 4.1: Numerical performance corresponding to individual computational models.

evaluate the condition of Eq. (4.7). All atoms within radius r_{ref} are again labelled as critical atoms.

Results

Numerical simulations of the nanoindentation test, as described in Section 4.2, are carried out to analyse the adaptive propagation of the fully-refined region associated with movements of individual dislocations.

In the full atomistic model, initially all atoms are displaced elastically until a critical penetration depth is reached, which triggers nucleation of four dislocations positioned symmetrically (due to the symmetry of the problem) under both indenter edges. Upon further loading, these dislocations propagate along preferred lattice directions until reaching the boundary of the specimen. During unloading, however, when the last symmetric dislocation pair annihilates, one direction is preferred due to numerical round-off errors, resulting in a nonsymmetric final shape of the indent (see Fig. 4.3 (right)). Results of the full simulation are used as the reference solution against which the QC simulations are compared, and are summarized along with the corresponding performance in Table 4.1. The force–displacement diagram is shown in Fig. 4.6.

In QC simulations, movements of individual dislocations can be captured properly only inside the fully-resolved region. The adaptive algorithms introduced in Section 4.3.3 are used to this end, providing results summarized in Fig. 4.5 for the Zienkiewicz–Zhu error estimator and loading steps number 28 (penetration of the first symmetric dislocation pair outside of the original area of high interest), 39 (one step before nucleation of the second symmetric dislocation pair), 55 (one step before the nucleation of the third symmetric dislocation pair), and 80 (maximum penetration depth). The following cases for error estimators/indicators in QC methodology have been tested:

- (1) two simulations with fixed fully-resolved regions of different sizes, see Fig. 4.4, referred to as *QC small* and *QC large*;
- (2) one simulation with an adaptive area of high interest using the ZZ criterion with $ZZ_{\text{tr}} = 0.015$, referred to as *QC zz*;
- (3) one simulation with an adaptive area of high interest based on local energy with refinement radius $r_{\text{ref}} = 5d_0$ and threshold value corresponding to 6% change of the initial potential energy (for a typical internal atom this value corresponds to $E_{\text{tr}} = -2.95$); and

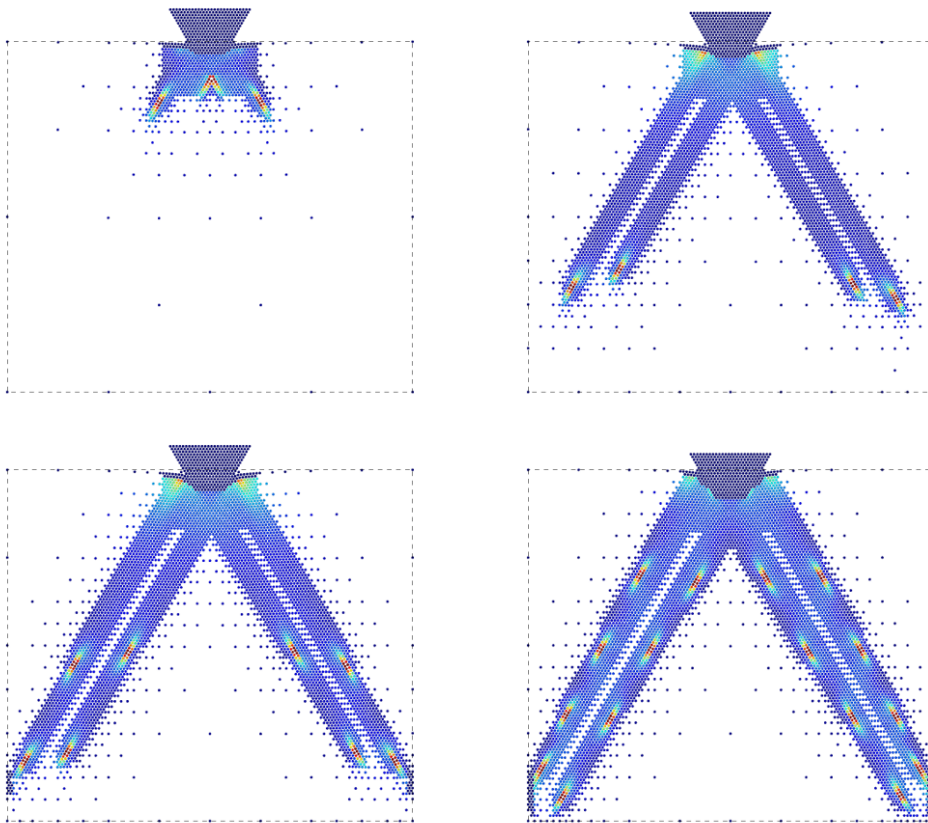


Figure 4.5: Results corresponding to QC simulations with Zienkiewicz–Zhu mesh refinement criterion. Reatoms in different loading steps are shown, corresponding to: loading step number 28 (top left), 39 (top right), 55 (bottom left), and 80 (bottom right). The colour of individual atoms corresponds to the local disregistry level. Dashed lines indicate the reference specimen shape.

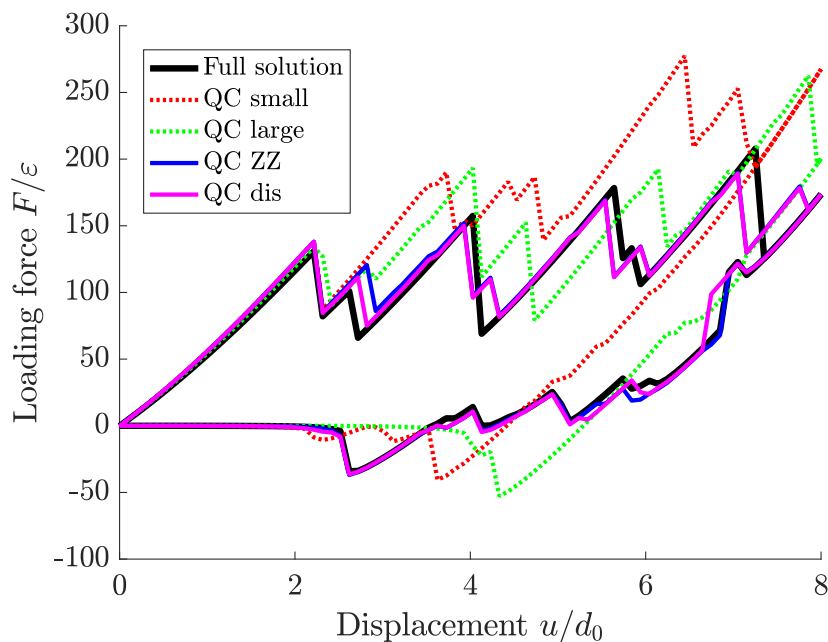


Figure 4.6: Normalized force–displacement diagrams corresponding to the different computational models.

- (4) one simulation with adaptive area of high interest based on lattice disregistry with threshold value $D_{\text{tr}} = 0.5d_0$, the nearest-neighbour option, and refinement radius $r_{\text{ref}} = 5d_0$, referred to as *QC dis*.

The simplest QC simulation with a small fixed fully-resolved area (QC small) provides a significant speed-up of a factor of 16 compared to the full atomistic model. The initial elastic behaviour and nucleation of the first symmetric dislocation pair is captured accurately, cf. Fig. 4.6, whereas in later stages (i.e. once the first symmetric dislocation pair reaches the boundary of the fully-resolved region), the resulting behaviour becomes overly stiff. This is clearly visible in the corresponding force–displacement diagram.

A partial improvement can be achieved by enlarging the fully-resolved QC region (QC large), which, nevertheless, suffers from the same shortcomings. The overestimation of the force–displacement diagram is less significant, capturing more accurately the unloading branch. The shapes of local force peaks do not correspond, however, to the exact solution due to the obstructed dislocation movements. The achieved speed-up is approximately of the order of 10.

Clearly, only the adaptive schemes are able to capture properly the dislocation movement under the tip of the indenter. Note that all adaptive QC examples are initialized with the fully-resolved area of the same size as used for the QC small simulation. The ZZ criterion detects and refines elements near individual dislocations, allowing for their propagation throughout the entire specimen. This is reflected in the corresponding force–displacement curve in Fig. 4.6, where a significant improvement in accuracy compared to the approaches with fixed meshes can be observed.

Finally, the local lattice deflection criterion is used, which provides (in the case considered) practically the same results as the energy criterion (not shown). Generally, both criteria are not equivalent and differences can be observed in examples with different type

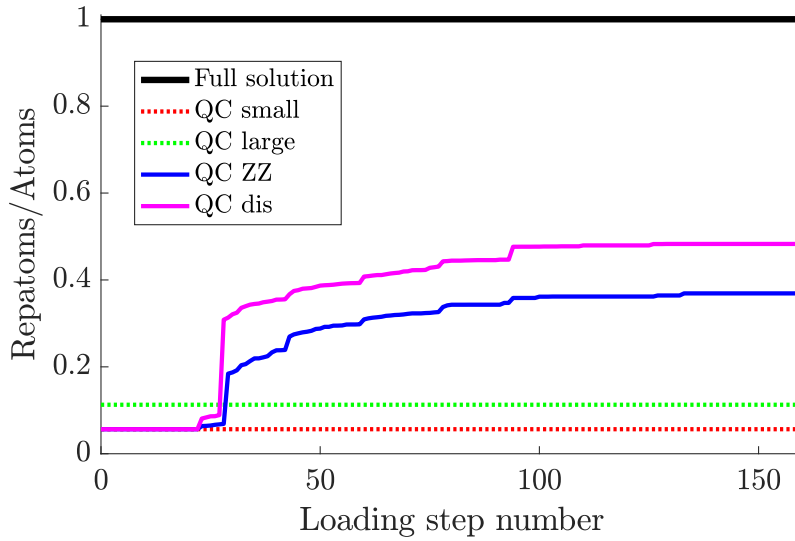


Figure 4.7: The number of repatoms relative to the number of all atoms as a function of load increment for the different computational models.

of atoms, where the energy criterion is more robust at the interface. However, in case of a single crystal with one type of atom, for each value of disregistry threshold a corresponding value of energy threshold that provides virtually the same results can be found. Compared to the ZZ condition, local lattice deflection provides similar accuracy in the resulting reaction force, while requiring a slightly higher number of repatoms (cf. Fig. 4.7). In spite of this fact, its overall performance is slightly faster compared to ZZ (cf. Tab. 4.1), explained by the fewer number of mesh iterations needed. Unlike ZZ, the indicator based on the local disregistry provides two parameters, D_{tr} and r_{ref} , for controlling the mesh evolution. Whereas D_{tr} locates the position inside the dislocation core region (see colours in Fig. 4.5), r_{ref} reflects the size of the fully-resolved region considered around that position. Large values of r_{ref} therefore provide fast propagation in the direction of the dislocation movement, but at the same time may require too many repatoms in the perpendicular direction. The value $r_{ref} = 5d_0$ proved to provide a good balance.

The performance of all QC approaches is summarized in Tab. 4.1, where the number of repatoms, required number of solver and mesh iterations, and computational times are reported. All adaptive QC approaches provide accurate descriptions during the loading as well as unloading stages, resulting in acceptable estimates of the corresponding reaction force. Although the obtained gain in computation time is relatively small (about 25% compared to the full simulation), a more substantial speed-up is expected for simulations with larger domains.

Conclusions

In this contribution, a QuasiContinuum (QC) method with different mesh refinement strategies has been compared against the full molecular statics simulation for the case of a two-dimensional nanoindentation test. It has been shown that all three tested adaptive QC approaches provide acceptable agreement with the underlying full atomistic simulation.

Two adaptive approaches (based on local energy and lattice disregistry) provide equiv-

alent results compared to the widely used Zienkiewicz–Zhu error estimator, while performing slightly faster due to fewer mesh iterations. Overall, adaptive QC approaches reduce computational time by approximately 25% compared to the full simulation. For large domains, more significant speed-ups with similar accuracy can be expected.

Chapter 5

Quasicontinuum method combined with microplane model

Abstract:

In this paper, we show how certain ideas of the microplane theory can be used in the quasicontinuum method for an irregular set of particles with axial interactions representing a heterogeneous material. The paper first analyzes the microplane material model, and then the relation between the particle model and the microplane model is described. Based on this analogy, a microplane-based summation rule for the quasicontinuum method is proposed. Five simplified approaches adopting various levels of simplification are introduced using interpolation, global or local microplane-based homogenization, and an isotropic or anisotropic microplane model. For an adaptive quasicontinuum method, a new refinement criterion based on strain at individual microplanes is proposed and investigated. All presented approaches have been implemented in OOFEM [75], an open-source object-oriented code. Accuracy, efficiency and specific properties of all simplified models based on the quasicontinuum idea are evaluated by comparing the results with the fully resolved particle model for a number of examples in 2D and 3D. The presented results show that using the proposed microplane-based quasicontinuum approaches, a significant simplification of the problem can be reached while keeping the error acceptable.

Introduction

Numerical simulations play an important role across all engineering fields. However, simulations of real problems are usually associated with enormous computational costs. Therefore, multiple numerical techniques have been developed to simplify simulations of large problems. In this paper, we focus on the QuasiContinuum (QC) method, which combines an accurate but expensive discrete description with a cheaper continuum approximation. The main idea of the QC method is to reduce the number of degrees of freedom (DOFs) and the associated computational cost without losing the exact atomistic/particle description in regions where it is required. Therefore, the investigated domain is divided into two parts: (i) the fully-resolved region (so-called region of high interest), in which the full non-local discrete model is used, seamlessly coupled with (ii) a coarse-grained continuum region (so-called region of low interest), in which interpolation through triangular elements along with an efficient summation scheme is introduced.

The QC method was originally introduced in 1996 [99, 100] to simplify large atomistic systems with long-range conservative interaction potentials. The original version of the QC method has been successfully used for simulation of localized phenomena, such as crack nucleation and propagation [45, 67], motion and interaction of dislocations [80], or nanoindentation [46, 96]. Afterwards, the QC method was extended to regular discrete lattice networks with short-range nearest-neighbor interactions with both conservative [11, 12] and non-conservative [13, 14] interaction potentials including dissipation and fiber sliding. A further extension was provided for planar beam lattices [16, 10] and general periodic beam lattices with nonlinear deformations [81]. Additional extensions include the goal-oriented adaptivity [3, 58], meshless QC method [48], or finite-temperature QC method [35, 97]. The energy-based variational formulation of a dissipative QC method has been developed for regular lattices with plasticity [83] and localized damage [85, 84]. The QC method was also extended to irregular lattices [65] and recently applied to irregular polymer networks [38].

In the present paper, we focus on randomly distributed discrete particle systems with elastoplastic axial interactions in a limited range (not necessarily just with nearest neighbors). Such systems are typically used in simulations of heterogeneous materials. This work provides a further extension of [65] where the QC approach was applied to irregular systems of particles with short-range elastic-brittle interactions. Here we proceed to the more general case of elastoplastic links, and we show how concepts borrowed from the microplane theory developed by Bažant and coworkers [8] can be exploited for an efficient replacement of the discrete model by an equivalent continuum in the so-called regions of low interest.

The idea of the microplane-inspired QC method was firstly introduced by the authors in [64] and illustrated by simple patch tests of two-dimensional purely elastic truss networks. In the present study, this idea is further extended to elastoplastic links in a general QC framework with a microplane-inspired summation rule and adaptive mesh refinement governed by a microplane-based refinement criterion. The proposed models and computational framework are implemented in OOFEM [75], an open-source object-oriented simulation platform.

Five approaches based on the QC idea combined with the microplane material are introduced here and compared with the fully resolved particle model, which is considered as the reference case. Accuracy is assessed in terms of stiffness and final yield force errors and the global response obtained with different approaches is compared in terms of force-

displacement diagrams for simple two- and three-dimensional patch tests as well as more challenging examples, including an adaptive refinement or crack localization for models with plastic softening.

The idea of quasicontinuum method

The main idea of the QC method is to reduce the number of DOFs and the associated computational cost without losing the exact (atomistic/particle) description in regions where it is required. Therefore, two types of regions are considered in the investigated domain. In *regions of high interest*, the pure particle approach is employed and all particles carry their own independent DOFs. By contrast, in *regions of low interest*, continuum assumptions can be used to simplify the original full model by applying interpolation and summation rules as illustrated in Fig. 5.1.

Interpolation

The first step in the QC reduction is *interpolation* of DOFs in the regions of low interest where only a small subset of particles, so-called *repnodes*, is selected to represent the kinematic behavior of the entire system. The position of all nodes, stored in column vector \mathbf{r} , is reconstructed according to interpolation rule

$$\mathbf{r} = \mathbf{\Phi} \mathbf{r}_{\text{rep}}, \quad (5.1)$$

where \mathbf{r}_{rep} is a column storing positions of all repnodes and $\mathbf{\Phi}$ is an interpolation matrix associated with the adopted triangulation.

On the other hand, in regions of high interest, all particles are selected as repnodes to provide the exact particle representation. Since the number of repnodes is usually significantly smaller than number of nodes, see, e.g., Fig. 5.1 (b), the interpolation step leads to a significant reduction of the number of DOFs without losing the exact particle description in regions where a high resolution is needed.

Summation

The interpolation provides a significant reduction of the number of DOFs but all bonds still need to be visited in order to evaluate the total potential energy and to construct the corresponding system of governing equations, which makes the solution process computationally expensive. Therefore, the second QC reduction step in the form of the so-called *summation* rule is introduced. To avoid the necessity of visiting all bonds when assembling the system, the energy contribution \mathcal{E}_e of all nodes located inside one triangular element are approximated by the energy of only a few, or even one *sampling node* and its corresponding weight factor w_α , i.e.

$$\mathcal{E}_e = \sum_{\alpha}^{N_S} w_\alpha \phi_\alpha. \quad (5.2)$$

where ϕ_α is the energy contribution of sampling node α and N_S is the total number of sampling nodes in a particular triangular element.

For regular lattices, multiple possibilities how to select the summation scheme, i.e., the sampling nodes and their corresponding weight factors, are available in the literature;

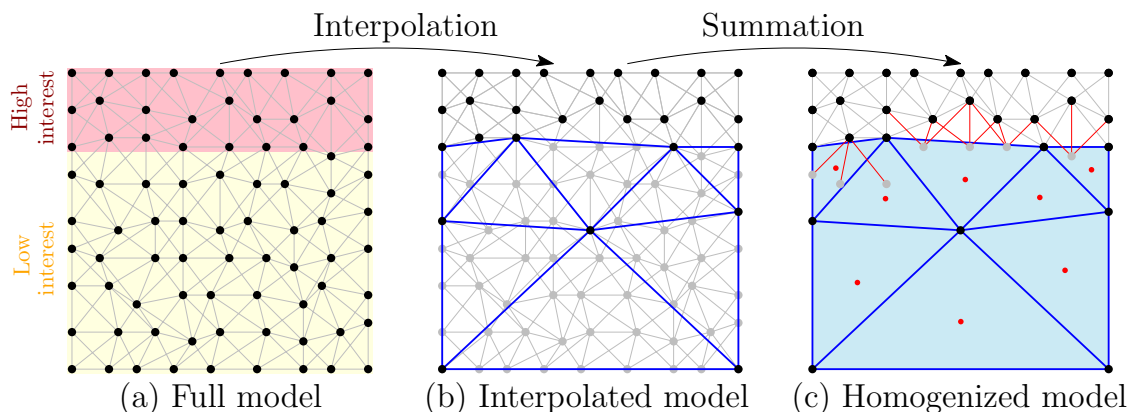


Figure 5.1: Illustration of the two-step simplification process: (a) full network of nodes (black) and links (gray) with denoted areas of low (yellow) and high (pink) interest; (b) interpolated model with repnodes (black circles), hanging nodes (gray circles), and interpolation elements (blue triangles), all gray links are evaluated explicitly; (c) simplified model with homogenized material (light blue), sampling points (red circles), and links modeled explicitly in area of high interest (gray lines) and on the interface (red lines).

see, e.g. [12, 54, 1] for more details.

In this paper, the summation procedure of a random elastoplastic network is realized by a homogenization of links contributing to the interpolation elements, based on an analogy with the microplane material model. In the homogenization-based summation scheme, interpolation elements (originally with zero stiffness) are considered to be made of a homogenized material with properties determined from the geometry of homogenized links. A special attention must be paid to the interface between regions of high interest (where all links are modeled explicitly) and regions of low interest (where links are replaced by a continuum). All links that connect a renode and an interpolated node which are not situated within the same interpolation element cannot be properly homogenized because of the fact that the deformation is considered as constant within each interpolation element while the deformations of individual links in the regions of high interest are evaluated exactly. Therefore, such links are processed exactly, in order to capture properly the interface between the fully resolved and interpolated domains, see the red lines in Fig. 5.1 (c). These explicit links ensure that both domain types are seamlessly coupled and no artificial hand shaking procedure is required. The details of various microplane-based summation schemes will be presented in section 5.4.3.

Adaptivity

The last ingredient of the QC method is an *adaptive* scheme that provides suitable changes of the regions of high interest during the simulation process. An appropriate modification of the regions of high interest leads to a substantial increase of accuracy. Moreover, in specific cases such as simulation of crack propagation or damage evolution, adaptivity is necessary in order to represent the correct physical behavior. The evolution of the area of high interest in an adaptive QC simulation is governed by an appropriate refinement criterion, optionally combined with an additional coarsening criterion. The available refinement criteria have been recently discussed in [25]. As described therein,

most of them are based on quantities that are relevant for regular atomistic lattices for metals and only several studies [58, 85, 84, 66, 25] presented a different concept applicable to (possibly irregular) structural lattices.

In the present study, we introduce a new refinement concept exploiting a microplane-based refinement criterion where local variables of individual microplanes (e.g., the microplane normal strain) can be used to evaluate the refinement criterion as defined in section 5.4.6.

Elastoplastic microplane model

If the links are assumed to behave as purely elastic, they are represented by elastic bars of axial stiffness

$$k = \frac{E_t A_t}{L} \quad (5.3)$$

where L is the bar length (corresponding to the distance between connected particles) and $E_t A_t$ is the cross-sectional stiffness of the bar, which is the same for all bars and its value is calibrated based on the macroscopic elastic properties of the given material.

The material of 2D and 3D elements is represented by the 3×3 or 6×6 stiffness matrix obtained by using one of the homogenization procedures described in Section 5.4.4.

For QC simulations of plastic materials, the postulated uniaxial plastic model of links (truss elements) has to be transformed into an equivalent two- or three-dimensional model of the material used in 2D or 3D elements.

In this paper, the links are considered to be perfectly elasto-plastic in tension and elastic in compression. The yield limit in tension is denoted as S_{0t} . The elastic stiffness E_t and the cross-sectional area of each bar A_t are the same as for an elastic computation.

Basic equations

The description of the 2D and 3D continuous material with elastoplastic properties is based on the simplest version of the microplane theory. An introduction to microplane models can be found e.g. in Chapter 25 of [44]. The essential idea of the microplane theory is that the constitutive law is constructed in terms of stress and strain vectors instead of second-order tensors. The relation between the stress and strain vectors is used on planes with various orientations, called the microplanes. In kinematically constrained microplane models, the strain vector on each microplane is obtained by projection of the macroscopic strain tensor (i.e., by its contraction with a unit vector \mathbf{n} normal to the microplane). The macroscopic stress tensor is then constructed by integrating the contributions of the stress vectors on all microplanes, based on the principle of virtual work.

The kinematic constraint can be described by the formula

$$\varepsilon_i^n = \varepsilon_{ij} n_j \quad (5.4)$$

where ε_i^n is the i -th component of the microplane strain vector, ε_{ij} are the components of the strain tensor, and n_j are components of the unit vector \mathbf{n} that characterizes the microplane. The corresponding normal strain on the microplane is

$$\varepsilon_N = n_i \varepsilon_i^n = n_i \varepsilon_{ij} n_j = N_{ij} \varepsilon_{ij} \quad (5.5)$$

where $N_{ij} = n_i n_j$ are the components of the second-order tensor $\mathbf{N} = \mathbf{n} \otimes \mathbf{n}$.

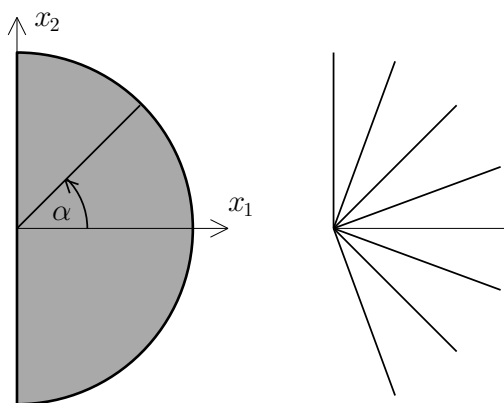


Figure 5.2: All possible directions of 2D microplane normal vectors (left). Example of a finite number of microplanes used in numerical integration (right).

The initial version of the microplane model [8] (later denoted as M1) is adopted here. It considers only the normal components of strain and stress microplane vectors (the shear components are not accounted for), which perfectly corresponds to the present particle model with links transmitting only axial forces.

In 2D, all possible directions of normal microplane vectors form a unit semicircle (because vectors \mathbf{n} and $-\mathbf{n}$ correspond to the same microplane), and each microplane can be characterized by the angle $\alpha \in (-\pi/2, \pi/2]$ for which $n_1 = \cos \alpha$ and $n_2 = \sin \alpha$; see Figure 5.2. The microplanes with values of α that differ by π are equivalent. This is why the integration is limited to one half of the unit circle. Similarly, in 3D the end points of normal microplane vectors fill the unit hemisphere. The unit semicircle for 2D models and the unit hemisphere for 3D models will be denoted here as domain Ω .

Each microplane can be in an elastic or a plastic state. For a monotonous loading process and perfect elastoplasticity, we can expect that those microplanes that get into the plastic state are never unloaded back to the elastic state. The microplane stress is then evaluated simply as

$$\sigma_N = \begin{cases} E_N \varepsilon_N & \text{for } \varepsilon_N < \varepsilon_0 \quad (\text{elastic state}) \\ S_0 & \text{for } \varepsilon_N \geq \varepsilon_0 \quad (\text{plastic state}) \end{cases} \quad (5.6)$$

Here, E_N is the elastic stiffness at the microplane level, S_0 is the yield stress at the microplane level, and $\varepsilon_0 = S_0/E_N$ is the limit elastic strain at the microplane level. The present model is based on the assumption that plastic yielding occurs only in tension while the compressive response at the microplane level is purely elastic.

To cover the general case with possible elastic unloading after previous plastic yielding, we can introduce the microplane yield function

$$f_N(\sigma_N) = \sigma_N - S_0 \quad (5.7)$$

and write the microplane constitutive law in the form

$$\sigma_N = E_N(\varepsilon_N - \varepsilon_{Np}) \quad (5.8)$$

$$\dot{\varepsilon}_{N_p} \geq 0, \quad f_N(\sigma_N) \leq 0, \quad \dot{\varepsilon}_{N_p} f_N(\sigma_N) = 0 \quad (5.9)$$

where ε_{N_p} is the plastic microplane strain.

Once the microplane stresses are known, the corresponding macroscopic stress tensor can be evaluated from the principle of virtual work, written as

$$\int_{\Omega} \sigma_N \delta \varepsilon_N d\Omega = V_0 \sigma_{ij} \delta \varepsilon_{ij} \quad (5.10)$$

The integral on the left-hand side is taken over all possible directions of microplanes, represented by the unit hemisphere in 3D and by the unit semicircle in 2D, and the factor V_0 on the right-hand side is equal to $2\pi/3$ in 3D (one half of the volume of the unit ball) and to $\pi/2$ in 2D (one half of the area of the unit disk). Due to the kinematic constraint (5.5), the virtual microplane strains $\delta \varepsilon_N$ can be expressed in terms of the components of the virtual strain tensor $\delta \varepsilon_{ij}$. Substituting the relation $\delta \varepsilon_N = \delta \varepsilon_{ij} N_{ij}$ into (5.10) and taking into account independence of the virtual strains $\delta \varepsilon_{ij}$, we obtain the following integral formula for the evaluation of macroscopic stresses:

$$\sigma_{ij} = \frac{1}{V_0} \int_{\Omega} \sigma_N N_{ij} d\Omega \quad (5.11)$$

In two dimensions, we have $V_0 = \pi/2$, and the components of the unit vector \mathbf{n} can be expressed as $n_1 = \cos \alpha$ and $n_2 = \sin \alpha$ where $\alpha \in (-\pi/2, \pi/2]$. The stress evaluation formula (5.11) then gives

$$\sigma_{11} = \frac{2}{\pi} \int_{-\pi/2}^{\pi/2} \sigma_N \cos^2 \alpha d\alpha \quad (5.12)$$

$$\sigma_{22} = \frac{2}{\pi} \int_{-\pi/2}^{\pi/2} \sigma_N \sin^2 \alpha d\alpha \quad (5.13)$$

$$\sigma_{12} = \frac{2}{\pi} \int_{-\pi/2}^{\pi/2} \sigma_N \cos \alpha \sin \alpha d\alpha \quad (5.14)$$

In the numerical implementation, the integral in eq. (5.11) over the surface of a hemisphere or a semicircle is evaluated numerically by a numerical integration formula with a sum over a finite number of integration points represented by selected microplanes, i.e.,

$$\sigma_{ij} = \sum_i^{N_M} w_i \sigma_{N_i} \quad (5.15)$$

where N_M is the number of selected microplanes (see Fig. 5.2 right) and w_i are integration weights. For the isotropic version of microplane model, a list of microplane directions and corresponding weights can be found in the literature, see, e.g., [8].

Analysis of macroscopic response

Let us now investigate the macroscopic response of the microplane model described in the previous subsection. It will be demonstrated that the stress-strain curves obtained in a given proportional loading program can be evaluated analytically. Before the onset of plastic yielding, the microplane stresses are given by $\sigma_N = E_N \varepsilon_N$ on all microplanes, and

formula (5.11) combined with the kinematic constraint (5.5) gives

$$\sigma_{ij} = \frac{1}{V_0} \int_{\Omega} E_N N_{kl} \varepsilon_{kl} N_{ij} d\Omega = D_{ijkl} \varepsilon_{kl} \quad (5.16)$$

where

$$D_{ijkl} = \frac{E_N}{V_0} \int_{\Omega} N_{ij} N_{kl} d\Omega = \frac{E_N}{V_0} \int_{\Omega} n_i n_j n_k n_l d\Omega \quad (5.17)$$

are components of the elastic stiffness tensor.

The integral in (5.17) can be evaluated in closed form. The result is a fourth-order tensor with components invariant with respect to any permutation of subscripts i, j, k and l . Consequently, it must be a scalar multiple of the tensor with components $\delta_{ij}\delta_{kl} + \delta_{ik}\delta_{jl} + \delta_{il}\delta_{jk}$. The scalar factor can be determined by contracting both sides of the equality

$$\int_{\Omega} n_i n_j n_k n_l d\Omega = C(\delta_{ij}\delta_{kl} + \delta_{ik}\delta_{jl} + \delta_{il}\delta_{jk}) \quad (5.18)$$

with the tensor $\delta_{ij}\delta_{kl}$. Taking into account that $\delta_{ij}n_i n_j = n_i n_i = 1$ and that the trace of the unit second-order tensor, $\delta_{ij}\delta_{ij} = \delta_{ii}$, is equal to the number of spatial dimensions, denoted here as d (with $d = 2$ in 2D and $d = 3$ in 3D), we obtain

$$\int_{\Omega} d\Omega = C(d^2 + d + d) \quad (5.19)$$

Factor C is thus given by

$$C = \frac{\int_{\Omega} d\Omega}{d(d+2)} = \begin{cases} \frac{\pi}{2 \cdot (2+2)} = \frac{\pi}{8} & \text{in 2D} \\ \frac{2\pi}{3 \cdot (3+2)} = \frac{2\pi}{15} & \text{in 3D} \end{cases} \quad (5.20)$$

Using (5.18) and (5.20) in (5.17) and recalling that $V_0 = \pi/2$ in 2D and $V_0 = 2\pi/3$ in 3D, we finally obtain the stiffness coefficients

$$D_{ijkl} = \frac{E_N}{V_0} \int_{\Omega} n_i n_j n_k n_l d\Omega = \begin{cases} \frac{E_N}{4} (\delta_{ij}\delta_{kl} + \delta_{ik}\delta_{jl} + \delta_{il}\delta_{jk}) & \text{in 2D} \\ \frac{E_N}{5} (\delta_{ij}\delta_{kl} + \delta_{ik}\delta_{jl} + \delta_{il}\delta_{jk}) & \text{in 3D} \end{cases} \quad (5.21)$$

In 3D, the resulting stiffness corresponds to an isotropic elastic material with Lamé coefficients

$$\lambda = \mu = \frac{E_N}{5} \quad (5.22)$$

Such a material has Young's modulus

$$E = \frac{(3\lambda + 2\mu)\mu}{\lambda + \mu} = \frac{E_N}{2} \quad (5.23)$$

and Poisson's ratio

$$\nu = \frac{\lambda}{2(\lambda + \mu)} = 0.25 \quad (5.24)$$

In 2D, formula (5.21) gives

$$D_{1111} = D_{2222} = \frac{3E_N}{4} \quad (5.25)$$

$$D_{1122} = D_{2211} = D_{1212} = D_{1221} = D_{2112} = D_{2121} = \frac{E_N}{4} \quad (5.26)$$

and all other stiffness coefficients are zero. In the matrix notation, the resulting elastic stress-strain law reads

$$\begin{Bmatrix} \sigma_{11} \\ \sigma_{22} \\ \tau_{12} \end{Bmatrix} = \frac{E_N}{4} \begin{bmatrix} 3 & 1 & 0 \\ 1 & 3 & 0 \\ 0 & 0 & 1 \end{bmatrix} \begin{Bmatrix} \varepsilon_{11} \\ \varepsilon_{22} \\ \gamma_{12} \end{Bmatrix} \quad (5.27)$$

If the 2D microplane model is applied under plane stress conditions, the corresponding macroscopic elastic constants are $E = 2E_N/3$ and $\nu = 1/3$. Under plane strain, one would get $E = 5E_N/8$ and $\nu = 1/4$.

Plastic flow is initiated when the normal strain on a microplane reaches for the first time the value of ε_0 . The maximum of normal strains over all microplanes corresponds to the maximum principal strain, and so the initial elastic domain can be characterized by the condition $\max_I \varepsilon_I < \varepsilon_0$ where ε_I , $I = 1, 2, 3$, are the principal strains (not necessarily ordered). In terms of macroscopic stresses, the initial yield function is given by

$$f_{\text{in}}(\boldsymbol{\sigma}) = (1 + \nu)\sigma_{\text{max}}(\boldsymbol{\sigma}) - \nu I_1(\boldsymbol{\sigma}) - f_{t,\text{in}} \quad (5.28)$$

where σ_{max} is the maximum principal stress, I_1 is the first invariant of the stress tensor (sum of principal stresses), and

$$f_{t,\text{in}} = E\varepsilon_0 = \frac{E}{E_N} S_0 \quad (5.29)$$

is the initial macroscopic yield stress under uniaxial tension. For a 3D microplane model, we get $f_{t,\text{in}} = S_0/2$, and the initial yield condition in terms of ordered principal stresses ($\sigma_1 \geq \sigma_2 \geq \sigma_3$) reads

$$\sigma_1 - \frac{\sigma_2 + \sigma_3}{4} = \frac{S_0}{2} \quad (5.30)$$

For a 2D microplane model, we get $f_{t,\text{in}} = 2S_0/3$, and the initial yield condition in terms of ordered principal in-plane stresses ($\sigma_1 \geq \sigma_2$) reads

$$\sigma_1 - \frac{\sigma_2}{3} = \frac{2S_0}{3} \quad (5.31)$$

The corresponding initial yield surface is plotted in Figure 5.3 by the dashed black line.

After the onset of plastic yielding on the first microplane (normal to the direction of maximum principal stress), the macroscopic stress can still increase because the stress at other microplanes is below the microplane yield limit, S_0 . The only exception is the case when all microplanes attain the yield limit simultaneously, which happens under hydrostatic tension ($\sigma_1 = \sigma_2 = \sigma_3$) for the 3D model and under equibiaxial tension ($\sigma_1 = \sigma_2$) for the 2D model. For all other types of stress, the macroscopic response is expected to exhibit hardening, i.e., an expansion of the elastic domain. However, macroscopic stresses cannot grow without any limits, because the microplane stresses are bounded by

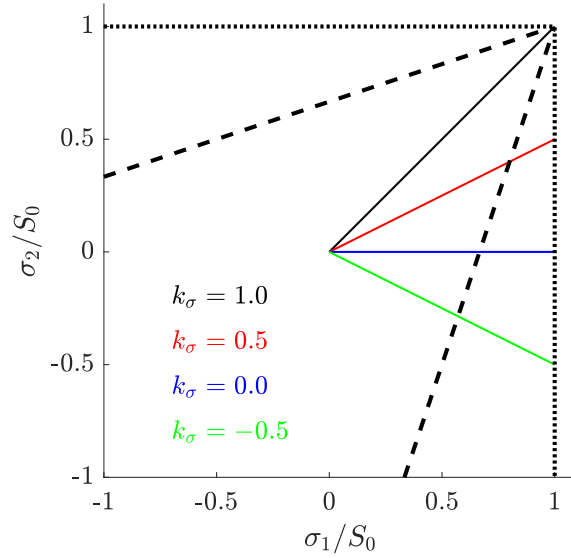


Figure 5.3: Initial yield surface (dashed black), final yield surface (dotted black), and examples of loading trajectories for $k_\sigma = 1.0$ (solid black), $k_\sigma = 0.5$ (red), $k_\sigma = 0$ (blue) and $k_\sigma = -0.5$ (green).

S_0 . Making use of (5.11), we can derive the estimate

$$\sigma_{11} = \frac{1}{V_0} \int_{\Omega} \sigma_N N_{11} d\Omega \leq \frac{S_0}{V_0} \int_{\Omega} N_{11} d\Omega \quad (5.32)$$

and the same upper bound applies to normal stresses σ_{22} and σ_{33} (and in fact to the normal stress in an arbitrary direction). Since $\int_{\Omega} N_{11} d\Omega$ is equal to V_0 in 3D as well as in 2D, the maximum principal stress cannot exceed S_0 . At the same time, the inequality in (5.32) can turn into an equality only if $\sigma_N = S_0$ for almost all microplanes (by “almost” we mean “with possible exception of a set of microplanes that has zero measure”). When this happens, not only stress component σ_{11} but also σ_{22} and, in 3D, also σ_{33} become equal to S_0 , and so the stress state is hydrostatic (in the 3D case) or equibiaxial (in the 2D case). It is thus interesting to explore how the stress grows if the ratio between the principal stresses differs from 1.

Consider the 2D microplane model and proportional loading with a fixed ratio between the in-plane principal stresses, $k_\sigma = \sigma_2/\sigma_1$, where $\sigma_1 \geq \sigma_2$. Substituting $\sigma_2 = k_\sigma \sigma_1$ into (5.31), we find that the stresses at the onset of plastic yielding are

$$\sigma_1 = \frac{2S_0}{3 - k_\sigma}, \quad \sigma_2 = k_\sigma \sigma_1 = \frac{2k_\sigma S_0}{3 - k_\sigma} \quad (5.33)$$

and the corresponding principal strains can be evaluated from the elastic stress-strain law, with $\nu = 1/3$ and $E = 2E_N/3$:

$$\varepsilon_1 = \frac{1}{E}(\sigma_1 - \nu\sigma_2) = \frac{1 - \nu k_\sigma}{E} \sigma_1 = \frac{1 - k_\sigma/3}{E} \frac{2S_0}{3 - k_\sigma} = \frac{2S_0}{3E} = \varepsilon_0 \quad (5.34)$$

$$\varepsilon_2 = \frac{1}{E}(\sigma_2 - \nu\sigma_1) = \frac{k_\sigma - \nu}{E} \sigma_1 = \frac{k_\sigma - 1/3}{E} \frac{2S_0}{3 - k_\sigma} = \frac{3k_\sigma - 1}{3 - k_\sigma} \varepsilon_0 \quad (5.35)$$

Loading beyond the elastic limit leads to the extension of plastic yielding from one microplane to a range of microplanes with normals near the direction of maximum principal strain. Without loss of generality we can assume that the direction of maximum principal strain corresponds to $\alpha = 0$ and remains fixed (no rotation of principal axes). For principal strains ε_1 and ε_2 , with $\varepsilon_1 > \varepsilon_2$, the limit elastic strain ε_0 is attained on the microplanes characterized by angles $\pm\alpha_0$ that satisfy the condition

$$\varepsilon_N = \varepsilon_{11}n_1^2 + \varepsilon_{22}n_2^2 = \varepsilon_1 \cos^2 \alpha_0 + \varepsilon_2 \sin^2 \alpha_0 = \varepsilon_0 \quad (5.36)$$

from which

$$\alpha_0 = \arcsin \sqrt{\frac{\varepsilon_1 - \varepsilon_0}{\varepsilon_1 - \varepsilon_2}} \quad (5.37)$$

Initially, $\alpha_0 = 0$. As long as α_0 keeps growing, microplanes with $|\alpha| < \alpha_0$ are in a plastic state, and microplanes with $|\alpha| > \alpha_0$ are still in an elastic state. The microplane stresses σ_N are easily obtained from (5.6), and the principal stresses, which are equal to the normal stresses σ_{11} and σ_{22} , can be evaluated according to (5.12)–(5.13) as

$$\begin{aligned} \sigma_1 &= \frac{4}{\pi} \int_0^{\alpha_0} S_0 \cos^2 \alpha \, d\alpha + \frac{4}{\pi} \int_{\alpha_0}^{\pi/2} E_N (\varepsilon_1 \cos^2 \alpha + \varepsilon_2 \sin^2 \alpha) \cos^2 \alpha \, d\alpha = \\ &= \frac{S_0}{\pi} (2\alpha_0 + \sin 2\alpha_0) + \\ &\quad + \frac{E_N}{8\pi} [\varepsilon_1 (6\pi - 12\alpha_0 - 8 \sin 2\alpha_0 - \sin 4\alpha_0) + \varepsilon_2 (2\pi - 4\alpha_0 + \sin 4\alpha_0)] \end{aligned} \quad (5.38)$$

$$\begin{aligned} \sigma_2 &= \frac{4}{\pi} \int_0^{\alpha_0} S_0 \sin^2 \alpha \, d\alpha + \frac{4}{\pi} \int_{\alpha_0}^{\pi/2} E_N (\varepsilon_1 \cos^2 \alpha + \varepsilon_2 \sin^2 \alpha) \sin^2 \alpha \, d\alpha = \\ &= \frac{S_0}{\pi} (2\alpha_0 - \sin 2\alpha_0) + \\ &\quad + \frac{E_N}{8\pi} [\varepsilon_1 (2\pi - 4\alpha_0 + \sin 4\alpha_0) + \varepsilon_2 (6\pi - 12\alpha_0 + 8 \sin 2\alpha_0 - \sin 4\alpha_0)] \end{aligned} \quad (5.39)$$

Equations (5.36) and (5.38)–(5.39) combined with the constraint $\sigma_2 = k_\sigma \sigma_1$ form a set of four equations for five unknowns, σ_1 , σ_2 , ε_1 , ε_2 and α_0 . One unknown needs to be selected as the parameter that controls the loading process and the other four can then be calculated from the equations. It is convenient to consider α_0 as the “loading parameter”, because the other unknowns are involved in all the governing equations in a linear fashion, and so, for fixed α_0 , the equations can be solved in closed form.

Making use of an auxiliary function

$$\begin{aligned} B(\alpha_0, k_\sigma) &= (k_\sigma + 1)(2\pi - 4\alpha_0 - \sin 4\alpha_0) + 4(k_\sigma - 1) \sin 2\alpha_0 + \\ &\quad + 8(2\alpha_0 - \pi) (k_\sigma \sin^2 \alpha_0 + \cos^2 \alpha_0) \end{aligned} \quad (5.40)$$

we can express the resulting maximum in-plane principal strain as

$$\begin{aligned} \varepsilon_1 &= \frac{\varepsilon_0}{B(\alpha_0, k_\sigma)} \left[(k_\sigma - 3)(2\pi - 4\alpha_0) + 16(k_\sigma - 1)\alpha_0 \sin^2 \alpha_0 + \right. \\ &\quad \left. + 8(k_\sigma \sin^2 \alpha_0 - \cos^2 \alpha_0) \sin 2\alpha_0 + (k_\sigma + 1) \sin 4\alpha_0 \right] \end{aligned} \quad (5.41)$$

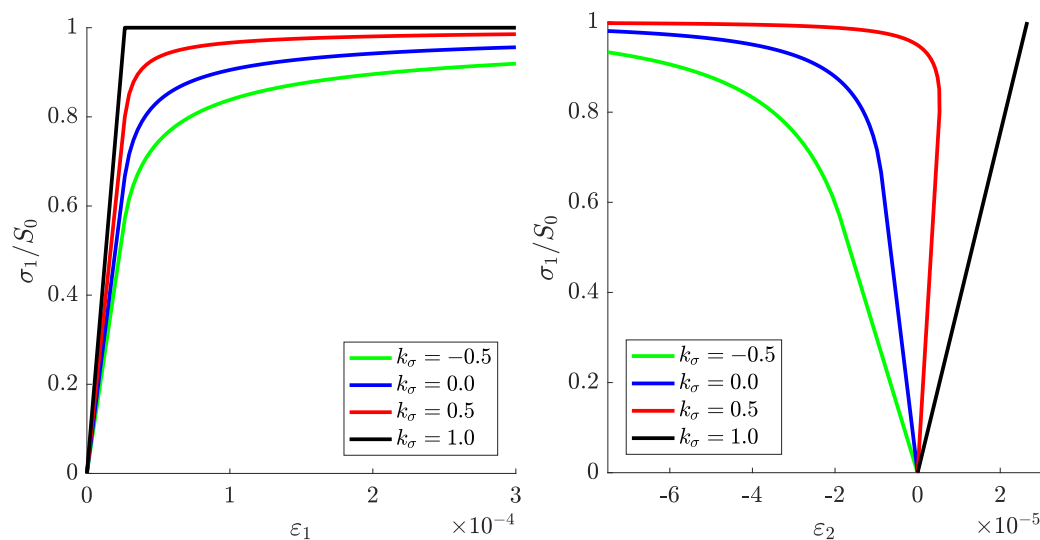


Figure 5.4: Stress-strain diagrams for microplane model under proportional biaxial loading with different ratios k_σ between principal stresses: major principal stress versus major principal strain (left), major principal stress versus minor principal strain (right).

The minimum in-plane principal strain is then evaluated as

$$\varepsilon_2 = \frac{\varepsilon_0 - \varepsilon_1 \cos^2 \alpha_0}{\sin^2 \alpha_0} \quad (5.42)$$

and the principal stresses are obtained by substituting (5.41)–(5.42) into (5.38)–(5.39).

In Figure 5.4, the stress-strain diagrams are plotted for four proportional loading programs, characterized by $k_\sigma = -0.5, 0, 0.5$, and 1 . The value of $k_\sigma = 1$ corresponds to equibiaxial tension with $\sigma_1 = \sigma_2$. In this special case, plastic flow starts at all microplanes simultaneously and the macroscopic response is elastic-perfectly plastic; see the black line in Figure 5.4a. In all other cases, plastic flow starts on one microplane and then gradually extends to a growing range of microplanes, which is accompanied by hardening. The major principal stress σ_1 at the onset of yielding depends on the minor principal stress, σ_2 , but the hardening process always tends asymptotically to $\sigma_1 = S_0$, independently of σ_2 . This means that the ultimate yield surface is described by the Rankine criterion of maximum principal stress, with S_0 playing the role of the ultimate yield stress.

In addition to the basic stress-strain diagrams in Figure 5.4a, plotted in terms of σ_1 and ε_1 , Figure 5.4b shows the relation between σ_1 and ε_2 . In the elastic range, the ratio between ε_2 and ε_1 is fixed and depends exclusively on the stress ratio, k_σ (since the Poisson ratio $\nu = 1/3$ is fixed). After the onset of yielding, the evolution of ε_2 is affected by plastic flow. It is interesting to note that for $k_\sigma = 0.5$, the minor principal strain ε_2 is initially positive but during plastic yielding changes its sign. For $k_\sigma = 1$ (equibiaxial tension), the evolution of plastic strains is not uniquely defined because the stress state corresponds to a vertex of the yield surface. As long as both ε_1 and ε_2 keep growing, all microplanes are yielding and the stress state remains equibiaxial.

It is also interesting to explore how the yield surface evolves during the hardening process. As already explained, the initial yield surface is described by condition (5.31), derived from the criterion of maximum principal strain, and the ultimate one by condition

$\sigma_1 = S_0$, which corresponds to the criterion of maximum principal stress. Both conditions are represented by straight lines in the half-plane where $\sigma_1 \geq \sigma_2$, intersecting in the vertex on the symmetry axis that corresponds to $\sigma_1 = \sigma_2$; see the dashed and dotted black lines in Figure 5.3. Suppose that the material has been hardening under a proportional loading by principal stresses σ_1 and $\sigma_2 = k_\sigma \sigma_1$, up to the current state at which the principal strains are $\varepsilon_1 = \bar{\varepsilon}_1$ and $\varepsilon_2 = \bar{\varepsilon}_2$, and the angle that characterizes the range of yielding microplanes is $\alpha_0 = \bar{\alpha}_0$ and satisfies the condition $\bar{\varepsilon}_1 \cos^2 \bar{\alpha}_0 + \bar{\varepsilon}_2 \sin^2 \bar{\alpha}_0 = \varepsilon_0$. Our objective is to describe the current elastic domain, i.e., all the states that can be attained by an elastic process (with no further plastic flow) starting from the current state. For simplicity, we restrict attention to processes that do not lead to a rotation of principal directions (of both stress and strain).

The current elastic domain can be conveniently described in terms of principal strains. If none of the microplanes exhibits additional plastic flow, the normal strains on those microplanes that are currently in a plastic state must not exceed their current normal strains, and the normal strains on those microplanes that are currently in an elastic state must not exceed the elastic limit strain, ε_0 . This condition may be written as

$$\varepsilon_1 \cos^2 \alpha + \varepsilon_2 \sin^2 \alpha \leq \begin{cases} \bar{\varepsilon}_1 \cos^2 \alpha + \bar{\varepsilon}_2 \sin^2 \alpha & \text{for } 0 \leq \alpha \leq \bar{\alpha}_0 \\ \varepsilon_0 & \text{for } \bar{\alpha}_0 \leq \alpha \leq \pi/2 \end{cases} \quad (5.43)$$

Here, ε_1 and ε_2 are the principal strains in the state that belongs to the elastic domain (if the foregoing condition is satisfied). We assume that the current principal strains $\bar{\varepsilon}_1$ and $\bar{\varepsilon}_2$ have been attained by proportional loading and are ordered (i.e., $\bar{\varepsilon}_1 \geq \bar{\varepsilon}_2$), but since we are now exploring an arbitrary continuation of the loading process, we admit that ε_2 could become greater than ε_1 .

The inequality in the second line of (5.43) is satisfied for all $\alpha \in [\bar{\alpha}_0, \pi/2]$ if it is satisfied for $\alpha = \bar{\alpha}_0$ and for $\alpha = \pi/2$, which leads to conditions

$$\varepsilon_1 \cos^2 \bar{\alpha}_0 + \varepsilon_2 \sin^2 \bar{\alpha}_0 \leq \varepsilon_0 \quad (5.44)$$

$$\varepsilon_2 \leq \varepsilon_0 \quad (5.45)$$

The first line of (5.43) can equivalently be written as

$$(\varepsilon_1 - \bar{\varepsilon}_1) \cos^2 \alpha + (\varepsilon_2 - \bar{\varepsilon}_2) \sin^2 \alpha \leq 0 \quad (5.46)$$

This inequality is satisfied for all $\alpha \in [0, \bar{\alpha}_0]$ if it is satisfied for $\alpha = 0$ and for $\alpha = \bar{\alpha}_0$. Setting $\alpha = 0$ we get

$$\varepsilon_1 \leq \bar{\varepsilon}_1 \quad (5.47)$$

while for $\alpha = \bar{\alpha}_0$ we would obtain a condition equivalent with (5.45), which has already been imposed. In summary, the elastic domain in the plane of principal strains is described by linear inequalities (5.44)–(5.45) and (5.47), which have to be satisfied simultaneously.

Transformation of the elastic domain to the principal stress plane is easy if we realize that the current principal stresses $\bar{\sigma}_1$ and $\bar{\sigma}_2$ are known and the process leading to an arbitrary state in the elastic domain is purely elastic. It is thus possible to apply the

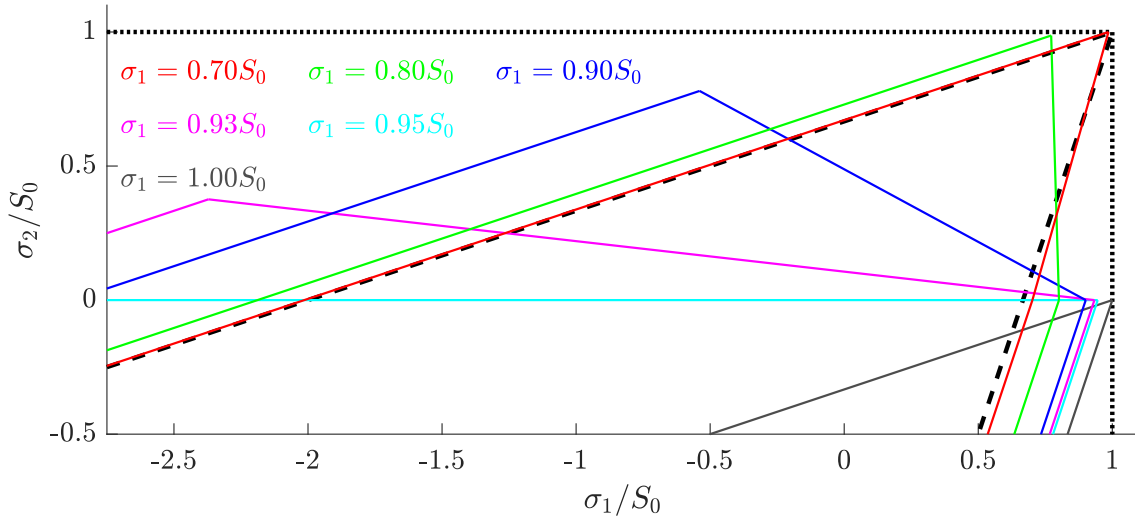


Figure 5.5: Initial yield surface (dashed black) and its evolution during hardening under uniaxial tension (red, green, blue, magenta, cyan and gray). The dotted black lines correspond to the ultimate yield surface.

elastic stress-strain law in the incremental form

$$\sigma_1 = \bar{\sigma}_1 + \frac{E_N}{4} [3(\varepsilon_1 - \bar{\varepsilon}_1) + \varepsilon_2 - \bar{\varepsilon}_2] \quad (5.48)$$

$$\sigma_2 = \bar{\sigma}_2 + \frac{E_N}{4} [\varepsilon_1 - \bar{\varepsilon}_1 + 3(\varepsilon_2 - \bar{\varepsilon}_2)] \quad (5.49)$$

which can be inverted to

$$\varepsilon_1 = \bar{\varepsilon}_1 + \frac{1}{2E_N} [3(\sigma_1 - \bar{\sigma}_1) - (\sigma_2 - \bar{\sigma}_2)] \quad (5.50)$$

$$\varepsilon_2 = \bar{\varepsilon}_2 + \frac{1}{2E_N} [-(\sigma_1 - \bar{\sigma}_1) + 3(\sigma_2 - \bar{\sigma}_2)] \quad (5.51)$$

Substituting (5.50)–(5.51) into (5.44)–(5.45) and (5.47), we finally get

$$\sigma_1 + \sigma_2 + 2(\sigma_1 - \sigma_2) \cos 2\bar{\alpha}_0 \leq \bar{\sigma}_1 + \bar{\sigma}_2 + 2(\bar{\sigma}_1 - \bar{\sigma}_2) \cos 2\bar{\alpha}_0 \quad (5.52)$$

$$3\sigma_2 - \sigma_1 \leq 3\bar{\sigma}_2 - \bar{\sigma}_1 + 2E_N(\varepsilon_0 - \bar{\varepsilon}_2) \quad (5.53)$$

$$3\sigma_1 - \sigma_2 \leq 3\bar{\sigma}_1 - \bar{\sigma}_2 \quad (5.54)$$

The resulting inequalities are again linear, and the elastic domain in the principal stress plane is an intersection of three half-planes.

For the initial value of $\bar{\alpha}_0 = 0$, conditions (5.52)–(5.54) coincide, which is consistent with the fact that the initial elastic domain is an intersection of two half-planes (symmetric about the axis $\sigma_1 = \sigma_2$) and has a vertex at $\sigma_1 = \sigma_2 = S_0$. The evolution of the elastic domain during plastic flow leads to the development of an additional vertex of the yield surface. This is documented in Figure 5.5, which shows several stages of the yield surface evolution under uniaxial tension. For $\sigma_1 = \bar{\sigma}_1$ and $\sigma_2 = \bar{\sigma}_2$, conditions (5.52) and (5.54) are satisfied as equalities. Consequently, the “second vertex” is always located at the current stress point and moves towards the ultimate yield surface. At the same time, the

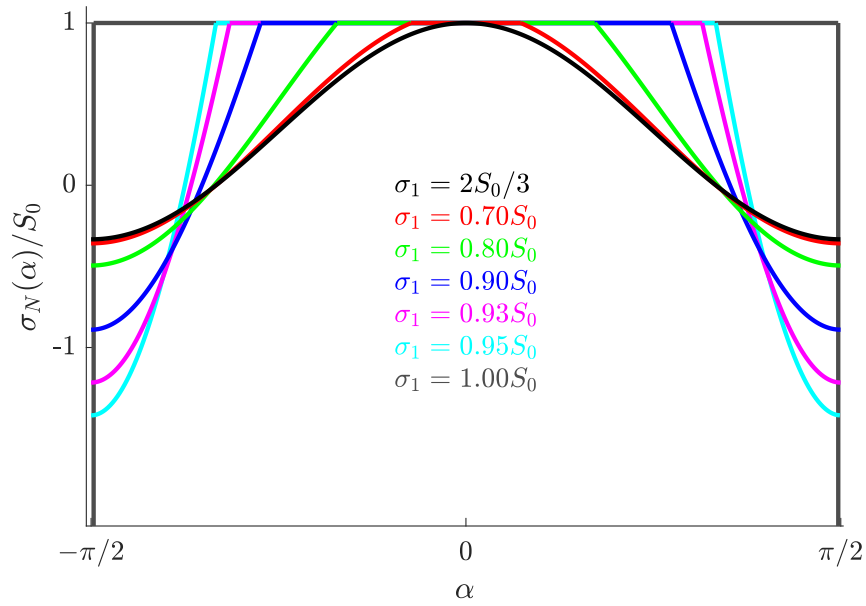


Figure 5.6: Distribution of microplane stresses during loading by various levels of uniaxial stress.

“first vertex” also changes its position and moves in Figure 5.5 to the left and downwards, away from the ultimate yield surface. As the uniaxial stress grows from the initial yield stress $2S_0/3$ to the ultimate yield stress S_0 , the yield surface in Figure 5.5 evolves from the initial one (marked by black dashed lines) to those plotted in red, green, blue, magenta, cyan and gray.

It may be somewhat surprising that, at late stages of the process, the elastic domain no longer contains the origin (stress-free state). This phenomenon is related to the residual microplane stresses. Figure 5.6 illustrates the distribution of microplane stresses over directions α ranging from $-\pi/2$ to $\pi/2$ under uniaxial tension. The solid black curve corresponds to the elastic limit state, when the microplane yield limit is reached on the microplane with $\alpha = 0$. The solid magenta curve in Figure 5.7 corresponds to the state at macroscopic stress $\sigma_1 = S_0.93$, when the plastic range extends from $\alpha = -0.990$ to $\alpha = 0.990$, and the dotted magenta curve corresponds to the state after unloading of the macroscopic stress from $\sigma_1 = 0.93S_0$ to 0. In this case, the unloading is indeed purely elastic for all microplanes, and residual microplane stresses are developed. These stresses are compressive for directions near $\alpha = 0$ and $\alpha = \pm\pi/2$ and also tensile for some directions in between; see Figure 5.7. These residual stresses are self-equilibrated in the sense that their macroscopic counterparts evaluated from (5.12)–(5.14) are zero. In Figure 5.7, the solid gray curve corresponds to the state at macroscopic stress $\sigma_1 = S_0$, when the plastic range extends from $\alpha = -\pi/2$ to $\alpha = \pi/2$, and the dotted gray curve corresponds to the fictitious state that would be attained after unloading of the macroscopic stress to 0 if the process was purely elastic on all microplanes. It is clear that residual stresses computed in this way would exceed the microplane yield stress S_0 . Therefore, the actual unloading process is accompanied by plastic yielding on some microplanes; the resulting distribution of residual microplane stresses is plotted by the dashed gray curve. The value $\sigma_1 = 0.95S_0$ corresponds to the plastic range from $\alpha = -\pi/3$ to $\alpha = \pi/3$ and it is the largest uniaxial stress for which the unloading process is still elastic; see cyan curves in Figures 5.5 and 5.7.

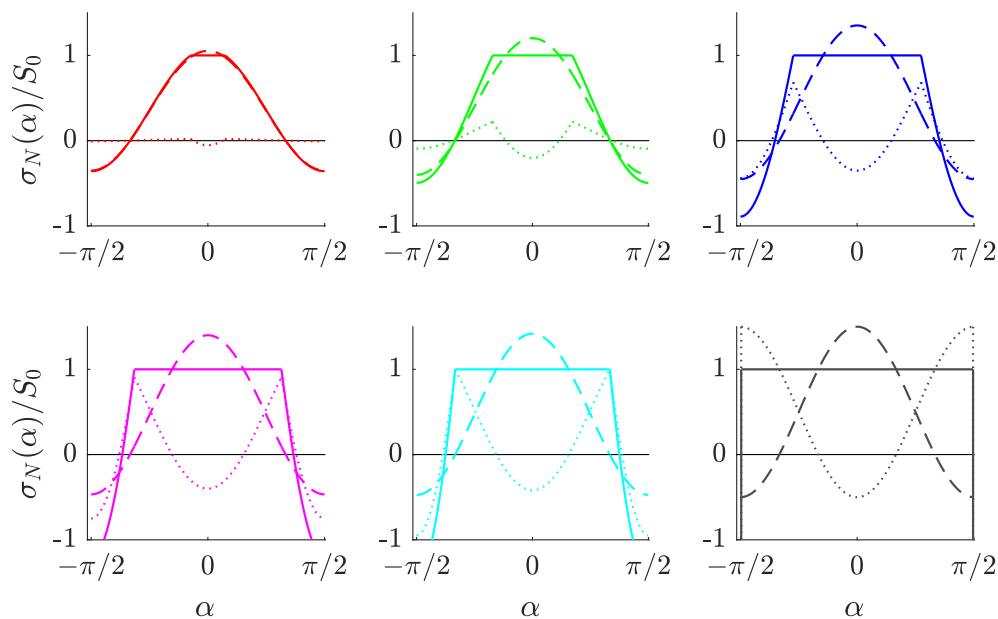


Figure 5.7: Distribution of microplane stresses during loading by uniaxial stress (solid), elastic stress distribution which is unloaded (dashed), and of residual stresses after unloading (dotted). The maximum attained stress level is $\sigma_1 = 0.70 S_0$ (red), $\sigma_1 = 0.80 S_0$ (green), $\sigma_1 = 0.90 S_0$ (blue), $\sigma_1 = 0.93 S_0$ (magenta), $\sigma_1 = 0.95 S_0$ (cyan), $\sigma_1 = 1.00 S_0$ (gray).

In numerical simulations, the stress-evaluation integral (5.11) is approximated using a suitable quadrature formula. The microplane stress is calculated for a finite number of selected microplanes (see Figure 5.2), and the integral is replaced by a weighted sum over the selected microplanes with predefined weights that depend on the quadrature rule. Figure 5.8 compares the analytically described stress-strain diagram for a 2D microplane model under uniaxial tension with diagrams computed numerically, using integration schemes with various numbers of microplanes. Already for 10 microplanes, the results are very satisfactory.

Comparison of particle model and microplane model

The microplane model with a perfectly elastoplastic behavior at the microplane level has many features similar to the particle model with perfectly elastoplastic links. For both models, the basic unit (a microplane or a link connecting particles) transmits only normal stress or axial force, exhibits linear elastic behavior up to the yield limit and perfectly plastic behavior when the yield limit is attained. Links in a particle model are finite in number and their directions are random. The microplane model theoretically deals with an infinite number of microplanes and the macroscopic stress is evaluated by integration but, in a numerical simulation, the integral is replaced by a sum over a finite number of selected representative microplanes.

For both models, it can be expected that the cumulative response of a large number of perfectly elastoplastic units (links or microplanes) of different directions will result into a gradual transition from the elastic regime to plastic yielding, with hardening up to saturation. Indeed, the stress-strain diagram for the microplane model (Figure 5.8) has

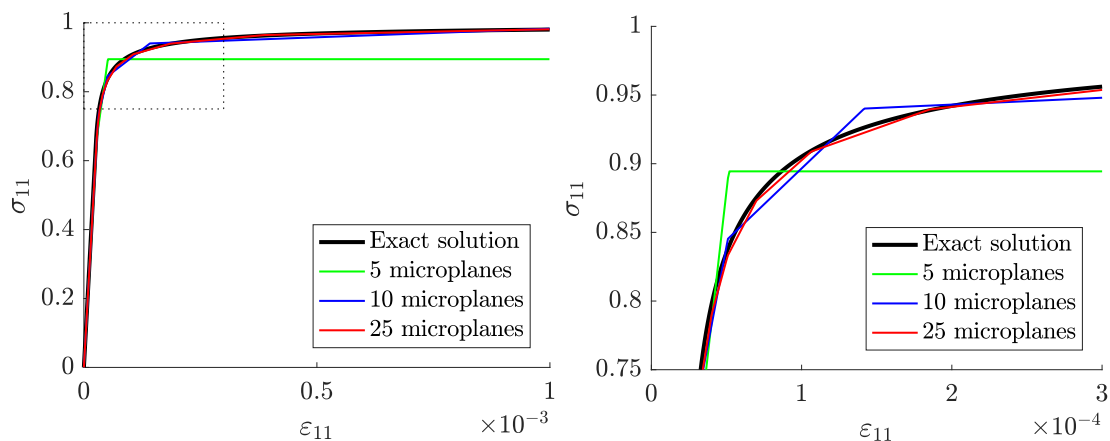


Figure 5.8: Stress-strain diagrams of microplane model in a uniaxial tensile test obtained analytically (black) and by numerical integration with various numbers of microplanes; full diagrams (left), close-up of the highlighted region (right).

a shape similar to the force-displacement diagram of an elongated specimen simulated by the particle model (Figure 5.24). Both diagrams are characterized by two important states: the limit elastic state, at which the first microplane or first link start yielding, and the saturated hardening state, at which almost all microplanes are in the plastic regime or the links form a plastic mechanism.

For the microplane model, both characteristic states can be investigated analytically, which has been done in the previous subsection. Graphical representation of the initial and ultimate yield surfaces in the principal stress plane is provided in Figure 5.3. For the equibiaxial loading scenario with $k_\sigma = 1$, the limit elastic state and the state of saturated hardening coincide (all microplanes get into the plastic state at the same time).

For the particle model, the characteristic states cannot be predicted exactly because they depend on the random position of particles. However, a particle model with an almost uniform directional distribution of links can be expected to be very close to the microplane model, provided that both models are properly calibrated to the same macroscopic properties. Constitutive equations of the microplane model at the microplane level contain two independent basic parameters E_N and S_0 , from which $\varepsilon_0 = S_0/E_N$ can be obtained. From these intrinsic parameters, the macroscopic properties can be determined by methods described in the previous subsection. For a two-dimensional model, the resulting macroscopic elastic constants are $E = 2E_N/3$ and $\nu = 1/3$, the initial yield condition is given by (5.31), and the ultimate yield surface, approached asymptotically during the hardening process, corresponds to the Rankine condition with tensile strength $f_t = S_0$.

The particle model has intrinsic material parameters $E_t A_t$ and $S_{0t} A_t$, but its behavior also depends on the geometry of the network of links. The micro-to-macro scale transition relation considered for homogenization of a truss lattice to the microplane material is based on the so-called Hill-Mandel macrohomogeneity condition [40], which requires that the virtual macroscopic work density at a point be equal to the average microscopic virtual work in a corresponding volume of the microstructure. Based on this postulate, it was shown in [65] that the effective elastic stiffness tensor corresponding to the network of

links is given by

$$\mathbf{D}_e = \frac{1}{V} \sum_{p=1}^{N_t} L_p E_{tp} A_{tp} (\mathbf{N}_p \otimes \mathbf{N}_p) \quad (5.55)$$

where $\mathbf{N}_p = \mathbf{n}_p \otimes \mathbf{n}_p$ is a second-order tensor, \mathbf{n}_p is the unit vector specifying the direction of link number p , E_{tp} is the Young modulus of the link, A_{tp} is its cross-sectional area and L_p is its length. The sum is taken over N_t links occupying volume V (here the microplane element or multiple elements). If $E_t A_t$ is considered to be the same for all links, formula (5.55) can be rewritten as

$$\mathbf{D}_e = \frac{E_t A_t}{V} \sum_{p=1}^{N_t} L_p (\mathbf{N}_p \otimes \mathbf{N}_p) \quad (5.56)$$

If the links are randomly oriented, with uniform probability density, we can estimate

$$\sum_{p=1}^{N_t} L_p N_{pij} N_{pkl} \approx C (\delta_{ij} \delta_{kl} + \delta_{ik} \delta_{jl} + \delta_{il} \delta_{jk}) \quad (5.57)$$

because the components of the tensor should be invariant with respect to a permutation of subscripts. The scaling constant C can be determined by contracting both sides of the foregoing equation from the left and from the right with the unit second-order tensor, which gives

$$\sum_{p=1}^{N_t} L_p = C(d^2 + d + d) \quad (5.58)$$

where d is the number of spatial dimensions ($d = 2$ for 2D and $d = 3$ for 3D). This means that

$$C = \frac{\sum_{p=1}^{N_t} L_p}{d^2 + 2d} \quad (5.59)$$

and the components of the material stiffness tensor \mathbf{D}_e from (5.56) can be estimated as

$$\begin{aligned} D_{eijkl} &\approx \frac{E_t A_t}{V} \frac{1}{d^2 + 2d} \left(\sum_{p=1}^{N_t} L_p \right) (\delta_{ij} \delta_{kl} + \delta_{ik} \delta_{jl} + \delta_{il} \delta_{jk}) = \\ &= \frac{E_t \rho}{d(d+2)} (\delta_{ij} \delta_{kl} + \delta_{ik} \delta_{jl} + \delta_{il} \delta_{jk}) \end{aligned} \quad (5.60)$$

where

$$\rho = \frac{1}{V} \sum_{p=1}^{N_t} A_t L_p \quad (5.61)$$

is the dimensionless volume fraction of the links (volume of the links per unit volume of the space that they occupy).

In the 3D case ($d = 3$), the right-hand side of (5.60) corresponds to an isotropic elastic material with Lamé coefficients $\lambda = \mu = E_t \rho / 15$, Poisson's ratio $\nu = 1/4$ and Young's modulus $E = E_t \rho / 6$. Comparing this result with (5.23), we find that if the network of links should be replaced by a microplane model with equivalent elastic properties, the elastic parameter of the microplane model must be set to $E_N = 2E = E_t \rho / 3$.

The ultimate macroscopic yield stress can be evaluated as

$$\sigma_0 = \frac{1}{3V} \sum_{p=1}^{N_t} L_p S_{0t} A_t = \frac{S_{0t}}{3} \frac{1}{V} \sum_{p=1}^{N_t} L_p A_t = \frac{S_{0t} \rho}{3} \quad (5.62)$$

Since, for the microplane model, we have $\sigma_0 = S_0$, parameter S_0 of the microplane model must be set to $S_{0t} \rho / 3$ to get a microplane model with plastic properties equivalent to the network of links.

Extension to additional material phenomena

So far the microplane model has been considered as perfectly elastoplastic. However, one of the important advantages of microplane-based homogenization approach is the definition of the constitutive law on the level of a microplane in a vectorial form and, in the case of model M1 with normal components only, even in a scalar form. Such a definition is in perfect analogy with a constitutive law of one-dimensional truss elements. Therefore, both models can be easily extended and a number of material phenomena such as plastic softening, hardening, damage, etc. can be covered once the appropriate constitutive law is defined on the truss level as well as on the microplane level. A numerical example with plastic softening is presented in section 5.5.6.

Microplane-base quasicontinuum approaches with different level of simplification

In this section, the idea of the standard quasicontinuum method summarized in section 5.2 is combined with the concept of microplane material model defined in section 5.3. Six different approaches using various levels of simplification are considered. For brevity, these approaches are referred to as A0, A1, A2i, A2a, A3i and A3a, as defined in the following subsections.

Fully resolved particle model approach (A0)

This approach (referred to as A0) corresponds to the reference particle model (or alternatively to the QC model where the whole domain is considered as the area of high interest). Therefore, no simplification is involved in this approach. No interpolation elements are needed and only the particles and links defined in the original particle model are used. Every single particle represents a node with independent DOFs (displacements) and the links are described by 1D truss elements. Consequently, all links are taken into account explicitly and contribute directly to the internal forces and to the stiffness matrix.

The results of this fully resolved model are used as a reference solution for evaluation of accuracy and efficiency of the following simplified approaches.

Interpolated model with explicit summation (A1)

In this approach (referred to as A1), only the interpolation, i.e., the first step of QC simplification, is adopted. The second simplification step, i.e., summation, is not considered and therefore the microplane model is not employed. The simplification of the pure particle model consists in approximation of DOFs of those particles that have not

been selected as renodes. Such particles, the so-called hanging nodes, have no independent unknown DOFs (displacements) but they are “hanging” on auxiliary elements and their displacements are interpolated from the neighboring renodes. For that purpose, triangular (in 2D) or tetrahedral (in 3D) linear interpolation elements with vertices at the renodes are used. For each hanging node, the corresponding interpolation element is found. It is either the element in which the hanging node is located, or the nearest element if the hanging node is not located in any interpolation elements, which may occur at a curved part of the physical boundary of the particle system.

All links (truss elements connecting particles) are considered explicitly and contribute to the structural stiffness matrix, but only the renodes have independent DOFs while the displacements of all hanging nodes are interpolated (or extrapolated) using the DOFs of renodes as the primary unknowns. Interpolation elements are used only for approximation of displacements of hanging nodes and do not provide a direct contribution to the internal force vector and the structural stiffness matrix. The treatment of the model that corresponds to the A2 approach is illustrated in Fig. 5.1 (b). The displacement of each hanging node (gray dots) is a linear combination of the displacements of the vertices (black dots) of the corresponding interpolation element (blue triangles). All links (gray lines) are evaluated explicitly.

Microplane-based summation rule

In the summation rule for the standard QC method, the energy contribution \mathcal{E}_e of a particular element is evaluated as a sum over its sampling nodes; recall (5.2). Similarly, in a numerical representation of the microplane material, the energy is evaluated by summation over individual microplanes, see eq. (5.15). This analogy can be exploited to construct a microplane-based summation rule where individual microplanes work as sampling nodes. Therefore, the original summation formula (5.2) can be rewritten in terms of microplanes in analogy with microplane numerical integration formula (5.15) as follows

$$\mathcal{E}_e = \sum_{\alpha}^{N_S} w_{\alpha} \phi_{\alpha} = \sum_i^{N_M} w_i \phi_N(\varepsilon_{Ni}). \quad (5.63)$$

where the original sum over N_S sampling points is replaced with a sum over N_M microplanes, $\phi_N(\varepsilon_{Ni})$ represents the energy of the i -th microplane, and w_i is the corresponding weight factor. Both isotropic and anisotropic versions of microplane model can be considered. For the isotropic microplane model, the uniform distribution of microplane directions with equal weight factors is assumed. On the other hand, for anisotropic microplane models, the directions of individual microplanes as well as their weight factors can be generally different to represent the directions and lengths of individual links in the original microstructure.

This microplane-based summation rule is employed in the microplane-based homogenization approach where the microplane material is used to represent the original microstructure. This approach uses 2D triangular or 3D tetrahedral elements with renodes at their vertices in order to evaluate an approximation of the stiffness that corresponds to the links (1D truss elements) in the regions of low interest. Thereby, a substantial number of truss elements can be removed from the assembly procedure, and the number of operations is significantly reduced. Material properties of the 2D or 3D elements are identified by homogenization of the system of links connecting the particles as described in section 5.3.3. The details of homogenization procedures for isotropic and anisotropic

microplane models are discussed in the following subsections.

Triangular or tetrahedral elements, which were before considered as interpolation elements for hanging nodes, are now used directly for evaluation of the structural stiffness matrix, based on the material stiffness tensor obtained in the homogenization process. Thus, all hanging nodes with interpolated DOFs and all truss elements connecting them can be removed from the computational model. This leads to a significant reduction of the computational cost, but the reduction must be done carefully.

Links connecting two hanging nodes (residing in the same element or in two different elements) can be removed because their stiffness is represented by the effective stiffness of the homogenized microplane material assigned to the elements. Links connecting one renode and one hanging node located in the same element can be removed too, because their stiffness is also reflected by the effective material stiffness.

A problem occurs if a link connects one hanging node with one renode which is not located in the same element. This can happen if the interpolation elements are too small, or on the interface between regions of low and high interest; see the red links in Fig. 5.1 (c). Such links cannot be removed because their stiffness is not reflected by the homogenized material. Therefore, the involved hanging nodes must not be removed and the contribution of the links is taken into account separately from the contribution of the triangular or tetrahedral elements.

Microplane-based global homogenization approach (A2)

In this approach (referred to as A2), the microplane-based homogenization process is applied globally for all elements. It means that the same microplane material properties are evaluated for all microplane elements by averaging the geometrical properties of all links in the original microstructure.

For sufficiently large samples of generally randomized microstructures, the global properties tend to be similar in all directions. Therefore, an isotropic microplane approach is usually employed in this homogenization scheme (A2i). Application of the anisotropic microplane model in the global homogenization approach (A2a) is justifiable only if the original microstructure is generated with specific anisotropy.

A significant advantage of A2 is that the original problem is substantially reduced. At the same time, the evaluation of global homogenization properties is relatively fast because it depends only on the geometry of the microstructure and is not affected by the triangulation of microplane elements. On the other hand, A2 suffers from a lower level of accuracy because of the assumption that the material properties are the same in all points of the investigated domain, while in reality the local arrangement of links can be variable across the domain. On top of that, in the A2 approach, the effective material stiffness takes into account all links. However, certain links that partially cross homogenized elements are treated explicitly, and thus a part of their stiffness is actually accounted for twice, which artificially increases the resulting structural stiffness. This effect can be observed if microplane elements are too small in comparison with microstructure links or at the interface between areas of high and low interest.

Microplane-based local homogenization approach (A3)

This approach (referred to as A3) removes the deficiencies of A2 by identifying microplane properties of the homogenized material for each element separately. For each homogenized element, the microplane material properties are evaluated only from the

contributions of those parts of the links which are really located inside the element. Certain links are still treated explicitly as 1D truss elements and do not contribute to the microplanes of any homogenized element.

The microplane material model can again be considered as isotropic (A3i) or generally anisotropic (A3a). For computation of the local material parameters, it makes sense to consider general anisotropy even if the overall material behavior is isotropic. The reason is that for small elements, the particular local arrangement of a few links can result in a significant deviation from isotropy.

The A3 approach removes all disadvantages of the A2 approach that may result in reduction of accuracy. However, the local homogenization is significantly slower in comparison with the global approach. In the local homogenization, the loop over all links is realized similarly to the global approach, but in addition the contribution of every link to individual microplane elements must be evaluated, which requires an extra computational effort at the beginning of simulation.

Microplane-based adaptive refinement criterion

The refinement criterion for an adaptive scheme is based on local variables of individual microplanes. In this case, the microplane normal strain ε_N is used as alluded to in section 5.2.3. The refinement criterion based on parameters ε_{ref} , k_{ref} , and N_{ref} reads

$$\frac{1}{N_{\text{ref}}} \sum_i^{N_M} k_i \geq k_{\text{ref}} \quad \text{where} \quad k_i = \begin{cases} 1 & \text{if } \varepsilon_{N_i} \geq \varepsilon_{\text{ref}} \\ 0 & \text{otherwise} \end{cases} \quad (5.64)$$

where $\sum k_i$ is the number of microplanes where normal strain ε_{N_i} reaches or exceeds the critical refinement strain ε_{ref} . This number is compared with the refinement threshold k_{ref} . The normalizing factor N_{ref} can be selected as $N_{\text{ref}} = 1$ or $N_{\text{ref}} = N_M$ to evaluate the relative or absolute number of satisfying microplanes, respectively. Individual versions of the microplane-based refinement criterion (5.64) is investigated in section 5.5.5.

At the end of each simulation step, refinement criterion (5.64) is evaluated for all microplane elements. All elements that satisfy this criterion are refined, i.e., all nodes inside refined elements are labeled as renodes and all links connected to refined nodes are added to be solved explicitly. After updating the area of high interest, the current step is resolved to provide equilibrium of newly created renodes before the loading increment of the next solution step is applied.

In this simple refinement approach, the fully resolved domain can be extended by refining of existing elements, but coarsening of the refined area is not considered in the present study and the topology of original triangulation is not changed.

Results

In this section, five different examples are presented to evaluate the accuracy and efficiency of the previously defined simplified approaches using interpolation (A1), global microplane-based homogenization (A2), and local microplane-based homogenization (A3). The full particle model (A0) serves as the reference solution.

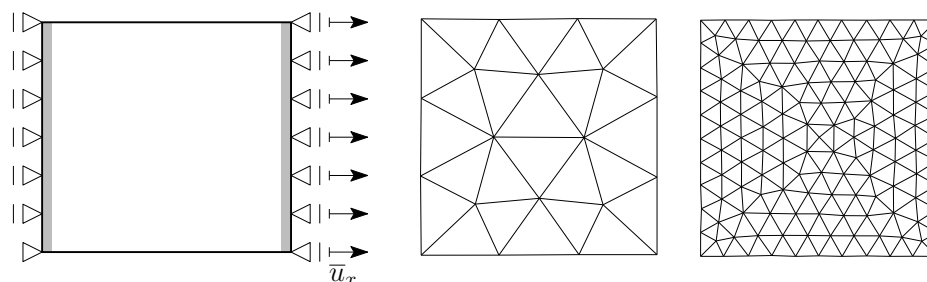


Figure 5.9: Geometry of the patch test: Sketch of boundary conditions applied in gray areas (left), interpolation mesh with 3 elements per edge (middle) and 10 elements per edge (right).

2D patch tests

Simple patch tests of two-dimensional rectangular domain with size $100 l_0 \times 100 l_0$ have been performed. Particles in the domain have been first generated in a regular grid with lattice size l_0 and then randomized by a superimposed random displacement with magnitude uniformly distributed from $-0.4 l_0$ to $0.4 l_0$. The random shift has been considered for both directions but only within the rectangular domain. The particles have been connected by links (1D truss elements) only within the interaction radius $R_{cut} = 3.5 l_0$ (evaluated in the regular configuration), which provides second-next-to-nearest interactions. The perfectly elastic-plastic constitutive law of the link has been considered in tension and pure elasticity in compression.

The rectangular domain has been subjected to tension in the horizontal direction. For that purpose, boundary conditions in the form of prescribed displacements have been realized in two external vertical bands of width $4l_0$ located on the outside of the domain, see the gray areas in Fig. 5.9 (a), to avoid weakening of the domain due to missing links in the direction of tension near the vertical boundaries.

Two different scenarios of the tension test have been considered. In the first case (referred to as pure tension), boundary conditions have been realized according to Fig. 5.9 (a) to allow lateral contraction in the vertical direction. In the second case (referred to as direct tension), lateral contraction has not been allowed and vertical displacements in regions of boundary conditions have been fixed. This geometrical setting results in a model with 11,009 particles, 192,732 links, and 21,006 independent DOFs. The histograms of orientation and lengths of links are shown in Fig. 5.10. For simplified models, 14 different triangulations have been considered, with various numbers of elements increasing from 1 to 14 elements per edge, see Fig. 5.9 (b-c). The results have been evaluated as an average of 10 different random realizations.

A typical macroscopic response in the pure tension test in terms of force-displacement diagrams is shown in Fig. 5.11 for the coarsest mesh refinements with only one element per edge, i.e., 4 elements in total. All simplified approaches provide the equivalent type of macroscopic response but the initial stiffness and final yield force are captured with different accuracy. Relative errors of the initial stiffness and final yield force (evaluated at 1 % strain) are depicted in Figs. 5.12–5.13 as a function of the number of elements for various mesh refinements.

The A1 approach with interpolation provides a consistent error of around 2 % for all refinements because the deformation in the pure tension test is almost homogeneous. The local anisotropic microplane-based homogenization rule employed in the A3 approach turns

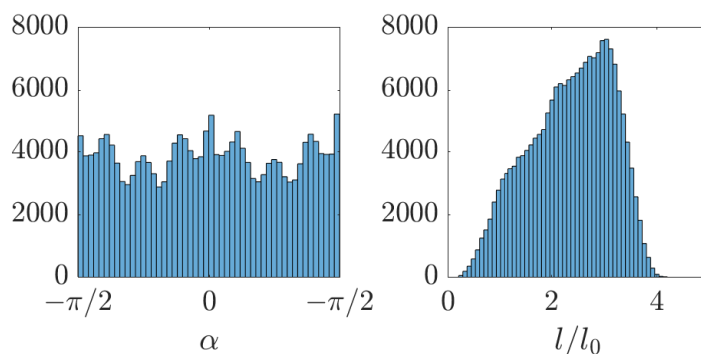


Figure 5.10: Properties of the randomized patch test: Histogram of link orientation angles α (left) and histogram of normalized link lengths l/l_0 (right).

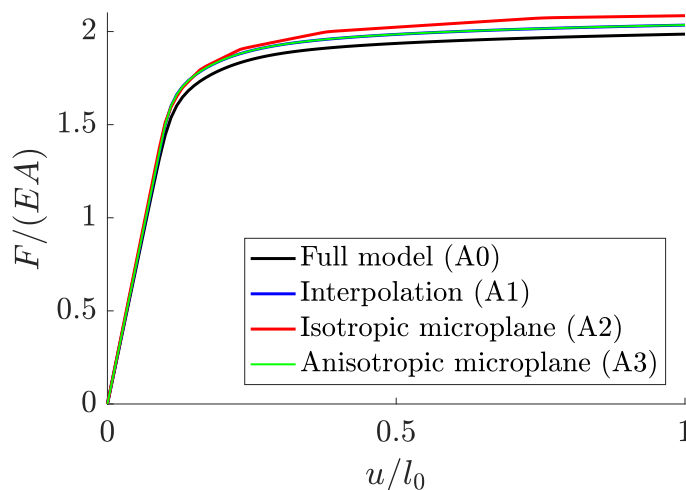


Figure 5.11: Force-displacement diagram for 2D pure tension test.

out to be very accurate and to provide an almost zero homogenization error. Therefore, the A3 results are almost overlapping with A1, for which only the interpolation is employed. On the other hand, the isotropic homogenization in the A2 approach may underestimate the final yield force, which then seems to be more accurate (in comparison with A1 and A3). At the same time, this approach significantly overestimates the initial stiffness, especially for a large number of elements, when the microplane elements become so small that multiple links have to be evaluated explicitly and their stiffness is then accounted for twice.

Analogous relative errors for the direct tension test are compared in Figs. 5.14–5.15. In the direct tension test, lateral contraction takes place mostly in the center. Therefore, a large error can be observed for refinements with a small number of elements, which are not able to capture significantly non-homogeneous deformation. However, for a sufficient level of refinement (i.e., with more than approx. 100 elements) the errors for both A1 and A2 approaches tend to similar values near 2-3 % observed in the pure tension test. The global isotropic homogenization in the A2 approach again slightly underestimates the yield force and significantly overestimates the initial stiffness.

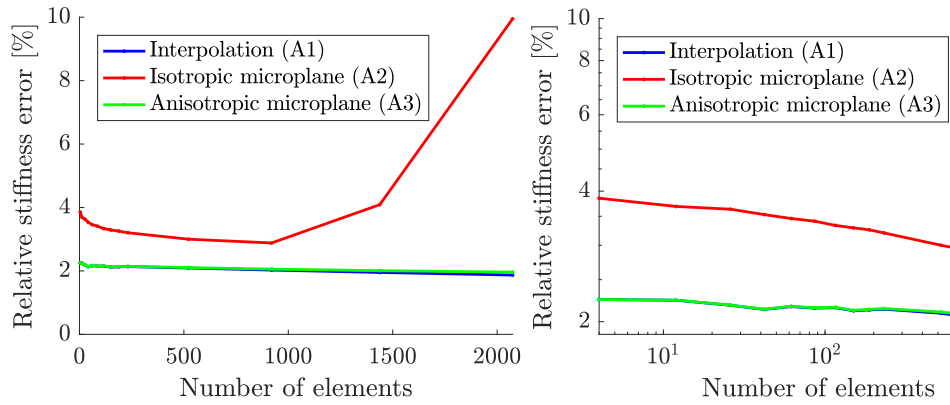


Figure 5.12: 2D pure tension test results: Relative stiffness error in linear scale (left) and in logarithmic scale (right).

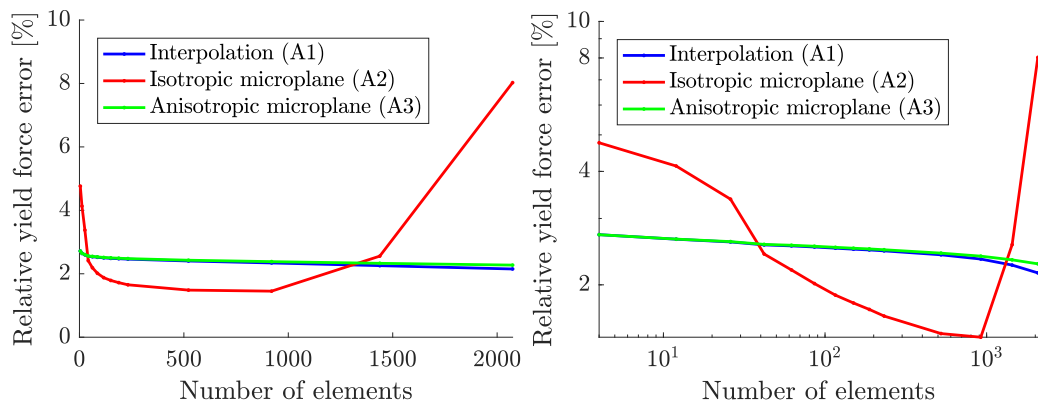


Figure 5.13: 2D pure tension test results: Relative yield force error in linear scale (left) and in logarithmic scale (right).

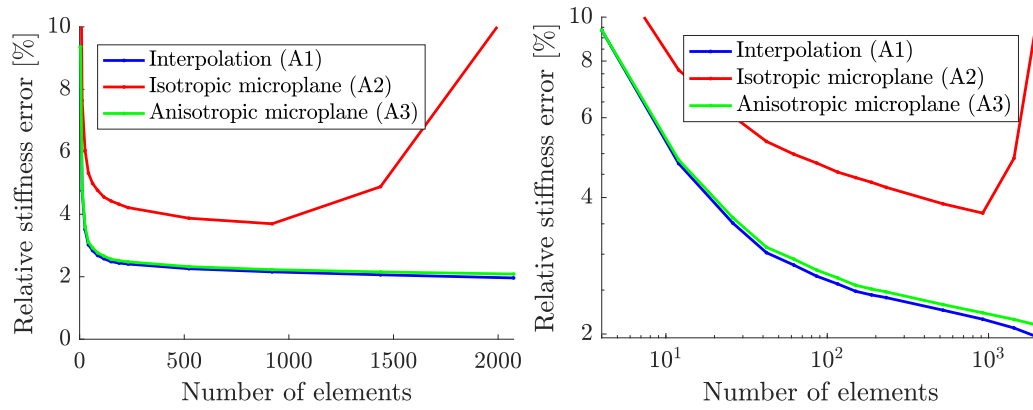


Figure 5.14: 2D direct tension test results: Relative stiffness error in linear scale (left) and in logarithmic scale (right).

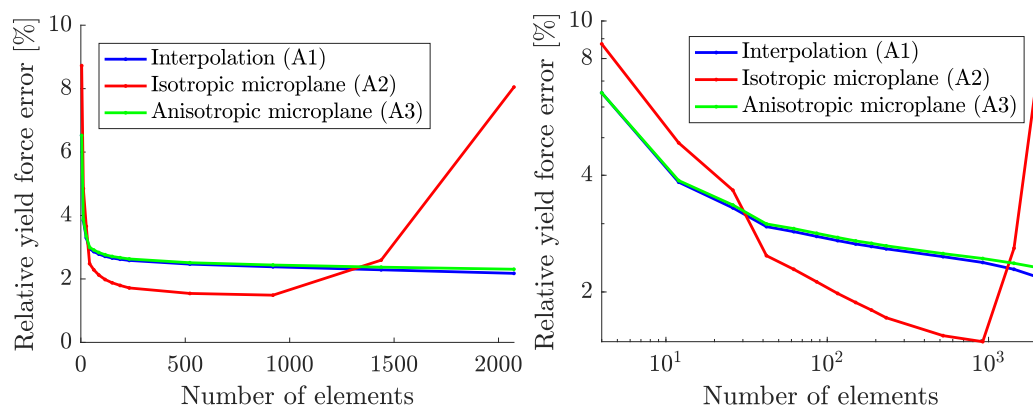


Figure 5.15: 2D direct tension test results: Relative yield force error in linear scale (left) and in logarithmic scale (right).

The results of the pure tension test with a refinement of 10 elements per edge are summarized in Tab. 5.1. The A1 approach is able to reduce the number of DOFs by more than 96 %, however, the computational savings are less than 40 % because the original number of links is processed and the localization procedure for individual hanging nodes of the link distribution is not optimized in the current implementation. In contrast to that, homogenization-based approaches A2 and A3 evaluate only 9 % of original links located along and inside areas with prescribed boundary conditions. Therefore, the A2 and A3 approaches provide a speed-up of a factor of 35. In this case, the A3 approach is only slightly slower because the computation of local directions of individual microplanes has to be done only once at the beginning of the simulation.

Approach	DOFs	Links	Elements	Comp. time	Stiffness error	Force error
A0	21,006	192,732	0	1.000	-	-
A1	1,238	192,732	232	0.632	2.08 %	2.44 %
A2i	1,238	17,614	232	0.027	3.20 %	0.86 %
A3a	1,238	17,614	232	0.029	2.08 %	2.46 %

Table 5.1: Summary of results for 2D pure tensile for test with refinement of 10 elements per edge.

2D clustering analysis

The original number of microplane directions considered for a single microplane element can be reduced to simplify the numerical integration process. For that purpose, the original microplanes are divided into several clusters based on their orientation α . Then, each cluster is represented by a single microplane with a direction obtained by the corresponding clustering rule and a weight factor calculated as a sum of all weights of individual microplanes represented by this cluster.

Two types of clustering rules are considered here. The first one is the simple uniform clustering rule where a given number of cluster directions are generated uniformly distributed in all possible directions with a fixed step. An alternative is represented by an advanced clustering rule based on the idea of the k-mean clustering algorithm [55], in which the geometry of original links (i.e., original microplanes) is used to determine important directions for a given number of clusters.

In the considered example of a significantly randomized microstructure, the distribution of link directions is rather uniform, see Fig. 5.10 (left). Therefore, uniform clustering and k-mean clustering provide similar results as presented in Fig. 5.16, where the orientation of each link α is plotted against its length l . However, for systems with a dominance of specific link directions, the k-mean clustering is able to detect the significant directions of the microstructure and consequently provides a significantly better microplane representation. To illustrate this ability, both clustering rules are compared for a microstructure with a small random perturbation ($0.2l_0$) and only nearest-neighbor interactions ($R_{cut} = 1.5l_0$), which leads to four specific directions (horizontal, vertical, and two diagonal ones). The results are shown in Fig. 5.17. The k-mean clustering provides an exact representation of all four significant directions even if five clusters are considered.

The results for the A3a approach with various clustering rules and various numbers of clusters are compared in the pure tension test of a rectangular domain of size $20l_0 \times 20l_0$

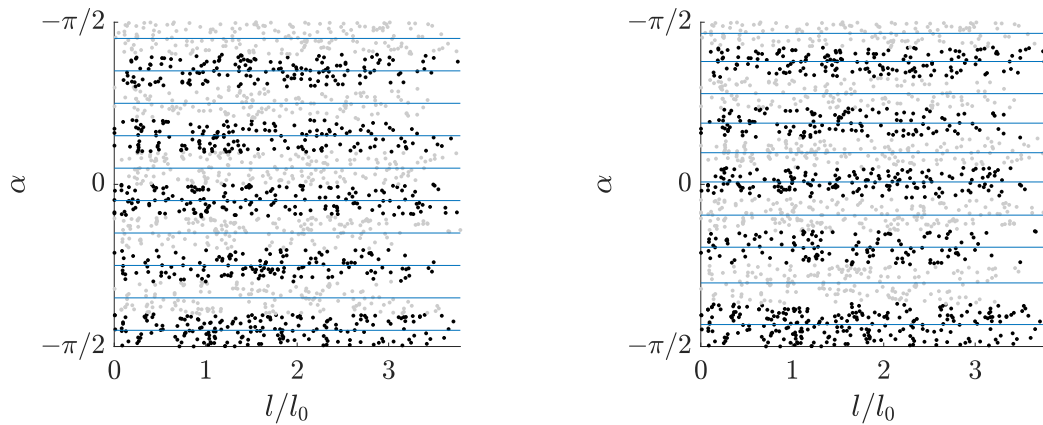


Figure 5.16: Clustering results for microstructure with maximal perturbation $\pm 0.4l_0$ and interaction radius $R_{cut} = 3.5l_0$: Contributions of individual links associated with one 2D microplane element divided into 10 clusters according to their orientations computed by the uniform clustering rule (left) and the k-means clustering rule (right). Black and gray dots represent links in individual clusters and blue lines show the cluster orientation.

with the maximal random shift $\pm 0.4l_0$ and interaction within the radius $R_{cut} = 3.5l_0$. The triangulation for microplane elements is generated with four elements per edge. This setting provides approximately 200 link directions in an average microplane element, which are represented by 10 or 25 cluster directions. The force-displacement diagrams are plotted in Fig. 5.18. The most significant discrepancies can be observed in the highlighted region where individual microplanes are transforming from an elastic to a plastic state. According to the expectation, the k-mean clustering provides a slightly better result than uniform clustering. However, this difference becomes less important with an increasing number of clusters.

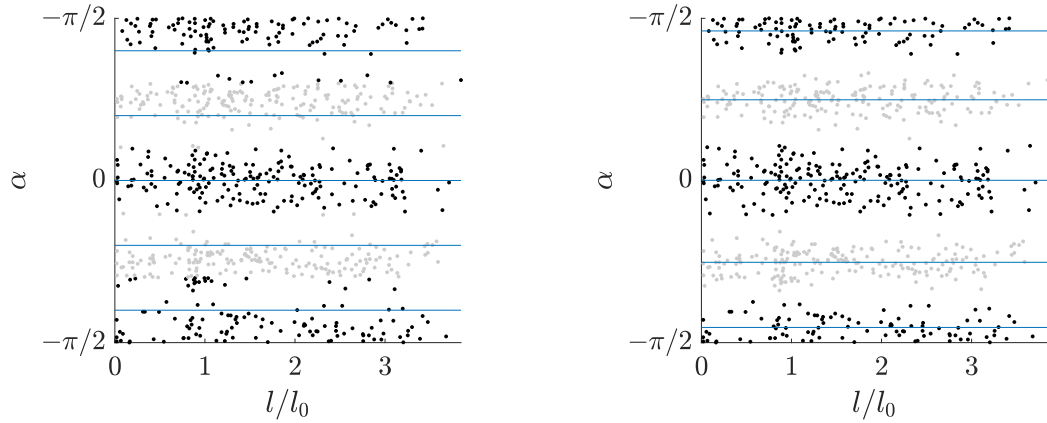


Figure 5.17: Clustering results for a microstructure with small maximal perturbation $\pm 0.2l_0$ and nearest-neighbor interaction ($R_{cut} = 1.5l_0$): Contributions of individual links associated with one 2D microplane element divided into 10 clusters according to their orientations computed by the uniform clustering rule (left) and the k-means clustering rule (right). Black and gray dots represent links in individual clusters and blue lines show the cluster orientation.

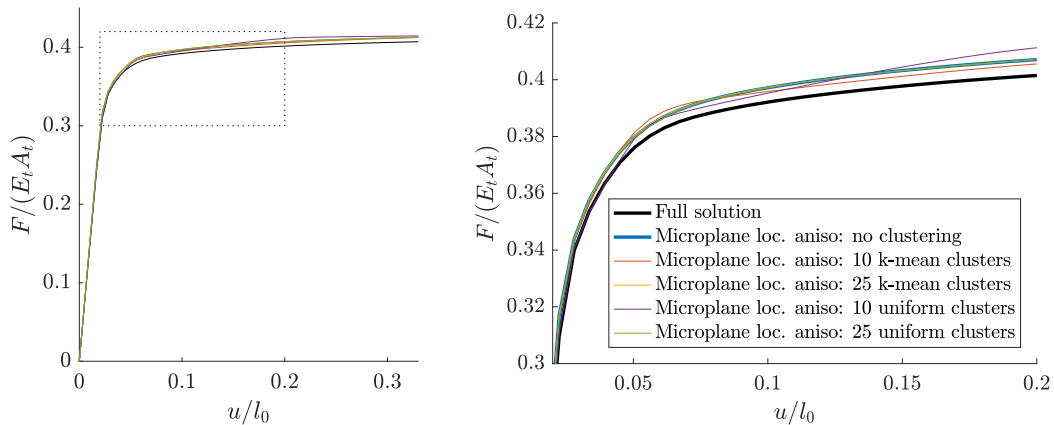


Figure 5.18: Comparison of force-displacement diagrams for various clustering rules: full diagrams (left), close-up of the highlighted region (right).

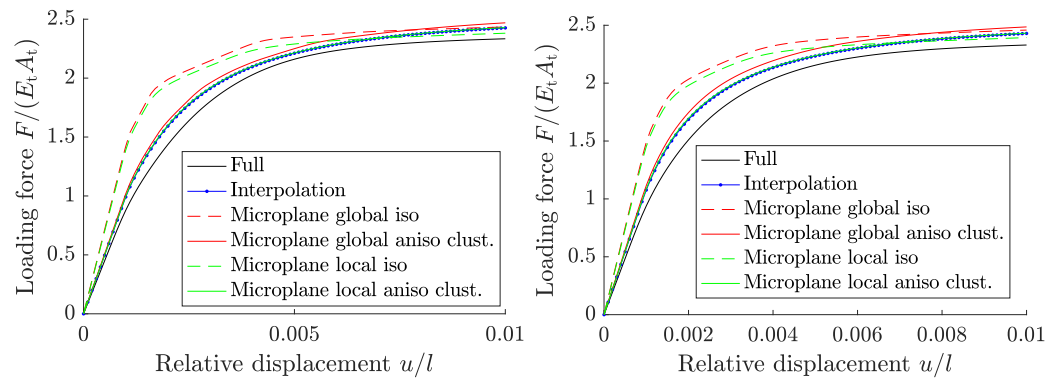


Figure 5.19: 3D patch test: Force-displacement diagrams for pure tension (left) and direct tension (right).

3D patch tests

Similarly to the previous 2D patch tests, analogous pure tension and direct tension patch tests have been run for a three-dimensional square domain of size $20l_0 \times 20l_0 \times 20l_0$ consisting of a regular grid with lattice size l_0 randomized with maximal random perturbation $\pm 0.3l_0$. In this case, particles are connected by links (1D truss elements) only within the interaction radius $R_{cut} = 1.8l_0$ (evaluated in the regular configuration), which provides only nearest-neighbor interactions in 3D. For simplified approaches, again multiple triangulations with various levels of refinement are considered.

Unlike the 2D case, here the external band for boundary conditions is not required because only nearest interactions are considered. Furthermore, both homogenization-based approaches (A2 and A3) are considered as isotropic or anisotropic.

3D patch tests have been evaluated for 10 different random realizations. Representative force-displacement diagrams for a sufficiently fine mesh are shown in Fig. 5.19. The initial stiffness error and final yield force errors for individual random realizations (colored dots) and corresponding average errors (colored lines) are plotted in Figs. 5.20-5.23.

In accordance with the 2D case, a homogeneous deformation in the pure tension test results in consistent errors for interpolation (A1) and local homogenization approaches (A3) whereas in direct tension test the errors decrease with increasing mesh refinement. For both test types, the final error values are around 4 % for the yield force and 12 % for the initial stiffness. Because the original 3D microstructure is significantly anisotropic with multiple preferred directions, both isotropic approaches (dashed lines) suffer from a large initial stiffness error around 60 % in both test types. At the same time, they underestimate the final yield force (in comparison with other simplified approaches), which then may seem to be more accurate in comparison with the full solution. In analogy to the 2D case, both global approaches (red lines) increase their errors if the refinement becomes too fine because then the stiffness of explicit links is accounted for twice.

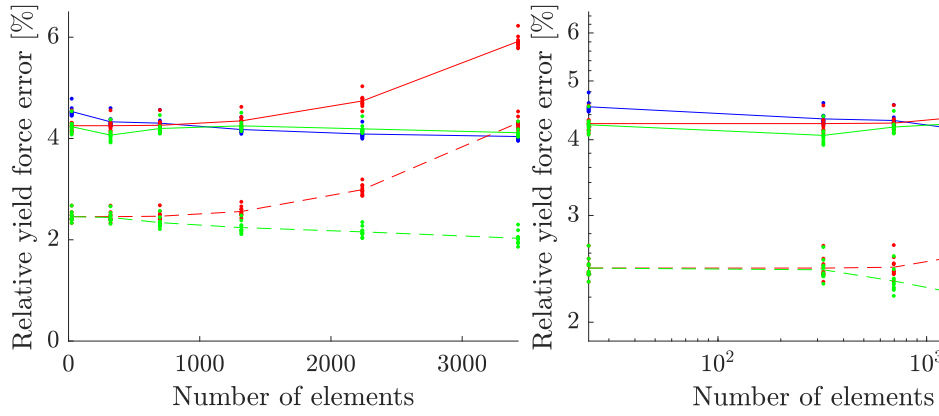


Figure 5.20: 3D pure tension test results: Relative yield force error in linear scale (left) and in logarithmic scale (right).

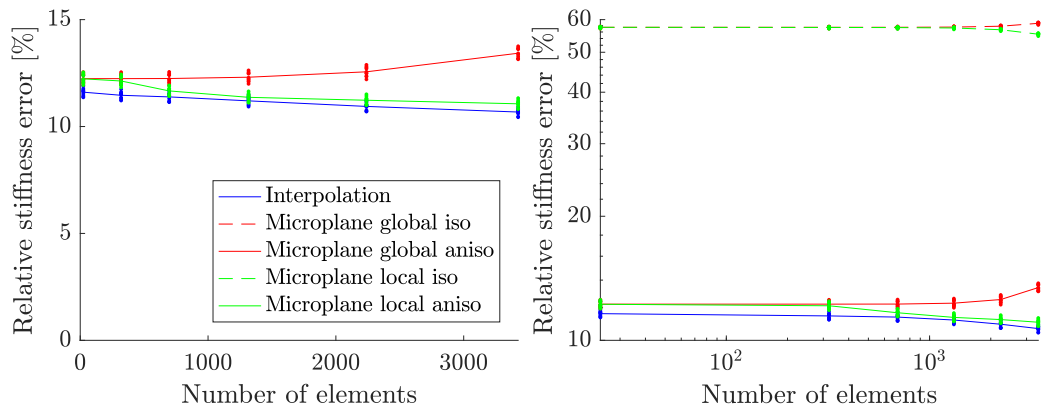


Figure 5.21: 3D pure tension test results: Relative stiffness error in linear scale (left) and in logarithmic scale (right).

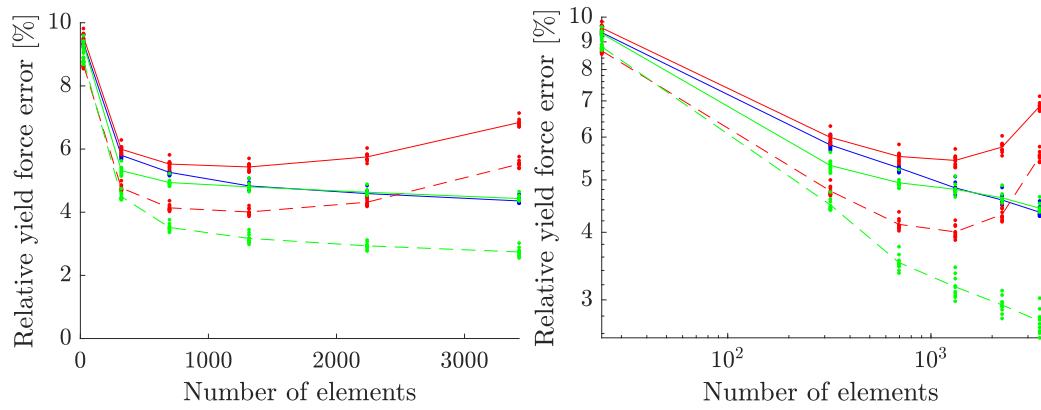


Figure 5.22: 3D direct tension test results: Relative yield force error in linear scale (left) and in logarithmic scale (right).

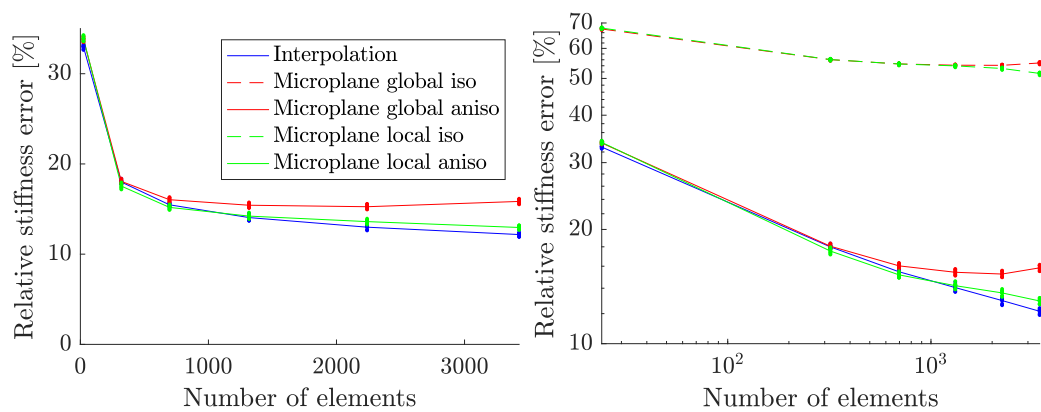


Figure 5.23: 3D direct tension test results: Relative stiffness error in linear scale (left) and in logarithmic scale (right).

3D bar tension test with area of high interest

The numerical example presented here corresponds to a three-dimensional particle model of a bar with a variable cross section (see the narrow central region in Fig. 5.24) subjected to tension. Particles and links are distributed fully randomly with a minimum position distance of l_0 and maximum interaction radius of $1.9l_0$, such that the resulting macroscopic properties are next-to isotropic on an average. The area of high interest, i.e., the fully refined region, is placed in the central narrow part of the bar and around the ending faces with prescribed boundary displacements. The geometry of particles and the interpolation mesh are depicted in Fig. 5.24 (left).

The results of elastic simulations are presented in Table 5.2. It is noteworthy that the A1 approach (with interpolation only) is slower than the exact A0 approach. Even if the number of independent DOFs is reduced, the current numerical implementation is unable to process A1 faster because of the structure of the stiffness matrix with multiple interpolated hanging nodes. The reason is that a node renumbering algorithm that optimizes the profile of the stiffness matrix for a direct solver works fine for A0 but not for A1.

The homogenization approaches (A2i and A3a) significantly reduce not only the number of DOFs but also the number of explicitly considered links and, consequently, the computational time. The A2i is slightly faster than A3a because the latter approach has to compute local distribution of individual links and then integrate over more microplanes. The error in the total stiffness for A2i is high because the stiffness on the interface between the regions of low and high interest is considered twice. This deficiency is remedied by A3a.

	Num. of Particles	Num. of Links	Num. of Elements	Num. of DOFs	Relat. Comp. Time	Stiffness Error	Yield Force Error
A0	16,519	123,668	0	46,080	1.00	-	-
A1	879	123,668	2,941	2,541	> 1.0	4.89%	0.28%
A2i	879	43,800	2,941	2,541	0.46	72.5%	3.48%
A3a	879	43,800	2,941	2,541	0.50	19.3%	0.44%

Table 5.2: Summary of results for the 3D plastic tensile test.

The stress-strain diagrams are depicted in Figure 5.24 (right). The results of approaches A1 and A3a are in a very good agreement with the exact result obtained with approach A0 (full particle model). The elastic response of A3a is a little stiffer but the final plastic behavior is captured exactly. In contrast to that, the A2i approach is generally stiffer and leads to a somewhat higher ultimate force.

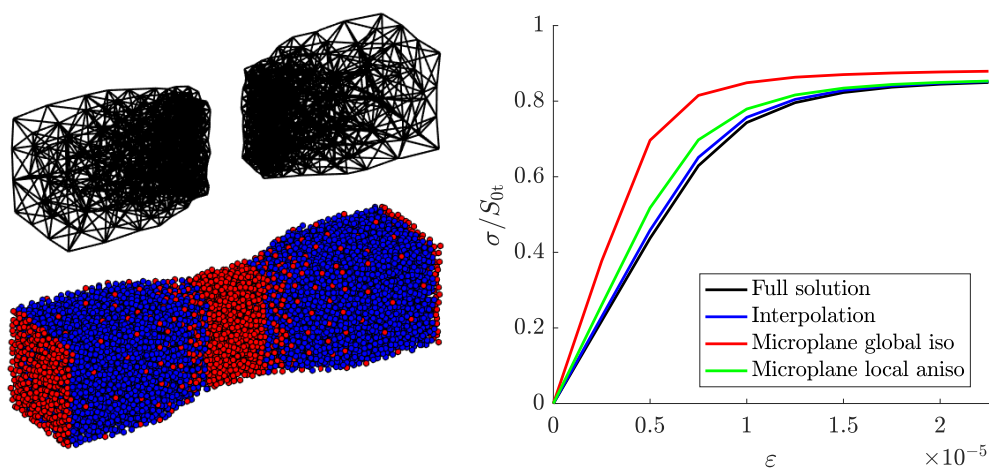


Figure 5.24: 3D bar tensile test: Geometry of 3D bar (left), particles (blue), renodes (red) and interpolation mesh (black). Stress-strain diagram for various computational approaches (right).

Adaptive bending test (2D)

To evaluate the microplane-based refinement criterion defined in section 5.4.6, a QC simulation with adaptive mesh refinement is presented in this section. For that purpose, a bending test of 2D cantilever with dimensions $80l_0 \times 20l_0$ has been performed. The initial triangulation has been generated with an average element size of $10/3l_0$, i.e., with 24×6 elements, which results in 337 triangular elements in total. No initial area of high interest has been considered. Only one simplified approach, namely the anisotropic local microplane (A3a), has been used. For this approach, the first simulation without refinement and then four simulations with various settings of refinement parameters were evaluated, see the legend in Fig. 5.25. In the first two adaptive simulations, the critical refinement strain ε_{ref} is below the critical yield strain ε_0 . This means that an element is refined before even a single microplane reaches the plastic state. The third case ($\varepsilon_{\text{ref}} = \varepsilon_0$ for one microplane) means that an element is refined exactly when the first microplane reaches a plastic state. In the last case, at least five microplanes of an element must be in a plastic state to initiate refinement of this element.

The results for adaptive QC simulations of A3a with various settings of refinement criteria are compared against the full solution in the form of force-displacement diagrams and the corresponding evolution of the relative number of refined nodes, see Fig. 5.25. The initial stiffness error of 10.23% is given by the initial triangulation and therefore it is the same for all QC simulations. The QC simulation without refinement remains significantly stiffer during the whole bending process and, consequently, the final yield force is overestimated by 17.19% if no refinement is employed. In contrast, all adaptive simulations are changing the stiffness similarly to the full solution because the stiffness error is reduced by increasing the fully refined region. For progressive refinements ($\varepsilon_{\text{ref}} < \varepsilon_0$), the macroscopic response is very close to the full solution, whereas for slower refinements ($\varepsilon_{\text{ref}} = \varepsilon_0$) a slightly larger stiffness error can be observed at early stages. However, this overestimation is reduced at later stages and the final plastic mechanism is captured exactly. The final yield force error remains below 0.25% for all adaptive simulations.

For the initial triangulation, the relative number of refined nodes is below 0.13. For progressive refinements, this number increases rapidly up to 0.75. For other refinements the propagation of the fully refined region is significantly slower and the final value around 0.5 is sufficient to capture the whole plastic mechanism. To make a refinement even less progressive, the refinement strain $\varepsilon_{\text{ref}} > \varepsilon_0$ can be used. In such a case, some parts of the final plastic mechanism may be covered by the microplane model instead of the fully refined region. Nevertheless, the relevant macroscopic response can still be obtained because the local anisotropic microplane model has turned out to be able to capture the plastic yield force with a high accuracy (as presented in the previous patch test).

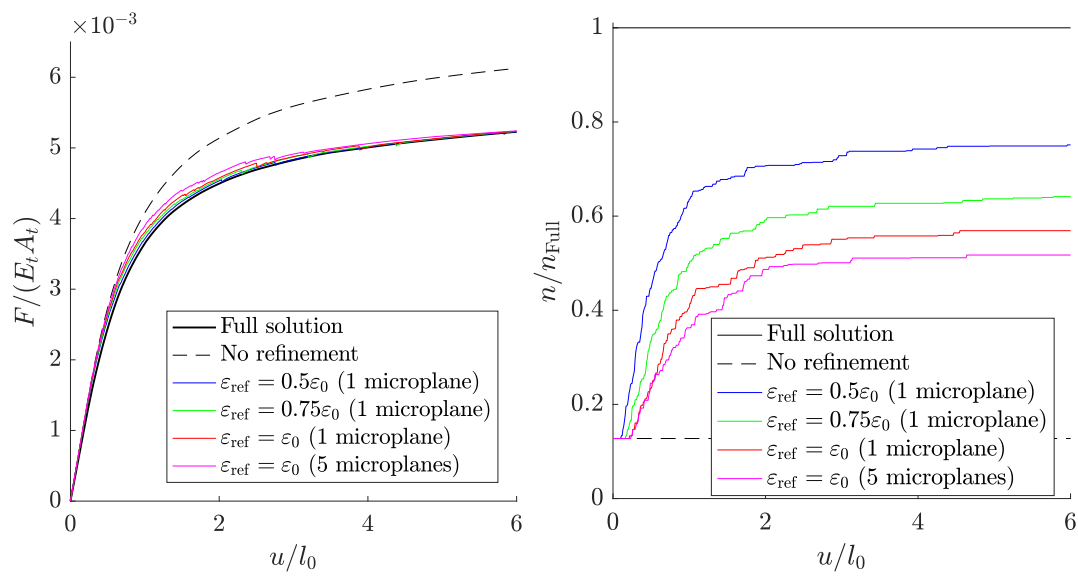


Figure 5.25: Results for adaptive bending test of 2D cantilever for anisotropic local microplane approach with various settings of adaptive refinement: force-displacement diagrams (left), an evolution of the relative number of refined nodes (right).

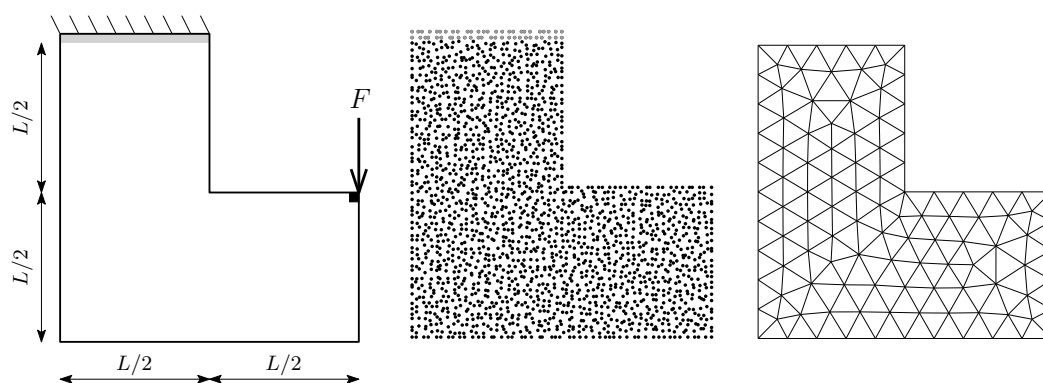


Figure 5.26: L-shaped specimen test: Sketch of the geometry and boundary conditions applied in gray areas (left), position of particles (middle), and considered triangulation (right).

L-shaped specimen with softening and crack localization

As the last example, an L-shaped test of a 2D cantilever with dimensions of $50 l_0 \times 50 l_0$ modeled by 2002 particles with a random shift up to the maximal magnitude of $\pm 0.4 l_0$ is presented in this section. The geometry of the considered specimen and its particle representation are shown in Fig. 5.26. For the purpose of QC simulations, a triangular mesh with 180 microplane elements according to Fig. 5.26 (right) has been employed. The particles have been connected within the radius of $2.5 l_0$, providing next-to-nearest interactions. Unlike the previous examples, here the interactions are not perfectly elastoplastic but instead an elastoplastic model with linear kinematic hardening/softening is considered. A negative hardening modulus $H_0 = -0.05 E_t$ has been used, which provides linear softening once the limit elastic strain ε_0 has been exceeded. Plastic softening is considered only in tension, while in compression all interactions remain purely elastic.

For this type of constitutive law, the failure mechanism is not characterized by the development of a large plastic zone but the plastic deformation localizes and propagates in a narrow band, which can be considered as a crack. The crack trajectory obtained in an adaptive QC simulation is depicted in Fig. 5.27 (right). Red lines represent links with plastic strain $\varepsilon_p > 10 \varepsilon_0$, which corresponds to softening to less than one half of the maximal yield stress σ_0 .

The results for local anisotropic microplane-based QC simulations with and without an adaptive algorithm are compared against the full solution in Fig. 5.27 (left). The adaptive simulation provides a significant speed-up factor of 7.5. On top of that, the obtained results are in a good agreement with the full solution. Even if a large initial stiffness error of 17.2 % can be observed, the shape of the force-displacement curve is very well captured. The maximal peak force error is only slightly overestimated by 7.8 %, and also the post-peak branch is predicted reasonably. In contrast, a QC simulation without refinement is unable to capture the localization process, and the peak force is significantly overestimated by more than 45 %. In this case, a speed-up of factor of 81 has been observed.

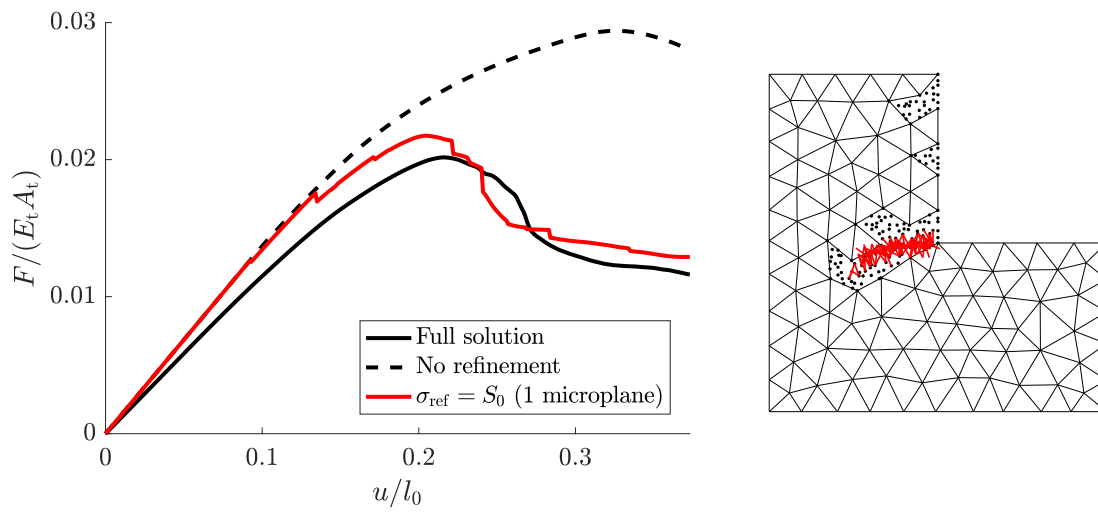


Figure 5.27: L-shaped specimen test results: Force-displacement diagrams (left) and refined QC model with crack path (right).

Conclusion

This paper combines the idea of the microplane model [8] with the quasicontinuum method for disordered particles with axial interactions. From an analogy between the particle model and the microplane model, a microplane-based summation rule for the quasicontinuum method has been derived. In the proposed microplane-homogenization-based QC method, the particle model in the areas of low interest is replaced by a continuum model exploiting the idea of microplanes. The macroscopic response is obtained using a corresponding integration formula, which can be used analogously to a QC sampling rule. The definition of the material constitutive law on the level of microplanes leads to a good agreement with the original discrete model, which represents the material behavior by links connecting individual particles. Five simplified approaches adopting various levels of simplification have been introduced using interpolation, global or local homogenization, and isotropic or anisotropic microplane model. Furthermore, a microplane-based refinement indicator for adaptive QC simulation has been proposed.

The presented examples have shown that the microplane-based QC method leads to a substantial reduction of the number of unknown DOFs and number of links that need to be processed during a simulation. This reduction provides a significant simplification of the original problem, which corresponds to an observed speed-up factor of 35 in 2D and 81 in 3D. Furthermore, the error caused by this reduction can be effectively reduced by suitably adjusting the region of high interest based on the proposed adaptive refinement criterion. Simplified approaches based on global homogenization are slightly faster but they suffer from a higher stiffness error because explicitly evaluated links are artificially accounted for twice. Similarly, simplified approaches with an isotropic microplane model turn out to overestimate the total stiffness and underestimate the yield force if the homogenized microstructure significantly deviates from isotropy. Thus, its application is limited to a certain types of microstructures. In contrast, the local homogenization approach with an anisotropic microplane model is able to capture the contribution of individual links in each element and represent them by relevant microplanes; thereby it provides very accurate results regardless of the microstructure type. For this model, an almost negligible homogenization error can be observed since almost all deviations from the full model are mainly caused by the interpolation error.

The presented inelastic model deals only with plasticity and the constitutive law of links and microplanes has been considered as perfectly elastoplastic or as elastoplastic with linear kinematic hardening (or softening). For the future work, an extension to additional material phenomena, e.g., to damage-based models, can be envisaged based on the analogy of the microplane and truss models. Another possible extension can consist in considering not only the axial interactions but also the shear or bending stiffness of the links.

Chapter 6

Comparison of multiscale techniques for materials with discrete microstructures

Abstract:

The evolution of local defects such as dislocations and cracks often determines the performance of engineering materials. For a proper description and understanding of these phenomena, one typically needs to descend to a very small scale, at which the discreteness of the material emerges. Fully-resolved discrete numerical models, although highly accurate, often suffer from excessive computing expenses when used for application-scale considerations. More efficient multiscale simulation procedures are thus called for, capable of capturing the most significant microscopic phenomena while being computationally tractable for macroscopic problems. Two broad classes of methods are available in the literature, which conceptually differ significantly. The first class considers the fully-resolved discrete system, which is subsequently reduced through suitable mathematical tools such as projection and reduced integration. The second class of methods first homogenizes the discrete system into an equivalent continuum formulation, into which the main phenomena are added through specific enrichments. This paper provides a thorough comparison of the two different modeling philosophies in terms of their theory, accuracy, and performance. To this goal, two typical representatives are adopted: the Quasicontinuum method for the first class, and an effective continuum with an embedded cohesive zone model for the second class. Two examples are employed to demonstrate capabilities and limitations of both approaches. In particular, dislocation propagation and pile-up against a coherent phase boundary is considered at the nanoscale level, whereas a three-point bending test of a concrete specimen with crack propagation is considered at the macroscale level. In both cases, the accuracy of the two methods is compared against the fully-resolved discrete reference model. It is shown that whereas continuum models with embedded cohesive zones offer good performance to accuracy ratios, they might fail to capture unexpected more complex mechanical behavior such as dislocation reflection or crack branching. The Quasicontinuum method, on the other hand, offers more flexibility and higher accuracy at a slightly higher computational cost.

Reproduced from: Mikeš, K., Bormann F., Rokoš. O., Peerlings R.H.J, Comparative study of multiscale computational strategies for materials with discrete microstructures (accepted).

Introduction

Numerical modeling of material behavior is an important ingredient in engineering. At sufficiently large scales, most materials can be considered as a continuum, whereas at smaller scales, materials such as foams, textiles, concrete, or paper, reveal discrete microstructures. At the smallest scale, i.e., nano-scale, all materials become discrete and their behavior is dictated by the underlying atomic lattice. When modeling of localized mechanical phenomena such as for instance the nucleation and propagation of dislocations, cracks or other defects, is of interest, the inherently non-local behavior of the underlying discrete microstructure comes into play. To capture those non-localities, accurate numerical models may be required.

The most accurate option is to use discrete models that fully resolve the microstructure and hence inherently incorporate the underlying non-locality at the level of the individual interactions. Typical examples at different scales are molecular statics [89, 23, 74] or dynamics [31, 94, 108] for atomic systems, or lattice or beam networks for mesoscopically discrete materials. Sophisticated discrete material models for various materials such as paper [52, 22], textile [17], fiber-reinforced composites [9, 109], other fibrous materials [106, 82], or concrete [87, 29, 51] can be found in the literature. For typical engineering applications, however, full-scale models suffer from prohibitive computational costs requiring simplifications, especially in problems with a large separation of scales between the application length scale and the length scale of the underlying lattice, or in problems in which multiple model evaluations are required such as optimization, parameter identification, or stochastic modeling.

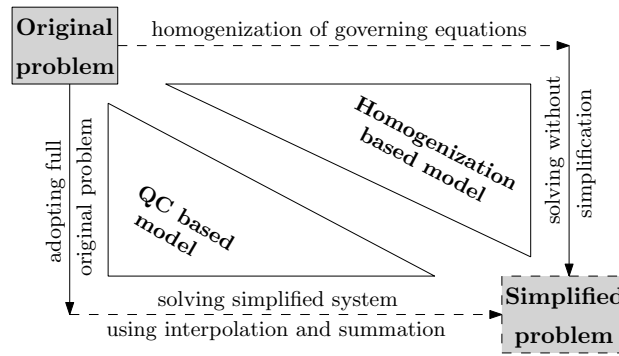
Two broad classes of conceptually distinct methodologies are available to provide computationally efficient numerical tools for such cases. The first class relies on considering directly the underlying model, which is subsequently reduced by suitable numerical and mathematical techniques such as projection on a reduced kinematical basis and reduced integration. The second class of methods first derives equivalent homogeneous governing equations from the underlying discrete microstructure. Afterwards, suitable enrichments are added to model the key mechanical phenomena. The resulting system is then solved using standard numerical techniques for continuum problems such as the Finite Element (FE) method. For the purposes of this paper, the QuasiContinuum (QC) method, originally introduced by Tadmor et al. [99], is adopted as a typical representative for the first class of approaches, whereas a continuum formulation with an embedded cohesive zone model is considered as a representative for the second class of approaches. The reduction of both classes is implemented at different levels of the problem formulation, as depicted in Fig. 6.1.

Quasicontinuum based approach

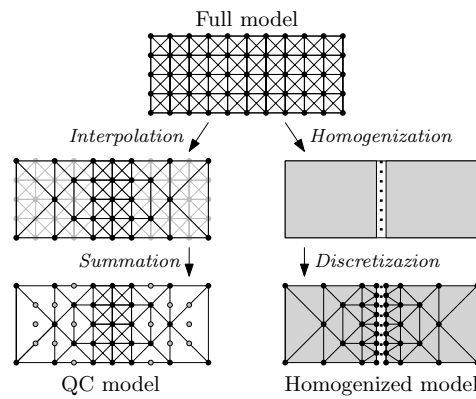
In the QC approximation, the original complexity of the full underlying problem is reduced to simplified model in two steps:

- (i) *Interpolation* is used to define the positions of all atoms or lattice sites of the original system from a set of representative atoms, the so-called repatoms;
- (ii) *Summation* efficiently estimates the stored energy and internal forces of the system in which the interpolation step has been applied, based on a set of the so-called sampling atoms.

The interpolation step considers only a small set of repatoms to represent the kinematic



(a) two-way simplification



(b) graphical representations

Figure 6.1: (a) A schematic illustration showing two ways of simplification of the original fully-resolved discrete model. In the first approach, the original system is reduced through suitable numerical and mathematical techniques, solving subsequently a simplified system (the left-bottom path). In the second approach, the original system is homogenized first to provide an equivalent continuum model with embedded key features, which is subsequently solved using standard techniques for continuum problems (the top-right path). (b) A graphical representation of the individual steps required by the two simplification approaches.

behavior of the entire system, typically chosen as vertices of an overlaid triangular Finite Element (FE) mesh. To accurately capture any localized phenomena, the considered domain is split into two parts. The first part is the area of high interest where all atoms of the underlying lattice are considered as repatoms and thus also as nodes of the triangular mesh, i.e., the overlaid triangulation is fully refined down to the level of the underlying lattice. Elsewhere, interpolation is adopted to coarse-grain the underlying lattice; in this region individual triangular elements contain multiple atoms or lattice sites. The fully-resolved region may be adaptively adjusted during the simulation to capture the relevant evolution of the microstructure. The main advantage of the QC approach is that since the response of the reduced model is governed by the underlying ‘exact’ discrete model, one expects a high fidelity, which is limited only by the coarsening away from the region of interest. The price to pay is (possibly) a more expensive simulation.

The QC method was originally introduced in 1996 [99, 100] for atomic systems with long-range conservative interaction potentials and has been successfully used for the simulation of localized phenomena, such as crack nucleation and propagation [45, 67], motion and interaction of dislocations [80], or processes related to nanoindentation [46, 96]. Later, the QC method was extended to regular discrete lattice networks with short-range nearest-neighbor interactions with both conservative [11] and non-conservative [13, 14] interaction potentials including dissipation and fibre sliding. A further extension was provided for planar beam lattices [16, 10] and periodic beam lattices in a co-rotational framework [81]. Additional research focused on goal-oriented adaptivity [3, 58], a meshless QC method [48], or an energy-based variational formulation for regular lattices with plasticity [83] and localized damage [85, 84]. Recently, the QC method was also extended to irregular lattices [65] or polymer networks [38]. A generalization to metallic lattice materials was introduced in [24], where different finite element shape functions are used for different types of lattice nodes

Homogenization based approach

In the second approach, homogenization of the underlying discrete system is first carried out, from which continuum governing equations follow. Usually a Cauchy continuum is adopted, which neglects any non-local interactions. A specific enrichment thus needs to be added, which is usually implemented through an appropriate interface model, e.g., a cohesive zone model for cracks. These interfaces allow for mutual displacements in tangential and normal directions, governed by appropriate effective constitutive laws.

The positioning and orientation of such interfaces is assumed to be known a priori and fixed hereafter, although more general models can be found in the literature, involving cohesive zones in between all elements [107], or an extended FE method with cohesive zone formulation [18, 5, 105]. Often, the interfaces positions can be set a priori on the basis of available knowledge of the underlying physics and to limit the computational expense. A crack path can in certain cases be estimated with sufficiently high accuracy to be fixed in all simulations, for instance. Thus, by design, this approach is capable of capturing only those phenomena that are considered in the homogenized model. In situations in which the positions of interfaces cannot be estimated in advance, homogenization based approaches are usually no longer advantageous. Even though generalized homogenized models (which, e.g., consider cohesive zones in between all elements) can be used even without any prior information on the position of the expected localized phenomena, it is usually computationally less expensive directly employ adaptive QC method in such situations, since induced computing costs might be comparable or exceed those of the QC method or even

of a full solution. Although many physical phenomena are excluded from the homogenized modeling, one generally expects this approach to be more efficient. The material parameters of the homogenized system as well as properties of the cohesive interfaces are fully determined by the underlying lattice physics. In most cases, a linear elastic isotropic material model is sufficient to provide an accurate description of the lattice behavior far from any localized phenomena, whereas in the close vicinity of a crack or a dislocation large deformations and strains may occur; these are, however, neglected in this contribution for simplicity. Interface constitutive laws range from simple closed-form uncoupled to numerical and coupled laws derived directly from numerical homogenization. Typical representatives of the homogenization based approaches, both considered in this paper, are the Peierls–Nabarro model introduced in [78, 70, 88, 41, 19] and cohesive zone model discussed in [6, 34, 30, 36, 43, 92]. Yet another representative is the Discrete Dislocation Dynamics (DDD) approach, e.g., [102, 26], which is not considered here further.

Objectives

The goal of this paper is a thorough comparison of the above two modeling philosophies in terms of their theoretical framework, accuracy, and numerical efficiency. To this end, two examples are considered with microstructures at the nano- and meso-scale level. At the nanoscale, dislocation propagation and pile-up against a coherent phase boundary in a two-dimensional atomic system with a hexagonal stacking of atoms is adopted. At the mesoscale, a three-point bending test of a concrete specimen with crack propagation through a two-dimensional regular X-braced lattice structure is examined. In both cases, a Quasicontinuum model and a FE approach equipped with cohesive zone interfaces, using either the Peierls–Nabarro model or a traction–separation law, are compared against a fully-resolved discrete model. The accuracy and efficiency of both homogenization techniques are discussed and evaluated.

Outline and notation

The remainder of this paper is organized as follows. Section 6.2 considers the molecular statics problem of dislocation propagation, starting with the theory of the fully-resolved discrete atomic problem, followed by a Quasicontinuum formulation, and closing with the FE Peierls–Nabarro homogenization based approach. In Section 6.3, an analogous comparison is made for the case of a three-point bending test considered at the mesoscale, mimicking quasi-brittle damage in a concrete specimen. The paper closes with a summary and conclusions in Section 6.4.

Throughout the paper, scalars are denoted a , vectors \vec{a} , position vectors in a two-dimensional continuum $\vec{x} = x\vec{e}_x + y\vec{e}_y$, and atom position vectors $\vec{r} = r_x\vec{e}_x + r_y\vec{e}_y$. Second-order tensors are denoted $\boldsymbol{\sigma}$, matrices \mathbf{A} , column matrices \underline{a} , scalar products of two vectors $\vec{a} \cdot \vec{b} = a_i b_j$, single contractions of two second-order tensors $\boldsymbol{\sigma} \cdot \boldsymbol{\varepsilon} = \sigma_{ik} \varepsilon_{kj} \vec{e}_i \vec{e}_j$, double contractions of two second-order tensors $\boldsymbol{\sigma} : \boldsymbol{\varepsilon} = \sigma_{ij} \varepsilon_{ji}$, whereas a transpose is denoted as $\boldsymbol{\sigma}^\top$, where $\sigma_{ij}^\top = \sigma_{ji}$. The gradient and divergence operators are denoted as $\vec{\nabla} \vec{a}(\vec{x}) = \frac{\partial a_j(\vec{x})}{\partial x_i} \vec{e}_i \vec{e}_j$ and $\vec{\nabla} \cdot \vec{a}(\vec{x}) = \frac{\partial a_i(\vec{x})}{\partial x_i}$, respectively. Throughout this contribution, Einstein’s summation convention is adopted on repeated indices i and j , and \vec{e}_x and \vec{e}_y denote the basis vectors of a two-dimensional Cartesian coordinate frame.

Molecular statics: dislocation transmission across a phase boundary

Full atomic model

To analyze a dislocation pile up against a material interface in two dimensions, a shear test with two different material phases is considered. Dislocation dipoles are nucleated at the center of the specimen, and are pushed towards boundaries by externally applied shear stress. As illustrated in Fig. 6.2a, the adopted bi-crystal, occupying a domain Ω , consists of a soft Phase A that is flanked by a stiffer Phase B. The individual subdomains Ω^A and Ω^B are separated by a phase boundary Γ_{pb} . The considered dimensions are summarized in Tab. 6.1. Inside Ω , hexagonal lattice structures of equal spacings a_0 are considered in both phases, comprising a total of n_{ato} atoms α , collected in an index set $N = N^A \cup N^B$ where N^A and N^B are sets of atoms associated with the individual phases. The crystal orientation is chosen such that one set of glide planes is oriented perpendicular to the two vertical coherent phase boundaries, whereas the other sets of glide planes are inclined by an angle of $\pm 60^\circ$.

The interatomic pair potentials employed within both phases, denoted ϕ^A and ϕ^B , are of the Lennard–Jones (LJ) type. To account for nearest and next-to-nearest interatomic interactions only, a cut-off radius $r_{\text{cut}} = 2.5 r_m$ is adopted, as indicated in Figs. 6.2a and 6.3a by the dashed circles. To ensure smoothness of the potential at the cut-off radius, cf. Fig. 6.3b, the LJ potential is modified according to

$$\phi(r) = \phi_{\text{LJ}}(r) - \phi_{\text{LJ}}(r_{\text{cut}}) - (r - r_{\text{cut}})\phi'_{\text{LJ}}(r_{\text{cut}}), \quad \text{with} \quad \phi'(r) = \frac{d\phi(r)}{dr}, \quad (6.1)$$

where r is a scalar measuring the distance between a pair of atoms, and

$$\phi_{\text{LJ}}(r) = \varepsilon \left[\left(\frac{r_m}{r} \right)^{12} - 2 \left(\frac{r_m}{r} \right)^6 \right] \quad (6.2)$$

is the standard LJ interatomic pair potential. In Eq. (6.2), ε denotes the depth of the energy well and r_m the distance for which the interaction energy reaches its minimum, as indicated in Fig. 6.3b. For further details see, e.g., [98]. Mixing of the interatomic potentials across the phase boundary Γ_{pb} is considered through averaging, i.e.,

$$\phi^{\alpha\beta}(r^{\alpha\beta}) = \frac{1}{2} \left[\phi^\alpha(r^{\alpha\beta}) + \phi^\beta(r^{\alpha\beta}) \right], \quad (6.3)$$

where $\vec{r}^\alpha = r_x^\alpha \vec{e}_x + r_y^\alpha \vec{e}_y$ denotes a current position of an atom α , $r^{\alpha\beta} = \|\vec{r}^{\alpha\beta}\|_2$ denotes the Euclidean distance between a pair of atoms α and β , $\vec{r}^{\alpha\beta} = \vec{r}^\beta - \vec{r}^\alpha$ is a vector of their relative positioning, and

$$\phi^\alpha = \begin{cases} \phi^A, & \text{if } \alpha \in N^A, \\ \phi^B, & \text{if } \alpha \in N^B, \end{cases} \quad \alpha = 1, \dots, n_{\text{ato}}. \quad (6.4)$$

Material parameters are specified in Tab. 6.2, which are all normalized with respect to ε^A and r_m^A .

If only the nearest-neighbor interactions are considered and there are no surface effects within a homogeneous crystal, i.e., an infinite homogeneous crystal is assumed, the

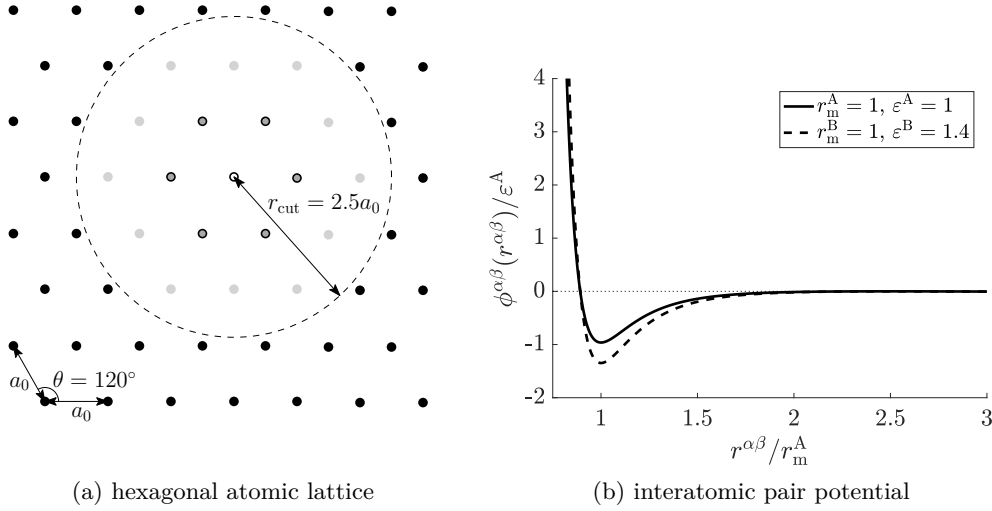


Figure 6.3: (a) The hexagonal lattice used for atomic simulations in two dimensions; current atom (white), nearest-neighbor atoms (bounded gray), and next-to-nearest atoms (gray). (b) Two versions of the Lennard–Jones potential corresponding to material contrast ratio $\rho = 1.4$.

lattice spacing $a_0 = r_m$ yields a stress-free configuration. For next-to-nearest interactions, however, such a lattice spacing invokes a pre-stress within the lattice, as calculated by a non-vanishing Virial stress tensor $\boldsymbol{\sigma}$ defined as

$$\boldsymbol{\sigma} = \frac{1}{2V} \sum_{\substack{\alpha, \beta=1 \\ \alpha \neq \beta, r^{\alpha\beta} < r_{\text{cut}}}}^{n_{\text{ato}}} [\phi^{\alpha\beta}(r^{\alpha\beta})]' \frac{\vec{r}^{\alpha\beta} \otimes \vec{r}^{\alpha\beta}}{r^{\alpha\beta}}, \quad (6.5)$$

where V denotes a volume considered in the deformed configuration over which the stress is computed, see, e.g., [98, Section 11.5.2] for more details. To attain a stress-free state, the system reduces its initial interatomic spacing $a_0 = r_m$ to $a_0 = 0.99296702 r_m$. Although such a change is geometrically negligible, it has significant influence on the macroscopic mechanical behavior of the resulting system.

For the application of the boundary conditions the behavior of an ideal, defect-free, and linear-elastic specimen is assumed under a state of constant shear stress τ , i.e.,

$$\tau(t) = \mu^A \gamma^A(t) = \mu^B \gamma^B(t). \quad (6.6)$$

As illustrated in Fig. 6.2b, this is achieved by prescribing shear strains γ inversely proportional to the effective shear moduli μ associated with the individual phases. In particular, the shear angles correspond to $t\bar{\gamma}$ in Phase A, and $t\bar{\gamma}/\rho$ in Phase B, where ρ is a material contrast ratio, and $\bar{\gamma}$ is a target shear angle in Phase A, and $t \in [0, T]$ is a parametrization pseudo-time. The requirement of constant shear stress translates to prescribing atom positions of the boundary atoms as

$$\begin{aligned} \vec{r}^\alpha &= \vec{r}_0^\alpha + [t\bar{\gamma} r_{0,x}^\alpha] \vec{e}_y, & \text{for } \alpha \in N^A \cap N^{\text{BC}}, \\ \vec{r}^\beta &= \vec{r}_0^\beta + \frac{t\bar{\gamma}}{\rho} [r_{0,x}^\beta + (\rho - 1)L_A \text{sgn}(r_{0,x}^\beta)] \vec{e}_y, & \text{for } \beta \in N^B \cap N^{\text{BC}}, \end{aligned} \quad t \in [0, 1], \quad (6.7)$$

where $N^{\text{BC}} \subset N$ are the atoms to which boundary conditions are applied, i.e., atoms positioned within the r_{cut} distance from the specimen's boundary $\partial\Omega$, indicated by the hollow circles in Fig. 6.2a.

The mechanical configuration of the system at each time step t_k for a time discretization of the time horizon

$$t \in [0, T], \quad 0 = t_0 < t_1 < \dots < t_{n_T} = T, \quad (6.8)$$

is governed by the minimization of the total potential energy of the system, i.e.,

$$\underline{r}_k \in \arg \min_{\underline{v}} \mathcal{V}(\underline{v}). \quad (6.9)$$

Here, $\underline{r}_k = \underline{r}(t_k)$ is a relaxed configuration at a time instant t_k , \underline{r} is a column matrix storing the components of the position vectors in the deformed configuration \bar{r}^α corresponding to all atoms $\alpha = 1, \dots, n_{\text{ato}}$, \underline{v} denotes an admissible configuration of the system reflecting the boundary conditions of Eq. (6.7) applied at a time instant t_k , and

$$\mathcal{V}(\underline{r}) = \frac{1}{2} \sum_{\substack{\alpha, \beta=1 \\ \alpha \neq \beta, r^{\alpha\beta} < r_{\text{cut}}}}^{n_{\text{ato}}} \phi^{\alpha\beta}(r^{\alpha\beta}) \quad (6.10)$$

is the internal free energy¹. No externally applied forces are considered, as only the prescribed displacements are used to load the atomic system, recall Eq. (6.7). The minimization problem of Eq. (6.9) is solved using a Trust-region algorithm, see, e.g., [27], which has been implemented within an in-house code.

To avoid potential occurrence of multiple glide planes, the numerical solver is initiated at the beginning of each time step t_k towards the preferred glide plane $\Gamma_{\text{gp}} = \{\vec{x} \in \mathbb{R}^2 : y = 0\}$ by means of the analytical Volterra solution; see Fig. 6.2a, where the preferred glide plane is depicted by the dotted line. A more detailed description of the same initialization procedure can be found in [19, Section 2.2].

Quasicontinuum model

The Quasicontinuum (QC) methodology is a concurrent multiscale technique, originally introduced in [99]. The main idea consists in combining an accurate but expensive full atomic description inside regions of high interest with a cheaper continuum-like approximation elsewhere. This is achieved through a finite element mesh overlaid on top of the underlying lattice, as shown in Fig. 6.4, where all mesh nodes (vertices of linear triangular elements) coincide with atoms. This set of atoms, the so-called repatoms, determines positions of all the remaining atoms through interpolation

$$\underline{r} = \mathbf{\Phi} \underline{r}_{\text{rep}}. \quad (6.11)$$

In Eq. (6.11), $\underline{r}_{\text{rep}}$ is a column storing positions of all repatoms, whereas $\mathbf{\Phi} = [\varphi_1, \dots, \varphi_{2n_{\text{rep}}}]$ stores the interpolation basis functions φ_i associated with the triangular mesh, see [98] for more details. By gradually refining the triangulation, a seamless transition between the fully-resolved discrete description in the region of high interest and an efficient con-

¹For pair potentials, the sum over all atoms in Eq. (6.10) may be replaced by a sum over all interatomic interactions, reducing thus the associated computing cost by a factor of two. An additional speed-up can be achieved by, e.g., parallelization.

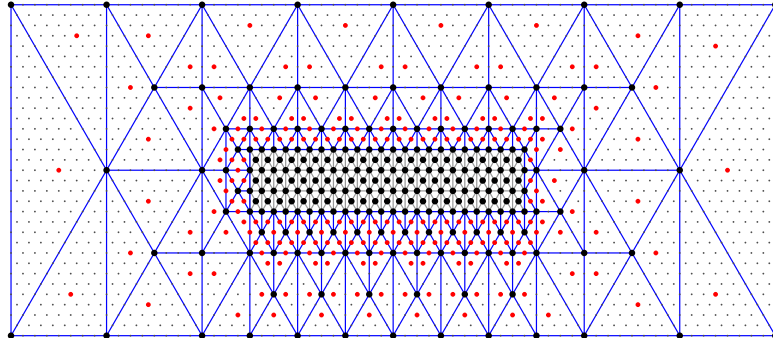


Figure 6.4: A typical triangulation of a small atomic domain with a predefined fully-resolved region. Repatoms are shown as black dots, sampling atoms as red dots, and all remaining atoms as gray dots. In the fully-resolved region the triangulation matches the underlying atomic structure (gray triangles), whereas elsewhere interpolation is used (blue triangles).

tinuum description elsewhere is achieved. A common practice is to choose the mesh such that the number of repatoms n_{rep} is much smaller than the total number of atoms n_{ato} , reducing substantially the number of Degrees Of Freedom (DOFs). This in turn yields computational savings, since the minimization problem of Eq. (6.9) is carried out with respect to $\underline{r}_{\text{rep}}$ instead of \underline{r} .

In order to construct the potential energy \mathcal{V} in Eq. (6.10) all lattice sites need to be visited, which is expensive and unnecessary. The second Quasicontinuum step is thus introduced to approximate the energy by

$$\mathcal{V}(\underline{r}) \approx \sum_{\alpha \in N_S} w^\alpha v^\alpha(\underline{r}), \quad (6.12)$$

where the energy associated with a lattice site α is specified as

$$v^\alpha(\underline{r}) = \frac{1}{2} \sum_{\substack{\beta=1 \\ \alpha \neq \beta, r^{\alpha\beta} < r_{\text{cut}}}}^{n_{\text{ato}}} \phi^{\alpha\beta}(r^{\alpha\beta}), \quad (6.13)$$

and where w^α is a summation weight associated with each sampling atom $\alpha \in N_S$. A set of all sampling atoms, N_S (indicated in Fig. 6.4 as red dots), is selected to accurately represent the energy of the entire system. The summation rule is tailored to a particular interpolation scheme used, for which multiple options exist, as reported, e.g., in [1, 16, 54]. In what follows, the central summation rule of Beex *et al.* [12] is used. A QC method thus minimizes the approximate energy of Eq. (6.12) with respect to the reduced kinematic variable $\underline{r}_{\text{rep}}$ related to the configuration of the entire atomic system through interpolation of Eq. (6.11).

The area of high interest, i.e., the fully-resolved region and hence the associated triangulation, need to adaptively evolve in time to properly accommodate dislocation motion while retaining QC efficiency. To this end, various adaptive criteria for atomic lattices can be found in the literature, see, e.g., [68, 81, 58, 101, 50, 4]. In this work, the Zienkiewicz–Zhu (ZZ) error estimator [110, 111, 90] is used as a refinement criterion, which is applied to the deformation gradient tensor computed within each element, see also [98, Section 12.6.5]. That is, the local error inside each element is estimated and compared

against a pre-selected threshold value ZZ_{tr} , to determine elements which need refinement. The fully-resolved region is updated sequentially as follows:

- (i) At each time increment, the QC system is equilibrated for a fixed fully-resolved region;
- (ii) The triangulation is checked by the mesh refinement criterion (using the ZZ error indicator) and refined if necessary;
- (iii) All required atoms are added as reatoms, the set of sampling atoms is amended, the interpolation matrix is updated, and the equilibrium is restored again.

This procedure is repeated until the mesh refinement criterion is satisfied for all mesh elements, proceeding subsequently to a new load increment in (i). Since in the here considered problem the same dislocation path is followed by trailing dislocations, no coarsening is considered for the atomic problem.

Peierls–Nabarro formulation

The homogenization based simplification of the full atomic problem of Section 6.2.1, shown in Fig. 6.2a, employs the FE Peierls–Nabarro model (abbreviated FE-PN; for more details see [20]). The problem domain Ω is split into two regions, Ω^A and Ω^B . These regions are separated by perfectly and fully coherent phase boundaries of zero thickness Γ_{pb} , which are normal to \vec{e}_x . Displacement and traction continuity conditions are enforced on Γ_{pb} as

$$\begin{aligned} \vec{u}^A &= \vec{u}^B, & \text{on } \Gamma_{\text{pb}}, \\ \boldsymbol{\sigma}^A \cdot \vec{e}_x &= \boldsymbol{\sigma}^B \cdot \vec{e}_x, & \text{on } \Gamma_{\text{pb}}, \end{aligned} \quad (6.14)$$

where $\boldsymbol{\sigma}$ is the Cauchy stress tensor, and \vec{u} is the displacement field. Both phases Ω^i , $i \in \{A, B\}$, are modeled as an elastic continuum enriched with a Peierls–Nabarro glide plane Γ_{gp} . Any dislocation motion, and in fact all non-linearity in the system, is confined to this plane, inducing additional energy through a corresponding misfit potential. The glide plane is considered perpendicular to the phase boundary Γ_{pb} , i.e., oriented along \vec{e}_x . Γ_{gp} is assumed as continuous throughout the entire domain Ω , horizontally splitting each phase Ω^i into two subdomains Ω_{\pm}^i , $i \in \{A, B\}$, as shown in Fig. 6.5. A shear deformation is prescribed to the considered domain as a function of time $t \in [0, T]$ on the external boundary $\partial\Omega$, inducing initially constant shear stress throughout the specimen according to Eq. (6.6).

In analogy to the full atomic system and the QC formulation, the evolution of the FE-PN model is governed by minimization of the total potential energy (specified per unit thickness because plane strain conditions are assumed), i.e.,

$$\vec{u}_k \in \arg \min_{\vec{v}} \Psi(\vec{v}). \quad (6.15)$$

In Eq. (6.15), $\vec{u}_k = \vec{u}(t_k)$ is the relaxed displacement field at a time instant t_k and \vec{v} is a kinematically admissible displacement field respecting the kinematic constraints prescribed on $\partial\Omega$. The total potential energy is expressed as

$$\Psi(\vec{u}) = \int_{\Omega \setminus \Gamma_{\text{gp}}} \psi_e(\vec{u}) \, d\Omega + \int_{\Gamma_{\text{gp}}} \psi_{\text{gp}}(\vec{u}) \, d\Gamma, \quad (6.16)$$

where ψ_e is the elastic strain energy density (considered inside Ω_{\pm}^i), ψ_{gp} is the glide plane

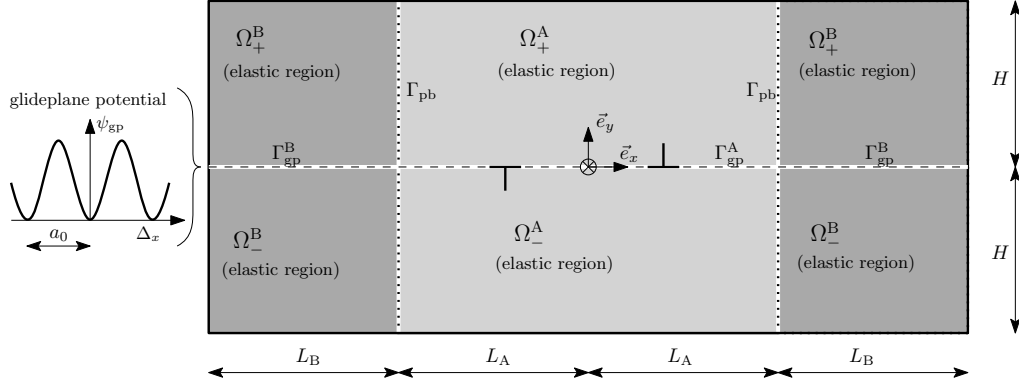


Figure 6.5: The FE-PN model for edge dislocation dipoles interacting with the phase boundary in a two-phase microstructure. Continuous representation of Phase A (bright gray solid) and Phase B (dark gray solid), glide plane (dashed line), and phase boundaries (dotted lines). Dislocation dipoles \perp are generated by the Frank–Read source denoted with \otimes .

potential (localized along the glide plane Γ_{gp}^i); any external forces have been neglected.

Within all subdomains Ω_{\pm}^i , small strain linear elasticity is assumed, i.e.,

$$\psi_e = \frac{1}{2} \boldsymbol{\varepsilon} : \mathbb{D} : \boldsymbol{\varepsilon}, \quad (6.17)$$

where

$$\boldsymbol{\varepsilon} = \frac{1}{2} (\vec{\nabla} \vec{u} + (\vec{\nabla} \vec{u})^\top) \quad (6.18)$$

is the small strain tensor, and $\vec{\nabla}$ denotes the gradient operator in the reference configuration. The energy density of Eq. (6.17) yields the linear elastic constitutive law

$$\boldsymbol{\sigma} = \mathbb{D} : \boldsymbol{\varepsilon}, \quad (6.19)$$

in which \mathbb{D} is a phase-specific isotropic fourth-order elasticity tensor.

Calibration

The elasticity tensor \mathbb{D} used in the FE-PN model in Eqs. (6.17) and (6.19), which is fully isotropic due to the considered hexagonal lattice, is obtained through homogenization of the atomic lattice as follows (see also [98]). First, a numerically homogenized stiffness tensor \mathbb{D}^{atm} , with components

$$D_{ijkl}^{\text{atm}} = \frac{1}{2V} \sum_{\substack{\alpha, \beta=1 \\ \alpha \neq \beta, r^{\alpha\beta} < r_{\text{cut}}}}^{n_{\text{ato}}} \left[\phi''(r^{\alpha\beta}) - \frac{\phi'(r^{\alpha\beta})}{r^{\alpha\beta}} \right] \frac{r_i^{\alpha\beta} r_j^{\alpha\beta} r_k^{\alpha\beta} r_l^{\alpha\beta}}{(r^{\alpha\beta})^2}, \quad \text{where } \phi''(r) = \frac{d^2 \phi^{\alpha\beta}(r)}{dr^2}, \quad (6.20)$$

is computed on the basis of the periodic unit cell of the atomic lattice. In Eq. (6.20), V denotes the volume of the simulation cell in the deformed configuration, whereas $r_i^{\alpha\beta}$ ($i = 1, 2$) are the components of the relative position vectors $\vec{r}^{\alpha\beta}$, cf. Eq. (6.5) and the discussion thereof. For nearest and next-to-nearest interactions the stiffness tensor \mathbb{D}^{atm}

Table 6.3: Homogenized constitutive parameters corresponding to Phase A. The constitutive parameters for Phase B are obtained by scaling with the material contrast ratio ρ .

parameter	$D_{1111}^{\text{atm}} = D_{2222}^{\text{atm}}$	$D_{1122}^{\text{atm}} = D_{1212}^{\text{atm}}$
Phase A	$102.520 \varepsilon / r_m^2$	$34.173 \varepsilon / r_m^2 (= D_{1111}^{\text{atm}} / 3)$

has been derived analytically for a unit hexagonal lattice by assembling the contributions of all relevant atoms (within the dashed circle in Fig. 6.3a). The computed parameters (tensor components) for Phase A are listed in Tab. 6.3 (the corresponding atomic properties are specified in Tab. 6.2); the parameters of Phase B are obtained simply by scaling those of Phase A with the material contrast ratio $\rho \in \{1.4, 4.0\}$. Next, an elastic isotropic plane strain stiffness tensor $\mathbb{D}(E_{\text{iso}}, \nu_{\text{iso}})$ is considered with the Young's modulus E_{iso} and Poisson's ratio ν_{iso} , in which effective parameters

$$E_{\text{iso}} = \frac{5}{6} D_{1111}^{\text{atm}} \quad \text{and} \quad \nu_{\text{iso}} = \frac{1}{4} \quad (6.21)$$

are obtained to match $\mathbb{D}^{\text{atm}} = \mathbb{D}(E_{\text{iso}}, \nu_{\text{iso}})$.

The glide plane potential ψ_{gp} is a function of the disregistry profile $\vec{\Delta}$, i.e., of the displacement jump across the glide plane Γ_{gp} ,

$$\vec{\Delta} = \llbracket \vec{u} \rrbracket = \vec{u}_+ - \vec{u}_- \quad \text{on} \quad \Gamma_{\text{pb}}, \quad (6.22)$$

which splits into a tangential Δ_t and a normal Δ_n part, i.e., $\vec{\Delta} = \Delta_t \vec{e}_t + \Delta_n \vec{e}_n$. To capture the effect of periodicity of the underlying atomic lattice, ψ_{gp} is a non-convex periodic function of Δ_t with a period a_0 . Different expressions have been introduced for ψ_{gp} in the literature, as discussed and compared, e.g., in [19]. Here it is based on the Generalized Stacking Fault Energy (GSFE) of the underlying atomic lattice, see, e.g., [104] where the GSFE was obtained from atomic calculations, or [33] where density functional theory was employed. In this paper, the GSFE is constructed through atomic calculations using a rectangular simulation box of size $20a_0 \times 12a_0\sqrt{3}$ with periodicity conditions between the vertical boundaries and free horizontal surfaces, as shown in Fig. 6.6a. A lattice with the stress-free spacing a_0 is considered, and the upper part is rigidly displaced as $\vec{\Delta} = \Delta_t \vec{e}_t + \Delta_n \vec{e}_n$. The GSFE computed for Phase A is shown in Fig. 6.6b, whereas the GSFE for Phase B is obtained again by multiplying with the corresponding material contrast ratio ρ . Within the specimen domain Ω , the glide plane potential is considered as a piecewise constant function. This is possible because the lattice considered in both phases is perfectly aligned, having the same lattice spacing a_0 . If the lattices within the different phases were not perfectly aligned with the same lattice spacing, or if they were oriented differently with respect to each other, additional simulations of the phase interface might be required.

Standard finite elements are used to discretize the elastic regions Ω_{\pm}^i . The glide plane Γ_{gp} is discretized by interface elements which are inserted between the bulk elasticity elements above and below it. Mechanical equilibrium is established by minimizing the total potential energy Ψ of Eq. (6.16) with respect to the DOFs of the considered FE triangulation. The non-convexity of ψ_{gp} is addressed by a truncated Newton optimization algorithm elaborated in [21]. Individual dislocations are initialized in analogy to the approach used for the fully-resolved atomic system, as described at the end of Section 6.2.1;

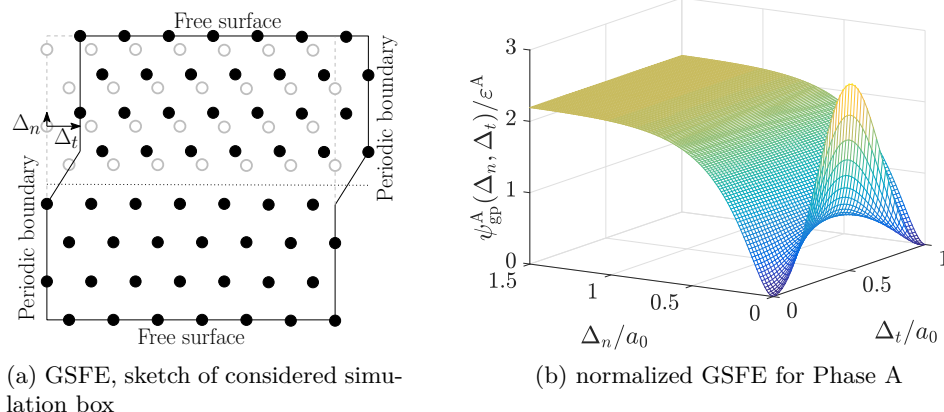


Figure 6.6: (a) Geometry of a rectangular simulation box with applied displacements Δ_n and Δ_t for the computation of the glide plane potential. Original positions of atoms are shown as gray circles, whereas atoms in the deformed configuration are shown as black dots. (b) Glide plane potential corresponding to Phase A, denoted $\psi_{\text{gp}}^A(\Delta_n, \Delta_t)$, normalized with respect to ε^A .

for more details see [20, Section 3.2].

Results and comparison

The behavior of the fully-resolved atomic system of Section 6.2.1 (referred to as Full) is described first, considering the material contrast ratio $\rho = 1.4$. Two QC systems of Section 6.2.2 are considered: (i) QC with a fixed mesh that is fully refined along the entire glide plane (referred to as QC fix), and (ii) QC with a mesh that has only a small fully-resolved region situated around the Frank–Read source equipped with adaptivity and a Zienkiewicz–Zhu error indicator of critical threshold $ZZ_{\text{tr}} = 0.001$, referred to as QC ZZ. The FE-PN model of Section 6.2.3 is considered for only one discretization with a fixed mesh refined along the glide plane down to an element size $h = a_0/16$. Although such an excessively small element size is not strictly necessary, see [20, 19] where 4–8 times coarser mesh was employed to obtain adequate macroscopic results such as transmission stress, it is used here to test the best accuracy of the FE-PN method, in particular to accurately capture the shape of the dislocation core. For coarser meshes a substantially better speed-up can be expected compared to the results presented here. The initial triangulations associated with the individual systems are shown in Fig. 6.7, whereas the corresponding (initial/final) number of DOFs are listed in Tab. 6.4. All reduced methods are compared against the full atomic system in terms of the total potential energy evolution, dislocation positions, critical transmission stresses, disregistry profiles, and computational effort.

Upon loading, for the fully-resolved atomic system at a certain time instance a critical resolved shear stress is reached (the activation stress of a Frank–Read source), resulting from the shear deformation applied on the remote boundary. At that moment, a new dislocation dipole is nucleated, which moves symmetrically under the increasing load and local Peach–Koehler force towards the phase boundary, where it is obstructed as a result of the phase contrast. By increasing the applied shear further, new dislocations are emitted and a dislocation pile-up is established in front of the interface. Further increasing the

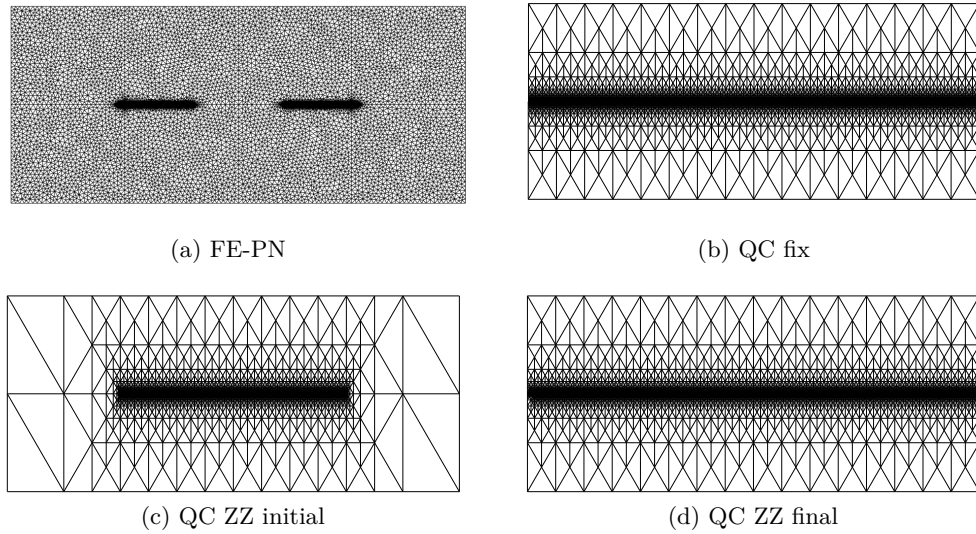


Figure 6.7: Employed initial triangulations for dislocation transmission across phase boundaries, corresponding to (a) FE-CZ model, (b) QC fix model, (c) QC ZZ model. (d) Triangulation for the QC ZZ model at the end of the simulation.

applied shear induces dislocation transmission into the neighboring Phase B. For visualization purposes, the quantity called Local Lattice Disregistry associated with an atom α (LLD^α), represents how much the current configuration of the hexagonal lattice around this atom differs from its initial configuration, and is defined as a sum of differences between the reference (undeformed) positions of its six nearest-neighbor atoms, \mathbf{r}_t^γ , and their current deformed positions located closest to their initial positions, \mathbf{r}^β , i.e.,

$$LLD^\alpha = \sum_{\gamma \in B_\alpha} \min_{\beta; \beta \neq \alpha} \|\mathbf{r}_t^\gamma - \mathbf{r}^\beta\|_2, \quad \forall \alpha \in N, \quad (6.23)$$

where $\min \|\mathbf{r}_t^\gamma - \mathbf{r}^\beta\|_2$ denotes the Euclidean distance of a one particular theoretical position from its closest atom β in the actual deformed configuration, and B_α is the initial set of nearest-neighbors associated with an atom α . The LLD indicator of Eq. (6.23) is shown in color for all atoms of the full atomic system in Fig. 6.8, corresponding to the case of a dislocation pile up with subsequent dislocation transmission (i.e., $\rho = 1.4$, Figs. 6.8a and 6.8c).

Global energy evolution profiles for all models are shown in Fig. 6.9a, where a good agreement is achieved, with the maximum energy error below 3% excluding jumps in energy evolutions. These jumps, present mostly in the early stages of the evolutions and observed mainly for the Full and both QC models, result from the initiation of new dislocations, which temporarily increases the energy. Upon further loading, the initially immobile but stable dislocations start to propagate towards the phase boundary and the energy drops. Similar behavior is not observed for the FE-PN model due to a vanishingly small Peierls-like barrier, as a consequence of a rather fine discretization (recall that $h = a_0/16$ has been adopted on the glide plane).

The corresponding evolutions of dislocation positions along the glide plane Γ_{gp} are shown in Fig. 6.9b against the externally applied normalized shear load τ/μ^A . Here we notice that all reduced methods cluster around the results corresponding to the full solu-

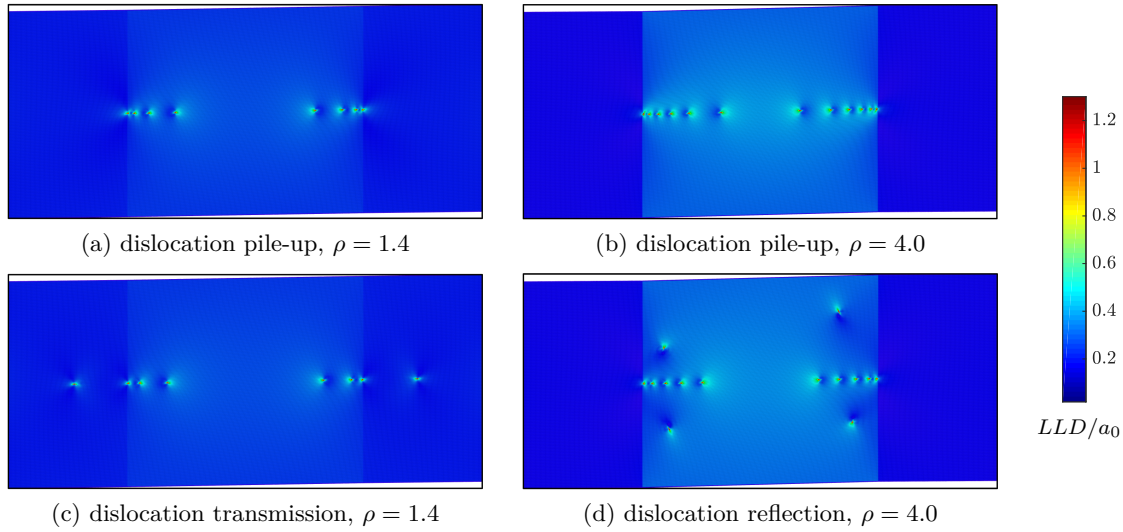


Figure 6.8: Local lattice disregistry of Eq. (6.23) for the full atomic model: (a) one step before, and (c) after transmission of the leading dislocation for the stiffness ratio $\rho = 1.4$; one step before (b), and after (d) reflection of the leading dislocation for the stiffness ratio $\rho = 4.0$.

tion, suggesting good agreement. If there is the same number of dislocations present in the compared models, then the maximum error in the dislocation position does not exceed $10 a_0$ once the dislocations start propagating towards the interface. However, more significant discrepancy in the dislocation position can be observed at early stages after initiation. All dislocations in the Full model and the second dislocation associated with the QC fix and QC ZZ method are initiated significantly earlier and closer to the specimen's center as compared to the FE-PN method. This can be explained by a vanishingly small Peierls barrier in the FE-PN method; in all the atomic simulations (Full and both QC), despite a negative Peach–Koehler force the dislocation does not annihilate upon initiation due to an existing Peierls barrier. This results in a delayed introduction of new dislocations in the FE-PN model. Since dislocation initiation is very sensitive to stress distribution along the glide plane, differences in the Full and both QC methods are also non-negligible. Numerical settings, such as discretization and interpolation, might have an impact on the evolution of the initial dislocations, affecting their final trajectories. We further notice that the critical transmission stress is underestimated by more than 30% by the FE-PN method and slightly overestimated by the QC ZZ method. For clarity, the transmission stresses corresponding to the individual methods are listed in Tab. 6.4. The significant underestimation of the critical transmission stress by the FE-PN method originates from several reasons. The first reason is an inaccurate representation of the dislocation core structure by the FE-PN model (because of adopted linear elasticity neglecting large deformations, discreteness, and non-locality of the underlying lattice), which may play a dominant role for dislocation-interface interactions. Dislocation cores obtained for the Full and FE-PN models are compared in Fig. 6.10, where we clearly see that the dislocation core provided by the FE-PN model is almost symmetric with respect to the horizontal glide plane unlike the strongly asymmetric core obtained from the Full model. The second reason is a missing Peierls barrier causing more compressed pile-up, resulting in higher stresses acting on the leading dislocation in the FE-PN model. The last but probably the most important

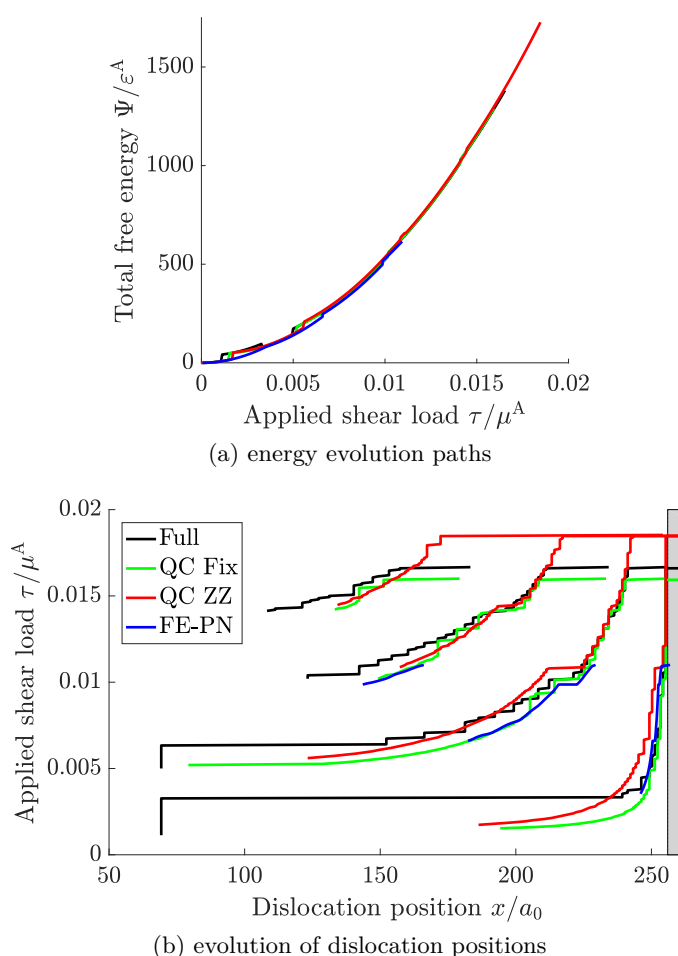


Figure 6.9: The global model response to the formation and evolution of a four-dislocation pile-up under the increasing externally applied shear load τ for all considered models. (a) Evolutions of the total elastic energies, and (b) evolutions of dislocation positions x/a_0 . The gray area indicates the stiffer Phase B.

reason is that in the atomic models, the leading dislocation dissociates partially into the secondary inclined glide planes (associated with dislocation reflection, discussed later in this section, see also Fig. 6.8d). As a result, the energy of the dislocation is split between the primary and secondary glide planes. On the other hand, because in the FE-PN model the entire energy is constrained to the primary glide plane associated with the transmission, the dislocation is located closer to the interface and dislocation transmission thus happens earlier. Additional simulations (not presented here for brevity) confirm that the shear stress needed for dislocation transmission increases significantly once the secondary inclined glide planes are introduced into the FE-PN model.

Normalized tangential Δ_t/a_0 and normal Δ_n/a_0 disregistry profiles, expressed as a function of the normalized coordinate x/a_0 along the glide plane Γ_{gp} , are shown in Fig. 6.11 for two load levels $\tau = 0.0068 \mu^A$ and $\tau = 0.01093 \mu^A$. In all discrete models (Full, QC fix, and QC ZZ), the disregistry profiles are evaluated from the displacements of individual atoms along the glide plane Γ_{gp} , whereas for the FE-CZ model the displacement discontinuity vector $\vec{\Delta}$ is plotted directly. From the presented results we conclude that, consistently with Fig. 6.9, at the lower applied shear level ($\tau = 0.0068 \mu^A$) the QC fix

Table 6.4: Performance of individual computational models considered for atomic problem.

	transmission stress τ/μ^A	dislocation position error, Eq. (6.24)	initial/final DOFs	computational demand
Full	(0.01667)	0	1,047,552	1
QC fix	-4.00%	7.83	34,576	$\approx 1/14$
QC ZZ	+11.16%	5.83	15,732/19,676	$\approx 1/9$
FE-PN	-34.01%	8.92	1,181,576	$\approx 1/5$

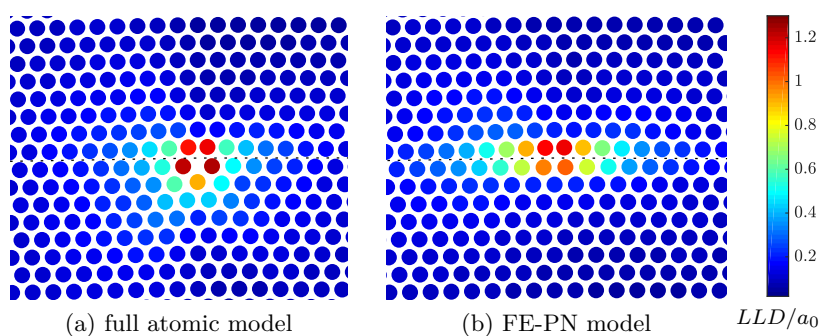


Figure 6.10: The detail of the dislocation core. (a) Deformed configuration obtained for the Full atomic model (the color shows the local lattice disregistry of Eq. (6.23) normalized by the lattice spacing, LLD/a_0). (b) Equivalent quantity evaluated from the displacement field of the FE-PN model projected on the positions of the underlying atomic lattice. The dotted lines denote the glide planes.

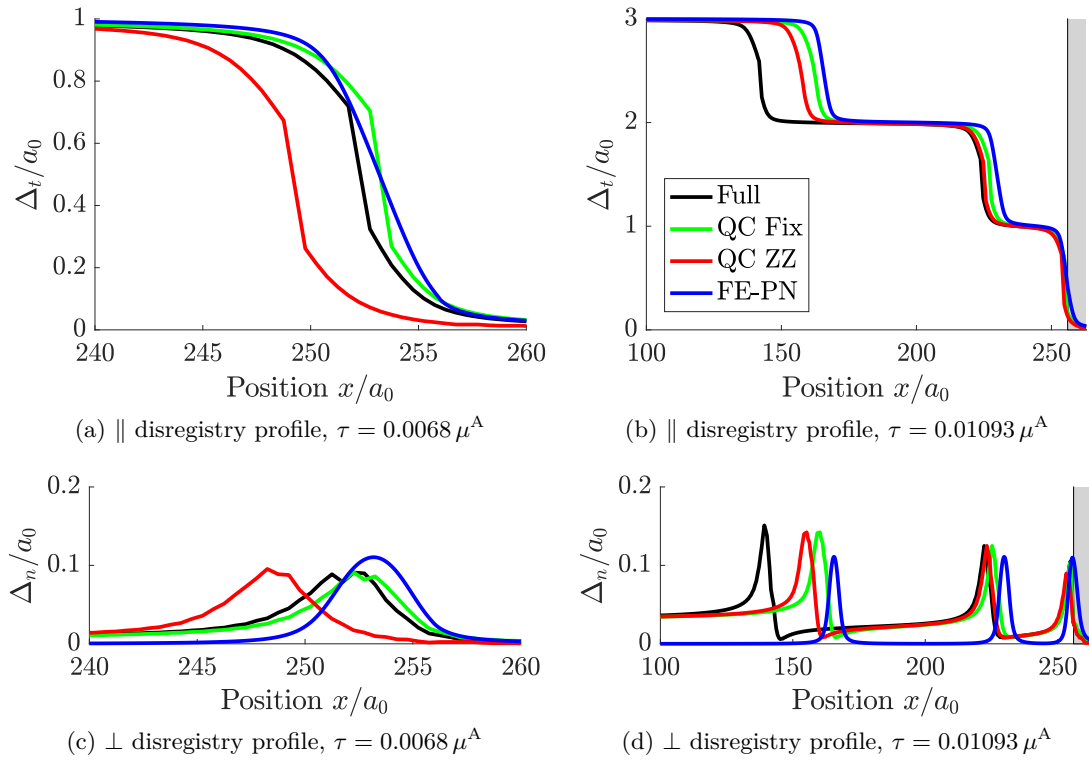


Figure 6.11: A comparison of normalized tangential \parallel and normal \perp disregistry profiles for different models. Tangential (a) and normal (c) disregistry profiles for applied shear stress $\tau = 0.0068 \mu^A$. Tangential (b) and normal (d) disregistry profiles for applied shear stress $\tau = 0.01093 \mu^A$. The gray area indicates the stiffer Phase B.

solution is very similar to the reference Full solution, whereas the FE-PN method achieves better accuracy as compared to the QC ZZ. A different situation occurs at later stages of loading ($\tau = 0.01093 \mu^A$), where the best accuracy is achieved by the QC ZZ method, while the FE-PN method leads to the highest error. This error is quantified in Tab. (6.4) by the Dislocation Position Error (*DPE*). For each reduced model, the *DPE* value represents how much on average the position of dislocation in this model differs (relative to a_0) from the exact solution. The averaging is realized for both distinct dislocations as well as distinct time steps, i.e.,

$$DPE^\bullet = \frac{1}{n_s} \sum_{i_s} \frac{1}{n_d} \sum_{i_d} \frac{|x_{i_d, i_s}^\bullet - x_{i_d, i_s}^{\text{Full}}|}{a_0}, \quad (6.24)$$

where $x_{i_d, i_s}^{\text{Full}}$ and x_{i_d, i_s}^\bullet denote horizontal position of i_d -th dislocation at i_s -th time step corresponding to the Full and one of the effective models (QC fix, QC ZZ, or FE-PN). n_s denotes the number of time steps used for the error evaluation, and n_d is the total number of dislocations at the given time step. In Tab. (6.4), the *DPE* quantity is evaluated as an average difference in position of three dislocations in the last two steps before transmission of the FE-PN model ($\tau = 0.01093 \mu^A$). The most accurate QC ZZ method exhibits an average difference of $5.83 a_0$, while the highest average difference of $8.92 a_0$ can be observed for the FE-PN method.

The computational performances obtained for the individual models are summarized in Tab. 6.4 in terms of the number of DOFs and computing times. Both QC models achieve significant reductions in the number of DOFs, which also results in considerable computational savings. The QC fix requires less computing time compared to the QC ZZ method because in the latter a significant amount of time is spent on mesh refinement procedures. The FE-PN model, on the other hand, uses relatively fine discretization along the glide plane (recall that $h_{\max} = a_0/16$ to capture dislocation core accurately), requiring even a higher number of DOFs as compared to the full atomic model. Only a five-fold speed-up is thus obtained, which can be significantly improved by employing much coarser meshes. Additional simulations show that 4–8 times coarser meshes relative to the fine $h_{\max} = a_0/16$ discretization do not change the results by more than 5% while approximately a ten-fold speed-up is achieved, cf. [20, 19].

Although the presented example was set to show dislocation pile up with subsequent dislocation transmission, another, rather unexpected, mechanism can be observed in the system depending on the choice of the material contrast ratio ρ . In particular, when $\rho = 4$, a dislocation pile up followed by dislocation reflection into Phase A is observed, as shown in Figs. 6.8b and 6.8d. Since both the QC fix as well as the FE-PN model were not set up for such a situation, i.e., no inclined glide planes or fully-resolved regions are present (recall Figs. 6.5 and 6.7b), they cannot account for dislocation reflection—unlike the fully flexible adaptive QC model.

It is worth noting that the presented speed-ups are obtained for two-dimensional atomic simulations only. In three-dimensional examples—which are more general and physically relevant—, a significantly larger number of atoms is present. The neighbor search algorithm within the considered cut-off radius will be significantly slower and the number of interatomic bonds is substantially higher. As a consequence, the QC simulations are expected to be much slower compared to the simulations of homogenized FE-PN model. Moreover, the presented example considers a simple Lennard–Jones pair potential. Use of a more advanced multibody potential, such as embedded atom model, will induce even further computing costs required by the QC simulations.

On the contrary, 3D extensions of the homogenized FE-PN model are expected to be relatively efficient provided that dislocation trajectories remain a priori known, and fixed glide planes can be considered. In a fully general case with arbitrary dislocation trajectories, however, sliding of glide planes should be considered in all possible lattice directions, which will result in small elastic regions representing individual atoms with multiple glide planes among them, each requiring its associated GSFE. Such a model may become computationally very expensive compared even to a full atomic simulation. In cases without any prior information on possible trajectories of dislocations, it is thus preferable to use adaptive QC approach instead.

Lattice model: crack propagation in a concrete specimen

Full lattice model

The second example considers a quasi-brittle (concrete) specimen subjected to a three-point bending test, modeled at the mesoscale as a discrete lattice system shown in Fig. 6.12a. The domain Ω is of size $L \times H$, inside which a homogeneous X-braced lattice with spacing l_0 is considered in between n_{par} particles α positioned at \vec{r}^α stored in an index set N . All lattice interactions are modeled as damageable with an exponential softening law. To

prevent spurious damage localization in the vicinity of prescribed displacements or applied loads, the lattice is made 100 times stiffer in padding regions with size $8l_0 \times 6l_0$ under the loading force and $22l_0 \times 4l_0$ around both supports. Upon loading, a localized crack growing along the symmetry plane from bottom to top is expected.

In analogy to the atomic system considered in the previous section, an inter-particle pair potential $\pi^{\alpha\beta}$ is introduced. It consists of two contributions, the elastically stored energy reflected by $\phi^{\alpha\beta}$, and a dissipation distance $\mathcal{D}^{\alpha\beta}$,

$$\pi_k^{\alpha\beta}(r^{\alpha\beta}, \omega^{\alpha\beta}; \omega_{k-1}^{\alpha\beta}) = (1 - \omega^{\alpha\beta})\phi^{\alpha\beta}(r_+^{\alpha\beta}) + \phi^{\alpha\beta}(r_-^{\alpha\beta}) + \mathcal{D}^{\alpha\beta}(\omega^{\alpha\beta}, \omega_{k-1}^{\alpha\beta}). \quad (6.25)$$

Because dissipative mechanisms are included, a variational formulation of rate-independent systems is considered [59, 60], and the interaction potential depends also on an internal variable $\omega^{\alpha\beta}$, reflecting the level of damage in the interaction connecting particles α and β . In addition, the pair potential is considered in an incremental fashion, i.e., at a time instance t_k , $\pi_k^{\alpha\beta} = \pi^{\alpha\beta}(t_k)$, and depends on the configuration of the system in the current as well as the previous time step. To allow damage processes to evolve only under tension and not under compression, the elastically stored energy is split into two parts, $(1 - \omega^{\alpha\beta})\phi^{\alpha\beta}(r_+^{\alpha\beta}) + \phi^{\alpha\beta}(r_-^{\alpha\beta})$, in which only the first term is affected by the damage variable. The two distance quantities, $r_+^{\alpha\beta} = \max(r^{\alpha\beta}, r_0^{\alpha\beta})$ and $r_-^{\alpha\beta} = \min(r^{\alpha\beta}, r_0^{\alpha\beta})$ (assuming $\phi^{\alpha\beta}(r_0^{\alpha\beta}) = 0$), ensure that the damage variable weakens the interaction only under tension, i.e., for $r^{\alpha\beta} > r_0^{\alpha\beta}$. A quadratic elastic potential is considered,

$$\phi^{\alpha\beta}(r^{\alpha\beta}) = \frac{1}{2}EA r_0^{\alpha\beta} (\varepsilon^{\alpha\beta}(r^{\alpha\beta}))^2, \quad (6.26)$$

expressed as a function of strain

$$\varepsilon^{\alpha\beta}(r^{\alpha\beta}) = \frac{r^{\alpha\beta} - r_0^{\alpha\beta}}{r_0^{\alpha\beta}}, \quad (6.27)$$

where, in analogy to the atomic system, $\vec{r}^{\alpha\beta} = \vec{r}^\beta - \vec{r}^\alpha$ is a vector of relative positioning, $r^{\alpha\beta} = \|\vec{r}^{\alpha\beta}\|_2$ the Euclidean distance between a pair of particles α and β , and EA is the normal cross-sectional stiffness of the bond.

The dissipation distance $\mathcal{D}^{\alpha\beta}$ measures the energy dissipated by a single interaction during the evolution of the damage variable between two consecutive states, $\omega_1^{\alpha\beta}$ and $\omega_2^{\alpha\beta}$, i.e.,

$$\mathcal{D}^{\alpha\beta}(\omega_2^{\alpha\beta}, \omega_1^{\alpha\beta}) = \begin{cases} D^{\alpha\beta}(\omega_2^{\alpha\beta}) - D^{\alpha\beta}(\omega_1^{\alpha\beta}), & \text{if } \omega_2^{\alpha\beta} \geq \omega_1^{\alpha\beta}, \\ +\infty, & \text{otherwise,} \end{cases} \quad (6.28)$$

where $D(\omega)$ is the energy dissipated during a unidirectional damage process up to the damage level ω . It is defined implicitly such that the following exponential damage law results

$$\omega(\varepsilon) = \begin{cases} 1 - \frac{\varepsilon_0}{\varepsilon} \exp\left(-\frac{\varepsilon - \varepsilon_0}{\varepsilon_f}\right), & \text{if } \varepsilon \geq \varepsilon_0, \\ 0, & \text{if } \varepsilon < \varepsilon_0, \end{cases} \quad (6.29)$$

where ε_0 is the limit elastic strain for which damage starts to evolve, and ε_f characterizes the slope of the softening branch in the associated stress-strain diagram, and where the upper index $\alpha\beta$ has been dropped for brevity; for more details see [85, Section 4.1]. The adopted constitutive parameters are specified in Tab. 6.5.

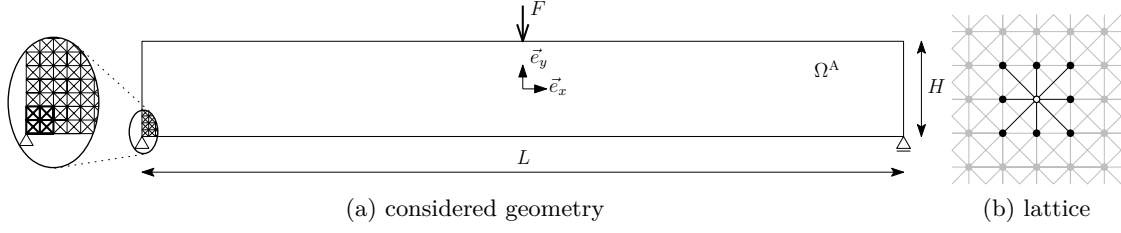


Figure 6.12: A quasi-brittle concrete specimen modeled as an X-braced damageable lattice of spacing l_0 . (a) A sketch of the considered geometry of a three-point bending example. (b) X-braced lattice (gray) with neighboring nodes and active interactions (black) for one particular lattice site (white circle).

Table 6.5: Geometric and constitutive parameters of the X-braced lattice used for the three-point bending test. l_0 denotes lattice spacing, ε_0 limit elastic strain for an exponential damage model, ε_f specifies slope of the softening branch, EA the normal cross-sectional stiffness, and $L \times H$ is size of considered domain.

parameters	l_0	EA	ε_0	$\varepsilon_f/\varepsilon_0$	L/l_0	H/l_0
values	1 [mm]	20 [MN]	0.005	10	2,048	256

In analogy to Eq. (6.9), with the introduction of a time discretization for a considered time horizon $t \in [0, T]$ from Eq. (6.8), the evolution of the fully-resolved damageable lattice system is governed by the minimization of the total incremental energy Π_k ,

$$\underline{q}_k \in \arg \min_{\underline{v}} \Pi_k(\underline{v}; \underline{q}_{k-1}), \quad k = 1, \dots, n_T, \quad (6.30)$$

minimized over all admissible configurations \underline{v} with an initial condition $\underline{q}_0^\top = [\underline{x}_0^\top, \underline{0}^\top]$, where $\underline{q}^\top = [\underline{r}^\top, \underline{z}^\top]$ is a state variable of the entire system, consisting of the kinematic variable \underline{r} storing the positions of all particles, whereas $\underline{z}^\top = [\omega_1, \dots, \omega_{n_{\text{int}}}]$ collects the damage variables of all n_{int} interactions, and $\underline{q}_k = \underline{q}(t_k)$. The incremental energy of the entire system is obtained by collecting contributions from all interactions, i.e.,

$$\Pi_k(\underline{q}; \underline{q}_{k-1}) = \mathcal{V}(\underline{q}) + \mathcal{D}(\underline{q}, \underline{q}_{k-1}) - \underline{f}_k^\top \underline{x}, \quad (6.31)$$

where

$$\mathcal{V}(\underline{q}) = \frac{1}{2} \sum_{\substack{\alpha=1 \\ \beta \in B_\alpha}}^{n_{\text{par}}} [(1 - \omega^{\alpha\beta}) \phi^{\alpha\beta}(r_+^{\alpha\beta}) + \phi^{\alpha\beta}(r_-^{\alpha\beta})] \quad (6.32)$$

is the internally stored energy², and

$$\mathcal{D}(\underline{q}_2, \underline{q}_1) = \frac{1}{2} \sum_{\substack{\alpha=1 \\ \beta \in B_\alpha}}^{n_{\text{par}}} \mathcal{D}^{\alpha\beta}(\underline{z}_2, \underline{z}_1) \quad (6.33)$$

is the global dissipation distance (recall also Eqs. (6.25) and (6.28)), B_α is the initial

²The numerical implementation of Eq. (6.32) is again conveniently converted from a sum over all particles into a sum over all interactions, recall Eq. (6.10) and the related Footnote 1.

set of nearest-neighbors associated with a particle α (cf. Fig. 6.12b), whereas \underline{f}_k is a vector of external forces applied at time instance t_k . At each time step, the minimization problem (6.30) is solved to obtain a local minimum. Because multiple minima may exist, the energetic solution corresponds to the one that satisfies the following energy balance

$$\mathcal{V}(\underline{q}_k) - \mathcal{V}(\underline{q}_0) + \text{Var}_{\mathcal{D}}(\underline{q}, t_k) = \mathcal{W}(\underline{q}, t_k), \quad k = 1, \dots, n_T, \quad (6.34)$$

which equates a sum of the internally stored energy and the dissipated energy, defined as

$$\text{Var}_{\mathcal{D}}(\underline{q}, t_k) = \sum_{i=1}^k \mathcal{D}(\underline{z}_i, \underline{z}_{i-1}), \quad (6.35)$$

with the work performed by the external forces

$$\mathcal{W}(\underline{q}, t_k) = \sum_{i=1}^k \frac{1}{2} (\underline{f}_i + \underline{f}_{i-1})^\top (\underline{r}_i - \underline{r}_{i-1}). \quad (6.36)$$

To ensure that obtained minimum corresponds to a physically relevant energetic solution, the energy balance constraint of Eq. (6.34) is closely monitored in each time increment. Upon its violation, the considered time step is restarted with a smaller loading increment. To avoid such situations from occurring, the evolution path of the system is controlled using a dissipation driven arc-length method or crack mouth opening displacement control, as elaborated in more detail below in Section 6.3.5. For further details on the variational formulation of rate independent systems see, e.g., [61] (Section 3.2), and for applications to lattice systems, e.g., [47, 83, 32, 84, 85].

Quasicontinuum model

In analogy to Section 6.2.2, the two QC steps are introduced as follows. First, the interpolation step is introduced for the kinematic variable, cf. Eq. (6.11),

$$\underline{r} \approx \Phi \underline{g}, \quad (6.37)$$

while the internal variable \underline{z} is not reduced for simplicity and to avoid issues with non-uniqueness in the prolongation operation and mesh coarsening as discussed in [83, Section 3.1]. The reduced QC state variable then reads $\underline{q}_{\text{red}}^\top = [\underline{g}^\top, \underline{z}^\top]$. To allow for crack paths to be independent of the mesh topology, an extended variant of a QC methodology introduced in [84] is adopted. This extension allows for an efficient mesh coarsening through Heaviside step function enrichments used in the interpolation matrix Φ . The generalized kinematic variable \underline{g} then stores the positions of all representative particles ($\underline{r}_{\text{rep}}$, analogous to atomic QC) as well as coefficients of linear combinations of the special function enrichments.

The summation step again samples the total incremental energy based on only a small set of selected sampling atoms stored in an index set N_S , i.e.,

$$\Pi_k(\underline{q}_k; \underline{q}_{k-1}) \approx \sum_{\alpha \in N_S} w^\alpha \pi_k^\alpha(\underline{q}_k; \underline{q}_{k-1}) - \underline{f}_k^\top \underline{r}, \quad (6.38)$$

where w^α and N_S correspond to the central summation rule of Beex *et al.* [12], generalized for Heaviside type of enrichments according to [84]. The energy associated with a lattice

site α is defined as

$$\pi_k^\alpha(\underline{q}_k; \underline{q}_{k-1}) = \frac{1}{2} \sum_{\beta \in B_\alpha} \pi_k^{\alpha\beta}(r_k^{\alpha\beta}, \omega_k^{\alpha\beta}; \omega_{k-1}^{\alpha\beta}), \quad (6.39)$$

where the incremental energy of a single interaction $\pi_k^{\alpha\beta}$ has been defined in Eq. (6.25). A QC method therefore minimizes the approximate total incremental energy of Eq. (6.38) with respect to the reduced state variable $\underline{q}_{\text{red}}$, mapped on the state of the entire system through the interpolation relation of Eq. (6.37).

The area of high interest, i.e., the fully-resolved region, is allowed to evolve adaptively throughout the simulation. Available options for the refinement criteria have been recently discussed in [25]. From the presented options, only a few studies presented concepts suitable for applications to structural lattices [58, 85, 84, 66, 25]. In this work, the following mesh error indicator, employed also in [85], is adopted for mesh refinement as well as for mesh coarsening. Interactions that are likely to be subjected to damage are identified through the refinement criterion, which compares the energy stored in an interaction (recall that damage is only allowed in tension) against a certain threshold energy, i.e.,

$$\varepsilon^{\alpha\beta} > 0, \quad \text{and} \quad (1 - \omega^{\alpha\beta})\phi^{\alpha\beta}(r^{\alpha\beta}) \geq \theta_r \phi_{\text{th}}^{\alpha\beta}, \quad \alpha\beta \in S_{\text{int}}^K, \quad (6.40)$$

where $\theta_r \in (0, 1)$ is a safety parameter and $\phi_{\text{th}}^{\alpha\beta} = \phi^{\alpha\beta}(r_0(1 + \varepsilon_0))$ is the elastic threshold energy at which the damage starts to evolve, and S_{int}^K denotes the set of all sampling interactions $\alpha\beta$ located inside an element K . If at least one bond in S_{int}^K satisfies the condition of Eq. (6.40), element K is fully refined (i.e., all lattice sites inside the triangle are added as renodes, and the triangulation is updated). Alternatively, element K is coarsened if the elastic energy of all bonds is lower than a given threshold, i.e.,

$$(1 - \omega^{\alpha\beta})\phi^{\alpha\beta}(r^{\alpha\beta}) \leq \theta_c \phi_{\text{th}}^{\alpha\beta}, \quad \alpha\beta \in S_{\text{int}}^K, \quad (6.41)$$

where $\theta_c \in (0, 1)$ is a coarsening parameter satisfying $\theta_c < \theta_r$. Note that in Eq. (6.41) all bonds, i.e., including those in compression, are considered. The fully-resolved region is adaptively updated following the same three steps (i)–(iii) presented at the end of Section 6.2.2. No initial mesh refinement is needed, unlike in the atomic QC system, since no initiation analogous to the Volterra perturbation is employed (which needs to be resolved by the adopted QC system).

Finite element cohesive zone model

The initial lattice problem of Fig. 6.12a is translated into a continuous Finite Element Cohesive Zone (FE-CZ) model shown in Fig. 6.13, in which it is assumed that only one potential crack path is present in an otherwise continuous specimen. In contrast to a discrete lattice, the continuous domain does not require local stiffening under the applied boundary conditions to prevent excessive deformation. A cohesive zone Γ_{cz} , located along the vertical axis of symmetry, splits the homogeneous domain Ω into two parts Ω^L and Ω^R ,

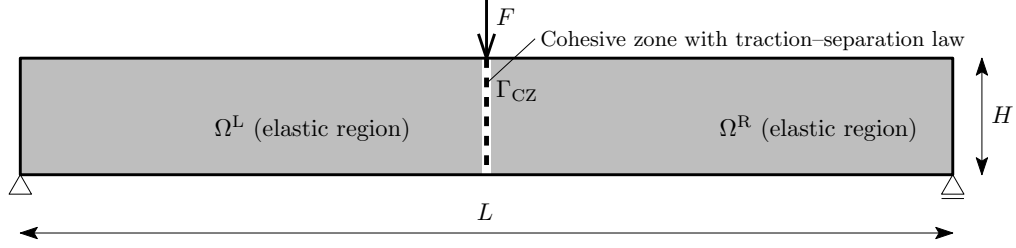


Figure 6.13: The FE-CZ model for a crack propagation in the three-point bending test, showing the elastic domain (gray), cohesive zone (dashed line), and applied boundary conditions.

i.e.,

$$\begin{aligned}
 \Gamma_{cz} &= \left\{ \vec{x} \in \mathbb{R}^2 : x = x_{cz}, |y| \leq H/2 \right\}, \\
 \Omega^L &= \left\{ \vec{x} \in \mathbb{R}^2 : -L/2 \leq x \leq x_{cz}, |y| \leq H/2 \right\}, \\
 \Omega^R &= \left\{ \vec{x} \in \mathbb{R}^2 : x_{cz} \leq x \leq L/2, |y| \leq H/2 \right\}, \\
 \Omega &= \Omega^L \cup \Omega^R,
 \end{aligned} \tag{6.42}$$

where $x_{cz} = 0$ denotes the horizontal position of the cohesive zone.

The mechanical behavior of the FE-CZ system is governed by the minimization of the total potential energy defined as

$$\vec{u}_k \in \arg \min_{\vec{v}} \left(\Psi(\vec{v}) - \int_{\Gamma_t} \vec{t} \cdot \vec{v} d\Gamma_t \right), \tag{6.43}$$

where the second term on the right-hand side represents a concentrated force F in Fig. 6.13, distributed through tractions \vec{t} over a small portion of the specimen boundary Γ_t . Both subdomains Ω^L and Ω^R are purely elastic isotropic and the deformation related to the crack propagation is localized within the cohesive zone Γ_{cz} . The total internal energy Ψ (cf. also Eq. (6.16)) reads

$$\Psi(\vec{u}) = \int_{\Omega \setminus \Gamma_{cz}} \psi_e(\vec{u}) d\Omega + \int_{\Gamma_{cz}} \psi_{cz}(\vec{u}) d\Gamma_{cz}, \tag{6.44}$$

where ψ_e is the elastic strain energy density defined in Eq. (6.17), and ψ_{cz} is the cohesive zone potential (defined solely on Γ_{cz}). Both are obtained through the homogenization of the underlying lattice as follows.

Calibration

For the calibration of the FE-CZ model, a single lattice unit cell as shown in Fig. 6.14a, is considered. The normal cross-sectional stiffness of the horizontal and vertical bonds are reduced to half of its true value to respect the considered periodicity. The corresponding assembled effective stiffness tensor \mathbb{D}^{lat} , listed in Tab. 6.6, is compared to an isotropic plane strain stiffness tensor $\mathbb{D}(E_{\text{iso}}, \nu_{\text{iso}})$. The resulting effective elastic parameters are identified as

$$E_{\text{iso}} = \frac{5 EA}{6 l_0 l_z} (1 + 1/\sqrt{2}) \quad \text{and} \quad \nu_{\text{iso}} = \frac{1}{4}, \tag{6.45}$$

Table 6.6: Homogenized constitutive parameters corresponding to the lattice unit cell.

parameters	$D_{1111}^{\text{lat}} = D_{2222}^{\text{lat}}$	$D_{1122}^{\text{lat}} = D_{1212}^{\text{lat}}$
	$(1 + 1/\sqrt{2}) EA/(l_0 l_z)$	$(1/\sqrt{2}) EA/(l_0 l_z)$

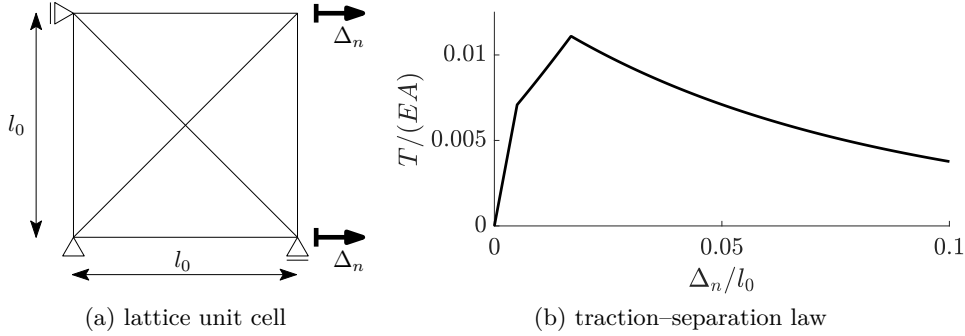


Figure 6.14: (a) The lattice unit cell used for the computation of the traction–separation law. (b) Normalized traction–separation law as a function of the normalized normal opening Δ_n/l_0 .

where l_z is the unit out-of-plane thickness. The fixed Poisson’s ratio is given by the fact that $D_{1122}^{\text{lat}} = D_{1212}^{\text{lat}}$ and the effective Young’s modulus is obtained by fitting $D_{1111}^{\text{lat}} = D_{1111}(E_{\text{iso}}, \nu_{\text{iso}})$. Note that for the considered setting of lattice structure (identical normal stiffness of all bonds), the resulting stiffness tensor \mathbb{D}^{lat} is not fully isotropic, cf., e.g., [65, Appendix B] for more details. The cohesive zone potential ψ_{cz} is a function of the displacement jump across the cohesive zone Γ_{cz} ,

$$\vec{\Delta} = \Delta_t \vec{e}_t + \Delta_n \vec{e}_n = \llbracket \vec{u} \rrbracket = \vec{u}^{\text{R}} - \vec{u}^{\text{L}}, \quad (6.46)$$

see also Eq. (6.22). Due to the symmetry of the considered problem, the tangential component Δ_t vanishes, i.e.,

$$\vec{u}^{\text{L}} \cdot \vec{e}_y = \vec{u}^{\text{R}} \cdot \vec{e}_y, \quad \text{on } \Gamma_{\text{cz}}, \quad (6.47)$$

and hence the cohesive zone potential ψ_{cz} becomes a function of the crack normal opening Δ_n only. The cohesive zone potential is obtained numerically from the response of the lattice unit cell subjected to a horizontal stretch of Δ_n/l_0 with the boundary conditions shown in Fig. 6.14a. The corresponding traction acting on the cohesive zone as a function of the normal crack opening is defined as

$$T(\Delta_n) = \frac{d\psi_{\text{cz}}(\Delta_n)}{d\Delta_n}, \quad (6.48)$$

and is plotted for the lattice constitutive parameters of Tab. 6.5 in Fig. 6.14b.

Results and comparison

Due to the present damage processes, arbitrarily small increments in externally applied boundary conditions might lead to an uncontrolled evolution of the crack, and hence also of the internal variable \underline{z} in both the fully-resolved and QC system (i.e., a snap-back

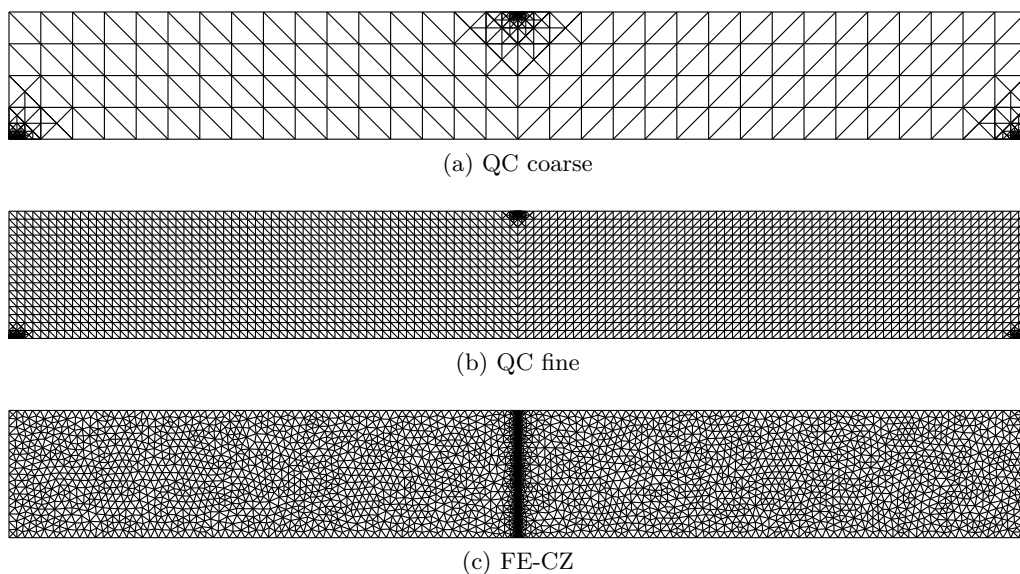


Figure 6.15: Employed initial triangulations for crack propagation in the three-point bending test of concrete specimen, corresponding to (a) QC coarse model, (b) QC fine model, and (c) FE-CZ model.

may occur), which in turn might result in the violation of the energy balance constraint of Eq. (6.34). To avoid such situations, the evolution path is closely controlled using a dissipation driven arc-length method, see, e.g., [103, 39, 57] for more details. For the FE-CZ approach, the standard Crack Mouth Opening Displacement (CMOD) control method [44] is sufficient to reliably compute a mechanical response of the system.

The mechanical behavior of the fully-resolved mesoscopic system of Section 6.3.1 (referred to as Full) is adopted as the underlying reference solution. Two QC models, as described in Section 6.3.2, are then considered: (i) one with a coarse triangulation of maximum element size $H/4$ (referred to as QC coarse), and (ii) one with a fine triangulation of maximum element size $H/16$ (referred to as QC fine), see Figs. 6.15a and 6.15b. The FE-CZ model, detailed in Section 6.3.3, is considered for only one triangulation with a fixed mesh. A maximum element size $H/16$ adopted far from the cohesive zone, which is gradually refined down to $H/256 = l_0$ towards the assumed crack path Γ_{cz} , cf. Fig. 6.15c. A mesh convergence study has been performed to verify that the adopted element size provides converged results. The initial triangulations of all reduced models are shown in Fig. 6.15, whereas the corresponding number of DOFs are listed in Tab. 6.7. All three effective models are compared against the fully-resolved simulation in terms of force–displacement curves, peak forces, crack lengths, and crack opening profiles.

With the increasing external load, individual bonds near the bottom center region start to damage until localization occurs, forming a full central crack propagating almost vertically across the specimen’s height, cf. Fig. 6.16b. The corresponding evolutions of the normalized magnitude of the externally applied force $F/(EA)$ are shown in Fig. 6.17 as a function of the normalized vertical displacement measured under the force, u/l_0 . The specimen exhibits, after the initial linear response, a significant softening followed by a severe snap-back once the central crack localizes. While both QC approaches manage to capture the initial ductile behavior (the QC fine being almost indistinguishable from the Full solution), the FE-CZ completely omits this mechanism. Upon crack localization,

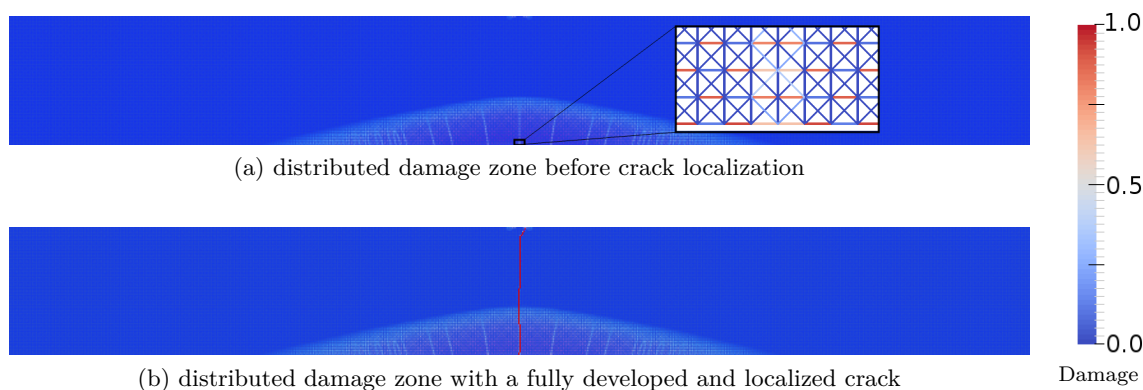


Figure 6.16: The damage level ω in all interactions computed with the full lattice model for the three-point bending test. The distributed damage zone, consisting of alternately unloading interactions under damage and elastically, is shown with a close-up of the lattice one step before crack initialization in (a), and in the last step of the simulation for the final distributed damage zone and fully developed crack path in (b).

however, all effective methods provide satisfactory qualitative description of the force–displacement curve. The QC coarse method suffers from an initially too stiff response as a consequence of a rather coarse mesh, although with adaptive refinement this discrepancy drops rapidly. To compare all methods quantitatively, the relative errors in the initial elastic stiffnesses and peak forces are summarized in Tab. 6.7. Here we conclude that the FE-CZ model underestimates the peak force by more than 23%, while being very accurate in the initial elastic stiffness. Although the QC coarse method overestimates the initial elastic stiffness by approximately 21%, it delivers an accurate peak force. The QC fine method provides very accurate results in both considered quantities.

The rather unexpected pronounced softening before crack localization is caused by an extensive damage region in which individual horizontal bonds are damaging or unload elastically in an alternating way, forming a checker-board pattern, cf. Fig. 6.16a. This region is hereafter referred to as the Distributed Damage Zone (DDZ). This partially damaged region expands progressively along the bottom edge of the specimen and upwards, featuring multiple possible crack paths (emerging in Fig. 6.16a) until localization occurs and the central crack is formed. A similar behavior is observed for both Full and QC models, whereas the FE-CZ model is unable to capture the initial DDZ as a consequence of the linear-elastic constitutive law used in the bulk material, which results in significant inaccuracies before the crack localizes (recall Fig. 6.17). Additional simulations (not shown) indicate that the observed errors further increase with increasing ductility of the considered exponential softening law of the individual bonds.

To verify that the distributed damage zone is at the root of the inaccuracy observed in the FE-CZ model, an additional simulation has been performed, in which damage was confined to evolve only in bonds located within $2l_0$ distance from the vertical axis of the symmetry, whereas the remainder of the specimen was considered as purely elastic. This version of the full model provided results (referred to as Lattice without DDZ) closely resembling those of the FE-CZ model. In particular, the relative error in the peak force of the FE-CZ model drops to 4.41% compared to this reduced version of the full model, thus revealing that the error in the peak force indeed results from the neglected distributed damage zone. To increase the accuracy of the FE-CZ model, multiple cohesive cracks should be realized in the distributed damage zone or a more involved constitutive model

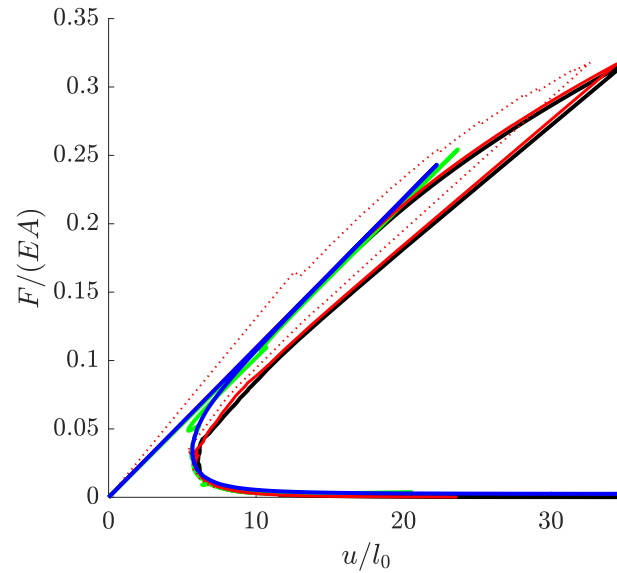
with damage should be employed for the bulk material.

To compare the crack lengths (Fig. 6.18) and the crack openings (Fig. 6.19), the central crack needs to be identified and its opening measured in discrete lattice systems. To this end, a fixed crack width of l_0 is considered, consisting of the most damaged bonds in each horizontal layer of bonds; if no damage occurs in a horizontal layer, the central bond (located at the specimen's vertical axis of symmetry) is used. The normal crack opening Δ_n is then defined as the difference between the horizontal displacements of the two end nodes of all crack bonds. Due to elasticity, negative crack openings are observed in compressive regions. The crack length, expressed as a function of the CMOD, is shown in Fig. 6.18. All approximate methods show comparable results, although both QC approaches are slightly more accurate, capturing also some of the initial irregularities of the Full model response. The FE-CZ method in general shows a smooth crack evolution as compared to the discrete models, initially overestimating the crack length, but then converging rapidly to the reference.

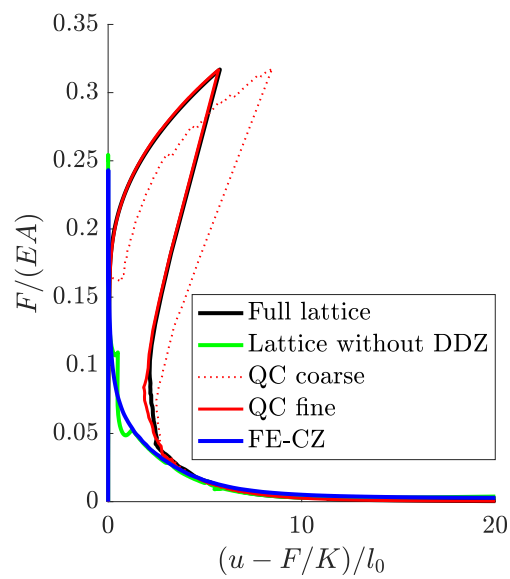
The corresponding crack opening diagrams, represented as the normalized normal opening Δ_n/l_0 and plotted against the normalized vertical coordinate y/l_0 , are shown in Fig. 6.19. The presented results correspond to a pre-peak configuration of $F/EA = 0.24$ (Fig. 6.19a), and to a post-peak configuration of $F/EA = 0.035$ (Fig. 6.19b). Here we clearly see that the FE-CZ and Full model without distributed damage zone (Lattice without distributed damage zone) tend to show significantly larger crack mouth openings before the crack localizes, whereas both QC models provide accurate predictions. Upon crack localization, in accordance with previously discussed results, all effective methods achieve a good accuracy.

The numerical performances of all methods are shown in Fig. 6.20 in terms of the number of DOFs relative to the number of DOFs of the fully-resolved system. Here we see that although both QC models start with noticeably different meshes (Figs. 6.15a and 6.15b), once the fully-resolved DDZ develops, the relative number of DOFs increases from approximately 0.5% to roughly 15% for both QC approaches. Upon crack localization, the mesh coarsens and the relative number of DOFs drops to 0.5% again. The FE-CZ model has no adaptivity, having a constant 1% relative number of DOFs. The achieved performance in terms of computing times is summarized in Tab 6.7. Here we see that in spite of relatively large savings in the number of DOFs, both QC methods attain a speed-up of only a factor of 2.5. This is caused mainly by the initial full refinement of the entire distributed damage zone (covering almost 1/7 of the domain in both QC models) and its subsequent coarsening, which require a substantial number of mesh iterations. This behavior can be avoided by using more aggressive mesh refinement/coarsening strategies, in which the mesh is updated only in selected steps or only a limited number of mesh iterations is allowed in each time step. Such modifications can significantly reduce the number of mesh iterations and thus speed up the simulation. However, if too aggressive, they may compromise the accuracy of the QC simulations. In cases with more localized phenomena, a higher computational gain by the QC methods is expected. The FE-CZ model, on the contrary, provides a substantial speed-up of the order of 50, but at the cost of a lower accuracy as compared to the Full solution.

Unlike the atomistic problem of Section 6.2, extensions to more relevant 3D structural lattices can be realized without significant changes to both the general QC as well as the homogenized model with fixed cohesive zones. In situations in which a crack trajectory is not known a priori and fixed cohesive zones cannot be used, alternative options for the homogenized model may be used. For instance, either multiple cohesive zones can



(a) force–displacement diagrams



(b) inelastic part of force–displacement diagrams

Figure 6.17: Normalized force–displacement diagrams for the three-point bending test. (a) Complete diagrams. (b) Inelastic parts of the force–displacement diagrams, in which the elastic part of the displacement, F/K , is subtracted from the total macroscopic displacement u and only the inelastic part is plotted.

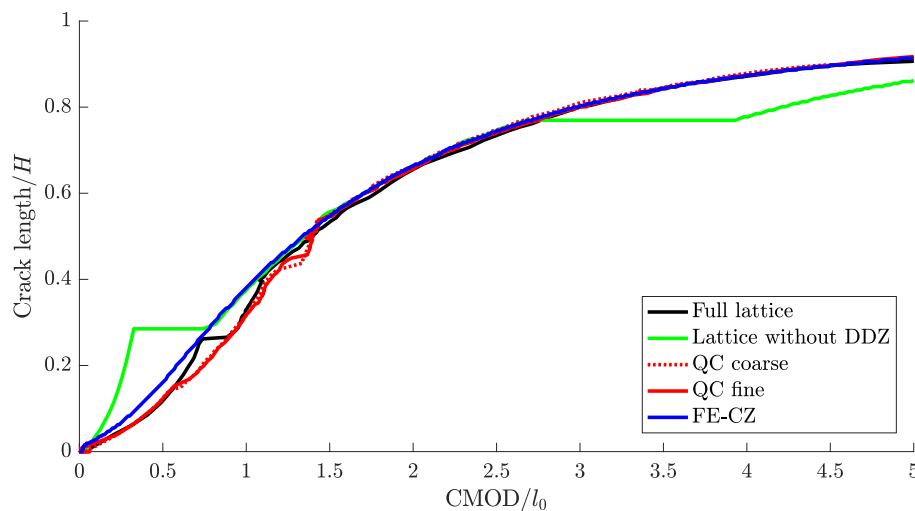


Figure 6.18: The normalized crack length as a function of the Crack Mouth Opening (CMOD).

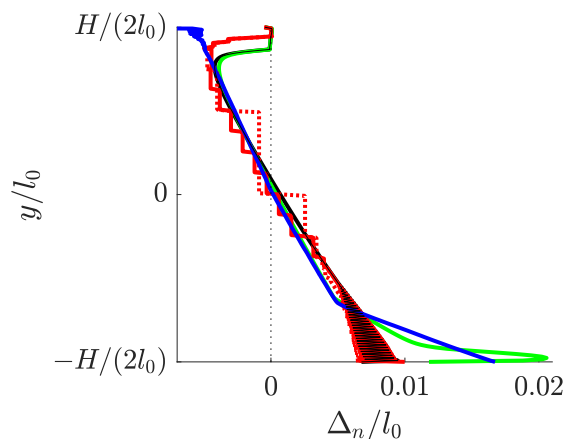
Table 6.7: The numerical performance corresponding to the individual computational models used for the three-point bending test example.

	elastic stiffness error	peak force error	minimal/maximal DOFs	computational demand
Full solution	0	0	1, 053, 183	1.0
QC coarse	+21.32%	+0.28%	1, 464/132, 380	$\approx 1/2.5$
QC fine	+1.61%	-0.03%	5, 408/152, 456	$\approx 1/2.5$
FE-CZ	+0.78%	-23.30%	10, 175	$\approx 1/50$

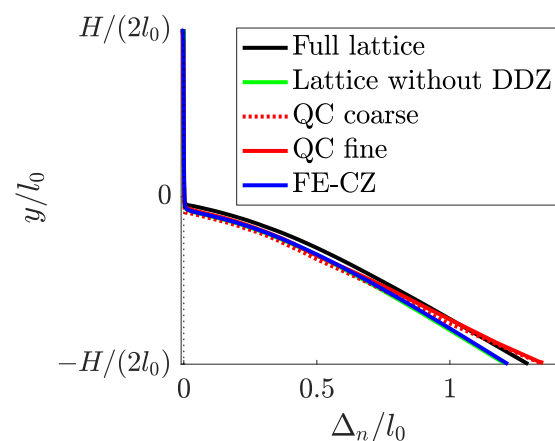
be considered in the region in which crack is expected, or cohesive zones can be built in between all elements [107]. However, the latter option significantly increases the induced computing efforts and the resulting crack trajectory may moreover be mesh dependent. The extended finite element method, with cohesive formulation, is another interesting alternative [105, 18, 107], suffering, nevertheless, from technical difficulties for situations involving crack curving and crack branching.

Summary and conclusion

This paper has provided a detailed description and thorough comparison of two classes of homogenization techniques towards effective representation of two-dimensional discrete systems. The first class, referred to as QuasiContinuum (QC) based methods, considers the fully-resolved underlying discrete system, which is subsequently reduced through suitable mathematical tools such as projection and reduced integration. The second class, referred to as homogenization based methods, consists in homogenizing the underlying discrete system first, into which localized discrete mechanisms are subsequently embedded. The necessary theoretical basis for both classes of methods has been reviewed, and their performance demonstrated on two representative examples considered at the nano- and meso-scale, revealing their strengths and weaknesses.



(a) crack opening, pre-peak load



(b) crack opening, post-peak load

Figure 6.19: Normalized crack opening profiles for the three-point bending test. (a) Pre-peak opening corresponding to loading force $F/EA = 0.24$, and (b) post-peak opening corresponding to loading force $F/EA = 0.035$. Due to lack of distributed damage, the FE-CZ model initially significantly deviates (a), whereas upon crack localization it becomes accurate (b).

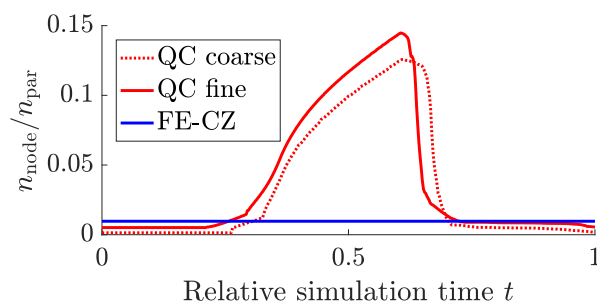


Figure 6.20: Evolution of the number of DOFs relative to that of the fully-resolved model.

The first class, i.e., QC based models, is capable of capturing all important phenomena of the underlying full model. The obtained results are thus sufficiently accurate for the examples considered at both scales, reproducing also unexpected mechanical behavior such as dislocation reflection and distributed cracking. At the same time, QC based models provide a significant reduction of the original problem in terms of the number of Degrees Of Freedom (DOFs), although the achieved savings in computing times might be less significant due to the computational cost involved with mesh adaptivity. Typical speed-ups achieved in this work are of the order of 2.5–15.

The second class, i.e., homogenization based approaches, represented by the Peierls–Nabarro model at the nanoscale and by the cohesive zone model at the mesoscale, is often more efficient as compared to the QC based methods in terms of computational speed-up, although it is usually less accurate because the effects that have their origin in the discreteness of a system (e.g., Peierls stress) cannot be captured by the continuum approach. Typical savings in computing times corresponded to 5–50 in comparison with the full model. Although primal kinematic quantities such as overall displacement, dislocation positions, or crack opening and crack length are usually captured with adequate accuracy, the associated conjugate quantities such as transmission stress or maximum peak force suffer from more significant errors. The most significant weakness of the homogenization-based models is that they are constructed based on prior assumptions on the response of the system, thus being unable to capture general behavior and unexpected phenomena such as dislocation reflection, distributed cracking, or crack branching. This may be acceptable if one is certain that no such phenomena will occur, or even desired if one particular phenomena is to be studied that would only be clouded by the unexpected phenomena. If this is not the case, model limitations can be lifted by adopting, e.g., multiple glide planes of different orientations, assuming all inter-element interfaces as cohesive zones, or using an extended formulation combined with cohesive zone models. Such extensions might, nevertheless, significantly complicate the entire procedure and increase the associated computing time.

The resulting computational savings achieved by all reduced models are substantially affected by the level of scale separation, which is not very large in the presented representative examples. With increasing scale separation, e.g., increasing the size of specimen domain while fixing the lattice spacing, a significant improvement in observed speed-ups may be reached.

Both presented classes are sufficiently general tools for predicting localized phenomena in discrete systems. The homogenization based models are usually more efficient, although they might lack a sufficient level of detail and accuracy. The QC based methods, on the other hand, exhibit greater flexibility compensated by higher computing costs. Which method to adopt thus strongly depends on the desired accuracy and the acceptable computational costs. However, one should keep in mind the potential occurrence of unexpected phenomena. The QC based methods can thus be considered a safe option that may bring, nevertheless, only limited gain. Larger gain may be achieved by dedicated homogenized models, but safe option would be to check their results by a flexible QC method to verify occurrence of any unexpected phenomena.

Chapter 7

Conclusions and summary

The objective of the thesis was to investigate and extend the applicability of the Quasi-Continuum (QC) method especially for problems related to modeling of inelastic materials with random microstructures.

In the first part of the thesis (Chapter 2), the QC method is extended to irregular lattices with elastic axial interactions. To achieve this goal, the homogenization-based summation rule is derived to simplify the energy of irregular lattices. Then the lattice network in the region of low interest is represented by the effective stiffness tensor which can be assembled from geometry of the lattice. Five different homogenization approaches with various levels of simplification have been proposed considering either global or local homogenization represented with an isotropic or anisotropic stiffness tensor. Accuracy and efficiency of individual approaches have been evaluated in two- and three-dimensional patch tests and then those approaches were used to model crack propagation in an elastic-brittle disordered lattice. The numerical examples have shown that the approaches with global homogenization are significantly faster but they suffer from a higher stiffness error because explicitly evaluated links are artificially accounted for twice. At the same time, approaches based on the isotropic homogenization tend to underestimate the global stiffness if the material is significantly anisotropic. In such cases, the global isotropic approach may seemingly appear to be more accurate in certain examples but accuracy and convergence are not guaranteed. On the other hand, the approach based on the local anisotropic homogenization turns out to be very powerful. The homogenization error observed for the local anisotropic approach is almost negligible and therefore this approach provides almost as accurate results as full particle model while running substantially faster. Macroscopic properties associated with the global stiffness are naturally affected by a certain error induced by interpolation, however, local phenomena such as cracking are well captured by a sufficiently large area of high interest. Altogether, the idea of the homogenization-based QC approach presented in this chapter provides a successful extension of the QC method to irregular lattices and has been recently adopted by Ghareeb and Elbanna [38] for modeling of irregular polymer networks.

In another part of the thesis (Chapter 5), the idea of the homogenization-based QC method for irregular lattices is further extended to a more general case of elastoplastic interactions. In this case, the concepts borrowed from the microplane theory developed by Bažant and coworkers [8] are exploited for an efficient replacement of the discrete model by an equivalent continuum in the regions of low interest. A corresponding microplane-based summation rule for the QC method is derived. In analogy with the elastic case, the adopted microplane model is considered as isotropic or anisotropic and assembled globally

or locally. The presented examples reveal the properties of individual microplane-based approaches analogous to the previous elastic case. The simplified approaches with the isotropic microplane model turned out to overestimate the total stiffness and underestimate the yield force if a homogenized microstructure significantly deviates from isotropy. In contrast, the local homogenization approach with the anisotropic microplane model is able to capture a contribution of individual links in each element and represent them by relevant microplanes and therefore provides very accurate results regardless of a microstructure type. Similarly to the elastic case, for the anisotropic local microplane model, almost negligible homogenization error can be observed since almost all deviations from the full model are mainly caused by the interpolation error. The presented microplane-based QC method has been used to model a structural failure caused by forming of a plastic mechanism or by localization of a cohesive crack.

An adaptive scheme that provides suitable changes of the region of high interest during the simulation is one of the key ingredients of the QC method. Not only that an appropriate modification of the regions of high interest leads to a substantial increase of accuracy but in specific cases such as simulation of crack propagation or damage evolution, adaptivity is necessary in order to represent the correct physical behavior. Therefore, two parts of this thesis (Chapters 3 and 4) are dedicated to the development of adaptive algorithms for the QC simulation. Firstly, the adaptive algorithm for disordered lattices is introduced and applied for modeling of crack propagation in elastic-brittle lattices. The proposed refinement criterion is based on an identification of broken links according to their maximum strain. This allows not only a propagation of an existing crack but also an initialization of new cracks. Secondly, three different adaptive refinement indicators for regular atomic lattices are proposed based on (i) the Zienkiewicz–Zhu criterion (used for the deformation gradient), (ii) local atoms' site energy, and (iii) local lattice registry. These indicators are used for modeling of dislocation propagation during a nanoindentation. All three proposed indicators are able to provide equivalent results and capture a motion of dislocation with a high accuracy. The adaptive approach based on the Zienkiewicz–Zhu error estimator requires more mesh iterations and therefore performs slightly slower in comparison with the other two indicators. In addition to that, for the adaptive modeling of plastic interactions (considered in Chapter 5), a new refinement criterion based on normal strain of individual microplanes is proposed and investigated. Unlike previous cases, this criterion does not need any additional computational effort and at the same time it reveals to be very effective to control the size of the fully refined region.

In the last part of this thesis (Chapter 6), two broad classes of multiscale techniques, which conceptually differ significantly are compared. The first class, represented by the QC method, considers the fully-resolved discrete system, which is subsequently reduced through suitable mathematical tools such as projection and reduced integration. The second class of methods first homogenizes the discrete system into an equivalent continuum formulation, to which the main phenomena are added through specific enrichments. To demonstrate capabilities and limitations of both modeling philosophies, two examples are employed on different scales. In particular, dislocation propagation and pile-up against a coherent phase boundary is considered at the nanoscale level, whereas a three-point bending test of a concrete specimen with crack propagation is considered at the macroscale level. It is shown that whereas continuum models with embedded cohesive zones offer good performance to accuracy ratios, they might fail to capture an unexpected more complex mechanical behavior such as dislocation reflection or a distributed damage zone before a crack localization. The QC method, on the other hand, offers more flexibility and a higher

accuracy for a slightly higher computational cost.

This thesis provides a new concept of the homogenization-based summation rule for the QC method applicable to irregular inelastic lattices. The resulting methods and algorithms proposed in this thesis provide successful extensions of the QC method and increase its applicability to a wider range of materials and phenomena which make the QC concept even more powerful. Accuracy and efficiency of all proposed methods are evaluated by comparing against the corresponding fully-resolved discrete reference models. Presented examples have shown that the proposed QC-based approaches lead to a substantial reduction of the number of unknown DOFs and the number of links that need to be processed during a simulation. This reduction provides a significant simplification of the original problem which corresponds to an observed speed-up (in some examples by two orders of magnitude). It is worth noting that the speed-ups observed in this thesis were obtained mostly for relatively small illustrative examples. If the same microstructure is considered for modeling of larger domains, the scale separation becomes more significant. Therefore, even better speed-ups with a similar or better accuracy can be expected for larger examples. At the same time, results show that presented QC approaches are able to capture all important phenomena of the underlying full model. Despite the initial elastic stiffness may suffer from a relative large interpolation error, the subsequent inelastic behavior provides an acceptable agreement with the full model and the important quantities such as a global shape of load-displacement curves, maximum loading force, and macroscopic crack trajectories are captured with a high accuracy. Furthermore, the error induced by the reduction can be kept within acceptable limits by a suitable adaptive updating of the region of high interest.

Potential extensions

The methods and approaches presented in this thesis significantly increase the applicability of the QC method. However, there is still a lot of space for further continuation or additional potential extensions. Selected ideas for a future work are listed below:

- For irregular lattices, the presented constitutive law of individual interactions (links) was considered as elastic-brittle, perfectly elastoplastic, and elastoplastic with a linear kinematic hardening (or softening). A subsequent step would be an extension to additional material phenomena, e.g., to damage-based models. For that purpose the analogy of the microplane and truss models can still be exploited but some additional effort may be needed to deal with localization phenomena.
- For regular lattices, the interactions have been modeled as damageable with exponential softening law. Consequently, the state of such system is described in terms of a non-dissipative kinematic variable \underline{r} (storing the positions of all particles) and a dissipative component \underline{z} (storing the damage of all bonds). However, the QC simplification steps (interpolation and summation) are applied only to the kinematic variable \underline{r} . It is an open challenge to introduce analogous simplification rules applicable also for the dissipative variable \underline{z} .
- The particle model with axial interaction may be limited in application to materials with microstructural interactions dominated by a pure stretching. Therefore, another possible extension can consist in considering more general interactions including shear or bending stiffness of the bonds. To make particle interaction more

general, not only the displacements but also the rotations of individual particles must be considered.

- It may be interesting to combine the extension for irregular lattices with the generalized variant of the QC method [24], in which different effectively superimposed finite element shape functions are used for different types of lattice nodes.
- The interpolation rule used in the QC method originates from the Cauchy-Born rule [37] which describes the kinematics of atoms in a lattice. The traditional Cauchy-Born theory can be extended, e.g, by considering higher-order gradients [93] or by adding a surface energy term [72, 73]. An application of extended Cauchy-Born rule in the QC method would increase an accuracy of modeling of nanoscale structures where surface effects play an important role [2].

Bibliography

- [1] Amelang, J., Venturini, G., Kochmann, D., 2015. Summation rules for a fully non-local energy-based quasicontinuum method. *Journal of the Mechanics and Physics of Solids* 82, 378–413.
- [2] Amelang, J. S., Kochmann, D. M., 2015. Surface effects in nanoscale structures investigated by a fully-nonlocal energy-based quasicontinuum method. *Mechanics of Materials* 90, 166–184.
- [3] Arndt, M., Luskin, M., 2007. Goal-oriented atomistic-continuum adaptivity for the quasicontinuum approximation. *International Journal for Multiscale Computational Engineering* 5 (5).
- [4] Arndt, M., Luskin, M., 2008. Error estimation and atomistic-continuum adaptivity for the quasicontinuum approximation of a Frenkel–Kontorova model. *Multiscale Modeling & Simulation* 7 (1), 147–170.
- [5] Asferg, J. L., Poulsen, P. N., Nielsen, L. O., 2007. A consistent partly cracked XFEM element for cohesive crack growth. *International Journal for Numerical Methods in Engineering* 72 (4), 464–485.
- [6] Barenblatt, G. I., 1962. The mathematical theory of equilibrium cracks in brittle fracture. In: *Advances in applied mechanics*. Vol. 7. Elsevier, pp. 55–129.
- [7] Bažant, Z. P., 2010. Can multiscale-multiphysics methods predict softening damage and structural failure? *International Journal for Multiscale Computational Engineering* 8 (1).
- [8] Bažant, Z. P., Oh, B. H., 1985. Microplane model for progressive fracture of concrete and rock. *Journal of Engineering Mechanics* 111 (4), 559–582.
- [9] Bažant, Z. P., Tabbara, M. R., Kazemi, M. T., Pijaudier-Cabot, G., 1990. Random particle model for fracture of aggregate or fiber composites. *Journal of engineering mechanics* 116 (8), 1686–1705.
- [10] Beex, L., Kerfriden, P., Rabczuk, T., Bordas, S. P. A., 2014. Quasicontinuum-based multiscale approaches for plate-like beam lattices experiencing in-plane and out-of-plane deformation. *Computer Methods in Applied Mechanics and Engineering* 279, 348–378.
- [11] Beex, L., Peerlings, R., Geers, M., 2011. A quasicontinuum methodology for multi-scale analyses of discrete microstructural models. *International Journal for Numerical Methods in Engineering* 87 (7), 701–718.

-
- [12] Beex, L., Peerlings, R., Geers, M., 2014. Central summation in the quasicontinuum method. *Journal of the Mechanics and Physics of Solids* 70, 242–261.
- [13] Beex, L., Peerlings, R., Geers, M., 2014. A multiscale quasicontinuum method for dissipative lattice models and discrete networks. *Journal of the Mechanics and Physics of Solids* 64, 154–169.
- [14] Beex, L., Peerlings, R., Geers, M., 2014. A multiscale quasicontinuum method for lattice models with bond failure and fiber sliding. *Computer Methods in Applied Mechanics and Engineering* 269, 108–122.
- [15] Beex, L., Peerlings, R., Van Os, K., Geers, M., 2015. The mechanical reliability of an electronic textile investigated using the virtual-power-based quasicontinuum method. *Mechanics of Materials* 80, 52–66.
- [16] Beex, L., Rokoš, O., Zeman, J., Bordas, S., 2015. Higher-order quasicontinuum methods for elastic and dissipative lattice models: uniaxial deformation and pure bending. *GAMM-Mitteilungen* 38 (2), 344–368.
- [17] Beex, L., Verberne, C., Peerlings, R., 2013. Experimental identification of a lattice model for woven fabrics: application to electronic textile. *Composites Part A: Applied Science and Manufacturing* 48, 82–92.
- [18] Benvenuti, E., 2008. A regularized XFEM framework for embedded cohesive interfaces. *Computer Methods in Applied Mechanics and Engineering* 197 (49-50), 4367–4378.
- [19] Bormann, F., Mikeš, K., Rokoš, O., Peerlings, R., 2020. The Peierls–Nabarro finite element model in two-phase microstructures—A comparison with atomistic. *Mechanics of Materials* 150, 103555.
- [20] Bormann, F., Peerlings, R. H., Geers, M. G., Svendsen, B., 2019. A computational approach towards modelling dislocation transmission across phase boundaries. *Philosophical Magazine* 99 (17), 2126–2151.
- [21] Bormann, F., Peerlings, R. H. J., Geers, M. G. D., 2018. Application and adaptation of the truncated Newton method for non-convex plasticity problems. arXiv preprint arXiv:1810.13393.
- [22] Bosco, E., Peerlings, R. H., Geers, M. G., 2015. Predicting hygro-elastic properties of paper sheets based on an idealized model of the underlying fibrous network. *International Journal of Solids and Structures* 56, 43–52.
- [23] Budarapu, P. R., Gracie, R., Bordas, S. P., Rabczuk, T., 2014. An adaptive multi-scale method for quasi-static crack growth. *Computational Mechanics* 53 (6), 1129–1148.
- [24] Chen, L., Beex, L. A., Berke, P. Z., Massart, T. J., Bordas, S. P., 2020. Generalized quasicontinuum modeling of metallic lattices with geometrical and material nonlinearity and variability. *Computer Methods in Applied Mechanics and Engineering* 366, 112878.

- [25] Chen, L., Berke, P. Z., Massart, T. J., Beex, L. A., Magliulo, M., Bordas, S. P., 2021. A refinement indicator for adaptive quasicontinuum approaches for structural lattices. *International Journal for Numerical Methods in Engineering*.
- [26] Cleveringa, H., Van der Giessen, E., Needleman, A., 2000. A discrete dislocation analysis of mode I crack growth. *Journal of the Mechanics and Physics of Solids* 48 (6-7), 1133–1157.
- [27] Conn, A. R., Gould, N. I., Toint, P. L., 2000. Trust region methods. SIAM.
- [28] Curtin, W. A., Miller, R. E., 2003. Atomistic/continuum coupling in computational materials science. *Modelling and simulation in materials science and engineering* 11 (3), R33.
- [29] Cusatis, G., Pelessone, D., Mencarelli, A., 2011. Lattice discrete particle model (LDPM) for failure behavior of concrete. I: Theory. *Cement and Concrete Composites* 33 (9), 881–890.
- [30] de Borst, R., 2003. Numerical aspects of cohesive-zone models. *Engineering Fracture Mechanics* 70 (14), 1743–1757.
- [31] Decelis, B., Argon, A. S., Yip, S., 1983. Molecular dynamics simulation of crack tip processes in alpha-iron and copper. *Journal of Applied Physics* 54 (9), 4864–4878.
- [32] Desmoulins, A., Kochmann, D. M., 2017. Local and nonlocal continuum modeling of inelastic periodic networks applied to stretching-dominated trusses. *Computer Methods in Applied Mechanics and Engineering* 313, 85–105.
- [33] Duesbery, M., Michel, D., Joos, B., 1989. Molecular dynamics studies of dislocations in Si. *MRS Proceedings* 163, 941.
- [34] Dugdale, D. S., 1960. Yielding of steel sheets containing slits. *Journal of the Mechanics and Physics of Solids* 8 (2), 100–104.
- [35] Dupuy, L. M., Tadmor, E. B., Miller, R. E., Phillips, R., 2005. Finite-temperature quasicontinuum: Molecular dynamics without all the atoms. *Physical Review Letters* 95 (6), 060202.
- [36] Elices, M. G. G. V., Guinea, G. V., Gomez, J., Planas, J., 2002. The cohesive zone model: advantages, limitations and challenges. *Engineering Fracture Mechanics* 69 (2), 137–163.
- [37] Ericksen, J. L., 1984. The Cauchy and Born hypotheses for crystals. *Phase Transformations and Material Instabilities in Solids*, 61–77.
- [38] Ghareeb, A., Elbanna, A., 2020. An adaptive quasicontinuum approach for modeling fracture in networked materials: Application to modeling of polymer networks. *Journal of the Mechanics and Physics of Solids* 137, 103819.
- [39] Gutiérrez, M. A., 2004. Energy release control for numerical simulations of failure in quasi-brittle solids. *Communications in Numerical Methods in Engineering* 20 (1), 19–29.

- [40] Hill, R., 1963. Elastic properties of reinforced solids: some theoretical principles. *Journal of the Mechanics and Physics of Solids* 11 (5), 357–372.
- [41] Hirth, J. P., Lothe, J., Mura, T., 1983. Theory of dislocations. *Journal of Applied Mechanics* 50, 476.
- [42] Jin, C., Buratti, N., Stacchini, M., Savoia, M., Cusatis, G., 2016. Lattice discrete particle modeling of fiber reinforced concrete: Experiments and simulations. *European Journal of Mechanics-A/Solids* 57, 85–107.
- [43] Jin, Z. H., Sun, C. T., 2006. A comparison of cohesive zone modeling and classical fracture mechanics based on near tip stress field. *International Journal of Solids and Structures* 43 (5), 1047–1060.
- [44] Jirásek, M., Bažant, Z. P., 2001. Inelastic analysis of structures. John Wiley & Sons.
- [45] Klein, P., Gao, H., 1998. Crack nucleation and growth as strain localization in a virtual-bond continuum. *Engineering Fracture Mechanics* 61 (1), 21–48.
- [46] Knap, J., Ortiz, M., 2001. An analysis of the quasicontinuum method. *Journal of the Mechanics and Physics of Solids* 49 (9), 1899–1923.
- [47] Kochmann, D. M., Amelang, J. S., 2016. The quasicontinuum method: Theory and applications. In: *Multiscale Materials Modeling for Nanomechanics*. Springer, pp. 159–193.
- [48] Kochmann, D. M., Venturini, G. N., 2014. A meshless quasicontinuum method based on local maximum-entropy interpolation. *Modelling and Simulation in Materials Science and Engineering* 22 (3), 034007.
- [49] Kulachenko, A., Uesaka, T., 2012. Direct simulations of fiber network deformation and failure. *Mechanics of Materials* 51, 1–14.
- [50] Kwon, S., Lee, Y., Park, J. Y., Sohn, D., Lim, J. H., Im, S., 2009. An efficient three-dimensional adaptive quasicontinuum method using variable-node elements. *Journal of Computational Physics* 228 (13), 4789–4810.
- [51] Lilliu, G., van Mier, J. G., 2003. 3D lattice type fracture model for concrete. *Engineering Fracture Mechanics* 70 (7-8), 927–941.
- [52] Liu, J., Chen, Z., Li, K., 2010. A 2-D lattice model for simulating the failure of paper. *Theoretical and Applied Fracture Mechanics* 54 (1), 1–10.
- [53] Liu, J., Deng, S., Zhang, J., Liang, N., 2007. Lattice type of fracture model for concrete. *Theoretical and Applied Fracture Mechanics* 48 (3), 269–284.
- [54] Luskin, M., Ortner, C., 2009. An analysis of node-based cluster summation rules in the quasicontinuum method. *SIAM Journal on Numerical Analysis* 47 (4), 3070–3086.
- [55] MacQueen, J., et al., 1967. Some methods for classification and analysis of multivariate observations. In: *Proceedings of the fifth Berkeley symposium on mathematical statistics and probability*. Vol. 1. Oakland, CA, USA, pp. 281–297.

- [56] Mandel, J., 1972. *Plasticité classique et viscoplasticité*, Lectures Notes Int. Centre for Mech. Sci. (Udine, 1971).
- [57] May, S., Vignollet, J., de Borst, R., 2016. A new arc-length control method based on the rates of the internal and the dissipated energy. *Engineering Computations* 100 (115), 100–115.
- [58] Memarnahavandi, A., Larsson, F., Runesson, K., 2015. A goal-oriented adaptive procedure for the quasi-continuum method with cluster approximation. *Computational Mechanics* 55 (4), 617–642.
- [59] Mielke, A., 2003. Energetic formulation of multiplicative elasto-plasticity using dissipation distances. *Continuum Mechanics and Thermodynamics* 15 (4), 351–382.
- [60] Mielke, A., 2005. Evolution of rate-independent systems. *Evolutionary equations* 2, 461–559.
- [61] Mielke, A., Roubíček, T., 2015. *Rate-Independent Systems: Theory and Application*, 1st Edition. Springer-Verlag New York.
- [62] Mikeš, K., Jirásek, M., 2015. The quasicontinuum method extended to disordered materials. In: *Proc. 15th Int. Conf. on Civil, Structural and Environmental Engineering Computing*, Civil-Comp Press Ltd, Stirling.
- [63] Mikeš, K., Jirásek, M., 2017. Adaptive quasicontinuum simulation of elastic-brittle disordered lattices. *Acta Polytechnica CTU Proceedings* 13, 80–84.
- [64] Mikeš, K., Jirásek, M., 2017. Quasicontinuum method combined with anisotropic microplane model. In: *Advanced Materials Research*. Vol. 1144. Trans Tech Publ, pp. 142–147.
- [65] Mikeš, K., Jirásek, M., 2017. Quasicontinuum method extended to irregular lattices. *Computers & Structures* 192, 50–70.
- [66] Mikeš, K., Rokoš, O., Peerlings, R. H., 2018. Molecular statics simulation of nanoindentation using adaptive quasicontinuum method. *Acta Polytechnica CTU Proceedings* 15, 57–62.
- [67] Miller, R., Tadmor, E., Phillips, R., Ortiz, M., 1998. Quasicontinuum simulation of fracture at the atomic scale. *Modelling and Simulation in Materials Science and Engineering* 6 (5), 607.
- [68] Miller, R. E., Tadmor, E. B., 2002. The quasicontinuum method: Overview, applications and current directions. *Journal of Computer-Aided Materials Design* 9 (3), 203–239.
- [69] Miller, R. E., Tadmor, E. B., 2009. A unified framework and performance benchmark of fourteen multiscale atomistic/continuum coupling methods. *Modelling and Simulation in Materials Science and Engineering* 17 (5), 053001.
- [70] Nabarro, F. R. N., 1947. Dislocations in a simple cubic lattice. *Proceedings of the Physical Society* 59 (2), 256.

- [71] Ožbolt, J., Li, Y., Kožar, I., 2001. Microplane model for concrete with relaxed kinematic constraint. *International Journal of Solids and Structures* 38 (16), 2683–2711.
- [72] Park, H. S., Klein, P. A., 2007. Surface Cauchy-Born analysis of surface stress effects on metallic nanowires. *Physical Review B* 75 (8), 085408.
- [73] Park, H. S., Klein, P. A., 2008. A surface Cauchy-Born model for silicon nanostructures. *Computer methods in applied mechanics and engineering* 197 (41-42), 3249–3260.
- [74] Parthasarathy, T., Rao, S., Dimiduk, D., 1993. Molecular statics simulations of core structures and motion of dislocations in NiAl. *Philosophical Magazine A* 67 (3), 643–662.
- [75] Patzák, B., 2012. OOFEM—an object-oriented simulation tool for advanced modeling of materials and structures. *Acta Polytechnica* 52 (6).
- [76] Patzák, B., Bittnar, Z., 2001. Design of object oriented finite element code. *Advances in Engineering Software* 32 (10-11), 759–767.
- [77] Patzák, B., Rypel, D., 2012. Object-oriented, parallel finite element framework with dynamic load balancing. *Advances in Engineering Software* 47 (1), 35–50.
- [78] Peierls, R., 1940. The size of a dislocation. *Proceedings of the Physical Society* 52 (1), 34.
- [79] Peng, X., Cao, J., 2005. A continuum mechanics-based non-orthogonal constitutive model for woven composite fabrics. *Composites part A: Applied Science and manufacturing* 36 (6), 859–874.
- [80] Phillips, R., Rodney, D., Shenoy, V., Tadmor, E., Ortiz, M., 1999. Hierarchical models of plasticity: dislocation nucleation and interaction. *Modelling and Simulation in Materials Science and Engineering* 7 (5), 769.
- [81] Phlipot, G. P., Kochmann, D. M., 2019. A quasicontinuum theory for the nonlinear mechanical response of general periodic truss lattices. *Journal of the Mechanics and Physics of Solids* 124, 758–780.
- [82] Ridruejo, A., González, C., LLorca, J., 2010. Damage micromechanisms and notch sensitivity of glass-fiber non-woven felts: An experimental and numerical study. *Journal of the Mechanics and Physics of Solids* 58 (10), 1628–1645.
- [83] Rokoš, O., Beex, L. A. A., Zeman, J., Peerlings, R. H. J., 2016. A variational formulation of dissipative quasicontinuum methods. *International Journal of Solids and Structures* 102, 214–229.
- [84] Rokoš, O., Peerlings, R. H. J., Zeman, J., 2017. eXtended variational quasicontinuum methodology for lattice networks with damage and crack propagation. *Computer Methods in Applied Mechanics and Engineering* 320, 769–792.
- [85] Rokoš, O., Peerlings, R. H. J., Zeman, J., Beex, L. A. A., 2017. An adaptive variational quasicontinuum methodology for lattice networks with localized damage. *International Journal for Numerical Methods in Engineering* 112 (2), 174–200.

- [86] Rypl, D., 2004. T3D mesh generator. URL: <http://ksm.fsv.cvut.cz/dr/t3d.html>.
- [87] Schlangen, E., Garboczi, E., 1997. Fracture simulations of concrete using lattice models: computational aspects. *Engineering fracture mechanics* 57 (2-3), 319–332.
- [88] Schoeck, G., 1994. The generalized Peierls–Nabarro model. *Philosophical Magazine A* 69 (6), 1085–1095.
- [89] Shastry, V., Farkas, D., 1996. Molecular statics simulation of fracture in α -iron. *Modelling and Simulation in Materials Science and Engineering* 4 (5), 473.
- [90] Shenoy, V., Miller, R., Tadmor, E., Rodney, D., Phillips, R., Ortiz, M., 1999. An adaptive finite element approach to atomic-scale mechanics—the quasicontinuum method. *Journal of the Mechanics and Physics of Solids* 47 (3), 611–642.
- [91] Steinmann, P., Elizondo, A., Sunyk, R., 2006. Studies of validity of the Cauchy–Born rule by direct comparison of continuum and atomistic modelling. *Modelling and Simulation in Materials Science and Engineering* 15 (1), S271.
- [92] Sun, C. T., Jin, Z. H., 2012. Chapter 9 - Cohesive zone model. In: Sun, C. T., Jin, Z. H. (Eds.), *Fracture Mechanics*. Academic Press, Boston, pp. 227 – 246.
- [93] Sunyk, R., Steinmann, P., 2003. On higher gradients in continuum-atomistic modelling. *International Journal of Solids and Structures* 40 (24), 6877–6896.
- [94] Swadener, J., Baskes, M., Nastasi, M., 2002. Molecular dynamics simulation of brittle fracture in silicon. *Physical Review Letters* 89 (8), 085503.
- [95] Tadmor, E., Miller, R., 2005. The theory and implementation of the quasicontinuum method. In: *Handbook of Materials Modeling*. Springer, pp. 663–682.
- [96] Tadmor, E., Miller, R., Phillips, R., Ortiz, M., 1999. Nanoindentation and incipient plasticity. *Journal of Materials Research* 14 (6), 2233–2250.
- [97] Tadmor, E. B., Legoll, F., Kim, W., Dupuy, L., Miller, R. E., 2013. Finite-temperature quasi-continuum. *Applied Mechanics Reviews* 65 (1).
- [98] Tadmor, E. B., Miller, R. E., 2011. *Modeling materials: continuum, atomistic and multiscale techniques*. Cambridge University Press.
- [99] Tadmor, E. B., Ortiz, M., Phillips, R., 1996. Quasicontinuum analysis of defects in solids. *Philosophical magazine A* 73 (6), 1529–1563.
- [100] Tadmor, E. B., Phillips, R., Ortiz, M., 1996. Mixed atomistic and continuum models of deformation in solids. *Langmuir* 12 (19), 4529–4534.
- [101] Tembhekar, I., Amelang, J. S., Munk, L., Kochmann, D. M., 2017. Automatic adaptivity in the fully nonlocal quasicontinuum method for coarse-grained atomistic simulations. *International Journal for Numerical Methods in Engineering* 110 (9), 878–900.
- [102] Van der Giessen, E., Needleman, A., 1995. Discrete dislocation plasticity: a simple planar model. *Modelling and Simulation in Materials Science and Engineering* 3 (5), 689.

-
- [103] Verhoosel, C. V., Remmers, J. J. C., Gutiérrez, M. A., 2009. A dissipation-based arc-length method for robust simulation of brittle and ductile failure. *International Journal for Numerical Methods in Engineering* 77 (9), 1290–1321.
- [104] Vitek, V., 1968. Intrinsic stacking faults in body-centred cubic crystals. *The Philosophical Magazine: A Journal of Theoretical Experimental and Applied Physics* 18 (154), 773–786.
- [105] Wang, H., 2015. Numerical modeling of non-planar hydraulic fracture propagation in brittle and ductile rocks using XFEM with cohesive zone method. *Journal of Petroleum Science and Engineering* 135, 127–140.
- [106] Wilbrink, D., Beex, L., Peerlings, R., 2013. A discrete network model for bond failure and frictional sliding in fibrous materials. *International journal of Solids and Structures* 50 (9), 1354–1363.
- [107] Xu, X.-P., Needleman, A., 1994. Numerical simulations of fast crack growth in brittle solids. *Journal of the Mechanics and Physics of Solids* 42 (9), 1397–1434.
- [108] Yamakov, V., Wolf, D., Phillpot, S. R., Mukherjee, A. K., Gleiter, H., 2002. Dislocation processes in the deformation of nanocrystalline aluminium by molecular-dynamics simulation. *Nature materials* 1 (1), 45.
- [109] Zhou, S., Curtin, W. A., 1995. Failure of fiber composites: a lattice green function model. *Acta Metallurgica et Materialia* 43 (8), 3093–3104.
- [110] Zienkiewicz, O. C., Zhu, J. Z., 1987. A simple error estimator and adaptive procedure for practical engineering analysis. *International Journal for Numerical Methods in Engineering* 24 (2), 337–357.
- [111] Zienkiewicz, O. C., Zhu, J. Z., 1992. The superconvergent patch recovery and a posteriori error estimates. Part 2: Error estimates and adaptivity. *International Journal for Numerical Methods in Engineering* 33 (7), 1365–1382.